공학박사학위논문

저샘플링 및 고샘플링 신호를 이용한 불확실성 기반 고장 진단 프레임워크

An Uncertainty-Aware Framework for Fault Diagnosis Using Low and High Sampling Rate Signals

2023 년 8 월

서울대학교 대학원

기계항공공학부

나 규 민

저샘플링 및 고샘플링 신호를 이용한 불확실성 기반 고장 진단 프레임워크

An Uncertainty-Aware Framework for Fault Diagnosis Using Low and High Sampling Rate Signals

지도교수 윤 병 동

이 논문을 공학박사 학위논문으로 제출함

2023 년 4 월

서울대학교 대학원
기계항공공학부
나 규 민

나규민의 공학박사 학위논문을 인준함

2023 년 6 월

위 원 장 : 김 윤 영 (인)

부위원장 : 윤 병 동 (인)

위 원 : 김 도 년 (인)

위 원 : 조 규 진 (인)

위 원 : 윤 헌 준 (인)

Abstract

An Uncertainty-Aware Framework for Fault Diagnosis Using Low and High Sampling Rate Signals

Kyumin Na
Department of Mechanical and Aerospace Engineering
The Graduate School
Seoul National University

With the development of the 4th industrial revolution, industrial systems are growing in size and complexity, and automation systems are increasingly being introduced to manage and control them. However, unexpected fault in these systems can have significant social, economic, and human consequences. To prevent and diagnose such failures, researchers are focusing on failure diagnosis techniques for various components of the system. These techniques aim to analyze potential failures in the system, quantify them using health indicators, and manage the health status of the system.

In industry, a signal system is being developed to control and manage the industrial systems using various signals such as temperature, pressure, operation, vibration, and acoustic emission signals. Among these, vibration and acoustic emission signals are considered highly sensitive in evaluating the health of the system. These signals are typically acquired using data acquisition sensors and

systems with a high sampling frequency of 20 kHz or more. When such high-frequency signals are measured, the main method used for evaluating the health of the system is to perform spectrum analysis and compare the results with those expected in a normal state. The high-sampling signal-based spectrum analysis method is particularly effective for diagnosing early-stage gradual failure or small energy changes such as fine cracks. This approach has been validated in numerous studies and has even been successfully applied in industrial settings. However, for large-scale systems such as modern industrial systems, utilizing high-sampling signals for diagnosis is challenging. The data acquisition systems used for each sensor typically have limited computational capabilities, only able to perform simple calculations such as pre-amplification and linear frequency filtering. Analyzing high-sampling signals through time frequency analysis and other similar techniques requires additional computational facilities that are not readily available in these systems. To overcome the computational burden of analyzing high-sampling signals, low-sampling signals such as root mean square and band pass energy are commonly used in industrial systems for fault diagnosis. However, the applicability of such low-sampling signal-based methods is limited to detecting only radical or large-scale faults that increase energy in all frequency bands, and cannot detect specific frequency reactions. Additionally, a large number of sensors may be reacted to the fault because applicable range for fault diagnosis is restricted on the severe fault, causing inefficiency in maintenance after fault detection. Lastly, the signals measured in industrial sites are often affected by noise or external signals, which results in relatively greater uncertainty compared to signals acquired in laboratories. As a result, it is important to consider uncertainty in the methodology applied to industrial systems in order to estimate or prevent the degree of error that may occur during actual application.

Given the current state of industrial systems, it is possible to conduct a fault

diagnosis study that efficiently utilizes both low-sampling and high-sampling signals. However, conventional fault diagnosis techniques for industrial systems face three main problems that need to be addressed. Firstly, in low-sampling signal based fault diagnosis, a large number of sensors could respond, making it necessary to estimate the location of the fault for efficient maintenance. Secondly, high-sampling signal-based diagnosis requires a large amount of computation, so a technique capable of robust fault diagnosis is needed even when using a limited amount of data. Lastly, both low-sampling and high-sampling signal techniques need to consider the uncertainty of signals measured at industrial sites.

Based on these considerations, this dissertation propose a framework for uncertainty-based fault diagnosis in industrial systems. The first study proposes a methodology for estimating the location of a fault using low-sampling signals. The proposed method presents an energy probability model of the signal measured by a sensor when a fault signal is converted into a low-sampling signal, taking into account the energy difference between the normal state and the fault state signals. When a fault signal occurs at a specific location, the energy measured by numerous sensors can be probabilistically quantified. Then, the fault location can then be estimated probabilistically by deriving a probability value at various specific locations based on the energy ratio between the measured sensors, using the Bayesian inversion. In the second study, a methodology for robust fault diagnosis using high sampling rate signals is proposed. The first step is to evaluate signal similarity using Kullback-Leibler divergence and group similar signals reflecting the operating condition. Then, a probabilistic model of the time-frequency expression of signals is developed to handle variations in operating conditions. Even for a newly measured signal with an unknown operating condition, it can be compared with a group of similar operating conditions using this model. Next, a new feature is proposed to discriminate the fault state by comparing the newly measured signal with

the probability models estimated from the signals from the normal state. An adaptive threshold is also suggested, which reflects the range of time-frequency result and corresponding proposed features that vary for the state of signal, to perform robust fault diagnosis. Finally, the data sampling technique is applied based on the result values obtained through the suggested low-sampling signal based approach. This enables the use of the suggested high-sampling rate signal based technique, which helps to reduce the computational time required for analysis while ensuring the stochastic robustness of the final results. By utilizing this combined approach, the diagnostic process becomes more efficient and reliable, leading to improved fault detection and characterization in industrial systems.

Keywords: Fault diagnosis
Uncertainty probabilistic modeling
Spectral analysis
Low sampling rate signal
High sampling rate signal
Prognostics and health management (PHM)

Student Number: 2016-29867

Table of Contents

List of Tables

List of Figures

Nomenclature

RMS	root mean square
CFF	characteristic fault frequency
HSR	high sampling rate
LSR	low sampling rate
TFA	time frequency analysis
KLD	Kullback-Leibler divergence
n-DoF	n-degree-of-freedom
AE	acoustic emission
GMF	gear mesh frequency
DoE	design of experiment
RSM	Response surface methodology
STFT	short time Fourier transform
FFT	fast Fourier transform
WT	wavelet transform
WVD	Wigner-Ville distribution
EMD	empirical mode decomposition
TDOA	time difference of arrival
CFL	candidate fault location
RS(t)	leak-responsive sensor set at time t
$E[\cdot]$	expectation operator
$E_j[\cdot]$	expectation operator with respect to j
Corr[·]	correlation operator
$Var_j[\cdot]$	variance operator with respect to j
$Z_{\alpha/2}$	critical value for the given confidence level α
$\sigma_{i,\text{normal}}$	standard deviation of energy of a normal state signal
$s(f)$	Fourier transform of a measured signal at frequency f
$n(f)$	Fourier transform of a normal state signal at frequency f

$p(f)$	transfer function of the transmission of a signal at frequency f
$k(f)$	Fourier transform of a fault state signal at frequency f
$e(f)$	uncertainty used to quantify the variation of the spectrum of a normal state signal at frequency f
θ	difference of phase angle between a normal signal and a transmitted signal
$e_a(f)$	variation from a phase angle difference between a normal and fault signal
β_f	energy ratio of a normal and fault signal at frequency f
δ_r	coefficient of variation of estimated fault energy
m_{ab}	ratio of a measured fault energy at sensor a and b
al_i	assumed location i
Λ	restriction for preventing similar information from being calculated twice
$\mathrm{A}(\omega)$	amplitude of the leak signal for frequency ω
r	radial distance from the leak source
k	wave length
$\alpha_1(\omega)$	attenuation coefficient in air at frequency ω
$\mathrm{erf}(\cdot)$	Gauss error function
ω_{L} ω_H	lower/upper limit frequency of measured band-passed signal
CAE	computer-aided engineering
MPP	most probable point
$C_s(\tau, \omega)$	a spectrogram of the target signal s
$\mathrm{sn}(t)$	normal state simulation signal under the sinusoidal operating condition
$\mathrm{sf}(t)$	fault state simulation signal under the sinusoidal operating condition
$P(x,y)$	observed bi-variate probability distribution
$Q(x,y)$	reference bi-variate probability distribution
$D_{\mathrm{KL}}(\cdot\|\|\cdot)$	KLD value
$Y_s(\tau, \omega)$	normalized spectrogram of the target signal s
(T, Ω)	possible domain of (τ, ω) calculated by a signal length, and

	Nyquist frequency
$r(t)$	reference signal
RFS	set of reference signals
$nr_j(t)$	j-th non-reference signal
$\eta_j^{(i)}(t)$	signals labeled as i where j is the j^{th} sample of signals labeled as i
$\chi^2(2)$	2 DoF chi-square distribution
f_{chi}	probability density function (PDF) of the chi-square distribution
$\chi^2(2, \lambda)$	noncentral chi-square distribution with 2-DOF, and the noncentrality parameter λ
$f_{nc\text{-}chi}$	PDF of the noncentral chi-square distribution
U(a, b)	Uniform distribution with parameter a and b
N(a,b)	Gaussian distribution with parameter a and b
KDE	kernel density estimation
f_{KDE}	probability density function using KDE
ϕ	kernel for constructing KDE
h	hyper-parameter for ϕ
$C^{(i)}(\tau, \omega)$	mean value of energy $\eta_j^{(i)}(t)$ at (τ, ω),
$f^{(i,\tau,\omega)}(C^{(i)}(\tau, \omega))$	PDF for $C^{(i)}(\tau, \omega)$
CDF	cumulative density function
k_p	margin value for the probabilistic boundary
$b^{(i)}(\tau, \omega)$	probabilistic boundary of the time-frequency indices (τ, ω) of i labeled signal
aj(t)	is j^{th} segmented signal from the newly measured signal a(t)
$h(j)$	labeling for the aj(t) by comparing the set of reference signals
$W_a(ct, \omega)$	concatenated fault-affected indices
$C_a(ct, \omega)$	concatenated spectrogram
$C_\mu(ct, \omega)$	mean of the concatenated reference spectrogram
ψ_ω	the energy variance from the noise at frequency ω

Chapter 1

Introduction

1.1 Motivation

With the advent of the fourth industrial revolution, automation systems have become increasingly prevalent in society. In recent years, these systems have evolved to enable the implementation of increasingly sophisticated and complex mechanisms. However, as the size and complexity of these systems increase, the need to manage individual components within them also becomes more critical. This is because if any one component fails, it could result in issues with the entire system. As a result, industries are investing in research to prevent or promptly detect overall system failures at an early stage. This trend is evident from the increasing size of the condition monitoring market, which is expected to continue growing in the future. For example, the Asia Pacific Machine Condition Monitoring Market is forecasted to experience a Compound Annual Growth Rate (CAGR) of 7.8% during the period of 2022-2028. Thus, it is imperative to enhance the reliability of the system by developing a fault diagnosis framework that can be applied at a system level, while also meeting the demands of industry.

Modern industrial systems are composed of numerous components, which require a large number of measurement sensors to be installed throughout the system in order to diagnose its state. While various data related to operating conditions can also be acquired (E.g., pressure, speed, power, temperature, etc.), they are generally less suitable for diagnosis than data obtained from sensors specifically installed for this purpose. Typically, vibration sensors [1-4] and acoustic emission sensors [5-7]

are utilized to diagnose the target component/system. Signals obtained from these high-sampling sensors are typically highly sensitive, meaning that even small changes in the target system can have a significant impact on the measured signal from the corresponding sensor [8]. Because of this high sensitivity, many studies have been conducted that can diagnose the condition through spectral analysis even with a small fault. However, there is still a risk of signal distortion caused by other components within the system. To address this issue, the signal can be directly measured by attaching the sensor directly to the target component or to a casing that protects the component. Ideally, fully utilizing high sampling rate data from these sensors is beneficial for fault diagnosis. However, due to the size of the system or the number of components involved, fully utilizing high sampling data from multiple sensors in terms of data storage or processing is often considered uneconomical from an industrial viewpoint. For example, in thermal power plants, there are over 20,000 sensors used for system operation and maintenance [9]. Therefore, in the industrial field, signals are usually transformed and saved as features such as RMS (Root Mean Square) to address this economic issue. Additionally, one sensor can acquire information on multiple components rather than just one like the high sampling rate signal approach, making it a suitable methodology for large scale systems. However, since signals from various components are complexly received and converted into low-sampling signals, they are insensitive to diagnose the fault, and only the severe fault can be detectable.

Specific limitations for each high sampling rate and low sampling rate signal approach are followed. Firstly, the use of high sampling rate signals for fault diagnosis has limited performance by the conventional spectral analysis method. This method is generally used to investigate changes in energy at physically defined characteristic fault frequencies (CFF) to diagnose the state of the target component [10, 11]. However, in reality, it cannot be guaranteed that the signal change due to

the fault condition occurs only in the CFF, leading to misestimation of the fault state even when using high sampling rate signals. Therefore, the use of high sampling rate signals for fault diagnosis requires more advanced and sophisticated methods to address this limitation. Secondly, the use of low sampling rate signals for fault diagnosis has disadvantageous in terms of the posterior maintenance. In general, fault that can be diagnosed with a low sampling rate signal are severe faults in which energy increases in the entire frequency range. Therefore, it is highly likely that signals related to faults are measured in various distributed sensors at the entire system. As a result, it becomes difficult to limit the scope of fault location when performing maintenance. Thirdly, there is a high possibility of misdiagnosis due to the uncertainty of the measured signal in the both low-sampling and high-sampling approach [12].

To overcome these suggested limitations, this research proposes a uncertainty-aware fault diagnosis framework for industrial system using high and low sampling rate signal. Efficient fault diagnosis of industrial systems will be evaluated by utilizing the advantages of low-sampling and high-sampling signals and evaluating the reliability of the results with energy probabilistic modeling.

1.2 Research Scope and Overview

The goal of the research outlined in this doctoral dissertation is to develop two essential techniques using high sampling rate (HSR) / low sampling rate (LSR) signals measured in the system with considering the stochastic nature from the uncertainty in signals. Specific research thrusts include (1) Research Thrust 1 – LSR based fault localization with energy probabilistic modeling for LSRs; (2) Research Thrust 2 – HSR based robust fault diagnosis with energy probabilistic modeling for HSR's time frequency analysis (TFA).

Research Thrust 1: Probabilistic Energy Ratio based Localization (PERL) for estimation of the fault location

Research Thrust 1 proposes a novel method for fault localization considering the effect of signal transmission. In industrial settings, due to computational and storage capacity, the measured acoustic emission signal is often processed through the use of descriptors, such as the RMS, which is related to the signal energy. Computational and storage capacity issues make it difficult to use conventional methods, including time difference of arrival, which uses a high-sampling-rate signal. In addition, the measured RMS may have uncertainty that arises due to sensor disturbance or unpredictable process conditions. Thus, this study newly proposes an approach called probabilistic energy-ratio-based localization (PERL) to estimate the location of fault in the system. In the proposed approach, energy transmission model is used to calculate the ratio of the signal energy from the specific band energy. To account for background noises and sensor disturbance, the uncertainty of the measured RMS is characterized in a probabilistic manner. Using this information, the probability that fault has occurred at a specific location is estimated hypothetically. The first and second case study, which is for the localization of the leak position of thermal power plant, confirm that the proposed method enables localization of a boiler tube leak position with high accuracy. The third case study, which is for the localization of the fault in robot arm joint, confirm that the proposed method enables to find the location of fault joint.

Research Thrust 2: Fault-Affected Signal Energy Ratio (FASER) for robust fault diagnosis

Because signals are known to be sensitive in response to weak faults, vibration signal analysis has become a preferred tool for fault diagnosis. In general, however, the signals from any components cannot be uniformly measured due to their stochastic nature, which arises due to sensor noises, irregular physical property (such as gearbox for meshing surfaces), and related factors. In addition, it is difficult to know exactly how a particular signal is affected by a fault, especially under time-varying operating conditions. Therefore, it is hard to determine whether a change in a measured vibration signal is the result of the fault or if it is from the stochastic nature of the signal; this limitation has diminished the fault-diagnosis performance of currently proposed signal analysis approaches. Therefore, this paper proposes a new fault-diagnosis method that considers the uncertainty in the signals measured under nonstationary operating conditions; the new approach is named the fault-affected signal extraction ratio (FASER) method. In the proposed method, the uncertainty is estimated by using the probability distributions of coefficients from short-time Fourier transform for one period of the vibration signal, which are extracted by applying the Kullback-Leibler divergence (KLD) to the consecutively measured signal, using kernel density estimation and n-degree-of-freedom (n-DoF) chi-squared distribution. These estimated probability distributions are used to define the indices that have fault information; therefore, any fault signal can be applied adaptively without any physical information. The energy ratio calculated by the indices of the signals is utilized as a health feature. In addition, the robustness of the feature is secured by newly defining an FASER's adaptive threshold (FAT) that considers spectral leakage effect and correlation from the window function and overlap ratio. The proposed method is experimentally validated by applying it in two case studies, including a planetary gearbox and an industrial robot gearbox, which

are configured to imitate the non-stationary operating conditions of real-world manufacturing processes. The results show that the proposed method can accurately diagnose fault states in various speed conditions, while also being able to estimate the level of fault severity.

1.3 Dissertation Layout

The doctoral dissertation is organized as follows. Chapter 2 provides a technical background and literature review for the both HSR and LSR based fault diagnosis method. Chapter 3 shows a proposed PERL method for localization of the fault position using the uncertainty based probabilistic LSR's transmission modeling (Research Thrust 1). Chapter 4 presents a proposed FASER method for robust fault diagnosis using the uncertainty based probabilistic modeling of the HSR's energy represented as TFA (Research Thrust 2). Chapter 5 proposes a integration of the proposed PERL method and FASER method for efficient and robust fault diagnosis of industrial system. Finally, Chapter 6 concludes the doctoral dissertation with a summary of each thrust's contribution and suggests the future research related with the proposed methods.

Chapter 2

Technical Background and Literature Review

This chapter provides the uncertainty-aware framework for fault diagnosis in industrial system using LSR and HSR signals. Firstly, the brief introduction for the low and high sampling rate signals from industrial system is provided in Section 2.1. In Section 2.2, LSR signal based conventional fault diagnosis methods are reviewed. Next, HSR signal based conventional fault diagnosis methods are reviewed in Section 2.3. Lastly, a summary and discussion of the conventional research is provided in Section 2.4.

2.1 Low and High sampling rate signals from industrial system

As introduced in Chapter 1, industrial systems are becoming larger over time and changing from various complex components to consist a single system [13, 14]. In line with these changes, it is becoming an important issue to prevent accidents through condition monitoring while measuring and controlling various sensor data even within one unit system. In industrial systems, vibration and acoustic emission signals are crucial in evaluating the system's health, and they are typically acquired through data acquisition sensors and systems with a high sampling frequency of 20 kHz or more. The most common method used for analyzing these high-frequency signals is spectrum analysis, which is effective in diagnosing early-stage gradual failures or small energy changes such as fine cracks. However, for large-scale

systems, analyzing high-sampling signals is challenging due to the limited computational capabilities of data acquisition systems. Therefore, low-sampling signals like root mean square and band pass energy are commonly used for fault diagnosis in industrial systems. However, these methods are limited in their ability to detect only radical or large-scale faults that increase energy in all frequency bands, and they cannot detect specific frequency reactions. Furthermore, due to the limited applicable range of low-sampling signal-based methods, a large number of sensors may react to the fault, resulting in inefficiencies in maintenance after fault detection.

2.2 Low sampling rate signal based fault diagnosis

Before delving into the topic of LSR signal processing, this study provides a brief definition of LSR. The definition of LSR signal varies depending on the application. For example, in the case of acoustic emission (AE) signals, a signal below 20 kHz is considered an LSR signal. On the other hand, even if the signal is only about 1 kHz, it is not considered an LSR signal in the case of a tachometer. Therefore, in this study, an LSR signal is defined as a signal that cannot be sufficiently analyzed through spectral analysis. For instance, in gearbox fault diagnosis, gear mesh frequency (GMF) analysis is generally required. If the signal satisfies $f_s/2 << \text{GMF}$, where f_s is the sampling frequency of the signal, it can be classified as an LSR signal. Figure 2-1 shows the components of the fault diagnosis methodology using LSR.

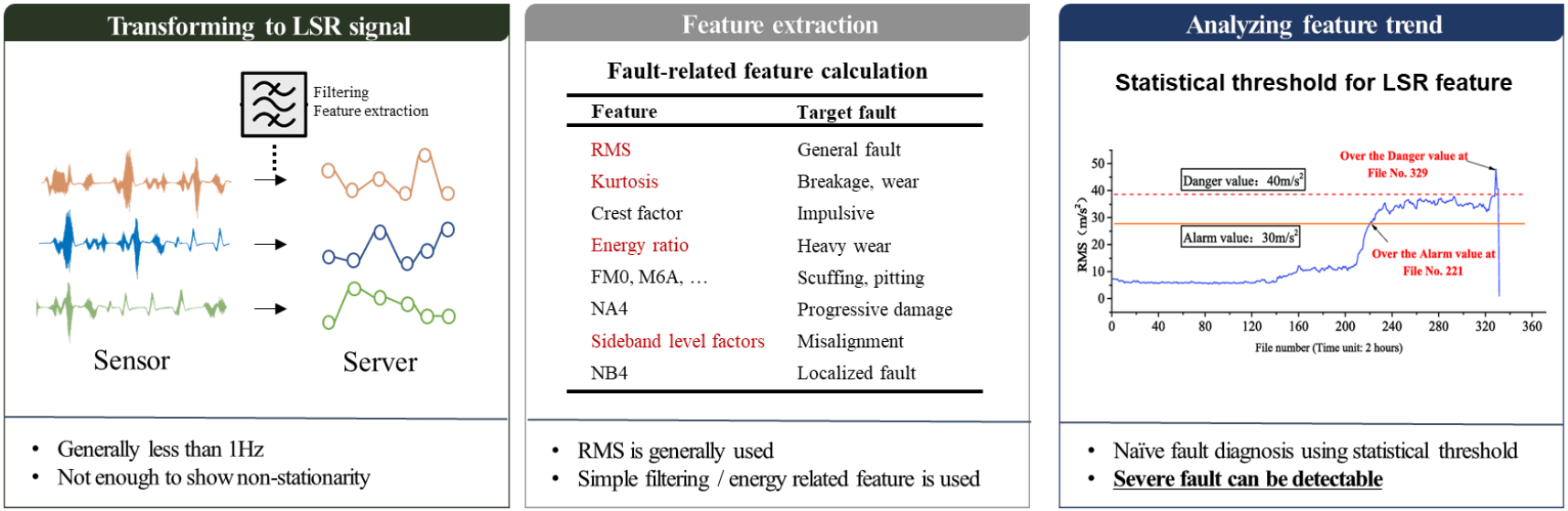

Figure 2-1 Three main components of framework for fault diagnosis using LSR

2.2.1 Feature extraction for transforming to LSR signals

Conventional LSR signal based fault diagnosis methods are generally utilized in the industrial site for the computational cost. For example, if only 20 sensors with a sampling frequency of 25.6 kHz, which are generally used in the vibration sensor for fault diagnosis, are used, the number of data to be processed per second exceeds 500k. Processing such large amounts of data in the central management center can incur a significant economic cost. Thus, in practice, operators often store and utilize descriptors such as RMS or specific band energy due to hardware limitations in data processing. Consequently, previous studies have focused on featurizing signals to diagnose conditions through feature engineering, taking into account these practical considerations [15, 16]. In Table 2-1, several features for health monitoring is provided [17]. Most of these features can be calculated through simple summation operations in the time domain or are based on methods that enable continuous and fast data processing based on spectrum filtering [18-21].

Table 2-1 Representative features for health monitoring

Feature	Statistical / physical meaning
RMS	Square root of the average of the sum of the squares of the signals
Crest Factor	Ratio of maximum positive peak value of the signal to RMS
Standard Deviation	The amount of variation from the mean value
Kurtosis	Fourth order normalized moment of the signal
Energy ratio	Ratio of RMS compared with the reference signal
Energy operator	Kurtosis of the resulting signal
FM0	Maximum peak-to-peak amplitude of the signal divided by the sum of energy from 1 to Nth harmonic
M6A/M8A	Sixth/eighth moment normalized by the variance
SLF[22]	The ratio of sum of the first order sideband about the fundamental frequency to the standard deviation of the time signal

In addition to the features introduced above, many studies have been conducted to diagnose faults through various features [23-25]. However, since most of the features introduce techniques that transform some signals from the mentioned features or utilize signals that have undergone preprocessing (such as a difference signal, residual signal), it can be said that they do not deviate greatly from the overall context. For instance, a difference signal and residual signal are generally used to diagnose the rotational operating mechanical components such as a bearing, gear, but the final feature is transformed as a feature related to the feature written in Table 2-1. In particular, the introduced features generally correspond to diagnostic methods using vibration signals and acoustic emission signals. In addition to these signals, studies using various signals such as operating condition related signals, temperature, and pressure have been proposed, but in this study, the range is limited to dealing with low-sampling signals in terms of energy of measured signals.

2.2.2 Analyzing feature trend and fault diagnosis

Recently, industrial systems tend to operate the system according to the purpose by changing the operating conditions according to the changing demand. For example, in the case of a thermal power plant dealt with in this doctoral research, the operating environment is optimized by adjusting the composition ratio or quantity of coal, etc. according to the demand for electricity and the price of raw materials. In the case of another example, robot system in manufacturing system, the operating environment is changed according to the plan considering the demand condition, and sophisticated nonstationary operating conditions using complex motions are requested. Therefore, when the features presented in 2.2.1 are used for fault diagnosis without any trend analysis, deviations caused by these nonstationary operating conditions occur, which is highly likely to lower fault diagnosis performance.

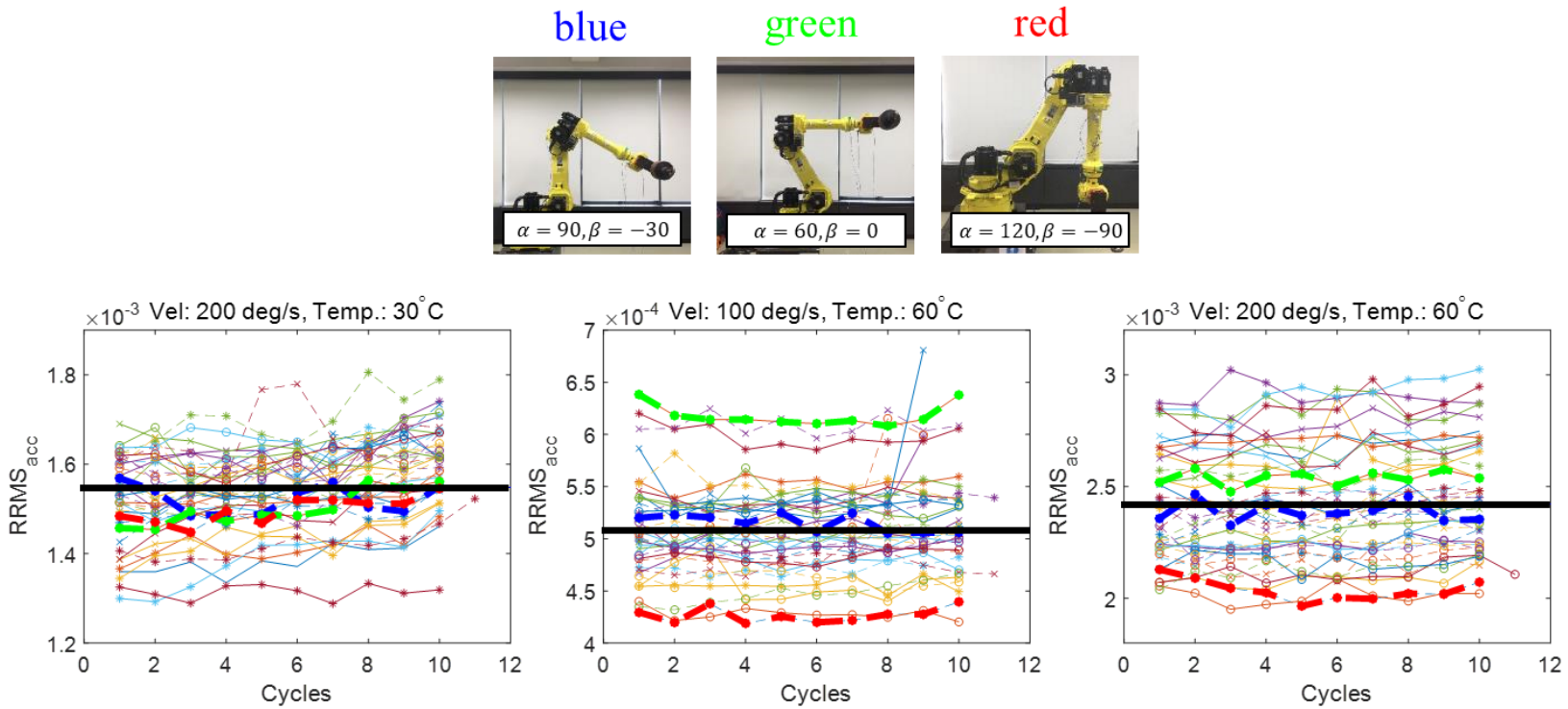

Figure 2-2 RMS feature tendency under the different operating condition

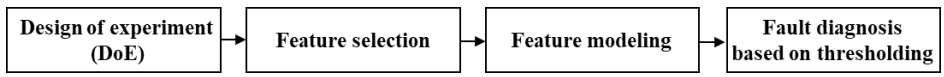

Figure 2-3 General procedure for LSR based fault diagnosis

To overcome such difficulties, variables related to operating conditions such as temperature, speed, and load are often used to analyze the trends of features. For instance, the RMS of a vibration signal tends to increase as the temperature rises, irrespective of the machine's state whether the machine is healthy or not. Similarly, as the speed of the machine increases, the energy in the low-frequency band of the vibration signal also increases, leading to an overall increase in energy and hence an increase in the RMS value. Figure 2-2 demonstrates that the RMS value of a vibration signal varies significantly with changes in operating conditions, such as the position of a robot arm, temperature, and angular velocity of the fourth joint. Hence, the conventional fault diagnosis approach that employs LSR signals usually involves a design of experiments (DoE) as the initial step to estimate the variability of features for different operating conditions, as depicted in Figure 2-3. There are some commonly used DoE approaches for obtaining the dataset for constructing the model for the feature variation with respect to the operating conditions. It is clearly best to experiment for all the possible operating condition such as full factorial design, it needs too much time to take the experiment. Therefore, most DoE research aims to minimize experiments while minimizing the loss of information. For example, commonly used DoE approaches include fractional factorial design [26], Plackett-Burman design [27], Taguchi method [28], central composite design [29], and others.

As explained in section 2.2.1, diagnosing the condition involves considering a range of conventionally used or newly developed features. After conducting various experiments through DoE, modeling of these features is performed. The most commonly used feature modeling method is the response surface methodology (RSM). The general expression for RSMs is given as:

$$\hat{f} = f(x_1, x_2, ..., x_n) + \varepsilon(x_1, x_2, ..., x_n) \tag{2.1}$$

where $\hat{f}$ is the response, which is the feature to model in our context, f is the true response function, which is generally unknown, x_i is the controllable input, which is the variable for representing the operating condition in our context, and ε is a term representing unexplainable error including the aleatory and epistemic uncertainty. Recently, many studies have been conducted on modeling such as RSM using deep learning (such as DANN [30, 31], CNN [32, 33], LSTM [34, 35]). Through the above modeling, the feature distribution of the normal state can be calculated. If the distribution can be approximated by a normal distribution, the feature boundary of the normal state can be determined as follows.

$$\left| \hat{f} - \mathrm{E}_{\mathrm{X}}\left[f(x_1, x_2, ..., x_n) \right] \right| \leq z_\alpha \sigma_\varepsilon \tag{2.2}$$

where $\mathrm{E}_{\mathrm{X}}[\cdot]$ is the expectation operator with respect to the X, X is the state of the variable for x_i, z_α is the confidence intervals with the confidence level α, σ_ε is the standard deviation depending on the controllable input. In general, if an energy-related feature such as RMS is used as the feature, a threshold criterion for determining a fault state can be set by assuming that energy increases in a fault state. Otherwise, if a new feature is created through coupling between features, there are cases where it is diagnosed as the fault state simply by whether the new feature satisfies condition given in equation (2.2). In Figure 2-4, the fault diagnosis based on RMS under different operating condition is presented. As shown in the figure as blue line, the expected feature is calculated by the response surface modeling (Kriging model). Additionally, the thresholding value, which are plotted as the dot-line, depends on the speed and temperature.

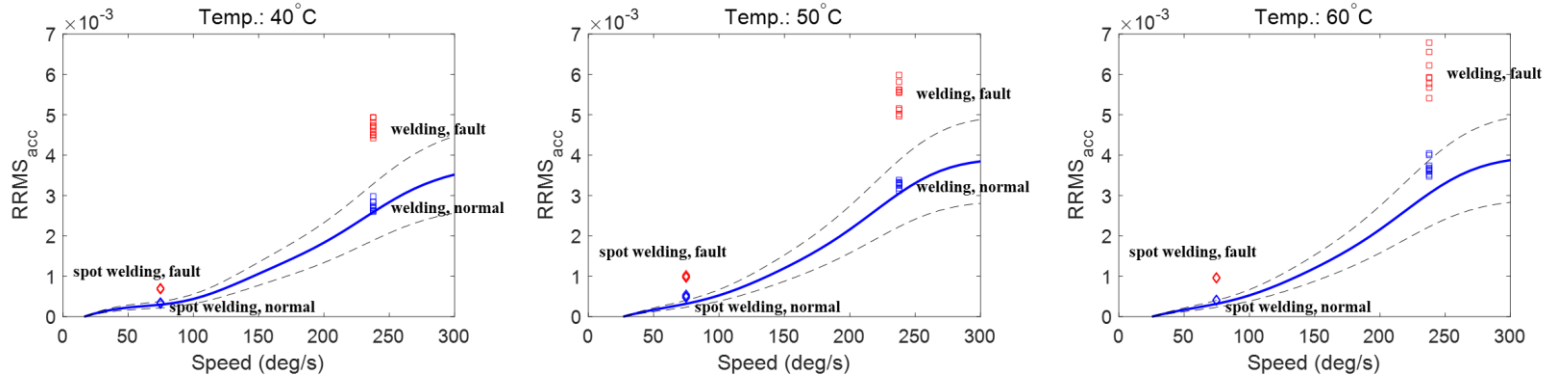

Figure 2-4 Examples of the fault diagnosis under different operating condition

2.3 High sampling rate signal based fault diagnosis

High sampling rate signal based approach is generally utilized when the spectral analysis is additionally required for the fault diagnosis. In general, the LSR approach described in Section 2.2 often targets severe faults that can be detected even through low-sampling signals such as RMS. However, it is difficult to diagnose with the LSR method because a change in frequency energy occurs only in a very localized band when the fault is a very minute fault or the initial state of progressive fault. Therefore, in general, studies have been conducted to determine the type or severity of faults as well as fault diagnosis through spectrum-based analysis of signals. Additionally, the researches on the calculating the CFF based on the dynamic behavior or related mechanism have been conducted. Recently, as mentioned several times before, the recent industrial system is generally under the nonstationary condition. Therefore, the time frequency analysis for analyzing the signal is necessary to consider the signal's nonstationary behavior. In conclusion, the recent HSR signal based fault diagnosis method is composed of three main contents as shown in Figure 2-5.

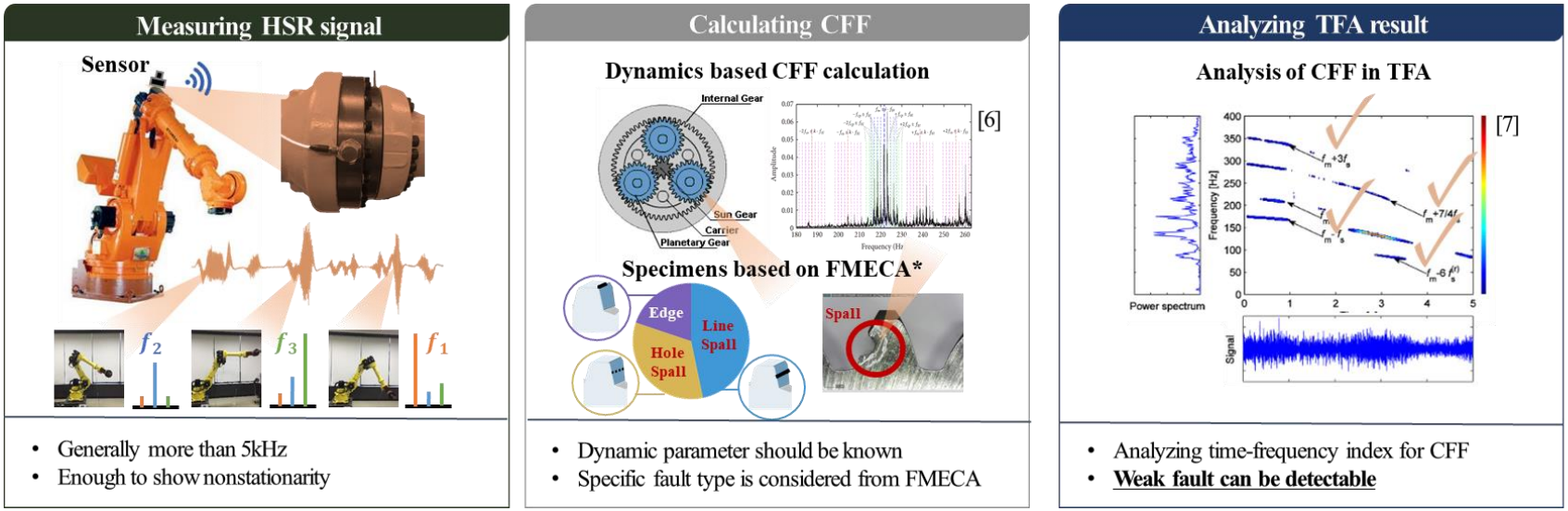

Figure 2-5 Three main components of framework for fault diagnosis using HSR

2.3.1 Time frequency analysis

Time frequency analysis (TFA) is widely utilized for analyzing the signal because the most of the signals measured in the real application have time-varying properties [36]. Specifically, the fault diagnosis using TFA has recently been conducted as the need for the diagnosis of the systems operated under the nonstationary condition increasing. Several generally utilized TFA method are given in this section briefly.

Short time Fourier transform (STFT)

$$\mathrm{STFT}\{x(t)\}(\tau,\omega)=\int_{-\infty}^{\infty}x(t)w(t-\tau)e^{-j\omega t}dt \tag{2.3}$$

where $x(t)$ is a signal, $w(t)$ is a window function, τ is a time index consisting STFT, and ω is a frequency index consisting STFT. For the window function, there are several window functions to consider the behavior of signals. However, in generally, the Gaussian window (Hanning window) is most preferred to utilize. The STFT method can be regarded as a method in which fast Fourier transform (FFT) is concatenated along the time axis assuming a quasi-stationary condition for a short time duration. Therefore, the time and frequency resolutions are determined and are generally determined in a region that satisfies the Heisenberg's uncertainty principle. Clearly, many researches based on the properties of STFT are conducted to diagnose the fault state of the system under nonstationary condition [37-39].

Wavelet transform (WT)

$$\mathrm{WT}\{x(t)\}(a,b)=\int_{-\infty}^{\infty}x(t)\frac{1}{\sqrt{|a|}}\psi\left(\frac{t-b}{a}\right)dt \tag{2.4}$$

where $x(t)$ is a signal, $\psi(t)$ is a wavelet function, a is the scaling parameter for dilation,

and *b* is the moving parameter for translation. In the signal context, the scaling parameter can be interpreted as the frequency, and the moving parameter can be interpreted as the time. Many studies have been conducted to determine the optimal wavelet function for fault diagnosis using time-frequency analysis [40, 41]. The choice of wavelet function can significantly affect the performance of the analysis, and different wavelet functions may be more suitable for different types of signals or faults [42]. Some commonly used wavelet functions include the Haar wavelet [43], Daubechies wavelet [44], Symlet wavelet [45], and Coiflet wavelet [46]. Additionally, wavelet packet decomposition, which involves decomposing a signal into multiple frequency bands using wavelets, has been used to improve the accuracy of fault diagnosis [47, 48].

Wigner-Ville distribution (WVD)

$$\mathrm{WVD}\{x(t)\}(\tau,\omega)=\int_{-\infty}^{\infty}x(\tau+\frac{\eta}{2})x^{*}(\tau-\frac{\eta}{2})e^{-2\pi j\eta\omega}d\eta \tag{2.5}$$

The equation (2.5) is one of the definitions for the WVD, but the most simple and zero-mean signal's representation for WVD. On the contrary to the STFT and Wavelet, the formula is based on the correlation function as represented as xx^{*}. Therefore, the WVD provides highest possible resolution in the view of temporal and frequency resolution, which is limited to the Heisenberg's uncertainty principle. However, the cross terms can exist from the correlation term, which makes difficult to apply the multi-component signals. Because these kinds of cross term would makes confusion on the analysis on the results, which of them cannot be distinguishable whether they are from the cross term or noise. To address this problem, studies have proposed separating signals into mono-components using methods such as empirical mode decomposition (EMD), performing WVD, and diagnosing faults [49-51].

In addition, there are various time frequency analysis techniques such as the Hilbert-Huang transform. In addition, there are lots of method related with the calibration for the TFA results (E.g. reassignment method for STFT) and combining the above-mentioned STFT, WT, and WVD methods (Gabor–Wigner distribution function). However, since dealing with all of these methodologies is out of scope, this doctoral dissertation proceeded with the scope aligned with the STFT considering the STFT is most intuitive representation and has the lowest computational cost.

2.3.2 Analyzing time frequency analysis results for fault diagnosis

In order to diagnose faults through TFA, the CFF must be calculated. In particular, it is not difficult to calculate the CFF if the dynamics of the machinery are known, since most machinery components with periodic properties are the main targets of spectral analysis.

As written in Section 2.3.1, STFT, one of the most popular TFA based approaches, has a low computation cost, as compared to other TFA methods such as WVD and WT [52]. The low computation cost of STFT implies that STFT has much more potential applicability in industrial fields than do the other more computationally intensive TFA methods. However, when measuring the vibration signal and transforming it to STFT, uncertainty can arise due to: 1) phase-delay by improper truncation of the consecutively measured signal, 2) the uncertainty principle in time-frequency representation, and 3) background noises and impact signals from other adjacent components, such as bearings. Vibration signals are generally measured consecutively in industrial fields and are not stored separately for each period of operation with matched phase. This implies that even though the operating condition of a vibration signal is periodic, it is unclear how to segment the signal for estimating the uncertainty in STFT. Although the encoder information from a tachometer can be used to determine the segmentation of vibration signals,

this approach may also incur error due to the indirectivity between the sensor and the tachometer. When fault diagnosis is performed without considering the uncertainty in STFT, the signal energy changes that arise due to noise or phase-mismatching could be misunderstood to be the effect of the fault, rather than the result of these other impacts. Further, there is the possibility that a small change in the signal energy can be ignored. Even though many STFT-based fault-diagnosis methods have been developed in prior research [53-57], to date, the uncertainty in STFT has only been considered in a limited way [58-61].

2.4 Summary and discussion

This doctoral dissertation aims to propose a framework for the industrial system using both LSR and HSR with considering the stochastic behavior from the uncertainty via measuring and transforming process in the signal. As described in Section 1.1, the LSR signal based fault diagnosis methods have low computational cost, but has low sensitivity for diagnosing the fault, especially in the weak fault. Therefore, the severe and abrupt fault (such as boiler tube fracture) is the main target of LSR approach. However, this condition causes various sensors to react when performing fault diagnosis, thereby causing an issue of which area to perform maintenance work even when fault diagnosis is performed well. This approach has not been done in previous studies, and the proposed method will solve the problem by considering the transmission effect of the signal to solve this problem. Alternatively, fault diagnosis methods based on HSR signals have a high computational cost. While these methods have been shown to have high sensitivity for fault diagnosis in previous studies, their practical utilization has been difficult due to the high computational demands. Therefore, to solve this problem, we proposed a methodology to analyze the HSR signal through STFT with the lowest computational cost. In addition, considering the energy deviation and uncertainty

caused by operating conditions when analyzing the STFT, a robust fault diagnosis method is needed even if only a part of the HSR signal could be used.

To achieve efficient and robust diagnosis at the system level, the proposed method and its limitations should be taken into account. Figure 2-6 illustrates a framework for integrating the LSR signal-based method and the HSR signal-based method in an industrial system, as proposed in the doctoral dissertation. The framework comprises two research thrusts to enable effective fault diagnosis. In the first research thrust, the fault location is probabilistically determined using signals acquired from multiple sensors. This probabilistic approach allows for the selection of samples that are likely to contain significant fault information. This step enhances the efficiency of the diagnosis process by focusing on relevant data. The second research thrust involves performing high sampling frequency analysis on the selected samples. By applying the proposed method, robust results can be obtained even when the root mean square (RMS) value does not exceed a predefined threshold. This aspect is crucial in addressing the uncertainty associated with signals and ensuring reliable fault diagnosis. By employing this integrated framework, it becomes possible to estimate fault location, perform fault diagnosis, and conduct fault frequency analysis while considering signal uncertainty. This comprehensive approach improves the effectiveness and reliability of fault analysis in industrial systems..

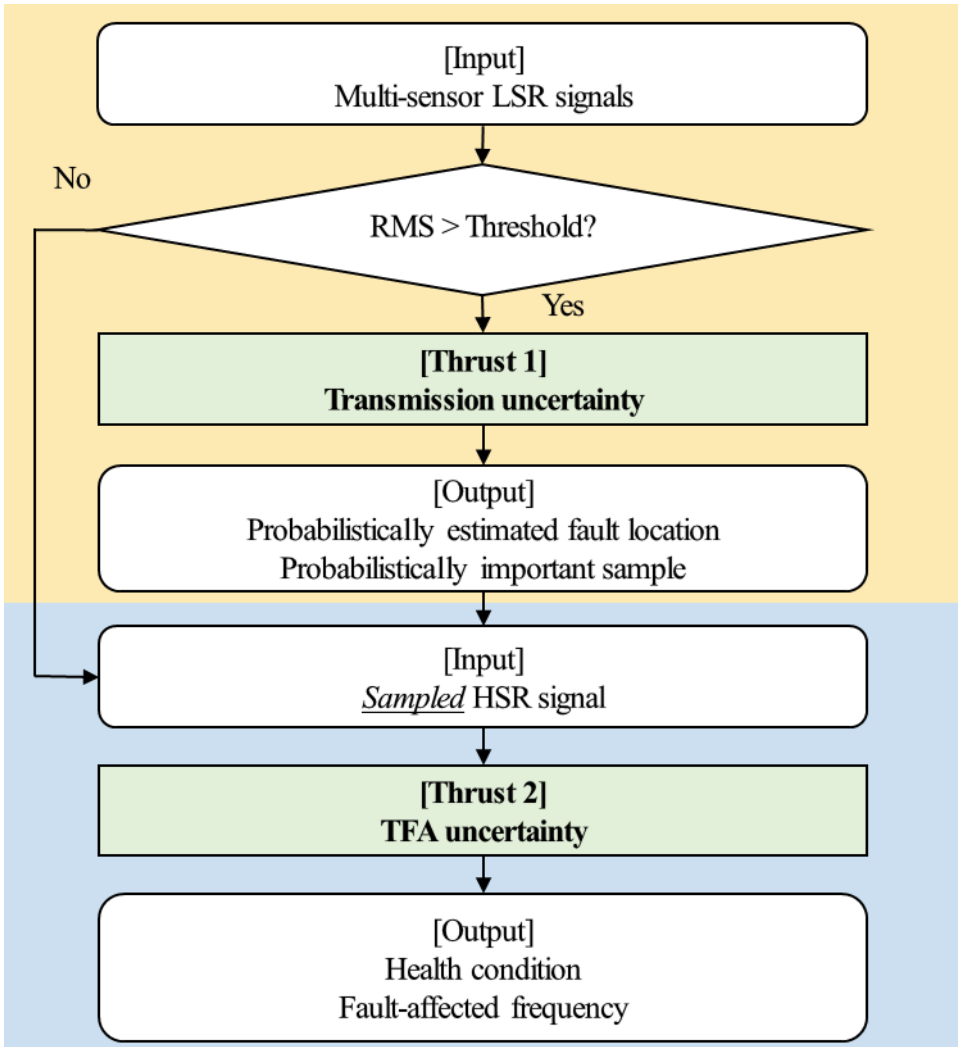

Figure 2-6 Proposed framework for fault diagnosis of the industrial system based on LSR and HSR signals

Chapter 3

Probabilistic Energy Ratio based Fault Localization (PERL)

In this chapter, we propose a new method to enhance the fault-related information from the low sampling rate signals measured by multiple equal type sensors. This chapter especially focuses on the estimation of fault location under the situation when low sampling rate signal (LSR) increases significantly enough to diagnose a fault. In industrial settings, due to computational and storage capacity, the measured signal is often processed through the use of descriptors, such as the root mean square (RMS), which is related to the signal energy. Computational and storage capacity issues make it difficult to use conventional methods, including time difference of arrival, which uses a high-sampling-rate signal. In addition, the measured RMS may have uncertainty that arises due to sensor disturbance or unpredictable process conditions. Thus, this study newly proposes an approach called probabilistic energy-ratio-based localization (PERL) to estimate the location of the fault. In the proposed approach, acoustic dissipation and attenuation theory are used to calculate the ratio of the signal energy from the specific band energy. To account for background noises and sensor disturbance, the uncertainty of the measured RMS is characterized in a probabilistic manner. Using this information, the probability that a boiler tube leak has occurred at a specific location is estimated hypothetically. Case studies from simulation data and industrial data confirm that the proposed method enables localization of a boiler tube leak position with high accuracy. Additionally, case study from experimental data of 6-DoF industrial robot system confirms the generality and applicability of the proposed. In this case, the

measured RMS based probabilistic modeling is based on the estimation for the transmission function of the vibration of sensor.

3.1 Background: Multiple Sensor Based Source Localization

In this section, the conventional studies about source localization techniques are reviewed. Conventionally utilized method for source localization technique is based on time difference of arrival (TDOA) method. A time difference of arrival (TDoA) method, which uses the difference in arrival time of acoustic emission (AE) signals [62-64], has been proposed by measuring sound pressure from multiple AE sensors with a high sampling rate and calculating the difference in time at which the AE sensors initially measured the leak signal using a generalized cross-correlation algorithm. Then, localization algorithms, such as Chan's algorithm and Fang's algorithm, can be performed using the calculated time difference [65, 66] to find the position of the leak. However, it is difficult to apply these methods in operating power plants for the following reasons. First, there is usually a significant amount of background noise in power plants, due to the combustion process and soot-blowing. In the case of soot-blowing, it is highly possible that the time delay found in the above-mentioned approaches might be calculated based on the soot-blowing, because the signal energy generated by soot-blowing could be dominant the energy of the measured signal, even in a leak situation. Second, the detection of a leak signal generally requires a high sampling frequency (e.g., more than 10 kHz [64]). In practice, however, operators typically store a descriptor (i.e., root mean square; RMS) of the AE signal or specific band energy because of the limitations of the hardware in data processing. In these cases, conventional methods are not usable because the time delay cannot be calculated properly with these data. In addition, the characteristic frequency of the leak signal generally depends on the leak type, flow rate, and internal pressure [67]. Therefore, even if we properly measure a high-

sampling-rate signal, it may be difficult to apply it properly if physical analysis of the frequency components is not performed. Lastly, localization algorithms may need at least four or more sensors in a three-dimensional space; however, it has been experienced in some cases that even four or more sensors may not respond when a leak occurs. In this case, when calculating the time delay, the wrong sensor may be used, which will adversely affect the result, and the localization algorithm itself may not be solved mathematically. The drawbacks of conventional TDOA method are not restrictly applied to the AE data. Source localization using the vibration signal analysis based on the transmission of signal also has the same problem.

3.2 Probabilistic Energy Ratio Based Fault Localization

The proposed probabilistic energy ratio based fault localization method is comprehensively discussed in this section with the mathematical expression and its following assumption. The goal of the method is to estimate the location of fault by comparing the energy of signals from the different, homogenous type sensors. The PERL method is predicated on the recognition of uncertainty in the energy level of a signal that may be classified as a fault signal. To address this uncertainty, a probabilistic model is utilized to estimate the location of the potential failure, based on the measured fault energy ratio between sensors. The proposed methodology involves three distinct steps as shown in Figure 3-1. In the first step, LSR signals are selected based on their potential to be classified as fault signals through conventional trend analysis. The second step entails the construction of a probabilistic model for the estimation of fault location, which involves the integration of two key elements. Firstly, an energy distribution model is developed based on the energy that can be measured in a normal state when a fault signal is detected. Secondly, a transmission model is established to account for the signal propagation from the candidate fault location (CFL) to the sensor. The resulting probabilistic energy ratio model for multiple sensors is then formulated. In the next stage, the fault probability model is computed using the measured sensor data and the probabilistic energy ratio model through Bayesian inversion. Finally, in step 3, the fault probability is calculated based on data obtained from three or more multi sensors, and time sequential data. This enables the determination of the final fault probability, thereby facilitating effective fault identification and subsequent maintenance and repair activities. The proposed method is described in detail with mathematical expressions in the following sections.

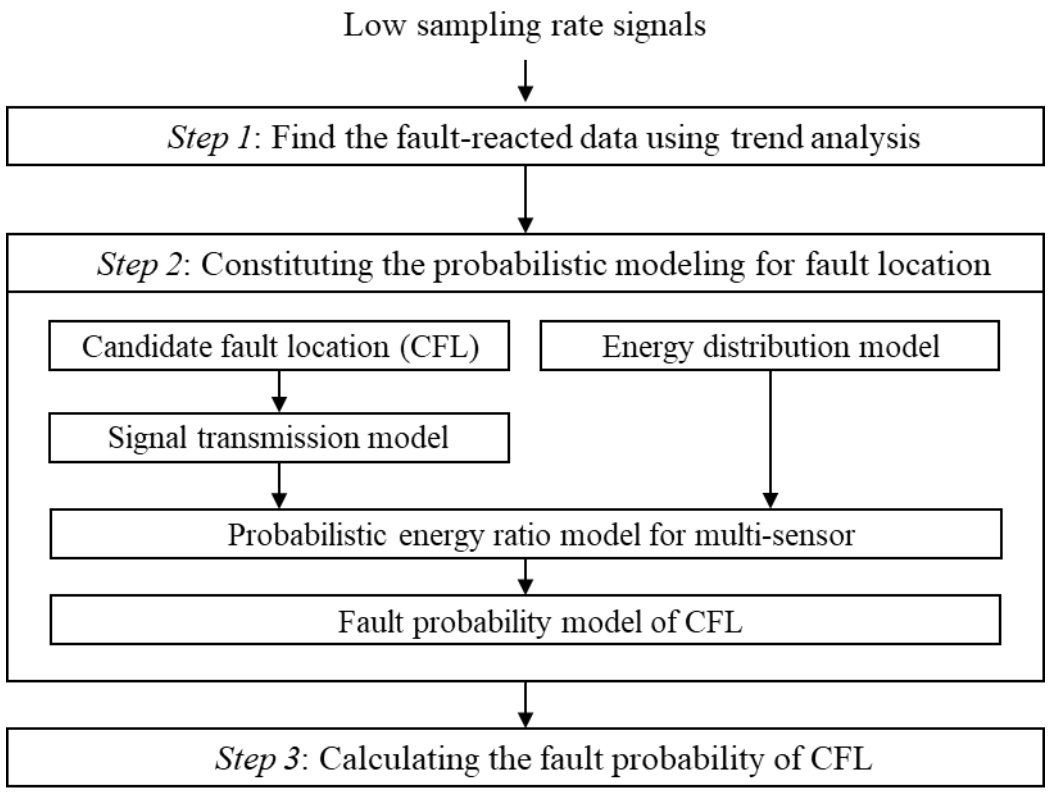

Figure 3-1 Flowchart of the proposed PERL method.

3.2.1 Find the fault-reacted data using trend analysis

Multi-sensor fault diagnosis is a widely used approach to improve the robustness of fault diagnosis algorithms [68, 69]. Our proposed methodology adopts a multi-sensor system, which considers the ability of multiple sensors to capture fault signals during signal transmission. In practice, vibration sensors are typically installed in a manner that enables them to monitor the target system effectively. For example, in a boiler system, AE sensors are placed strategically to cover the entire boiler, including the superheater, reheater, waterwall, economizer, etc. The number of sensors required for monitoring the entire boiler system generally ranges from 30 to 40, with some sensors specifically designed to detect leaks. Similarly, in a robot system, vibration sensors are installed on each joint to monitor the joint's condition, as it is typically the component most vulnerable to faults in terms of fault diagnosis. As a result, a n-DOF robot system would typically require n sensors to monitor the system as a whole.

First, some sensors that respond statistically to outlier data can be selected as the sensors that respond to the fault as:

$$\mathrm{RS}(t) = \left\{ i \middle| s_i(t) > \mathrm{E}[s_{i,\mathrm{normal}}] + Z_{\alpha/2}\sigma_{i,\mathrm{normal}} \right\} \tag{3.1}$$

where RS(t) is the leak-responsive sensor set at time t, E[•] is the expectation, $Z_{\alpha/2}$ is a critical value for the given confidence level α, $s_{i,\mathrm{normal}}$ is the energy of the normal-state signal, and $\sigma_{i,\mathrm{normal}}$ is the standard deviation of the energy of the normal-state signal. It is worth pointing out that the operating condition has variations [38, 39]. Depending on the operating state, as well as the installation location of the sensor, environmental noises may be measured differently, even if the same sensor is used. Therefore, the standard deviation of the signals measured from individual sensors is considered, as shown in the equation (3.1). In particular, in a thermal power plant, the variability in the operating conditions that arises due to changes in combustion or soot-blowing could affect the calculation of the mean and standard deviation of

the amplitude of the normal-state signal. Therefore, the data corresponding to soot-blowing should be excluded through the use of an additional outlier filtering technique, such as move-median outlier filtering. In addition, the mean and standard deviation are continuously updated to reduce the effect of variable operating conditions. In the research described in this chapter, the mean and standard deviation of the data are continuously updated for one day before the time when the leak is identified. If the fault-reacted signal is measured as suggested in Equation (3.1), there are cases where it is difficult to determine the fault as a fault if the variation of the signal due to the operating condition is too large. For this reason, we will introduce an example that can reduce the variation effect by operating conditions by utilizing specific conditions. In the case of an industrial robot, it generally repeats the same movement continuously and is often placed in a cyclo-stationary operating condition. In this case, even in the case of a signal converted to LSR, it has periodicity. Therefore, based on this periodicity, it is possible to calculate the mean value and standard deviation that the LSR signal can have for each operating state. In the case of a robot system to be presented as a case study in a later section, since the RMS variation due to these cyclostationary operating conditions is too large, the trend for this was analyzed in advance and the failure energy was extracted for the low-sampling signal where the failure signal was measured. The graphical illustration for this contents are shown in Figure 3-2.

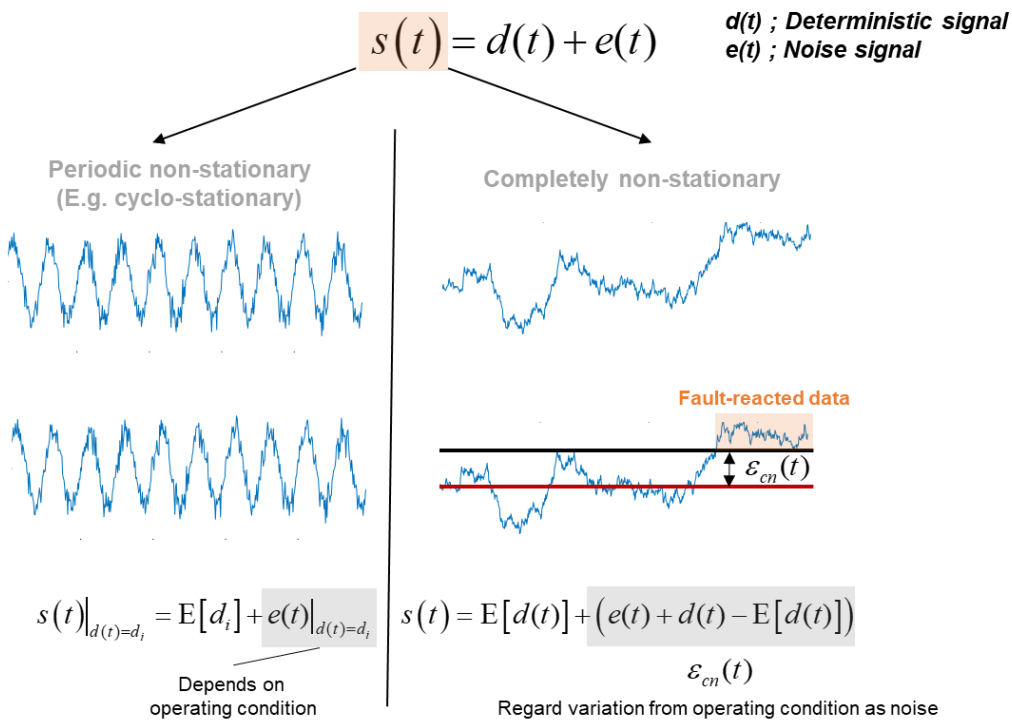

Figure 3-2 Graphical illustration for RMS based fault diagnosis under non-stationary operating condition.

3.2.2 Constituting the probabilistic model for the fault location

To estimate the location of a fault, the first step involves selecting a candidate fault location (CFL), which can vary depending on the target system. Typically, the region where a sensor is capable of detecting a fault is selected as the CFL, based on the position of the sensor. For instance, in the case of an AE sensor, as described in Section 3.1, the CFL for diagnosing the leak or fracture state of a boiler tube can be set as the position of the tube. Similarly, in the case of a vibration sensor, the CFL can be limited to the target component by mounting the sensor on its casing.

If the CFL is identified, it is possible to construct a model of the energy measured by the sensor when a fault signal is generated from the CFL. To develop such a model, the energy can be expressed as a sum of energies at each frequency component, according to Parseval's identity. To accomplish this, a signal transmission model is used that assumes a fault frequency is represented in the frequency domain. The fundamental equation used for modeling is as follows:

$$s(f) = n(f) + p(f)k(f) + e(f) \tag{3.2}$$

where $s(f)$ is the Fourier transform of the measured signal at frequency f, $n(f)$ is the Fourier transform of a normal state signal at frequency f, $p(f)$ is the transfer function for the transmission of the signal at frequency f, $k(f)$ is the Fourier transform of a fault state signal at frequency f, and $e(f)$ is the uncertainty used to quantify the variation of the spectrum of the normal state signal at frequency f. All of them are complex value, and graphical illustration is suggested in Figure 3-3.

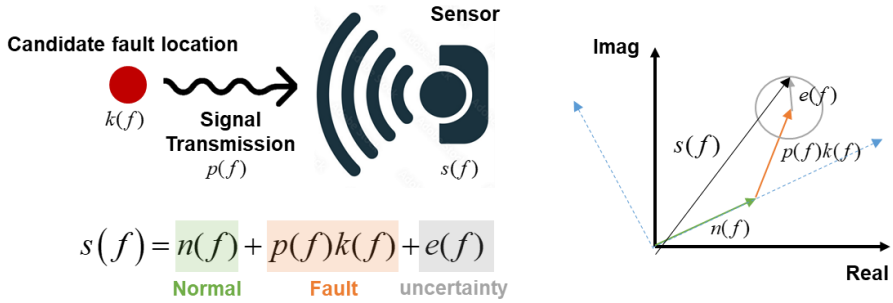

Figure 3-3 Graphical illustration for the assumed fault signal transmission model.

The next step is transforming the equation to RMS related term. There needs to basic assumption that 1) Phase difference is only in the direction of increasing energy compared with the normal state. 2) Error from the approximation of variation as Gaussian distribution is negligible.

The energy from the normal signal $n(f)$ and the transmitted fault signal $k(f)p(f)$ can be quantified as:

$$|n(f)|^2 + |p(f)k(f)|^2 - 2|n(f)||p(f)k(f)|\cos\theta \qquad (3.3)$$

where θ is the difference of angle between the normal signal $n(f)$ and the transmitted signal $k(f)p(f)$. From the assumption 1 and symmetricity on θ, the mean energy of the fault signal can be calculated using the equation (3.3) integral with respect to θ from α to π where $\cos\alpha = |p(f)k(f)|/(2|n(f)|)$.

$$|n(f)|^2 + |p(f)k(f)|^2 + \frac{2\sin\alpha}{\pi - \alpha}|n(f)||p(f)k(f)| \qquad (3.4)$$

From the simple mathematical implementation with trigonometric function, the equation (3.4) can be transformed as:

$$|n(f)|^2 + |p(f)k(f)|^2 + \frac{2\sqrt{1 - \dfrac{|n(f)|^2}{4|p(f)k(f)|^2}}}{\pi - \arccos\left(\dfrac{|p(f)k(f)|}{2|n(f)|}\right)}|n(f)||p(f)k(f)| \qquad (3.5)$$

Recalling that the assumed condition is that the severe fault occurs. Therefore, such case when $|p(f)k(f)|>2|n(f)|$, then the equation (3.4) can be simply expressed as:

$$\left|n(f)\right|^2+\left|p(f)k(f)\right|^2 \tag{3.6}$$

For the first case, which is under the weak fault energy measured, the variation can be calculated as:

$$\left|n(f)\right|^2\left|p(f)k(f)\right|^2\frac{\left((\alpha-\pi)\sin(2\alpha)+2\left((\alpha-\pi)^2+\cos(2\alpha)-1\right)\right)}{(\alpha-\pi)^2} \tag{3.7}$$

From the second case when the severe fault occur, the variation is:

$$2\left|n(f)\right|^2\left|p(f)k(f)\right|^2 \tag{3.8}$$

Under the weak fault symptom, and from the equations (3.5), and (3.7), the energy distribution from the phase difference can be modeled as:

$$\begin{aligned}&\left|s(f)\right|^2=\left|n(f)\right|^2+\left|p(f)k(f)\right|^2+\frac{2\sin\alpha}{\pi-\alpha}\left|n(f)\right|\left|p(f)k(f)\right|+e_a(f)\\&e_a(f)\sim N\left(0,{\sigma_a}^2\right)\\&\sigma_a=\frac{\sqrt{\left((\alpha-\pi)\sin(2\alpha)+2\left((\alpha-\pi)^2+\cos(2\alpha)-1\right)\right)}}{(\pi-\alpha)}\left|n(f)\right|\left|p(f)k(f)\right|\end{aligned} \tag{3.9}$$

Similarly, the severe fault symptom, and from the equations (3.6), and (3.8), the energy distribution from the phase difference can be modeled as:

$$\begin{aligned}&\left|s(f)\right|^2=\left|n(f)\right|^2+\left|p(f)k(f)\right|^2+e_a(f)\\&e_a(f)\sim N\left(0,\left(\sqrt{2}\left|n(f)\right|\left|p(f)k(f)\right|\right)^2\right)\end{aligned} \tag{3.10}$$

where $e_a(f)$ is the variation form the phase difference of the normal and the fault signal. From $\cos\alpha=|p(f)k(f)|/(2|n(f)|)$, and summation for the all frequency based on the equations (3.9) and (3.10) makes the following equations:

$$\sum_f |s(f)|^2 = \sum_f |n(f)|^2 + \sum_f \frac{\tan\alpha_f}{\pi - \alpha_f} |p(f)k(f)|^2 + \sum_f e_a(f) \tag{3.11}$$

$$\sum_f |s(f)|^2 = \sum_f |n(f)|^2 + \sum_f |p(f)k(f)|^2 + \sum_f e_a(f) \tag{3.12}$$

where $\cos\alpha_f = |p(f)k(f)|/(2|n(f)|)$. Firstly, from the Parseval's identity, the left term is same as square of RMS of the fault signal, and the first right term is same as expectation of square of RMS of the normal signal. Additionally, if the fault energy is distributed equally in the frequency domain, so the $2\cos\alpha_f$ can be approximated as the same value, the square root of the ratio of the fault energy to the normal energy, which is denoted as square root of $(\mathrm{RMS}_{\mathrm{fault}}^2 - \mathrm{E}[\mathrm{RMS}_{\mathrm{normal}}^2])/\mathrm{E}[\mathrm{RMS}_{\mathrm{normal}}^2]$. Alternatively, if the fault energy is larger than $|p(f)k(f)|>2|n(f)|$, which is impossible to define α_f, the square root of the ratio of the fault energy to the normal energy is newly defined as β. Lastly, the uncertainty from the normal signal is incorporated to the $e_a(f)$, then the following equation can be achieved:

$$\mathrm{RMS}_{\mathrm{fault}}^2 - \mathrm{E}\left[\mathrm{RMS}_{\mathrm{normal}}^2\right] \sim N\left(\frac{\tan\alpha}{\pi-\alpha}\sum_f |p(f)k(f)|^2, \left(\mathrm{E}[\bullet]\delta_r\right)^2\right)$$

$$\delta_r = \frac{\sqrt{\left((\alpha-\pi)\sin(2\alpha) + 2\left((\alpha-\pi)^2 + \cos(2\alpha) - 1\right)\right) + 6\delta_{normal}{}^2(\alpha-\pi)^2}}{2\sqrt{1-\beta^2/4} + \beta(\pi-\alpha)} \tag{3.13}$$

$$\mathrm{RMS}_{\mathrm{fault}}^2 - \mathrm{E}\left[\mathrm{RMS}_{\mathrm{normal}}^2\right] \sim N\left(\sum_f |p(f)k(f)|^2, \left(\mathrm{E}[\bullet]\frac{\sqrt{2\delta_{\mathrm{normal}}{}^2 + 2}}{\beta}\right)^2\right) \tag{3.14}$$

where δ_{normal} is the coefficient of variation (c.o.v.) of RMS^2 from the normal state. For the simple notation, the c.o.v. of $\mathrm{RMS}_{\mathrm{fault}}^2 - \mathrm{E}[\mathrm{RMS}_{\mathrm{normal}}^2]$ is denoted as δ_r. The equation (3.13) is for the weak fault, and the equation (3.14) is for the severe fault case. The validation for simulation is shown as Figure 3-4 and Figure 3-5. The simulation is based on the data satisfying the assumptions for deriving the equations.

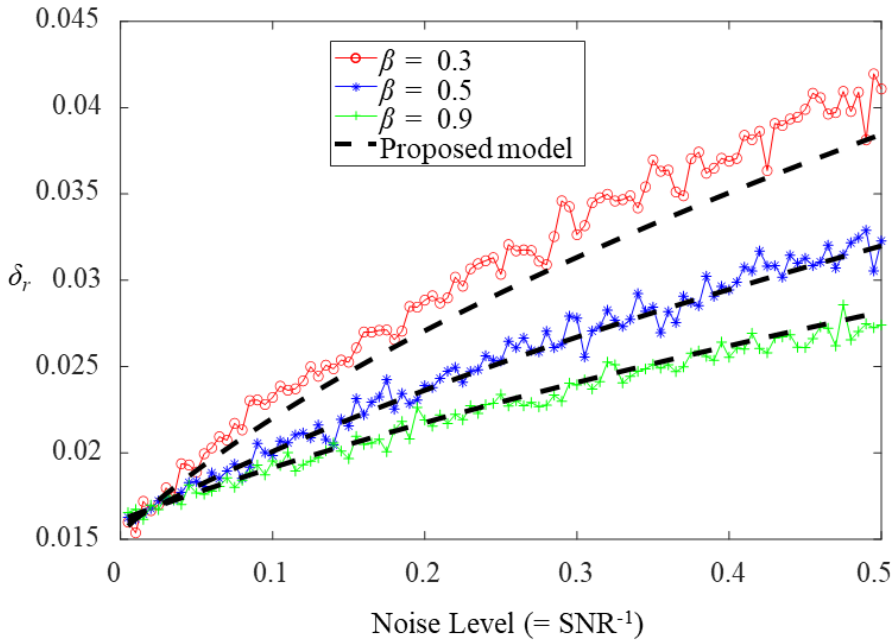

Figure 3-4 Simulation based model validation of the proposed probabilistic model for the weak fault case.

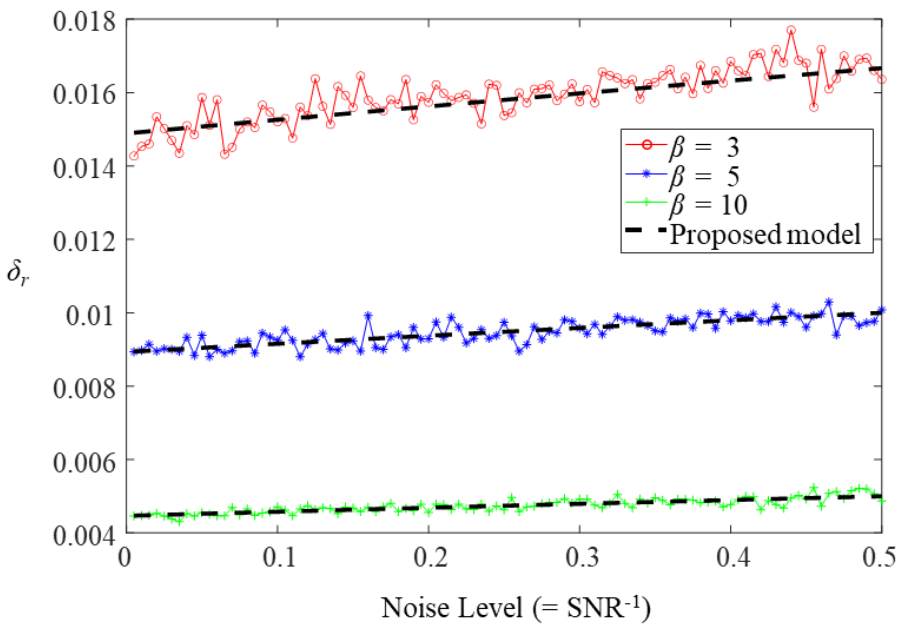

Figure 3-5 Simulation based model validation of the proposed probabilistic model for the severe fault case.

From equations (3.13) and (3.14), the uncertainty caused by amplitude variation from the phase difference is incorporated with the uncertainty caused by the noise observed from the variation of RMS of the normal state. Therefore, derived equation can be calculated from all the measurable and estimated terms except *p(f)k(f)*.

The next step is derivation of the probabilistic energy ratio model for the multi-sensor RMS data. The graphical illustration for this step is given in Figure 3-6.

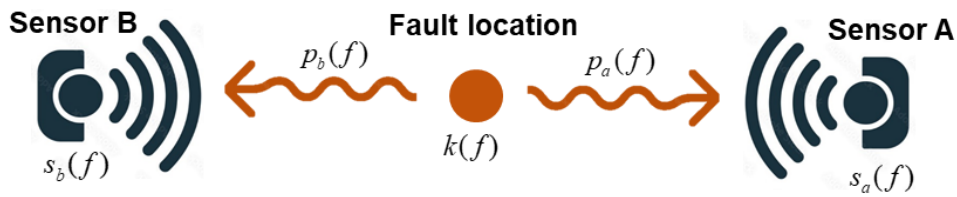

Figure 3-6 Graphical illustration for the derivation of probabilistic energy ratio model.

From equation (3.11), the probabilistic distribution of energy ratio between two sensor can be approximately quantified as [45]:

$$\ln(m_{ab}) \sim N\left(\ln\left(\frac{\sum_f |p_a(f)k(f)|^2}{\sum_f |p_b(f)k(f)|^2}\right), {\delta_{r,a}}^2 + {\delta_{r,b}}^2\right) \tag{3.15}$$

where $\delta_{r,a}$, $\delta_{r,b}$ is c.o.v. defined in the equations (3.13) and (3.14), and m_{ab} is the ratio of the measured fault energy at sensor *a* and *b*, calculated by the $RMS_{fault,a}^2$ – $E[RMS_{normal,a}^2]$ divided by $RMS_{fault,b}^2$ – $E[RMS_{normal,b}^2]$.

If the fault energy distribution in the frequency domain follows $k^2(f) \sim N(1,\varsigma^2)$, then the equation (3.15) can be approximated again by the ratio of two Gaussian distribution. Fortunately, it is the case that the mean value of equation (3.15) follows Gaussian distribution. Therefore, the closed form can be obtained as:

$$\ln(m_{ab}) \sim N\left(\ln\left(\frac{\sum_f |p_a(f)|^2}{\sum_f |p_b(f)|^2} \right), {\delta_{r,a}}^2 + {\delta_{r,b}}^2 + {\delta_k}^2 \right)$$
$$\delta_k^2 = \varsigma\left(\frac{\sqrt{\sum_f {p_a}^2(f)}}{\sum_f p_a(f)} + \frac{\sqrt{\sum_f {p_b}^2(f)}}{\sum_f p_b(f)} \right) \quad (3.16)$$

From the equation (3.16), it is possible to quantify the probability of the measured fault RMS ratio from the transmission of signal from CFL with considering the transmission uncertainty in sensor *a* and *b* as $\delta_{r,a}$, $\delta_{r,b}$, and the fault energy distribution in the frequency domain as δ_k. Therefore, the derived equation (3.16) can be calculated by all the known (transfer function of the transmission), and estimated value by removing the unknown $k(f)$. By removing the unknown $k(f)$ from the equation (3.13), the resulting equation can be used to calculate the probability of fault occurrence given the measured fault energy signal ratio and the known transfer function of the transmission, as well as the uncertainties in the system. However, in practical situations, the actual fault location may be unknown. To account for this, the Bayesian inversion method is applied to the equation (3.16) using the measured fault energy signal ratio as the condition of probability.

$$\mathrm{P}\left(X_{fault} = al_i \middle| m_{ab} \right) = \frac{\mathrm{P}\left(m_{ab} \middle| X_{fault} = al_i \right) \mathrm{P}\left(X_{fault} = al_i \right)}{\sum_i \mathrm{P}\left(m_{ab} \middle| X_{fault} = al_i \right) \mathrm{P}\left(X_{fault} = al_i \right)} \quad (3.17)$$

where $\mathrm{P}(X_{\mathrm{fault}} = al_i | m_{ab})$ is the conditional probability that the location of fault is equal to al_i when the measured fault energy ratio is m_{ab}, $\underline{al}_i$ is the i-th candidate fault location (CFL), $\mathrm{P}(X_{\mathrm{fault}} = al_i)$ is the prior assumption for the CFL, and $\mathrm{P}(m_{ab} | X_{\mathrm{fault}} = al_i)$ is the conditional probability that the measured fault energy ratio, m_{ab}. In summary, the conditional probability of the fault location being equal to a specific candidate fault location (CFL), given the measured fault energy ratio m_{ab}, can be expressed as $\mathrm{P}(X_{\mathrm{fault}} = al_i | m_{ab})$ in equation (3.17). In this equation, $\mathrm{P}(X_{\mathrm{fault}} = al_i)$

represents the prior assumption for the i^{th} CFL, while $P(m_{ab}| X_{fault} = al_i)$ is calculated using equation (3.13) and represents the conditional probability of the measured fault energy ratio being equal to m_{ab}, given the fault location al_i.

The final step is the calculating the fault probability of each CFL using the multiple (more than 2) and time sequential data. If more than 2 sensor has the fault energy, the following equation is derived:

$$P\left(X_{fault} = al_i, t\right) = \frac{\prod_{\Lambda} P\left(X_{fault} = al_i \middle| m_{kl}\right)}{\sum_i \left[\prod_{\Lambda} P\left(X_{fault} = al_i \middle| m_{kl}\right)\right]}, \ \Lambda = \left\{(k,l) \middle| m_{kl} > 1\right\} \tag{3.18}$$

where $P(X_{fault} = al_i, t)$ is the fault probability of ali at the time t, and Λ is a restriction for preventing similar information from being calculated twice. For instance, the ratio between two sensor can be achieved by selecting what is divided by the other. Therefore, it makes calculate the similar result twice. The equation involves the multiplication of the probabilities for each sensor's fault energy ratio, which is conditioned on the fault location al_i. The product is then divided by the denominator, which is calculated by the all probability on each CFL. This equation allows for the incorporation of multiple sensor data to calculate the fault probability of each CFL.

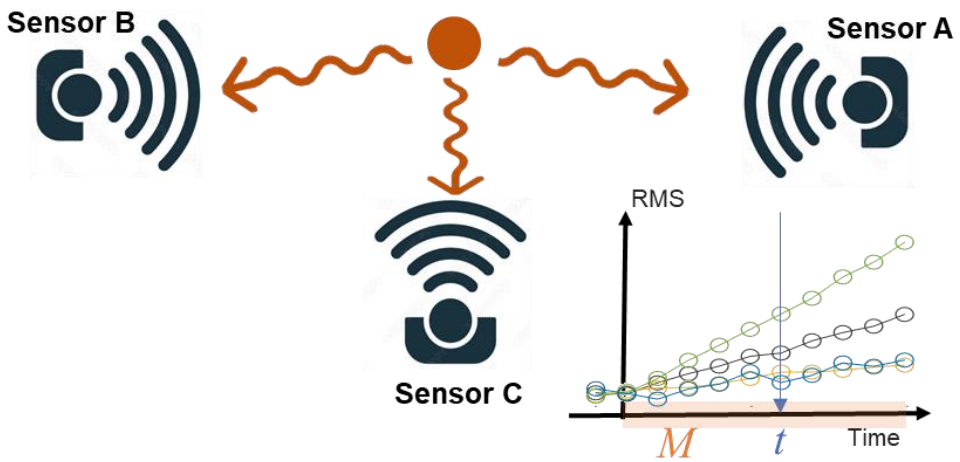

Figure 3-7 Graphical illustration for step 3.

Note that this equation assumes that the measurements from each sensor are independent, meaning that the measurement from one sensor does not affect the measurement from another sensor. If the measurements are not independent, then a more complex model would be needed to calculate the fault probability. Another assumption that can be made is that the sensors are located far enough from each other so that the fault occurrence at one sensor does not influence the fault occurrence at another sensor. This assumption ensures that the measurements from different sensors are independent of each other and can be considered separately. If the temporal information is independent, the measured fault energy at each time step is independent of the previous ones. In this case, the fault probability at time *t*, given the measured fault energy ratios for all candidate fault locations up to time *t*, can be calculated by multiplying the fault probabilities at the previous time step by the fault probabilities calculated using the current measured fault energy ratios. This can be expressed mathematically as:

$$\mathrm{P}\left(X_{\text{fault}} = al_i \middle| M\right) = \frac{\prod_{t \in M} \mathrm{P}\left(X_{\text{fault}} = al_i, t\right)}{\sum_{(x_l, y_l, z_l) \in \Omega} \left[\prod_{t \in M} \mathrm{P}\left(X_{\text{fault}} = al_i, t\right)\right]} \tag{3.19}$$

where $\mathrm{P}(X_{\text{fault}} = al_i|M)$ is the fault probability of al_i given all the measured fault

energy ratios up to time t, which is denoted by M, $P(X_{\text{fault}} = al_i, t)$ is the fault probability of al_i at time t given the measured fault energies. The graphical illustration for this step is given in Figure 3-7.

The proposed method aims to locate the fault in power systems using multiple sensors by calculating the probability of fault occurrence at different candidate fault locations (CFLs). The method uses the measured fault energy signal ratio and considers the transmission uncertainty in the sensors and the fault energy distribution in the frequency domain. The method employs a Bayesian inversion technique to calculate the probability of the measured fault energy signal ratio, given a specific CFL. The final step involves calculating the fault probability of each CFL using the multiple and time sequential data. The method assumes that the sensors are independent, and the temporal information is also independent. Overall, the proposed method is a probabilistic approach that considers uncertainties in the system and sensor measurements to accurately locate faults in power systems.

3.3 Experimental validation of the proposed method

This section describes the experimental validation of the proposed method. The validation consists of three case studies: a numerical simulation, and a practical application using actually measured data from an in-use power plant. In the numerical case study, the proposed algorithm is demonstrated to robustly estimate the leak position with a descriptor of the acoustic emission signal for a randomly selected leak position. In the practical application case study, the proposed algorithm is shown to estimate the leak position well in a real-world situation.

3.3.1 Preliminary work for applying the proposed method using the transmission function of the signal

In this section heading indicates that the following text will describe the preliminary work that was done to apply the proposed method using the transmission function of the signal.

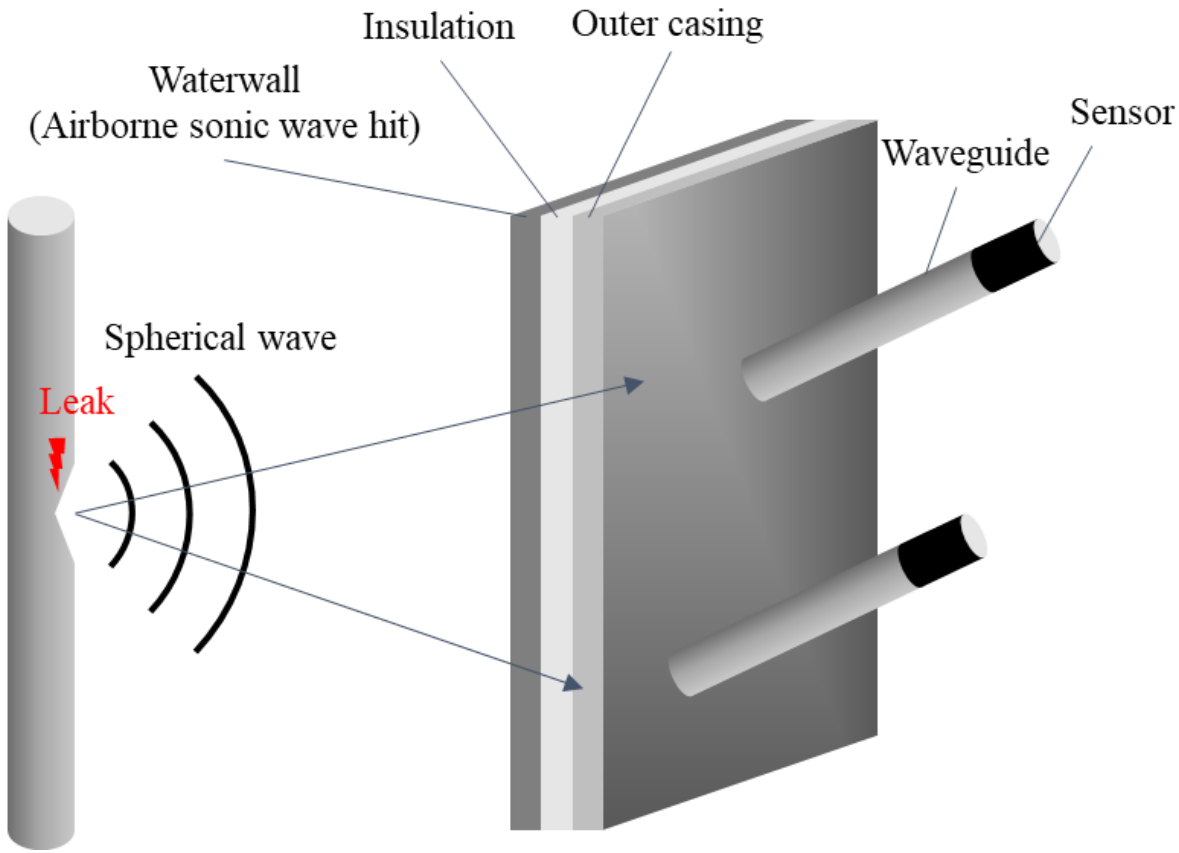

Figure 3-8 Sonic wave propagation & boiler tube leak detection system.

This case study focuses on the case in which a leak occurs in the interior casing of a boiler. In general, it is difficult to directly attach sensors to the tube inside the boiler casing; further, the vibro-acoustic leak signal cannot be measured because of attenuation [70]. As shown in Figure 3-8, AE sensors are attached to the outside of the boiler so that the sensor is not exposed to a high-temperature environment [71]. If a leak occurs in a boiler tube, a sonic wave is emitted into the air [72, 73]. As the sonic wave hits the boiler casing and waveguides, the AE sensors attached at the end of the waveguides can measure the signals. This implies that some AE sensors located adjacent to the leak position react significantly when a boiler tube leak occurs. The assumed sonic wave can be regarded as a spherical wave; thus, the wave equation is followed:

$$p(r,t) = \frac{A(\omega)}{r} e^{-j(\omega t - kr)} \tag{3.20}$$

where A(ω) is the amplitude of the leak signal for frequency ω, r is the radial distance from the leak source, and k is the wave length.

The sonic wave signal is attenuated exponentially by its propagation into the high-temperature air in the interior casing of the boiler [73, 74]. Therefore, the signal measured by the AE sensor is as follows:

$$p(r,t) = \frac{A(\omega)e^{-\alpha_1(\omega)r}}{r} e^{-j(\omega t - kr)} \tag{3.21}$$

where $\alpha_1(\omega)$ is the attenuation coefficient in air. Then, the power spectral density for a certain frequency ω can be calculated as follows:

$$\left|P(j\omega)\right|^2 = \frac{A^2(\omega)e^{-2\alpha_1(\omega)r}}{r^2} \tag{3.22}$$

Assuming that the attenuation coefficient follows a quadratic form on frequency in the local frequency region [75], and using the equation (3.15), the following equation can be achieved:

$$\ln(m_{ab}) \sim N\left(\ln\left(\frac{r_b^{\,2}\int_\omega e^{-2\alpha\omega^2 r_a}d\omega}{r_a^{\,2}\int_\omega e^{-2\alpha\omega^2 r_b}d\omega}\right), \delta_{r,a}^{\,2}+\delta_{r,b}^{\,2}+\delta_k^{\,2}\right) \tag{3.23}$$

where r_a and r_b are the distance of the sensor and assumed leak position. The mean of equation (3.20) can be expressed by an error function (erf) as followed:

$$\frac{r_b^{\,2}\int_\omega e^{-2\alpha\omega^2 r_a}d\omega}{r_a^{\,2}\int_\omega e^{-2\alpha\omega^2 r_b}d\omega} = \frac{r_b^{\,5/2}\left[\mathrm{erf}\left(\sqrt{2\alpha r_a}\,\omega_{\mathrm{H}}\right)-\mathrm{erf}\left(\sqrt{2\alpha r_a}\,\omega_{\mathrm{L}}\right)\right]}{r_a^{\,5/2}\left[\mathrm{erf}\left(\sqrt{2\alpha r_b}\,\omega_{\mathrm{H}}\right)-\mathrm{erf}\left(\sqrt{2\alpha r_b}\,\omega_{\mathrm{L}}\right)\right]} \tag{3.24}$$

where ω_{L} and ω_{H} is the lower and upper limit frequency of measured band-passed signal. Note that when the value of ω_{L} is zero and ω_{H} approaches zero frequency in equation (3.21), the attenuation effect is eliminated. This results in the expression of radial dissipation only, which can be represented as r_b^2/r_a^2, and it is same with the limit value of equation (3.21) is r_b^2/r_a^2. This result is utilized in the simulation case, which is described in case study 1, and experimental case, which is described in case study 2. The graphical illustration for easier understanding are shown in Figure 3-9.

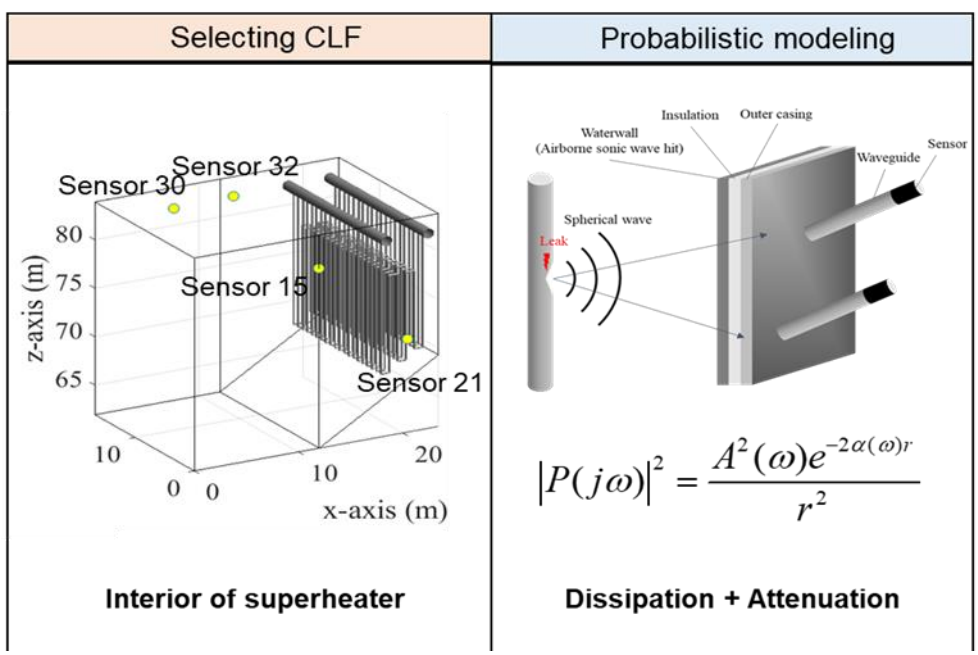

Figure 3-9 Graphical illustration of preliminary work for boiler system.

3.3.2 Case study 1: Numerical simulation with a randomly selected leak position

A raw leak signal with a high-sampling rate at a source location was modeled based on data measured by a power plant.

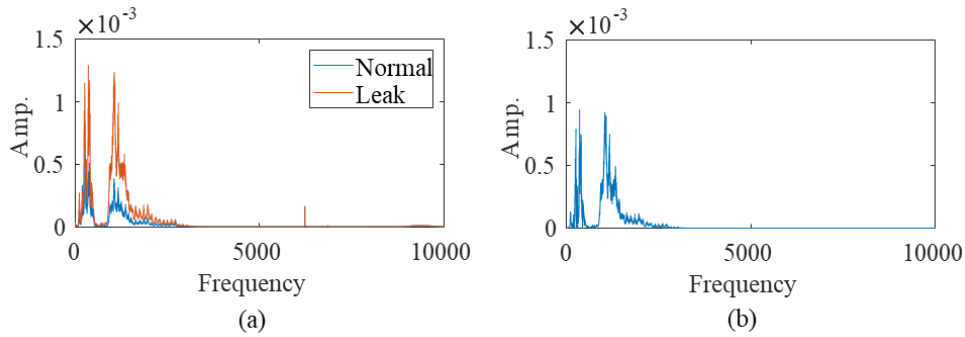

Figure 3-10 (a) Fast Fourier transform results of normal and leak signals (really measured) and (b) base simulation leak data.

Figure 3-10 (a) shows the results of the fast Fourier transform (FFT) of the high-sampling-rate (20,000 Hz) signals in normal- and leak-states, respectively. The difference in the amplitude can be interpreted as the tendency of the leak signal energy. Then, as shown in Figure 3-10 (b), the simulation data was modeled by considering the difference of the amplitude between the FFT of the leak- and normal-states.

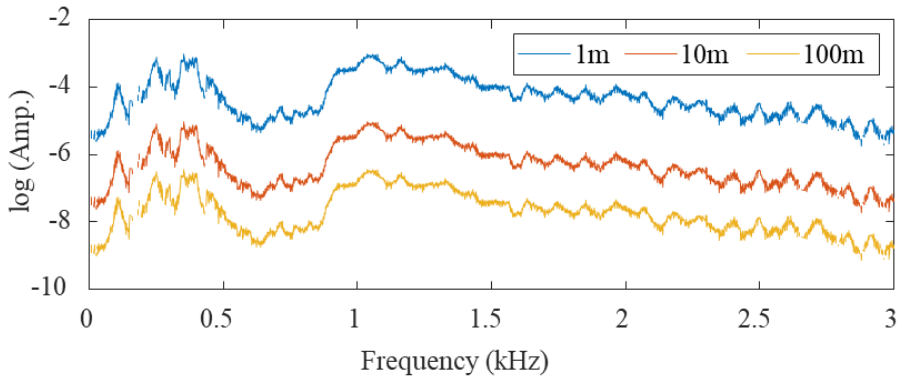

Figure 3-11 Signal attenuation and radial dissipation effect on distance.

The attenuation of a sonic wave is generally proportional to the square of the frequency, as explained in the equation (3.21). In this study, we calculated the attenuation coefficient considering the air condition (relative humidity, local atmospheric pressure, and temperature) in a thermal power plant, by referring to the published literature [75]. Figure 3-11 clearly shows that the signal energy decreases over the whole frequency range due to the signal attenuation and radial dissipation. Since the attenuation effect is relatively larger in the higher frequency region, it can be shown that the decrease in the signal energy with the distance is more pronounced in the high-frequency region.

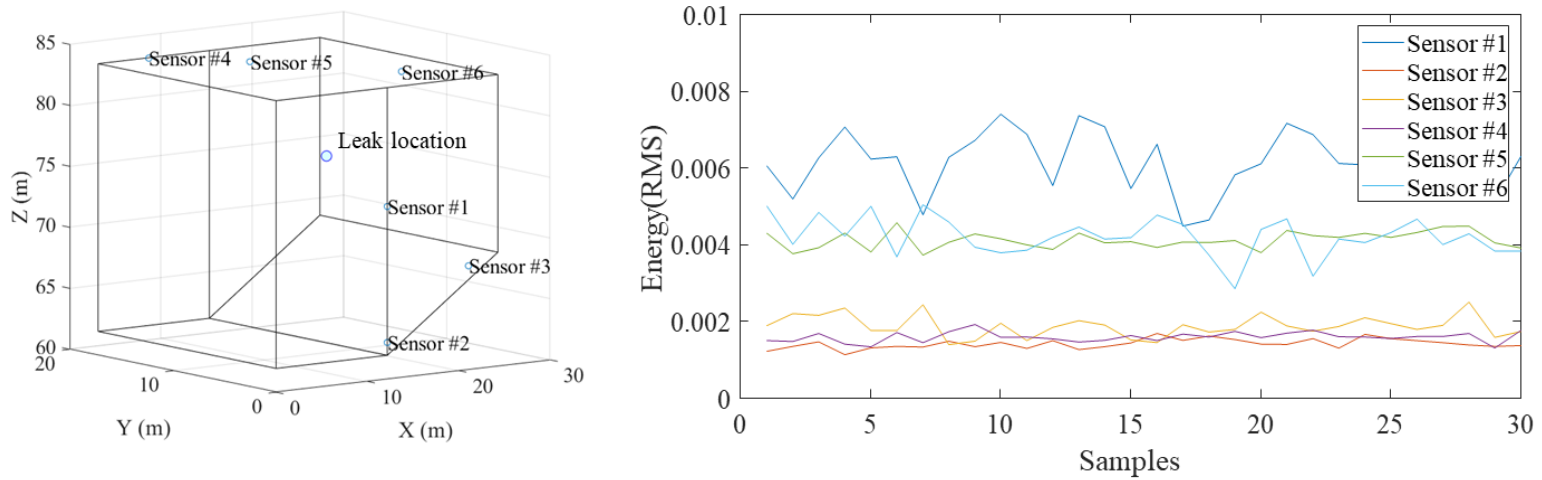

Figure 3-12 Sensor locations and simulated leak position in a boiler's final superheater (left) and trend of RMS at each sensor.

Table 3-1 Coordinates of AE sensors in the simulation study.

Description	Coordinate (mm)			Distance from leak (mm)	SNR
	X	Y	Z		
Sensor #1	12172	0	74150	7444	10.00
Sensor #2	12172	0	63000	15598	12.50
Sensor #3	21054	0	68500	13423	8.33
Sensor #4	5395	17111	83899	14657	11.11
Sensor #5	11251	12500	83899	9159	14.29
Sensor #6	18554	4277	83899	9090	8.33
Leak	13200	6800	77000	-	-

Figure 3-12 (left) shows the boiler dimensions and depicts the sensor locations in the final superheater of the boiler. The simulation is performed by referring to the locations and size of the sensor installations in the industrial power plant. The exact coordinates of the sensors' positions and leak position are given in Table 3-1.

Figure 3-12 (right) shows the trend of the simulation data of the six sensors when a leak occurs. The values of the signal-to-noise ratio (SNR) were set to 10.00, 12.50, 8.33, 11.11, 14.29, and 8.33, for Sensors #1 to #6, respectively. These SNR values were randomly perturbed with the mean of 10 and the standard deviation of 2, considering the field engineer's experience that the ratio of the leak signal to the noise is about 10. As shown in Figure 3-10, the base leak signal was generated by mimicking a high-sampling-rate signal measured from the actual leak signal. In order to apply the proposed method, it is necessary to transform the leak signal to the descriptor (i.e., RMS). First, the distance between the assumed leak position and the leak-responsive sensors is calculated. Then, the simulated leak signals at each sensor can be generated in the frequency domain through consideration of the SNR values given in Table 3-1 and the attenuation coefficient, as shown in Figure 3-12. Finally, the RMS shown in Figure 3-12 can be obtained by integrating with respect to ω for the simulated leak signals. In a real situation, it may be difficult to accurately

estimate the uncertainty of the sensor due to continuous changes in the surrounding environment. Therefore, there may be an error in estimating δ_{normal} in equation (3.11); here, all delta values of the sensor were assumed to be 0.1. In other words, assuming that the SNR is estimated as 10, analysis is performed for the case where there is a difference from the actual value assumed in Table 3-1 when the measurement was performed. A mesh is created for the region corresponding to the boiler, and the leakage probability value for each mesh can be approximated through equation (3.14) under the assumption that the probability is the same within the mesh. Then, the most probable point (MPP) is chosen as the mesh with the highest probability.

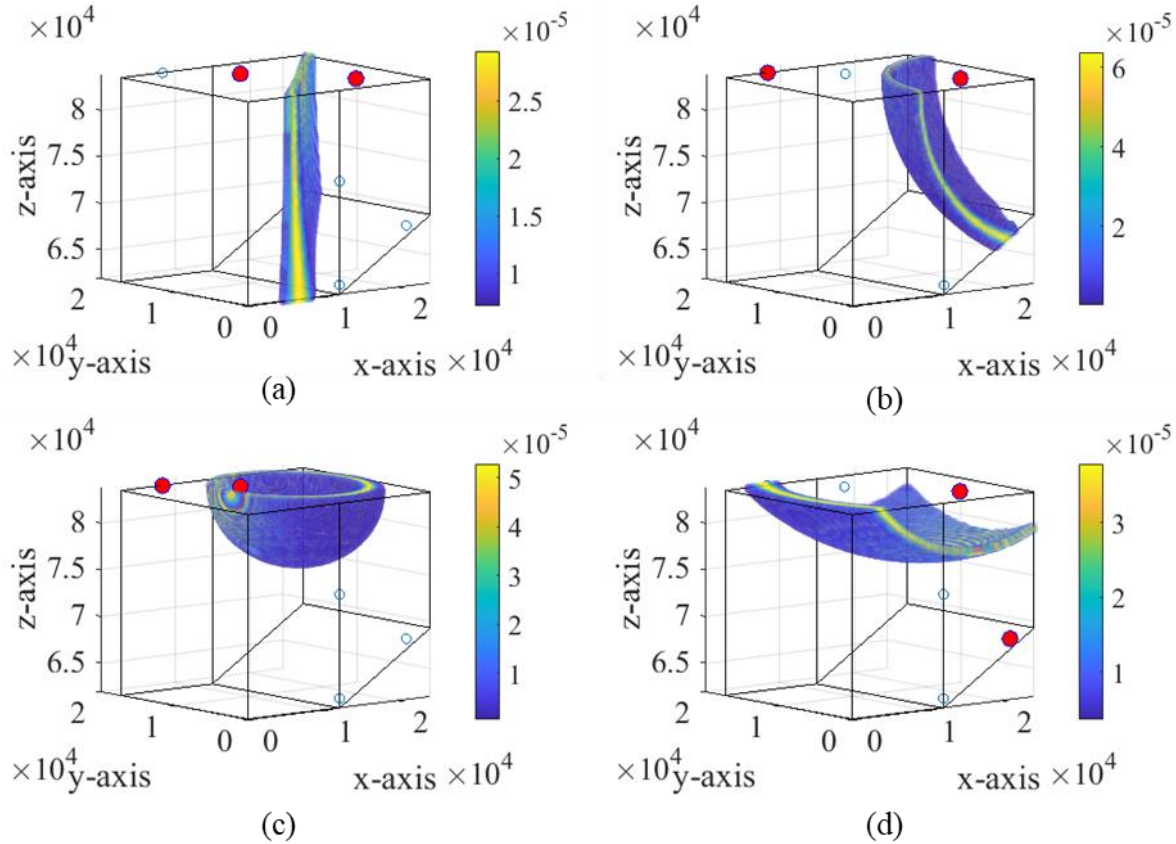

Figure 3-13 Simulation result: probability distribution from (a) sensors #5 and #6, (b) sensors #4 and #6, (c) sensors #4 and #5, (d) sensor #3 and #6.

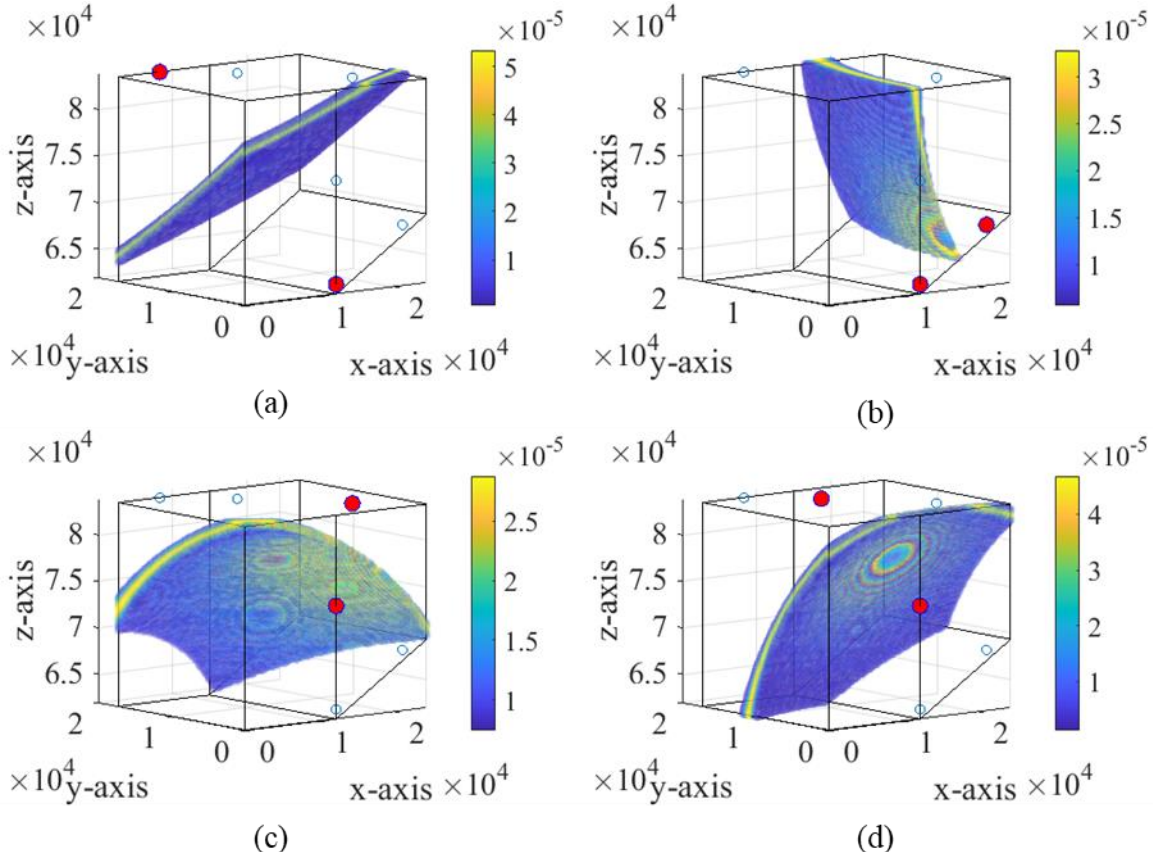

Figure 3-14 Simulation result: probability distribution from (a) sensors #3 and #5, (b) sensors #3 and #4, (c) sensors #2 and #6, (d) sensor #2 and #5.

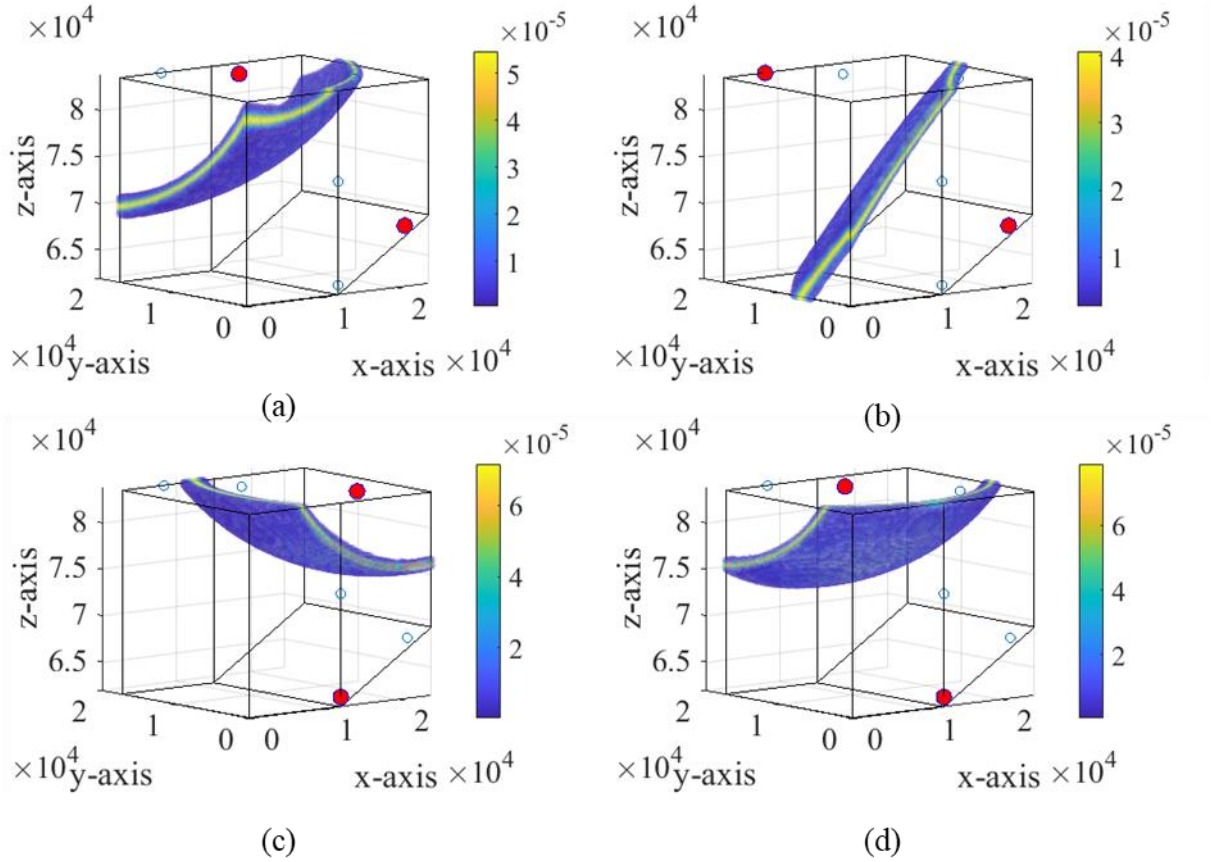

Figure 3-15 Simulation result: probability distribution from (a) sensors #2 and #4, (b) sensors #2 and #3, (c) sensors #1 and #6, (d) sensor #1 and #5.

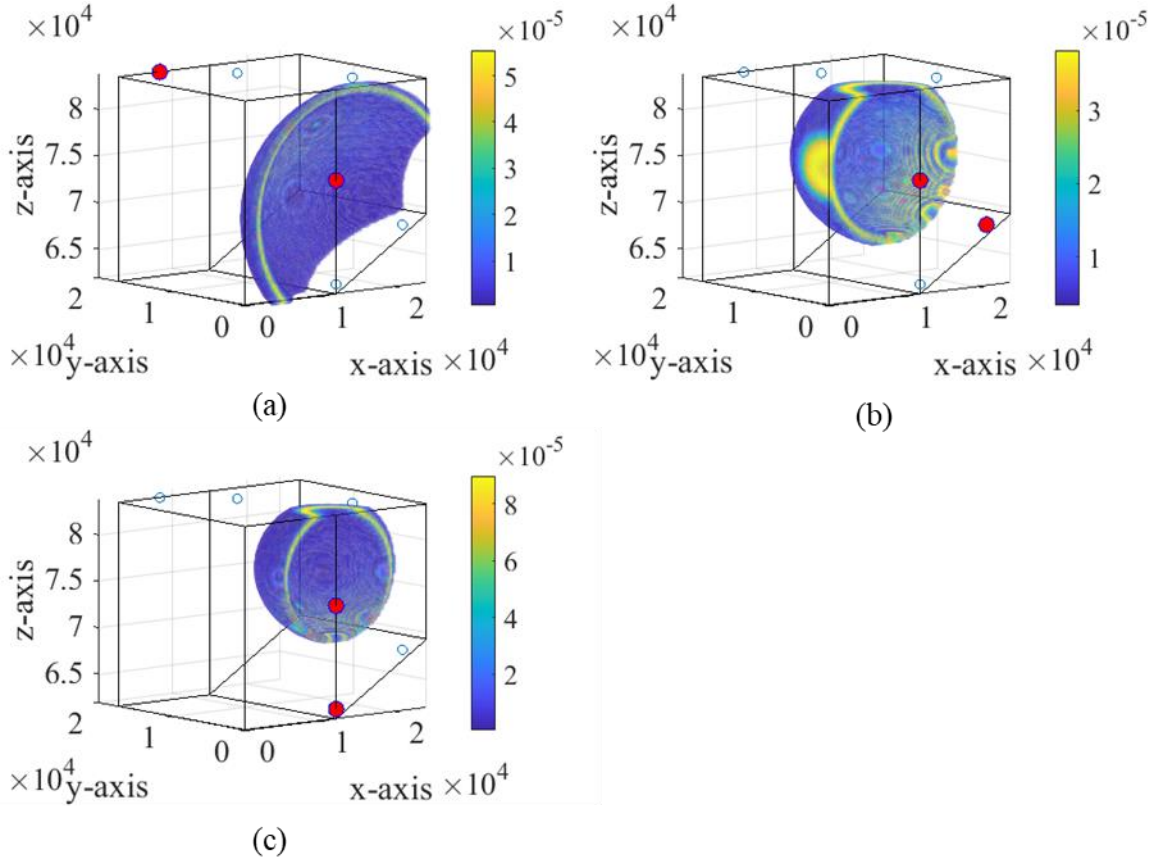

Figure 3-16 Simulation result: probability distribution from (a) sensors #1 and #4, (b) sensors #1 and #3, (c) sensors #1 and #2.

Using equation (3.13) with $\delta_k = 0$, the probability of the leakage at a specific point can be calculated by the energy ratio measured by sensors *i* and *j*. In the simulation, the number of leak-responsive sensors is 6, resulting in a total of 15 combinations. Figure 3-13 to Figure 3-16 show the probability distribution plots for all of 15 combinations; As shown in Figure 3-12 and Table 3-1, two sensors with the similar distance from each sensor to the leak position measure the similar energy for each other. As shown in Figure 3-13 (a), these results are consistent with the fact that meshes where the distance from the leak position to Sensor #5 and the distance to Sensor #6 are similar have the high probability of the leakage. Similarly, as shown in Figure 3-13 (b), the probability of the leakage is high at meshes that are closer to Sensor #6 than that to Sensor #4, this is because the leak energy measured by Sensor #4 is relatively lower than that measured by Sensor #6, as shown Figure 3-12. Therefore, the position having the high probability of the leakage can be thus confirmed from the energy ratio measured by leak-responsive sensors. Additionally, as the distance between the sensor and the location where the probability is estimated increases, the energy ratio may not be significantly different from that of the adjacent area. As shown in Figure 3-13 (a) and (b), it can be confirmed that this tendency is also reflected from the fact that the probability distribution becomes wider as it goes down in the z-axis direction. A similar tendency can be confirmed in the probability distribution among other sensors. The probability distribution among other sensors exhibits a similar trend, Figure 3-13 (c), and Figure 3-16 (a), (b), (c) show a nearly spherical probability distribution. This outcome is a result of the short distance between sensors and the similarity in the vector direction with the actual leak location. If the attenuation effect is slight, such as when the distance from the sensor is large or limited to the low frequency band, the probability distribution will approximate a spherical shape. On the other hand, if the attenuation effect is strong, such as when the distance to the sensor is small or limited to the high frequency band, the probability distribution shape will approach a sphere, which may be

approximated as an ellipse. Additionally, as mentioned earlier, the probability value tends to decrease symmetrically for a specific curved surface in all cases, and this tendency gradually decreases as the uncertainty increases. Therefore, by examining the thickness of the probability distribution, one can indirectly predict the uncertainty of the measured leakage energy.

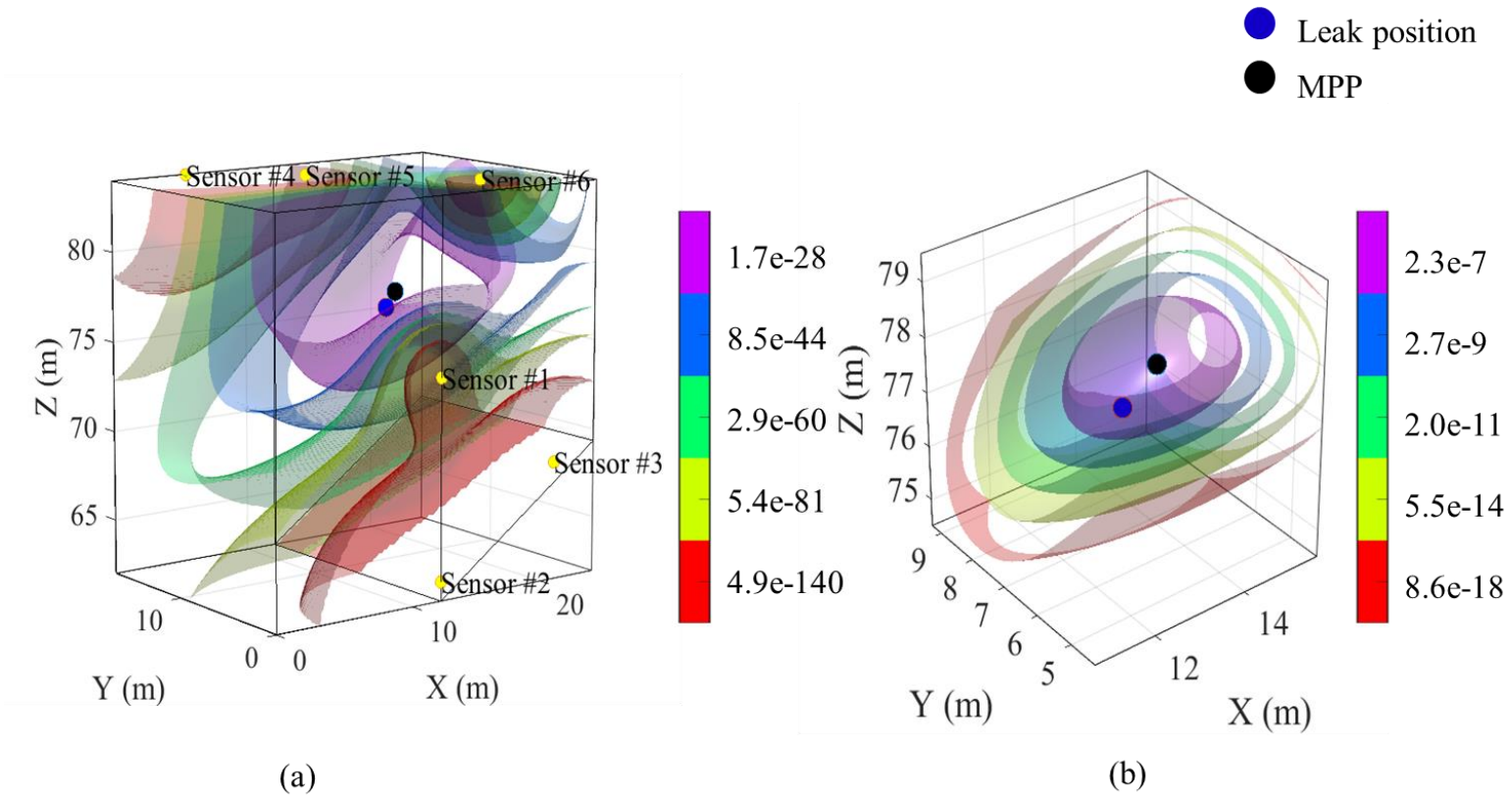

Figure 3-17 Simulation result of the isosurface of probability distribution; (a) whole target region (b) nearby leak position.

Figure 3-17 shows the isosurface of the probability distribution. From equation (3.16), it is possible to calculate a probability distribution that estimates the leak position by considering the energy measured from all leak-responsive sensors. As seen in Figure 3-17 (a), the results of the isosurface of the probability distribution are affected not only by the energy ratio of the signals measured from each sensor but also by the positions of each sensor. Comparing Figure 3-17 (a) and (b), a higher probability value is obtained in the vicinity of the simulated leak position. There is an error between the MPP and the simulated leak position, because the ratio of the measured energy is different due to uncertainty in the actual ratio energy, which is determined by the distance between sensors and the leak position. However, it can be seen that the simulated leak position has also relatively high probability because the proposed method can calculate the probability of the leakage while considering the sensor uncertainty.

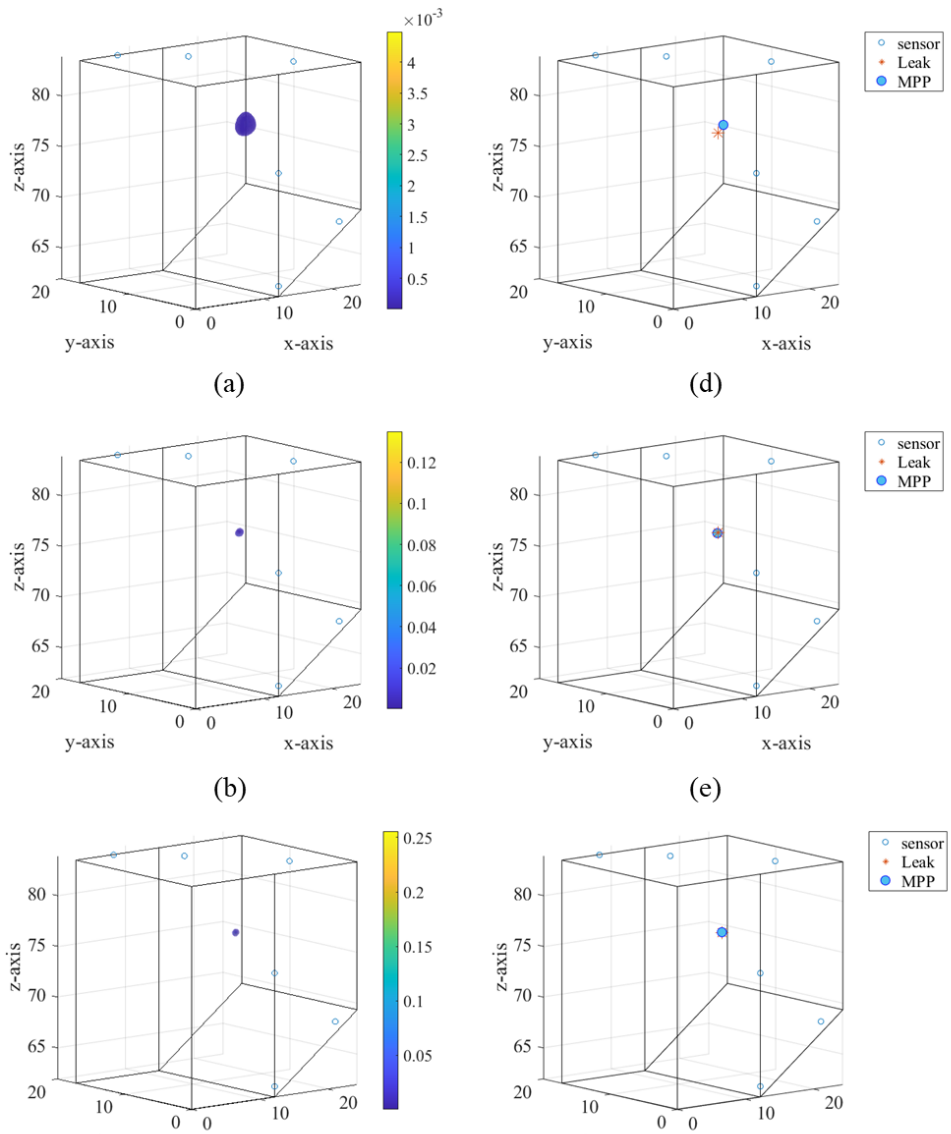

Figure 3-18 Simulation 1 results: probability distribution at sample times of (a) 1, (b) 15, (c) 30, and most probable point (MPP) at sample times of (d) 1, (e) 15, (f) 30.

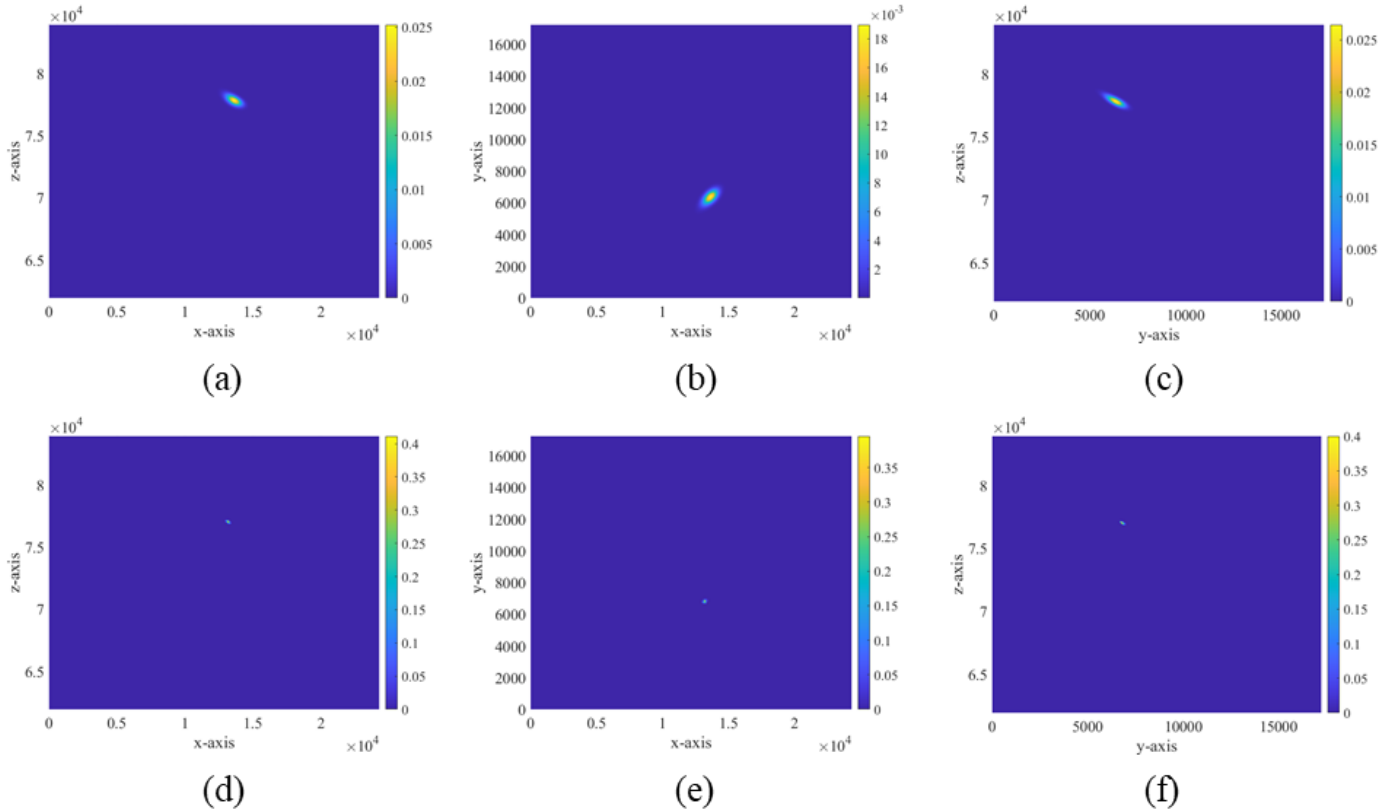

Figure 3-19 Marginalized probability distribution: (a) x-z plane, (b) x-y plane, and (c) y-z plane at 1 sample times; and (d) x-z plane, (e) x-y plane, and (f) y-z plane at 30 sample times.

Figure 3-18 shows the simulation results of the probability distribution and most probable point (MPP) calculated by the proposed method. In the mesh area, which is 99.99 % or more in total, is expressed using a scatter plot, along with probability values, to secure visibility. As shown in Figure 3-19 (a) to (c), we used 6 sensors to calculate the probability; thus, the result converges to a specific point as the sample times go on. As shown in Figure 3-19 (d) to (f), the MPP is closer to the simulated leak point. This means that even though there are errors in the delta estimation and the probability modeling approximation in the equation (3.15), the result is good enough to estimate the leak point. Figure 3-19 shows the marginalized probability distribution result of the proposed method. Each figure shows the x-y, x-z, and y-z marginal planes in increasing order. Simulation results show that the proposed method works well, considering that the final MPP result is very close to the simulated leak position. The final converged MPP (using 30 samples) is (13176, 6757, and 77061), which has an error of 78.3 mm from the simulated leak position (13200, 6800, and 77000), given in Table 3-1. Considering that the size of the mesh is (122, 86.6, and 110), the error is smaller than the size of the mesh itself (the length of a body diagonal = 185.7 mm); thus, it can be concluded that the estimated leak position is accurate.

3.3.3 Case study 2: Real-world industrial site data for the boiler tube fracture in the thermal power plant

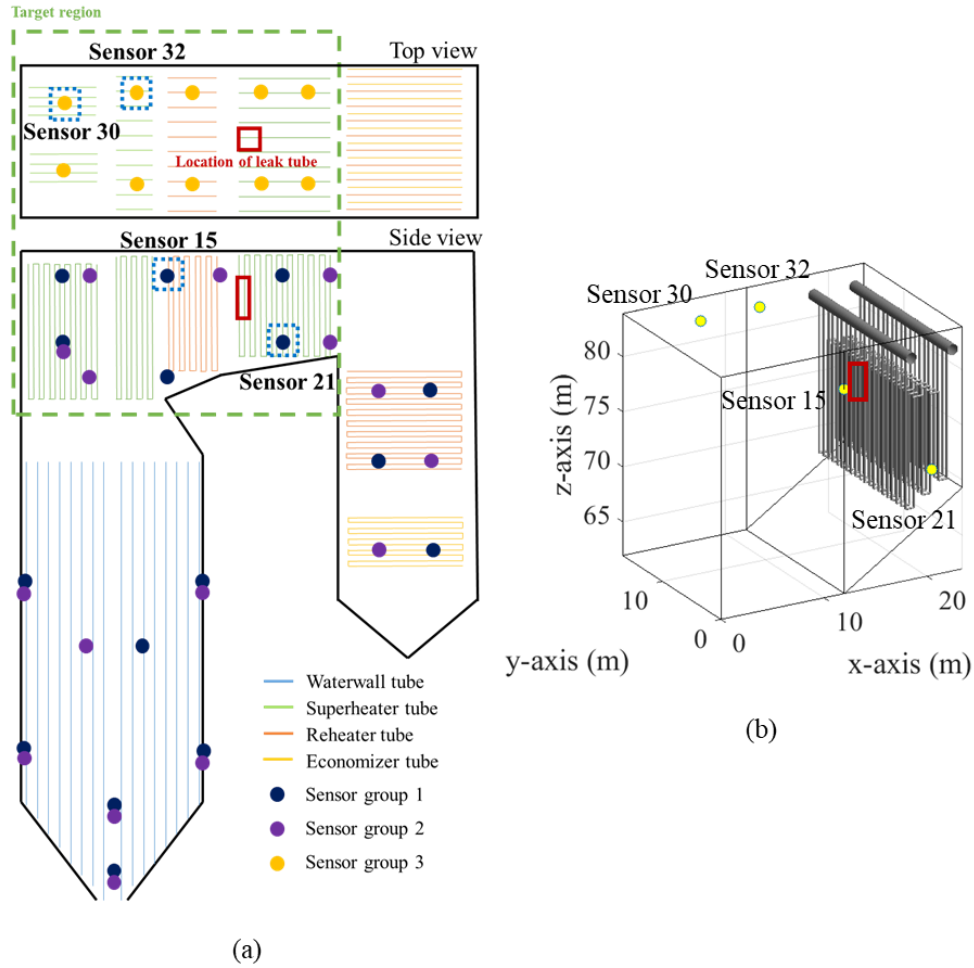

Figure 3-20 Layout of the boiler and sensor; (a) 2D layout for total structure, (b) 3D layout for target region.

In this case study, the boiler tube leak occurred in the final superheater. The sensitivity of the AE sensor used was 100 mV/g, and the effective frequency range was 0 to 20 kHz. The sampling rate of the measured AE signal was 1 sample/min. The layout of the boiler dimension and sensor location is given in Fig. 11. The sensors are deployed throughout the boiler and are categorized into three groups. Sensor group 1 is installed on the front side of the boiler, Sensor group 2 on the rear side, and Sensor group 3 on the header.

Table 3-2 Coordinates of AE sensors in the thermal power plant studied

Description	Coordinate (m)		
	X	Y	Z
Sensor #15	12.00	0.00	80.50
Sensor #21	20.50	0.00	71.51
Sensor #30	4.85	12.04	83.90
Sensor #32	10.79	12.38	83.90

The coordinates of the AE sensors that receive leak signals are given in Table 3-2. Sensors #15, #21, #30, and #32 are leak-responsive, which provided the measured leak signals in this case study; they are located at a certain distance from the leak tube. The other AE sensors do not measure a leak signal due to noise from surrounding components or their inability reach over the transmission path.

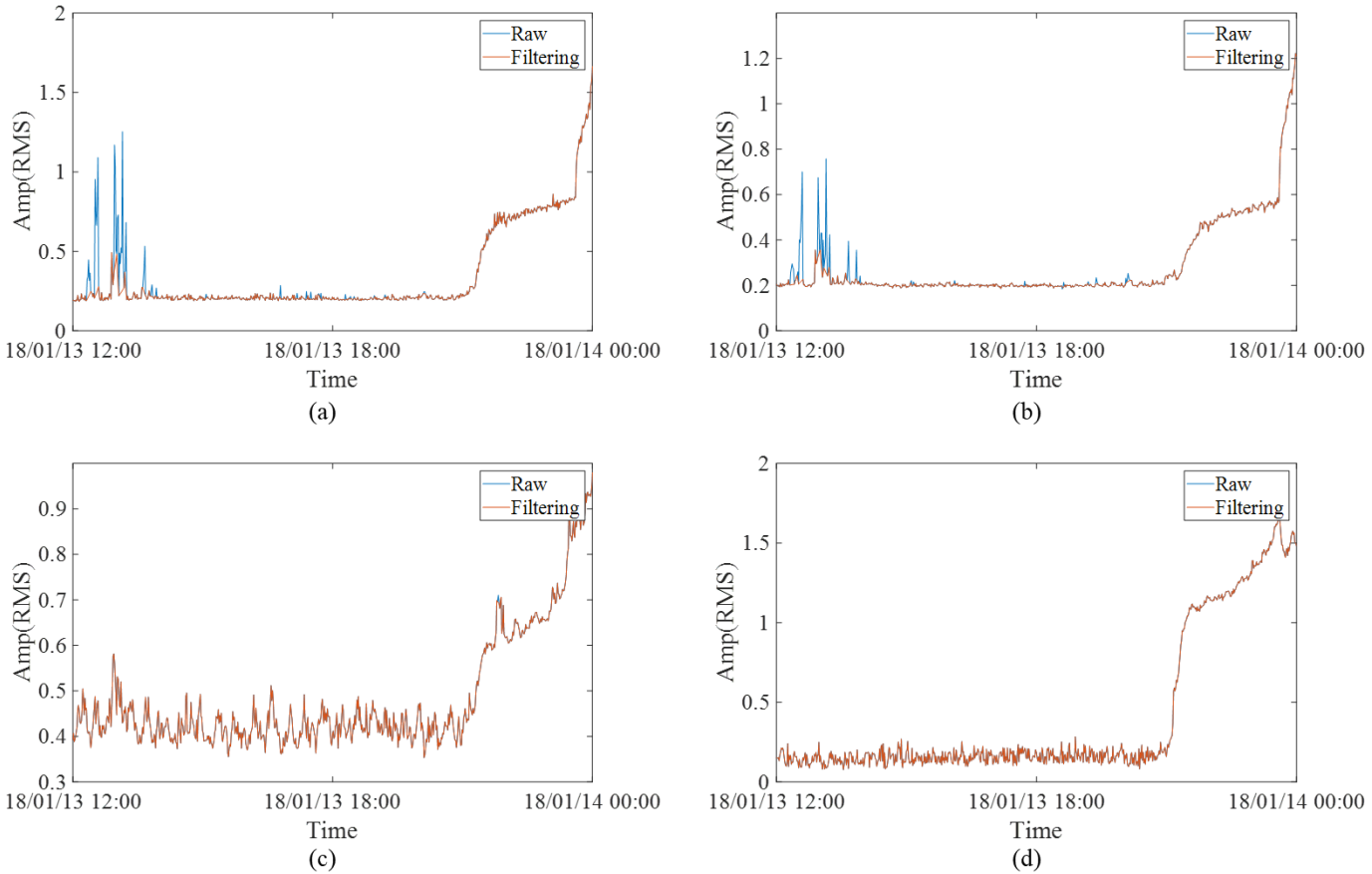

Figure 3-21 Signal trends of AE sensors in response to a leak (filtered vs raw); (a) Sensor 15, (b) Sensor 21, (c) Sensor 30, (d) Sensor 32.

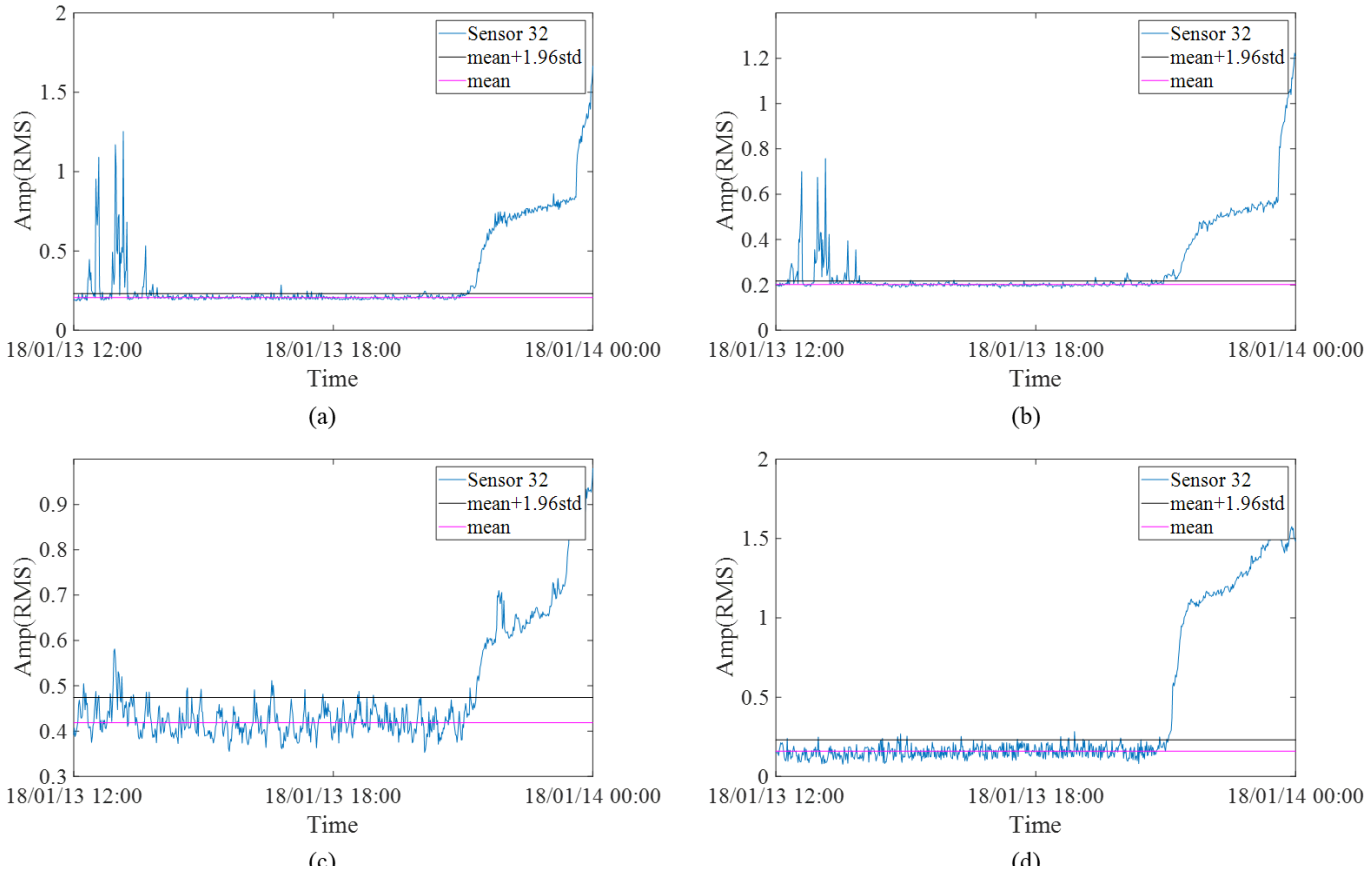

Figure 3-22 Signal trends of AE sensors in response to a leak (filtered with boundary); (a) Sensor 15, (b) Sensor 21, (c) Sensor 30, (d) Sensor 32.

Generally, the magnitude of the boiler signal depends on the operating condition. In particular, in-operation conditions (e.g., soot-blowing and extremely loud sound) may significantly affect the signal [30]. Therefore, this study considers si,normal when the operating condition is not dramatically changed by any unique operating state. As seen in Figure 3-19, the measured signals only have fluctuations when there is no change in the operating condition. The fluctuation of the signal varies for each sensor, because signals from surrounding components are introduced differently depending on the installed position of the sensor. For instance, Sensors #30 and #32, which are installed on the header of the boiler, could be affected by external noises, and thus the magnitude of the fluctuation is relatively larger; thereby, the corresponding δ is larger. To address the issue of soot-blowing signals, which are considered severe impulsiveness noise due to their significantly larger amplitude compared to the surrounding signals [30], a moving median outlier filtering method based on the three-sigma rule of thumb was employed for signal preprocessing. As illustrated in Figure 3-19 (a) and (b), this method effectively attenuates the soot-blowing signal, thereby preventing overestimation of the mean and standard deviation, without affecting the leak signal. In cases where the soot-blowing signal is absent, the filtered signal may be preferred over the raw signal. As demonstrated in Figure 3-19 (c) and (d), the absence of soot-blowing artifacts in the filtered signal results in a very similar profile to the raw signal, thus yielding desirable results.

Importantly, it can be seen that the signals gradually increase from the time when the leak occurs and that the RMS of the signal exceeds the boundary specified in the equation (3.1). The parameters used to calculate the probability equation are shown in Table 3-3. The attenuation coefficient constant for the equation (3.21) was calculated by considering the environmental condition and the upper and lower limit frequencies were set by sensor's effective frequency range. The coefficient of variation of each sensor was calculated using the outlier-preprocessed signal, which

is considered as the normal state.

Table 3-3 Parameters for calculating the probability equation.

Parameter	Description	Value
α	Attenuation coefficient constant ($Hz^{-2} \times m^{-1}$)	1.9363e-11
ω_H	Upper limit frequency (Hz)	20000
ω_L	Lower limit frequency (Hz)	0
δ_1	c.o.v. of Sensor #15	0.0603
δ_2	c.o.v. of Sensor #21	0.0397
δ_3	c.o.v. of Sensor #30	0.0679
δ_4	c.o.v. of Sensor #32	0.2275

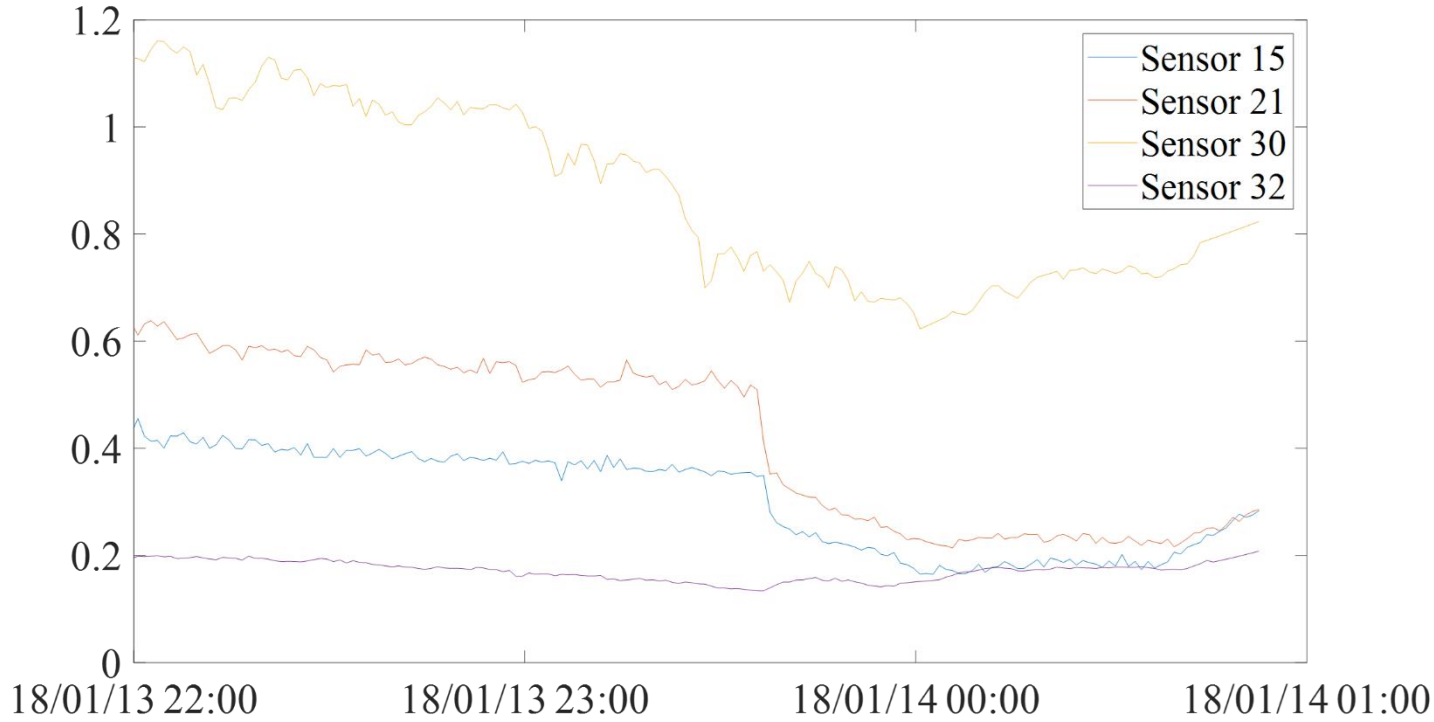

Figure 3-23 Trend of δ for each sensor after the occurrence of leak.

Figure 3-23 illustrates the δ values for each sensor calculated from the measured data after the leak occurrence, which is described in Figure 3-22. Examining the trend of sensor 30, it is evident that it has a high δ value throughout the entire duration. This can be attributed to two reasons based on Figure 3-22. Firstly, the ratio of the increased energy (from the leak) to normal state energy increased from the time of the leak is the smallest compared to the other sensor data. Secondly, the energy variation in the normal state is more significant than other sensor data. According to the equation (3.12), which demonstrates that β can be approximated as the same value, the ratio of the normal energy to the fault energy, denoted as the square root of $E[RMS_{normal}]/(RMS_{fault} - E[RMS_{normal}])$, should be larger when the fault energy (RMS) is small compared to other sensors, resulting in a larger δ. As indicated in equation (3.13), δ is proportional to δ_{normal}, which should be larger for the second reason. Thus, sensor 30 has the highest δ value, as shown in Figure 3-23. Conversely, sensor 32 has the smallest δ value due to the largest increase in fault energy shown in Figure 3-22. Although the variation in normal state energy is higher than that of sensors 15 and 21, the effect of the increase on δ is more significant than the effect of the variation of the normal state on δ. The delta value of the data exhibits a rapid change after 18/01/13 23:40, which can be verified by the sudden surge in energy shown in Figure 3-22. However, this change in the delta value trend is not attributed to a shift in the fault energy, but rather to a shift in the operating state resulting from the recognition of the fault itself. As a consequence, data after this point were excluded from the calculation.

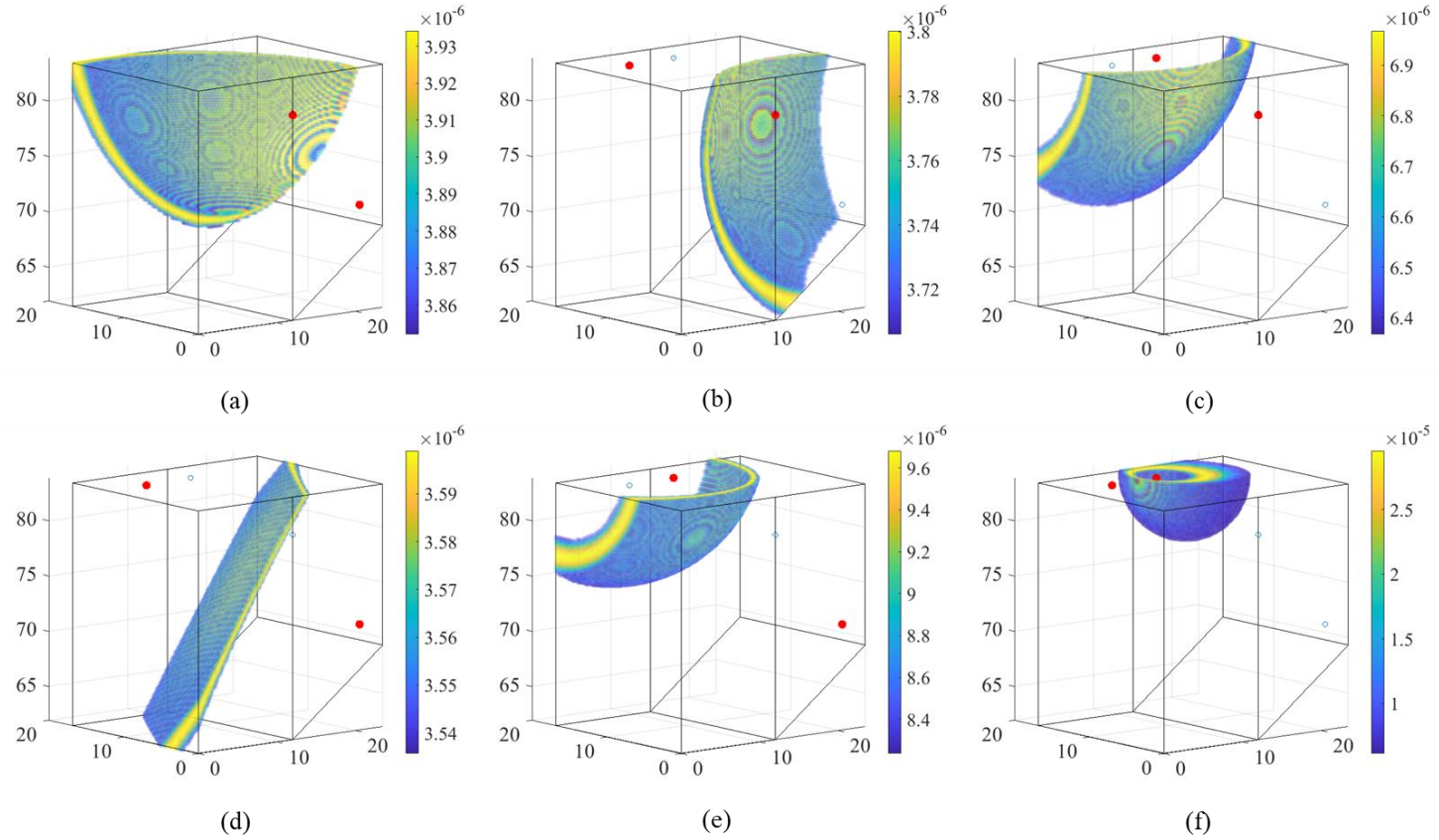

Figure 3-24 Experimental result: probability distribution from (a) sensors #15 and #21, (b) sensors #15 and #30, (c) sensors #15 and #32, (d) sensor #21 and #30, (e) sensor #21 and #32, (f) sensor #30 and #32.

The probability of a leak occurring at a specific point can be calculated using equation (3.15) with $\delta_k = 0$ and the energy ratio measured by sensors *i* and *j*. In the simulation, four number of leak-responsive sensors were used, resulting in a total of 6 combinations as depicted in Figure 3-24. The colored regions in each figure represent the probability, and their values are (0.1788, 0.1725, 0.3096, 0.1638, 0.4203, 0.7580), which are the same volume for each figure. This indicates that the areas corresponding to Figure 3-24 (f) produced the most reliable results. As previously mentioned, the relatively high uncertainty of the sensor 30 makes it difficult to attribute this outcome to uncertainty. Instead, it is likely due to the proximity of sensors 30 and 32, resulting in a more limited high-probability area. Similarly, Figure 3-24 (d) obtained from sensors 21 and 30 reveals that it is difficult to obtain a point with a high probability if the area is distributed over a wide range. In contrast, the relatively small uncertainty of sensor 32, as discussed earlier, results in its combination with other sensors in Figure 3-24 (c), (e), and (f) having a higher probability compared to other values. The analysis results for other items, such as the latent curve surface of the distribution, are consistent with those presented in case study 1 and will not be discussed further.

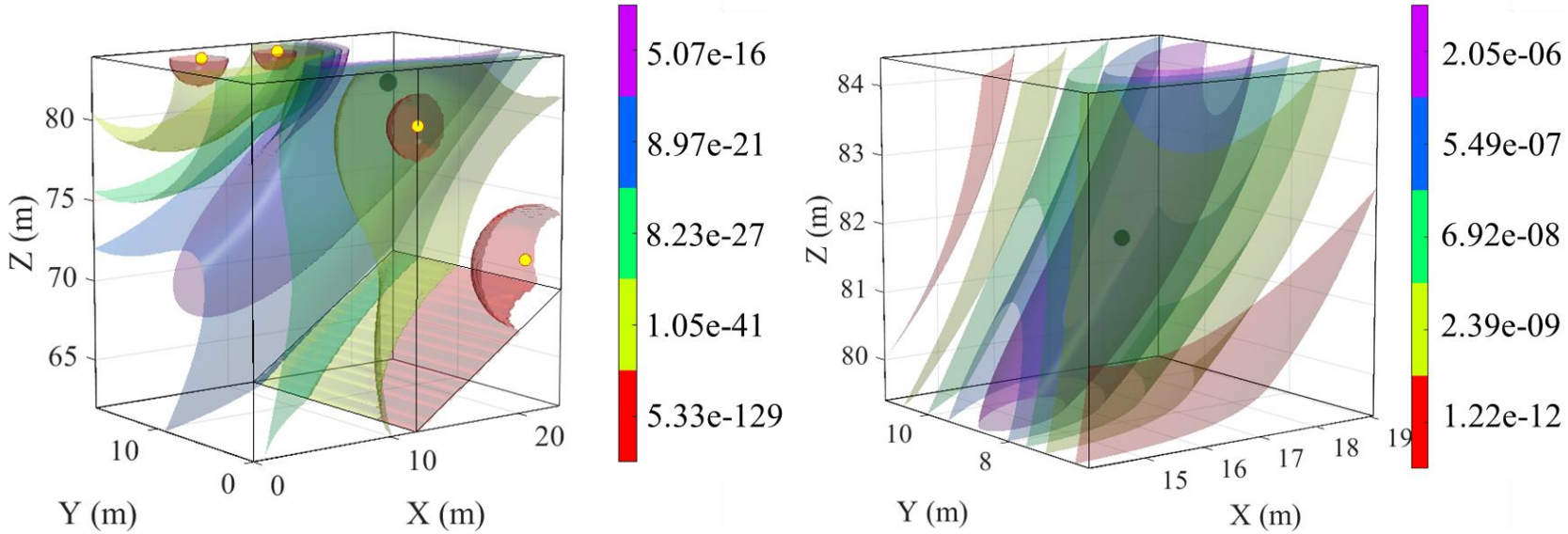

Figure 3-25 Experimental result of the isosurface of probability distribution; (a) whole target region (b) nearby leak position.

Figure 3-25 shows the isosurface of the probability distribution calculated using the proposed method. The probability distribution is obtained as 10 times updated from the measured signals from the sensor #15, #21, #30, and #32. The black circle is MPP obtained by the proposed method, and yellow circles are the position of sensors. It is worth noting that the proposed method was able to accurately identify the location of the leak using the measured signals from only four sensors. The black circle in Figure 3-25 (a) represents the MPP obtained by the proposed method, which corresponds to the location of the leak. Despite the fact that most of the sensors are distributed on a similar z-axis component, the proposed method was still able to accurately estimate the location of the leak. However, it should be noted that the precision of the z-axis value of the leak position may be poor due to the similar z-axis components of the leak-responsive sensors. One can observe similarities between the color bar values in Figure 3-17 and Figure 3-25 when comparing them. This can be attributed to the fact that there is no notable difference between the simulation data and experimental data in terms of uncertainty. Overall, the probability distribution obtained from the proposed method is consistent with the simulation results, indicating that the proposed method is effective in detecting and locating leaks even with a small number of sensors.

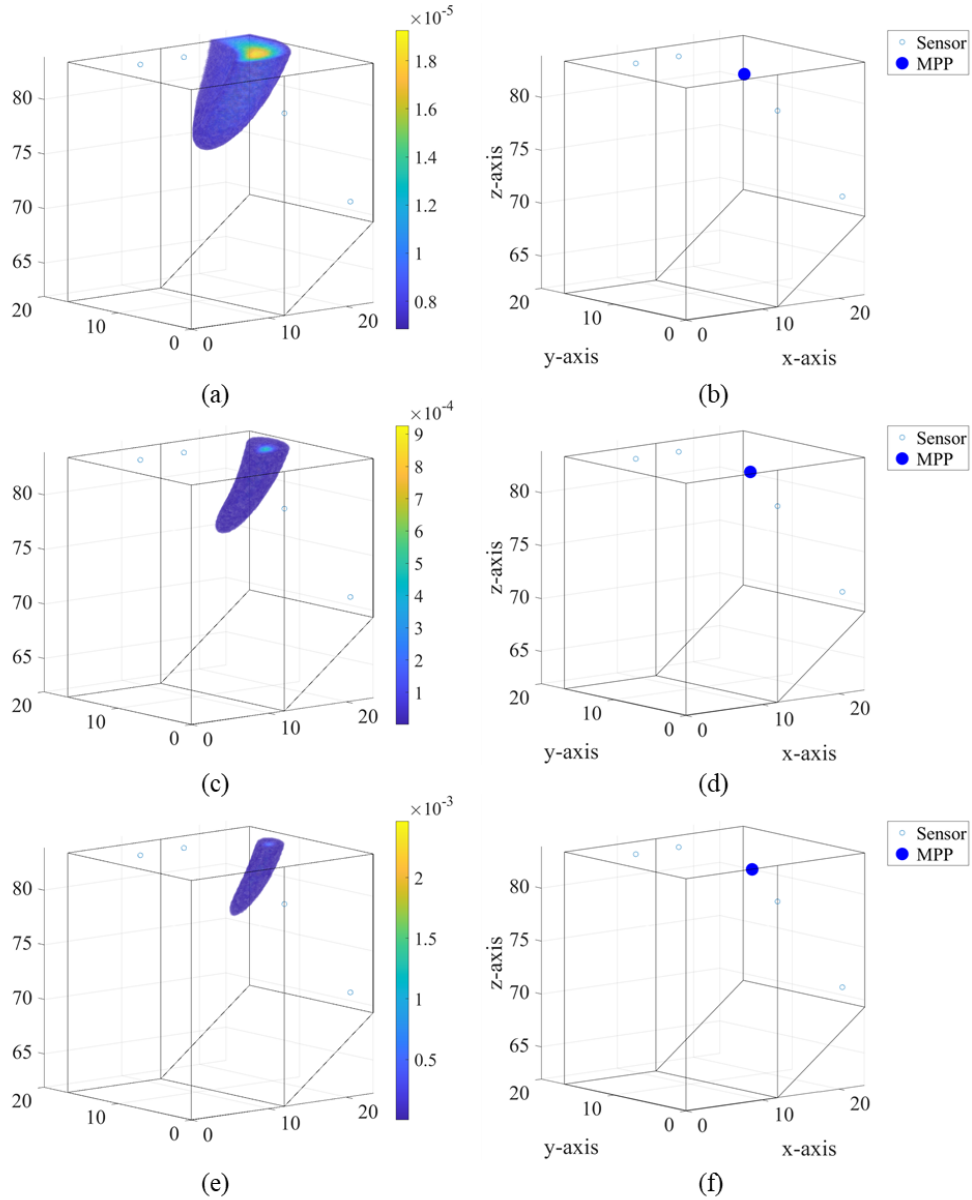

Figure 3-26 Experimental results: probability distribution at sample times of (a) 1, (b) 15, (c) 30, and most probable point (MPP) at sample times of (d) 1, (e) 15, (f) 30.

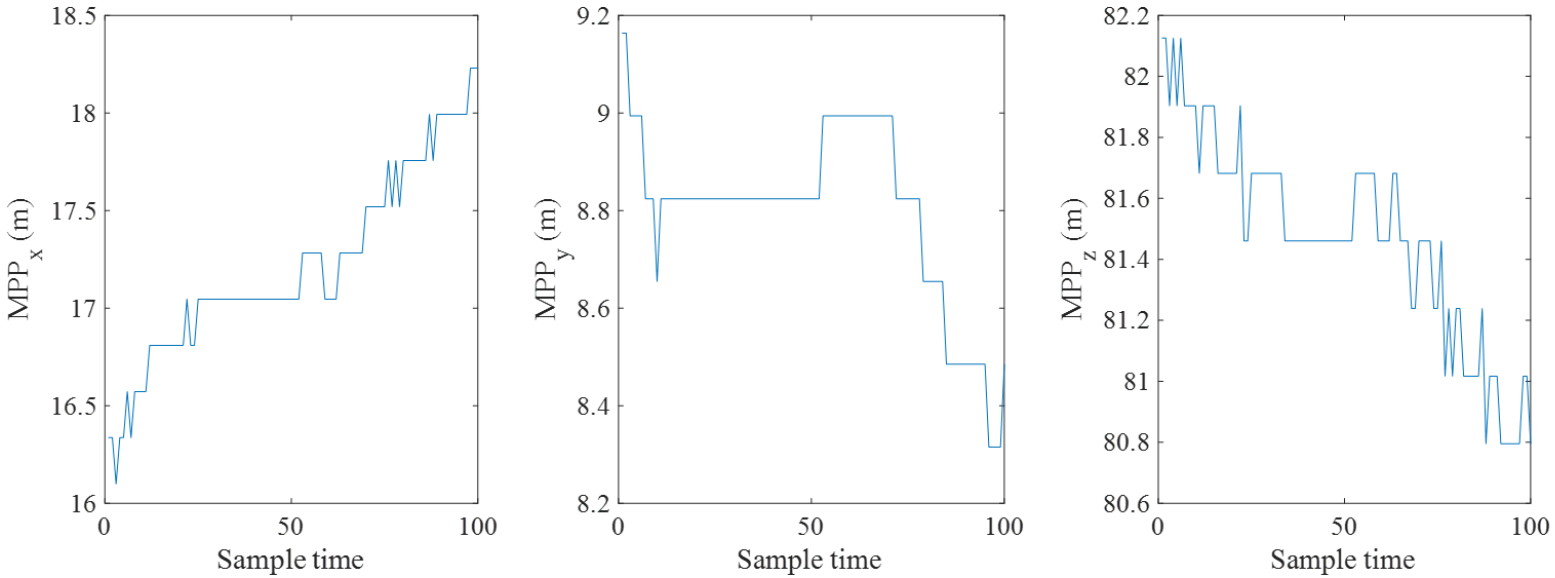

Figure 3-27 The trend of the MPP (most probable point) over time, with each data point representing the MPP at a specific time. (updated by the time sequential data using 1 sample time to the specific time).

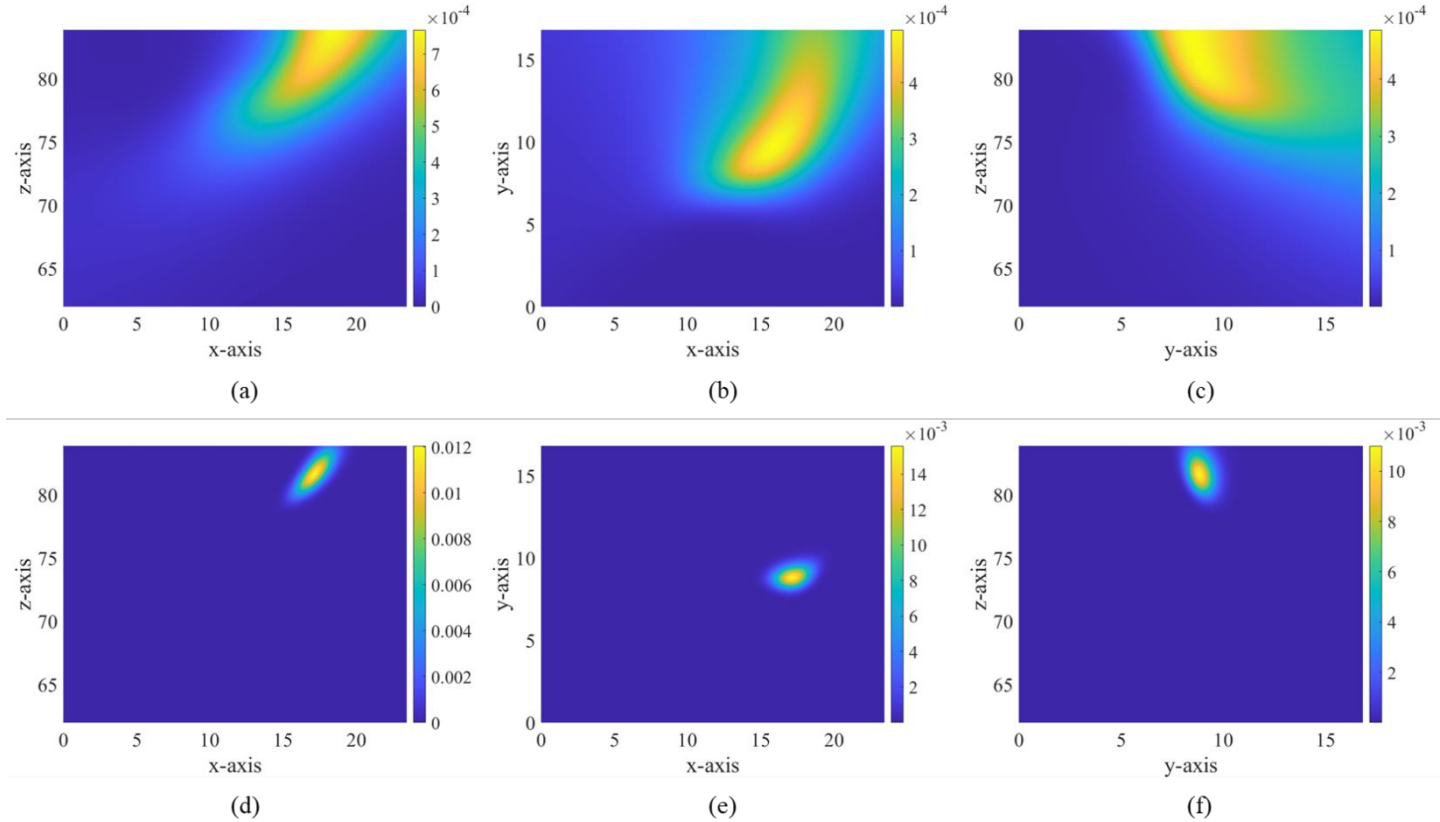

Figure 3-28 Marginalized probability distribution: (a) x-z plane, (b) x-y plane, and (c) y-z plane at 1 sample times; and (d) x-z plane, (e) x-y plane, and (f) y-z plane at 30 sample times.

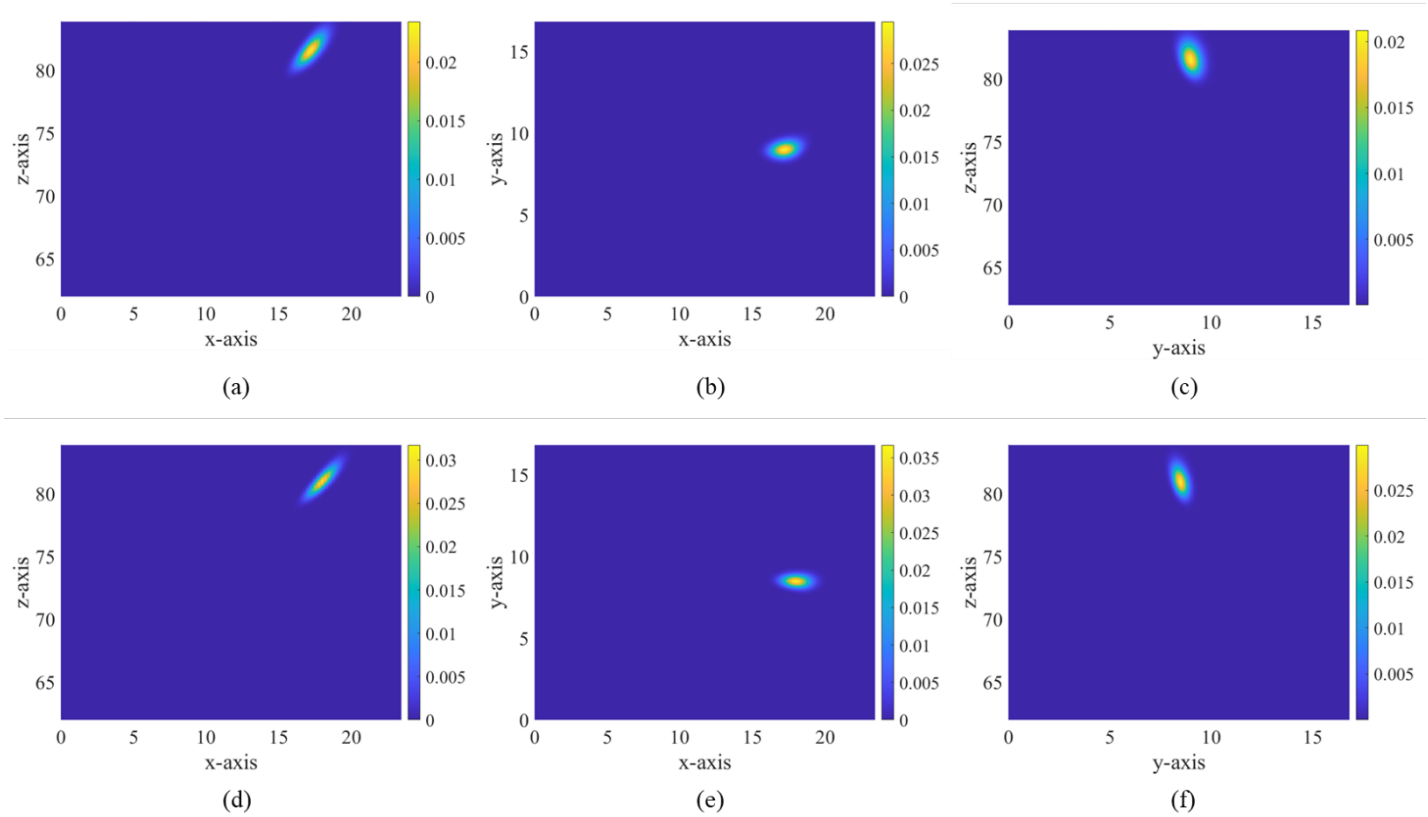

Figure 3-29 Marginalized probability distribution: (a) x-z plane, (b) x-y plane, and (c) y-z plane at 60 sample times; and (d) x-z plane, (e) x-y plane, and (f) y-z plane at 90 sample times.

Figure 3-26 presents the experimental results of the probability distribution and most probable point (MPP) obtained using the proposed method. In contrast to Figure 3-18, which shows the mesh area representing 99.99% or more of the total probability distribution, the probability values are presented as a scatter plot to enhance visibility due to the high uncertainty of the utilized data. The probability distribution at one sample time is limited to 48.42%. The figure shows that the high probability area gradually decreases over time, and this trend is observed up to 30 sample times, as indicated in Figure 3-27. Two reasons can explain this tendency: 1) the uncertainty of sensor location and measured data, and 2) changes in the measured energy ratio. In an ideal case such as the simulation case study presented in section 3.3.2, for the results to continue to converge, the fault energy ratio should remain constant and not change significantly over time. However, in the real situation depicted in this case study, the transmitted fault energy in the frequency band of the fault energy ratio does not appear to be consistent or maintained constant by various internal components, as shown in Figure 3-23. Therefore, the updated probability distribution gradually shifts to fit the leakage energy trend even after a long sample time. The trend mentioned earlier can be observed more clearly in the results presented in Figure 3-28 (d), (e), (f), and Figure 3-29. In the marginalized probability distribution of each axis, it can be observed that the position of the MPP gradually moves to fit the trend on the line, without significantly damaging the shape of the probability distribution. This observation validates the proposed update method. Additionally, as stated previously, the marginalized probability distribution indicates a large relative uncertainty in the z-axis. As shown in Figure 3-29, which shows a converging probability distribution shape, it is evident that the variation in the z-axis is wider than that in the x/y-axis. Additionally, since the converged region in the *x*-*y* plane is relatively small, it can be said that it is advantageous for the maintenance strategy to check the actual leak position while going down the *z*-axis in a specific region.

In summary of analysis of these probability distributions, Figure 3-28 shows the marginalized probability distributions for each axis at three different sample times. It can be observed that the distributions gradually become narrower and the peaks become sharper as more samples are acquired. This indicates that the uncertainty in the estimated leak location decreases over time, which is a desirable characteristic of the proposed method. Figure 3-29 shows the convergence of the probability distribution to a stable shape after a sufficient number of samples have been acquired. It can be observed that the shape of the distribution remains consistent beyond sample time 30, which suggests that the method has reached a stable estimate of the leak location. This is further supported by the fact that the MPP trend stabilizes after sample time 30 (as shown in Figure 3-26).

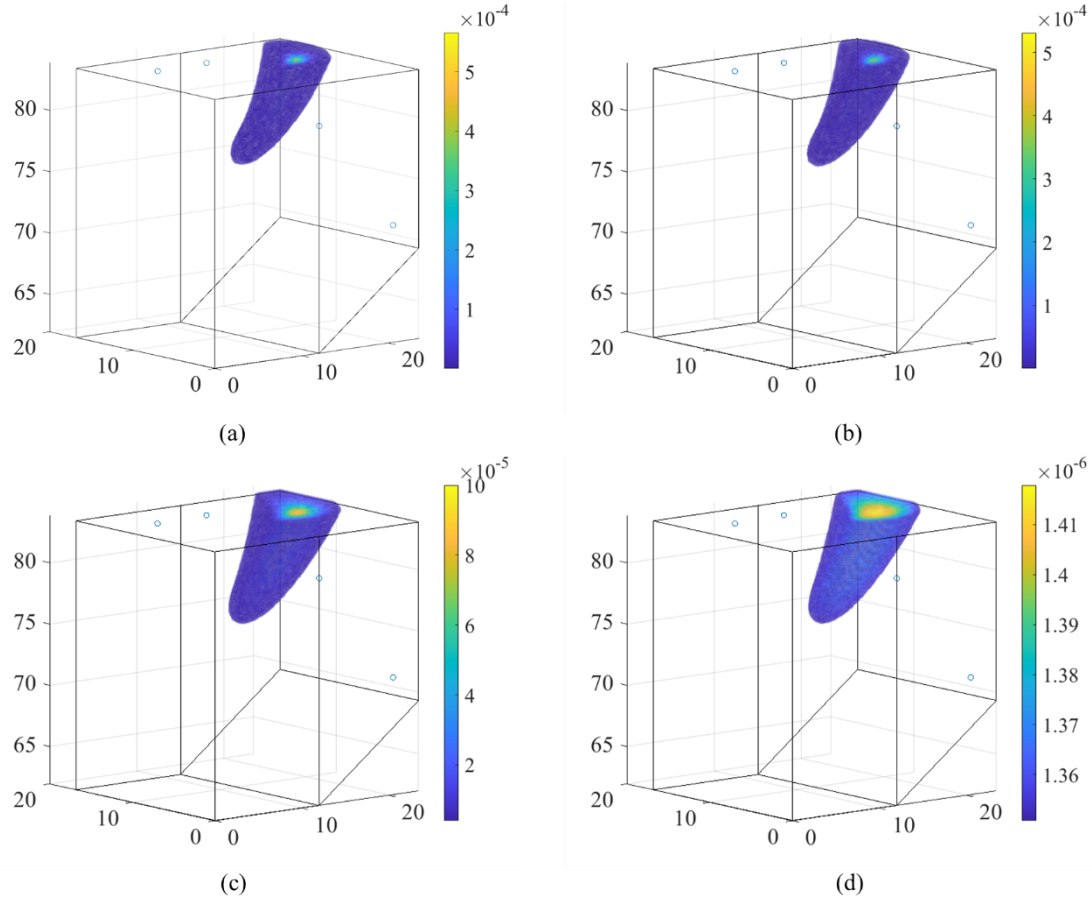

Figure 3-30 Different δ_k for calculating the probability distribution of fault location; (a) $\delta_k = 0$, (a) $\delta_k = 0.1$, (a) $\delta_k = 1$, (a) $\delta_k = 10$

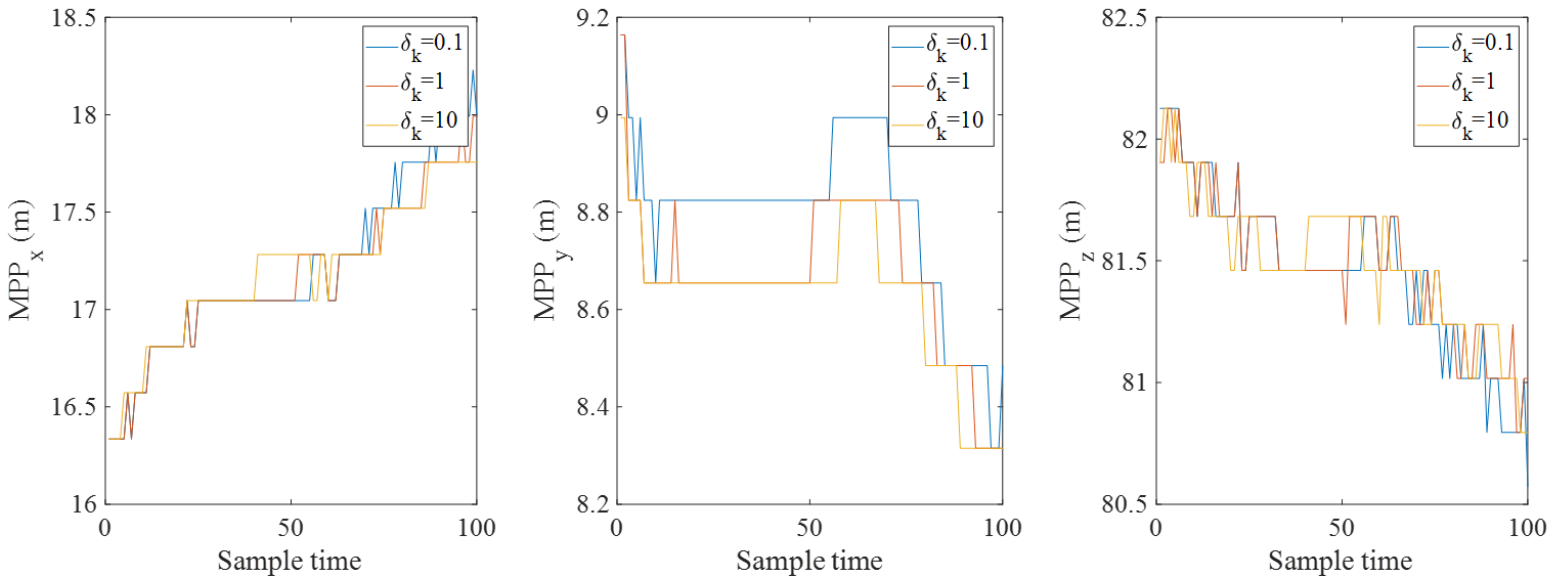

Figure 3-31 Different δ_k for obtaining MPP from the probability distribution of fault location; (a) x-axis, (b) y-axis, (c) z-axis

Figure 3-30 and Figure 3-31 show the effect of the δ_k value, which represents the uncertainty in the frequency domain of the fault energy, on the calculated probability distribution and MPP. As the δ_k value increases, the probability distribution becomes wider and the probability values decrease, indicating higher uncertainty in the estimated leak location. This is consistent with the intended effect of considering larger uncertainty in the measured energy.

In Figure 3-30, specifically in panels (c) and (d), although they may appear similar at a glance, a closer look at the probability values in the corresponding areas reveals a significant difference. For example, in panel (c), the probability values are around 0.9, while in panel (d), the probability values are much lower, around 0.06. This suggests that even a slight difference in the δ_k value can result in noticeable differences in the estimated probability distribution and MPP, as reflected in the colorbar values. This underscores the sensitivity of the method to the choice of δ_k value and the importance of properly accounting for uncertainty in the frequency domain of the fault energy in the estimation process.

In Figure 3-31, it appears that the MPP value does not vary significantly with different δ_k values. Even when the difference in δ_k values is the largest, the variation in the MPP value does not exceed the size level of one mesh set in the approximate probability distribution represented as a mesh. This is likely due to the fact that the proposed method uses average values that are fitted to a general model, excluding the uncertainty, when estimating the MPP coordinates.

When considering the results together, it can be inferred that the proposed method generates a wide probability distribution when the uncertainty around the MPP value increases (i.e., when the δ_k value increases), and a narrow probability distribution when the uncertainty is small. This suggests that the proposed method is able to effectively capture and represent the uncertainty in the estimated probability

distribution, and the reliability of the results is well demonstrated by the width or narrowness of the generated probability distribution.

The δ_k values used in the analysis require prior knowledge. In this case, the fault energy distribution is assumed to follow a normal distribution N(1, ς^2) as derived from Equation (3.15), which can be approximated using a transfer function that models the transmission effect. However, in practical scenarios, it may be challenging to accurately assume that the fault energy distribution in the frequency domain follows a normal distribution. Instead, it can be considered that the maximum available information has been derived from the probability distribution obtained, taking into account that when a severe fault occurs, the energy rise may happen across the entire frequency band and can only be approximated using a low-sampling signal.

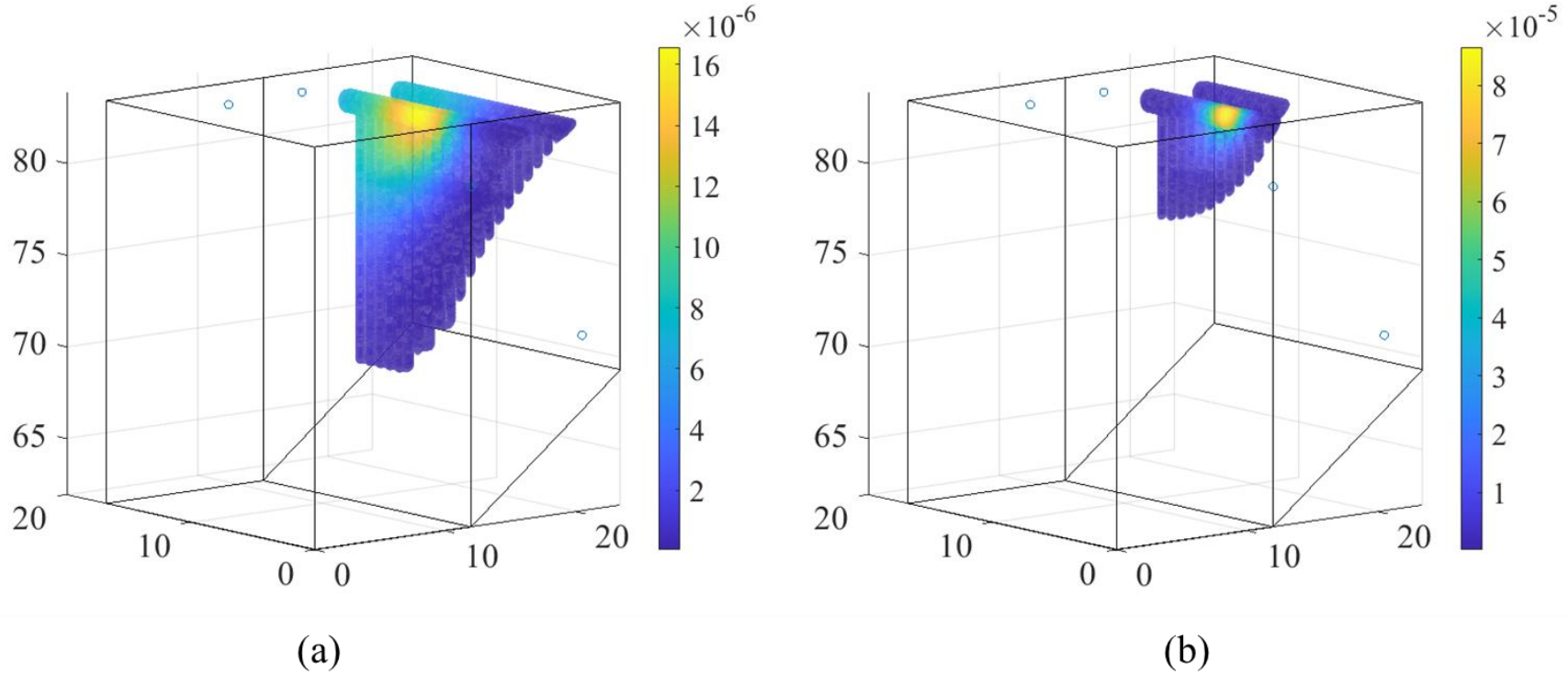

Figure 3-32 Fault probability using prior assumption on CFL; (a) 1 sample time, (b) 5 sample time.

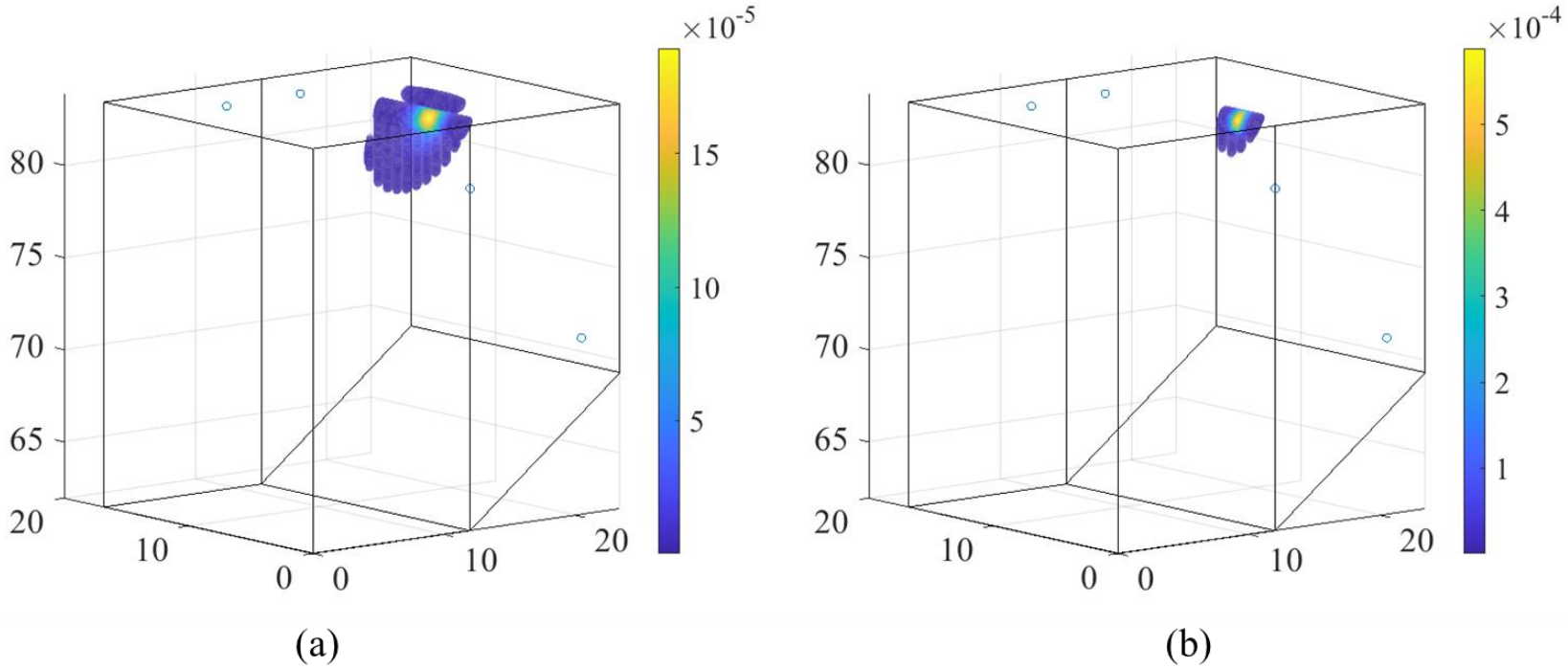

Figure 3-33 Fault probability using prior assumption on CFL; (a) 15 sample time, (b) 30 sample time.

Figure 3-32 and Figure 3-33 are the results when the probability distribution is obtained by limiting the CFL to the area of the boiler tube in the superheater, not the whole area of the superheater, which is the target system as shown until Figure 3-31. Based on the equation (3.16), it can be calculated by setting the prior probability of the area where the boiler tube exists to 1 and the rest to 0. Compared to Figure 3-26, it can be confirmed that the probability value is obtained as a large value for a narrower area because the area is limited. In addition, since the number of meshes to be calculated is reduced, the overall amount of calculation is also reduced.

The probability distribution considering the tube location can provide more accurate information for fault detection and diagnosis. As shown in Figure 3-32 (b), the probability distribution is more concentrated and the MPP is located near the actual tube location. This implies that considering the tube location can reduce the uncertainty in fault detection and diagnosis. However, it should be noted that assuming the tube location is known is not always practical. In real-world scenarios, the location of the tube may not be accurately known or may change over time. Therefore, it is important to consider the trade-off between the accuracy of fault detection and diagnosis and the practicality of obtaining the tube location information. Overall, the results demonstrate the potential of considering additional prior information in improving the accuracy and reliability of fault detection and diagnosis.

The probability distribution shown in Figure 3-33 may be considered to contain less information. However, assigning different initial probabilities to each tube location based on a more precise analysis of the tube location can lead to more reliable results than the probability distribution shown. For example, at joint points where horizontal and vertical tubes meet, a higher initial probability can be imposed due to the increased risk of leakage. Similarly, for bent parts of the tube where the flow of the internal fluid changes rapidly, a high initial probability can be assigned. Moreover,

since the internal fluid receives energy as it is transferred, the temperature and pressure of the tube passing later may rise. Hence, it is possible to develop a method of gradually increasing the probability for the tube passing later by considering this flow. By incorporating these factors into the initial probability assignment, the accuracy and reliability of the fault diagnosis results can be improved.

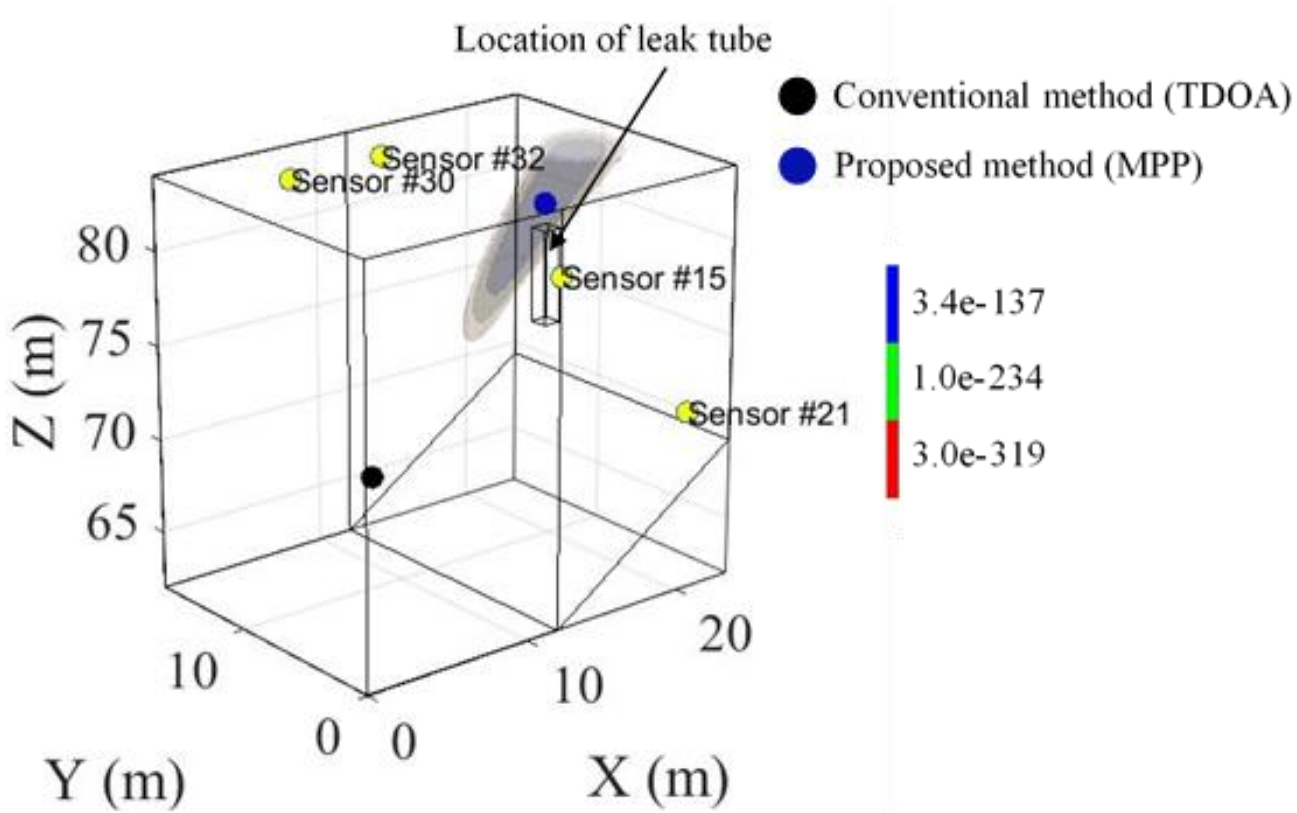

Figure 3-34 Comparison of the proposed method with TDoA

To show the superiority of the proposed method, the proposed method is compared with the conventional method, TDoA. The MPP and the probability distribution are calculated by examining 30 sample times after the leak occurs. When estimating the leak position through TDoA, the time difference of arrival of the leak signal is calculated through cross-correlation between leak signals. Here, TDoA is calculated by using the temporal-cross correlation based on the descriptor. Therefore, TDoA can be calculated in units of the time step size (1 second) of the measured descriptor, which causes a large error, as shown in Figure 3-34. On the other hand, unlike TDoA, the proposed method does not require a high-sampling rate signal because it is calculated based on the energy ratio.

3.4 Summary and discussion

This chapter proposed a probabilistic energy-ratio-based localization (PERL) method that used an energy-related descriptor of the signal. The radial dissipation of sonic waves and the attenuation in the the signal were considered. Since it is impossible to measure the signal energy directly at the fault source, the energy ratio equation was derived. To account for background noises and sensor disturbances, the uncertainty of the sensor energy was characterized in a probabilistic manner. Bayes theorem was used to calculate the probability that the signal was measured at the hypothesized location of the fault source. A probability distribution obtained for every sample time was utilized to localize the fault source and to prevent a local bias error that might arise due to outsourced large signals. Using the proposed method, it was found to be possible to calculate the probability that a boiler tube leak occurred at each mesh. In case study 1, for simulation data, the proposed method was able to estimate the leak position with an error of 78.3mm, which was less than the length of the body diagonal of the mesh. In case study 2, for the real-world industrial site data, the proposed method was able to estimate the leak position with an error of less than 5m.

1) The proposed probabilistic model can estimate the location of a fault using only the energy-related descriptor of the signal. By accurately reflecting the measurement uncertainty caused by the operating conditions or the disturbance noise of the sensor itself, it is possible to estimate a probable leak without much error, even in real-world operating conditions.

2) The results derived by the proposed method can be calculated effectively even if only two or three sensors respond to the fault. This has a great effect when the system’s size is huge and does not meet the conditions for reacting to four or more sensors, as required by conventional methods. Thus, this can solve the difficulty in finding a convergence point that must arise for success of conventional

methods; this issue can arise in real-world situations due to an insufficient number of fault-responsive sensors.

3) From the point of view of establishing a maintenance strategy in the case of the large scale system, efficient operation is possible by considering the probability distribution in three-dimensional space.

The proposed research assumes a situation where the leakage signal is significantly distorted due to the adjacent components or tubes in the propagation. It is generally reasonable to assume that the leaks occur in the bent ends that change the direction of the fluid flow; however, the error can be large when a leak occurs deep inside of the boiler, which results in serious distortion in the signal propagation. In this case, it is expected that the issue can be solved by utilizing the differential pressure signal that considers the internal fluid flow and by performing spectral analysis through the high-sampling signal. In future research, a method of applying a probabilistic model that considers these aspects for more precise localization will be studied, for use when high-sampling-rate data can be measured.

Sections of this chapter have been published as the following journal articles:

1) **Kyumin Na,** Heonjun Yoon, Jaedong Kim, Sungjong Kim, and Byeng D. Youn. "PERL: Probabilistic energy-ratio-based localization for boiler tube leaks using descriptors of acoustic emission signals." *Reliability Engineering & System Safety*, 230 (2023): 108923.

Chapter 4

Fault Affected Signal Energy Ratio (FASER)

In this chapter, we propose a novel method for extracting fault-affected signals from high-sampling-rate vibration signals using time-frequency analysis (TFA). Time-frequency analysis is a well-established approach for analyzing non-stationary signals in both the time and frequency domains. Among various TFA methods, short-time Fourier transform (STFT) is widely used due to its low computational cost compared to other methods such as the Wigner-Ville distribution (WVD) and wavelet transform (WT) [76]. The lower computational cost of STFT makes it more practical for industrial applications. However, transforming a vibration signal to STFT can result in uncertainties due to the uncertainty principle in time-frequency representation and the presence of background noise and impact signals from adjacent components, such as bearings. Moreover, as vibration signals are typically measured consecutively in industrial settings, it is challenging to store them separately while considering varying operating conditions. Therefore, it is unclear how to segment the signal for estimating the uncertainty in STFT even if the operating conditions are periodic. Although encoder information from a tachometer can be used to process consecutively measured vibration signals, this approach may also incur errors due to the indirectivity between the sensor and the tachometer. Furthermore, the use of encoder information may not be feasible due to economic considerations. These challenges make it difficult to accurately measure the uncertainty of non-stationary signals and approach them effectively. Neglecting the uncertainty in Short-time Fourier Transform (STFT) can result in misinterpreting

signal energy changes that are caused by noise or unsynchronized operating conditions as the effect of faults, rather than their underlying causes. Moreover, it may lead to the oversight of small changes in the signal energy originating from faults.

Despite the development of various STFT-based fault-diagnosis methods in previous studies [77-80], the uncertainty in STFT has only been partially considered. Therefore, this study proposes a novel probabilistic approach, called the fault-affected signal energy ratio (FASER) method, for diagnosing gearbox faults under variable-speed conditions. To extract signals affected by faults, it is essential to model the energy distribution of non-faulty signals in a probabilistic manner, accounting for operating conditions. To achieve this, we first build probabilistic models for each time-frequency index of the short-time Fourier transform (STFT) of the normal signal. STFT can be viewed as a concatenation of Fast Fourier Transform (FFT) results over short time periods, with each period's FFT depending on the operating condition. By computing the Kullback-Leibler divergence (KLD) between FFT results for each time period, their similarity can be evaluated, and uncertainty can be estimated by collecting signals under similar operating conditions. This enables us to quantify the uncertainty in the STFT of the normal signal and extract fault-affected signals more accurately. Two assumptions are made for this process to apply a newly measured signal: 1) the newly measured signal does not deviate from the operating state of the signal used to build the probability model, and 2) the fault state does not cause significant changes in the frequency energy distribution. With these assumptions, the newly measured signal can be matched with a probabilistic model from similar operating conditions. Then, the regions that have fault information in STFT are adaptively extracted using the matched probabilistic models and STFTs of the fault signals. The extracted time-frequency indices are then used as a time-frequency filter to calculate FASER as a fault feature. The last step is

to calculate an adaptive threshold of FASER to robustly classify the health state of the signal. To calculate the adaptive threshold for FASER, the covariance between the energies of time-frequency indices are computed, taking into account the window function employed to calculate the short-time Fourier transform. Specifically, we considered a scenario where the energy is located at a high value in the probabilistic view, which affected the boundary of the fault-affected signal energy ratio (FASER). This allowed us to determine an appropriate threshold for identifying the presence of fault symptom in the signal. In this research, the proposed method is experimentally validated by applying it in two case studies, including a planetary gearbox and an industrial robot gearbox; both cases are configured to imitate the operating conditions of real-world manufacturing processes.

The remainder of this paper is organized as follows. Section 4.1 provides a brief review of STFT and KLD. Section 4.2 illustrates the procedure of the proposed method, with detailed mathematical descriptions. The experimental setup and results are given in Section 4.3. Section 4.4 provides the conclusions of this research.

4.1 Background: Short Time Fourier Transform (STFT), Kullback-Leibler Divergence

This section provides the theoretical background of short-time Fourier transform (STFT) and Kullback-Leibler Divergence to understand the proposed method. In this section, we will first investigate the definition of the Short-Time Fourier Transform (STFT) and its advantages for diagnosing non-stationary signals, as demonstrated through simple simulation results. We will then explore the concept of Kullback-Leibler divergence (KLD), which can serve as a measure of signal similarity.

4.1.1 Short-time Fourier Transform (STFT)

The basic formulation of STFT can be represented as:

$$X_S(\tau,\omega) = \int s(t)w(t-\tau)e^{-j\omega t}dt \tag{4.1}$$

where τ is the time domain index, ω is the frequency domain index, s(t) is the target signal, and w is the window function. As can be seen in Eq. (1), the STFT is calculated by introducing an appropriate window function in the Fourier transform to describe how the spectral information changes over time [81]. Therefore, the selection of the window function is also important issue in the fault diagnosis. There are several researches on the window function in the view of the fault diagnosis [82, 83]. The window function moves along the time axis so that it can selectively choose the signal in a short duration. The selected signal can be considered to be quasi-stationary; thus, the selected signal can be properly analyzed by fast Fourier transform (FFT) [84]. Additionally, STFT has no cross term, unlike WVD as illustrated in Section 2.3.1; this is advantageous because a cross term can result in misunderstandings about the vibration signals.

Because the window function of STFT does not change with time and frequency, STFT gives a fixed resolution in the frequency domain. Therefore, STFT can efficiently calculate time-localized frequency information based on FFT, which needs much lower computation time compared with the other type of time frequency analysis such as Wavelet, Wigner-Ville distribution, and the similar Cohen class' time frequency analysis [52].

The result of STFT generally has a complex value; thus, it is hard to visualize in the time and frequency domains. Therefore, a spectrogram, which can be formulated as shown in the equation (4.2), can be used for visual representation of the time-varying signal.

$$C_s(\tau,\omega) = X_s(\tau,\omega)X_s^*(\tau,\omega) \tag{4.2}$$

where $C_s(\tau, \omega)$ is the spectrogram of the target signal *s* and the symbol * means complex conjugate.

In order to evaluate the performance of short-time Fourier transform (STFT) in extracting fault signals under varying conditions, the study performed modeling of signals that decay in amplitude to simulate fault symptoms as shown in the equation (4.3) and equation (4.4).

$$\mathrm{sn}(t) = \sin\left(1000\pi\sin\left(\frac{\pi t}{5}\right) + 2000\pi t\right) \tag{4.3}$$

$$\mathrm{sf}(t) = 5e^{-100\pi(t-t_{\mathrm{fc}})}\sin\left(2000\pi(t-t_{\mathrm{fc}})\right) \text{ for } t \geq t_{\mathrm{fc}} \tag{4.4}$$

where sn(*t*) indicates normal state simulation signal under the sinusoidal operating condition, sf(*t*) indicates fault state simulation signal, and t_{fc} is the time when fault signal occurs. For the simulation, 4 fault signal is imposed at t_{fc} = 2, 4, 6, 8 (s). The performance of STFT was then compared to that of fast Fourier transform (FFT) using the generated signals. The window function is the most generally used Hanning function with the length 1024, and sampling rate is 25600Hz. Figure 4-1 (a) and (b) presents time-varying, frequency-modulated sinusoidal signals with added impulse peak signals to model gear fault symptoms. FFT analysis of the signal in Figure 4-1 (c) and (d) showed no significant changes due to the presence of the peak, whereas STFT analysis in Figure 4-1 (e) and (f) revealed a spread vertical line in all frequency regions at the corresponding time where the peaks existed. Therefore, in cases where the energy of the peak is not sufficient to differentiate the gear state in the FFT domain, it is crucial to consider the TF domain and the effect of the peak signal. STFT analysis allows for the isolation of the peak signal over a short time, capturing the instantaneously changed signal in the corresponding indices. This approach allowed for an assessment of STFT's ability to accurately extract fault signals in real-world scenarios.

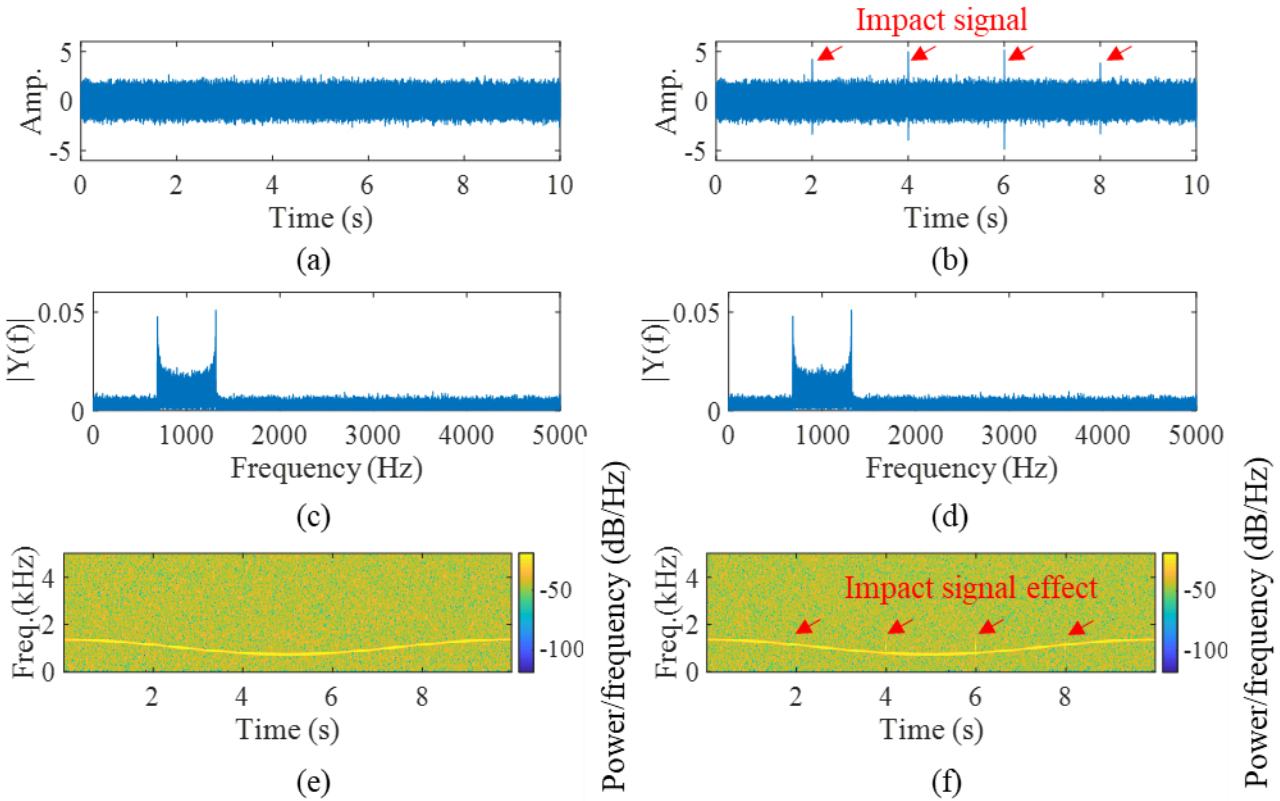

Figure 4-1 Comparison of normal and fault signal in time, frequency, time-frequency domain; (a) normal signal in time domain, (b) Fault signal in time domain, (c) normal signal in frequency domain, (d) fault signal in frequency domain, (e) normal signal in time-frequency domain, and (f) fault signal in time-frequency domain.

4.1.2 Kullback-Leibler Divergence (KLD)

KLD is a measure of how one probability distribution is different from a reference probability distribution [85]. If the KLD is 0, this indicates that the compared distributions are identical to each other. Additionally, if one KLD is larger than another KLD, the former probability distribution is more similar to the reference distribution than the latter probability distribution. Therefore, if the Fourier transform result of a particular signal is viewed from the perspective of energy distribution in the frequency domain, the Fourier transform result can be used as a measure to evaluate the similarity between signals when compared using the Kullback-Leibler Divergence (KLD).

The discrete version of KLD for univariate probability density functions P(x) and Q(x) is given as:

$$D_{KL}\left(P(x)\middle\|Q(x)\right) = -\sum_{x\in X} P(x)\log\left(\frac{Q(x)}{P(x)}\right) \tag{4.5}$$

where *P(x)* is an observed probability distribution, *Q(x)* is a reference probability distribution, and *X* is the domain of *x*. Additionally, it is calculated only as $Q(x)>0$ for all *x* where $P(x)>0$. In the 2-dimensional case, this formula can be transformed as:

$$D_{\mathrm{KL}}(P(x,y)\|Q(x,y)) = -\sum_{(x,y)\in(X,Y)} P(x,y)\log\left(\frac{Q(x,y)}{P(x,y)}\right) \tag{4.6}$$

where *P(x,y)* is an observed bi-variate probability distribution, and *Q(x,y)* is a reference bi-variate probability distribution, and *(X,Y)* is the domain of *(x,y)*. Similarly, it is calculated only as $Q(x,y)>0$ for all (x,y) where $P(x,y)>0$. To evaluate the similarity of signals using the KLD defined in Eq. (4.5) and Eq. (4.6), some procedures are required to apply the spectral analysis result. Detailed information on this process will be presented in section 4.2.1.

4.2 Fault-affected Signal Energy Ratio (FASER) for Robust Fault Diagnosis of Non-stationary signal

In this section, we present a detailed discussion of the proposed FASER method, including mathematical derivations and assumptions. The goal of the method is to extract fault-affected signals by comparing probabilistic models and actual measured energy based on STFT while minimizing errors from differences in operating conditions. Figure 4-2 depicts the overall procedure of the proposed FASER method.

In Step 1, a high-sampling signal is transformed into a spectrogram using pre-defined parameters such as the window function and FFT length to prevent energy differences due to changes in parameters. In Step 2, the spectrogram is segmented along the time axis, and each segmented spectrogram vector or matrix is matched with the probability distribution model of spectral energy to identify fault-affected indices. In Step 3, the FASER and its adaptive threshold are calculated based on the fault-affected indices to diagnose the signal state. The proposed method is described in detail with mathematical expressions in the following sections.

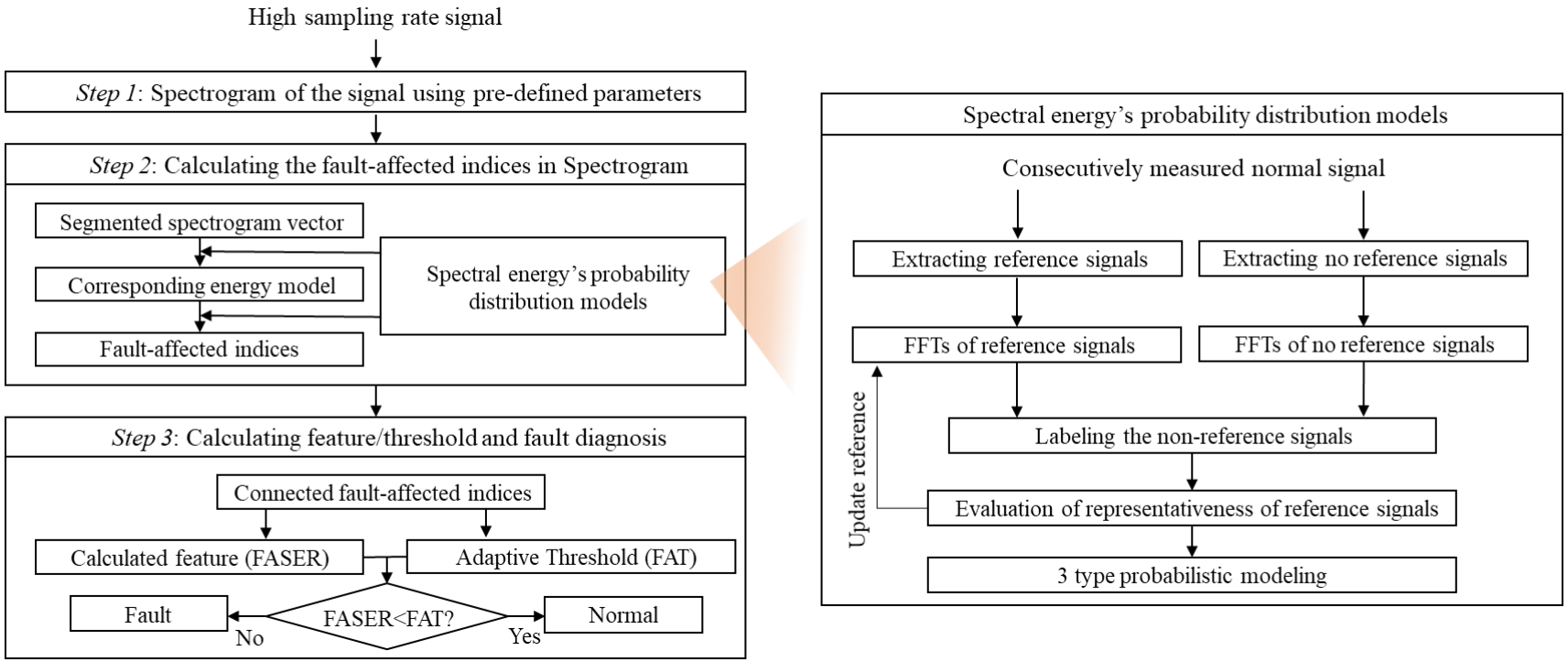

Figure 4-2 Proposed FASER's overall flowchart.

4.2.1 Spectral energy's probability distribution modeling

Vibration signals measured from the machinery with the same operating profile have a similar energy distribution in the time and frequency domains, provided the noise is not severe. A spectrogram using STFT can be interpreted as the energy distribution in the time and frequency domains. Since the spectrogram is always not negative, it can be used to compare the similarity of the signals without any loss of information. Because the measured signal is not a normalized signal, the spectrogram itself does not satisfy the probability distribution property, which requires that the marginalization of the energy in the time and frequency domains be 1. Therefore, the normalized spectrogram is calculated by dividing the spectrogram by the signal energy as:

$$Y_s(\tau,\omega) = \frac{C_s(\tau,\omega)}{\sum_{(\tau,\omega)\in(\mathrm{T},\Omega)} C_s(\tau,\omega)} \tag{4.7}$$

where $Y_s(\tau, \omega)$ is the normalized spectrogram of the target signal s, E[·] is the expectation operator, and (T, Ω) is the possible domain of (τ, ω) calculated by the signal length, and Nyquist frequency. Therefore, if one signal is more similar to the reference signal than another signal, the KLD of the spectrogram of the first signal should be less than the KLD of the other one. This study uses a 2-dimensional distribution in the time and frequency domains; KLD can be thus represented as:

$$D_{\mathrm{KL}}(s(t)\|r(t)) = -\sum_{(\tau,\omega)\in(\mathrm{T},\Omega)} Y_s(\tau,\omega)\log\left(\frac{Y_r(\tau,\omega)}{Y_s(\tau,\omega)}\right) \tag{4.8}$$

where $r(t)$ is the reference signal and $Y_r(\tau, \omega)$ is the normalized spectrogram of the reference signal. Thus, the similarity between any target signal and the reference signal can be quantified by the equation (4.8). Generally, the variability in the speed condition has a great influence on the energy distribution of the vibration signal. Therefore, the difference in the operation phases could have a bias effect on the building of probabilistic models for each time-frequency index of STFT of the normal signal, which will be shown in later.

Estimating uncertainty requires a diverse set of data. However, it is commonly easier to obtain signals in a normal state, which is why it is a self-evident approach to estimate uncertainty based on normal state signals and perform energy modeling to ensure robustness. This process is illustrated in Figure 4-2. To model the spectral energy distribution in a probabilistic manner, reference signals are first extracted to sufficiently explain changes in spectral energy from changes in the operating condition. Since the spectrogram is quasi-stationary within each time index and the operating speed greatly influences changes in energy distribution of frequency, a set of reference signals should be extracted for any of signal measured at a specific possible operating speed and acceleration. An initial set of reference signals, denoted as RFS=$r_i(t)$, i = 1, …, N, where N is the number of reference signals, can be extracted from consecutively measured signal. The normalized spectrogram of each reference signal is then calculated using Eq. (4.9), where $Y_{r,i}(\tau, \omega)$ represents the normalized spectrogram of the i-th reference signal.

From the consecutively measured signal, there can be extracted initial set of reference signals, referred as RFS, i = 1, …, N, and N is the number of the reference signals. Then, the normalized spectrogram of the reference signals are followed:

$$Y_{r,i}(\tau,\omega)=\frac{C_{r_i}(\tau,\omega)}{\sum C_{r_i}(\tau,\omega)} \tag{4.9}$$

where $Y_{r,i}(\tau, \omega)$ represents the normalized spectrogram of the i-th reference signal. For non-reference signals, labeling is performed using Eq. (4.8) and Eq. (4.9), as shown in Eq. (4.10).

$$\text{label for signal } nr_j(t)=\text{argmin}_i\left\{D_{\text{KL}}\left(nr_j(t)\middle\|r_i(t)\right)\right\} \tag{4.10}$$

where $nr_j(t)$ is j-th non-reference signal. Graphical illustrations for these processes are given in Figure 4-3.

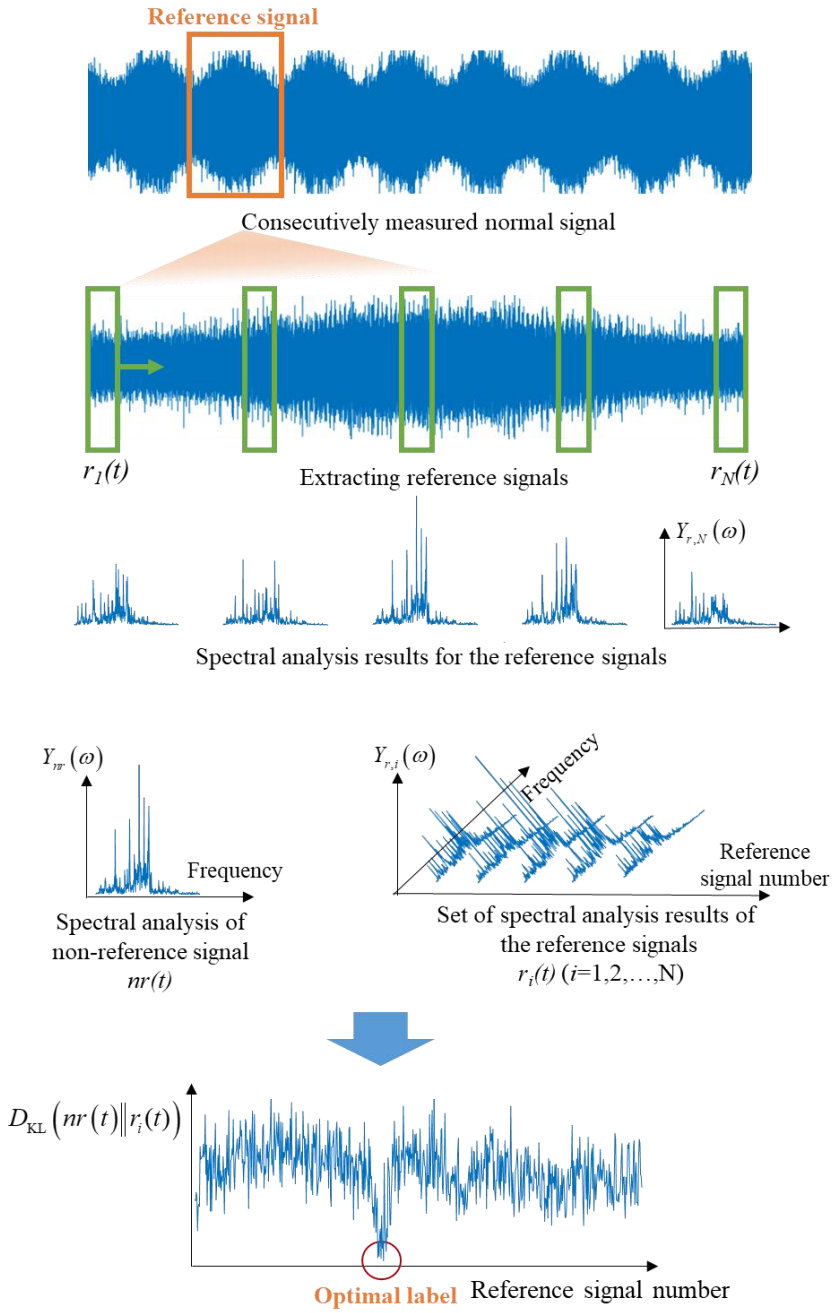

Figure 4-3 Graphical illustration for selecting reference signals and finding optimal label of non-reference signal.

From these labeling, the representativeness of the reference signals can be evaluated in two way:

(1) Number of signal labeled as $i > 5$

(2) $\min_i \left\{ D_{\mathrm{KL}} \left(nr_j(t) \middle\| r_i(t) \right) \right\} > threshold$

If condition (1) is not satisfied for a reference signal ri(t), it should be removed from the RFS because it would not provide sufficient representativeness for the specific operating condition and would not allow for accurate estimation of uncertainty due to a lack of data. In the case of condition (2), the threshold can be calculated using the median and standard deviation (std.) of the values, which expressed simply as (median + 3 × std.) of $\min_i\{D_{KL}(nr_j(t) \| r_i(t))\}$. If this condition is satisfied, it implies that the non-reference signal $nr_j(t)$ could have a different operating condition that is not matched with any of the reference signals. Therefore, in such cases, the non-reference signal $nr_j(t)$ should be added to the RFS. From these conditions, RFS can be properly selected with having 1) enough data to estimate the uncertainty, 2) a set of reference signals could be extracted for any of signal measured at a specific possible operating speed and acceleration. The graphical illustration for these steps is given in Figure 4-4.

.

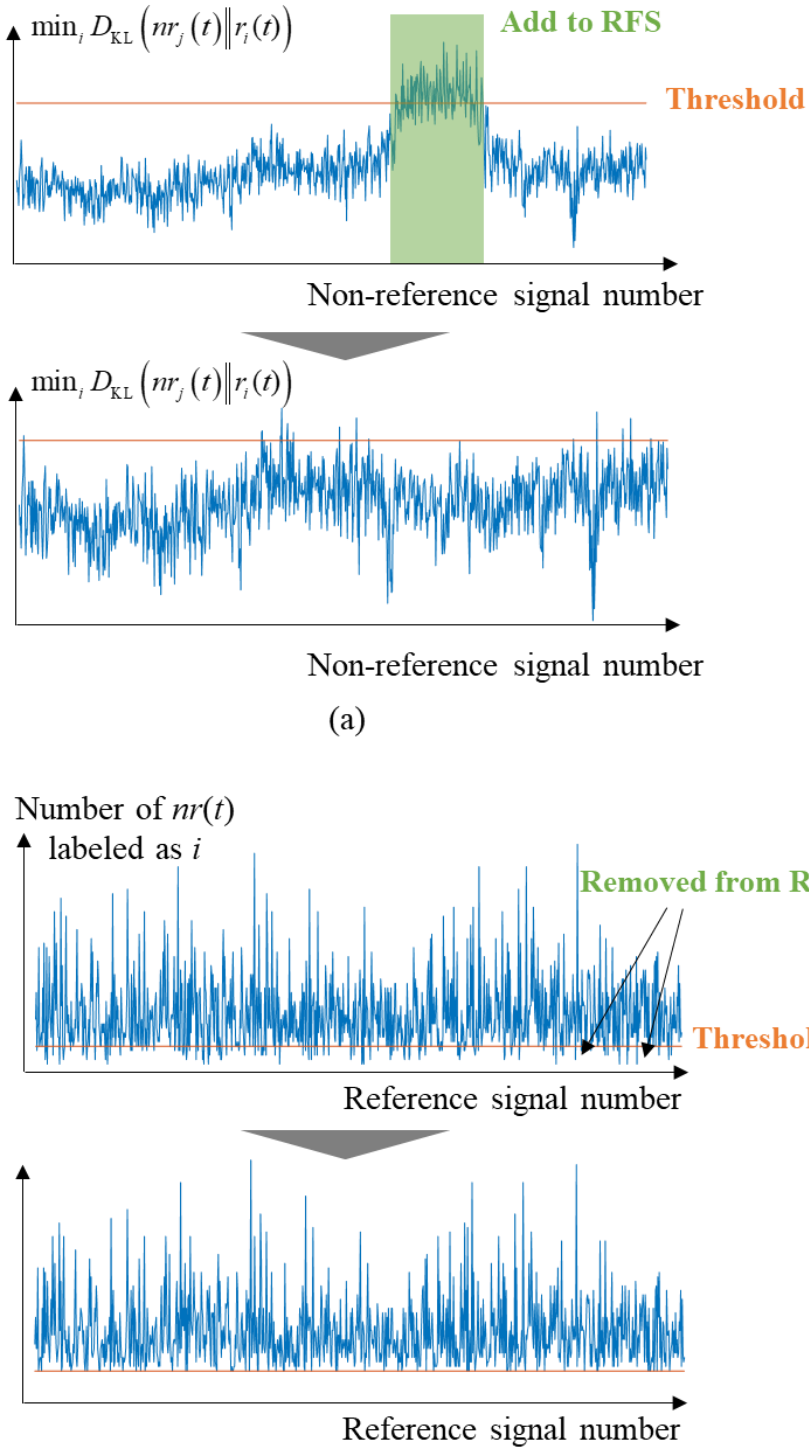

Figure 4-4 Graphical illustration for evaluation of representativeness of the reference signals; (a) condition (1), (b) condition (2).

The final step is probabilistic energy distribution modeling for each RFS. From the previous step, signals under similar operating conditions were clustered by reference signal number. To simplify the mathematical equation, we let the RFS be composed of N signal's spectrogram by the previous procedure, and the signals labeled as i (i = 1, 2, …, N) is denoted as $\eta_j^{(i)}(t)$ where j is the j^{th} sample of them (j = 1, 2, …, number of signals labeled as i). The expression is followed:

$$\arg\min_k \left\{ D_{\text{KL}} \left(\eta_j^{(i)}(t) \| r_k(t) \right) \right\} = i \tag{4.11}$$

As delineated in the introduction of Chapter 4, when dealing with signals, it is imperative to consider the presence of uncertainty, which necessitates the use of a suitable probability model. With the removal of variance associated with operational conditions through the previous step, it is plausible to assume that modeling can be accomplished with two signals: a Gaussian noise and a deterministic signal featuring only phase changes. Figure 4-5 (a) and (b) depict conceptual illustrations for spectrum analysis on the complex domain, which can manifest in two distinct ways contingent upon the presence or absence of a deterministic signal.

It is well known that when only Gaussian noise signals exist, the following distribution follows.

$$\frac{2\left|X(\tau,\omega)\right|^2}{\sigma^2} \sim \chi^2(2) \tag{4.12}$$

where σ is variance of noise and $\chi^2(2)$ is 2-degree of freedom (DOF) chi-square distribution described as followed:

$$f_{chi}(x;k) = \frac{x^{\frac{k}{2}-1} e^{-\frac{x}{2}}}{2^{\frac{k}{2}} \Gamma\left(\frac{k}{2}\right)} \tag{4.13}$$

where f_{chi} is probability density function (PDF) of the chi-square distribution with variable x, k is DOF parameter, and the function is valid for x>0, otherwise 0. In

order to estimate the parameter σ in Eq. (4.12), a probability function must be employed. The clustered $\eta_j^{(i)}(t)$ from the previous step can serve as a basis for estimating σ. Assuming that the energy in the spectrogram index (τ, ω) conforms to Eq. (4.12) with parameter $\sigma = \sigma^{(i)}(\tau, \omega)$, the mean can be computed as shown in Eq. (4.14).

$$\mathrm{E}_j\left[C_{\eta_j^{(i)}}(\tau,\omega)\right] = \sigma^{(i)}(\tau,\omega)^2 \tag{4.14}$$

where $\mathrm{E}_j[\cdot]$ denotes the expectation operator with respect to j. Thus, the method of moments can be readily implemented for parameter estimation. Subsequently, it is imperative to verify whether the energy probability distribution, which was estimated by validating the model, accurately represents the acquired energy. However, the conventional method of model validation is limited to check the normality, thus requiring the use of the Lilliefors test for validating the estimated energy probability distribution. The Lilliefors test, a variant of the well-established Kolmogorov-Smirnov test, performs better when the distribution's expectation and variance are unknown. Recalling that the parameter σ is estimated from the data, which is same situation when the true values of expectation and variance are unknown. Furthermore, it can also be used to test the null hypothesis that the data follows an exponentially distributed scenario. Fortunately, for our research, the chi-square distribution with degrees of freedom equal to two is an exponentially distributed situation, enabling the possibility of testing the estimated distribution.

If the Lilliefors test rejects the null hypothesis (indicating that the distribution cannot be modeled by the chi-square distribution), it suggests the presence of non-Gaussian noise or a deterministic signal. In this scenario, we will initially proceed with modeling for the cases of deterministic signals and Gaussian noise. It is derived in published literature [58] that when both Gaussian noise signal and deterministic signal exist, the following distribution follows. Additionally, There was an error in the non-centrality parameter of the derived expression, so it was corrected and

reflected:

$$\frac{2\left|X\left(\tau,\omega\right)\right|^2}{\sigma^2} \sim \chi^2\left(2,\frac{2}{\sigma^2}\gamma\right) \tag{4.15}$$

where σ is variance of noise and $\chi^2(2, \lambda)$ is a noncentral chi-square distribution with 2-DOF, and the noncentrality parameter λ. And, the noncentral chi-square distribution described as followed:

$$f_{nc-chi}\left(x;k,\lambda\right)=\frac{1}{2}e^{-\frac{\left(x+\lambda\right)}{2}}\left(\frac{x}{\lambda}\right)^{\frac{k}{4}-\frac{1}{2}}I_{\frac{k}{2}-1}\left(\sqrt{\lambda x}\right) \tag{4.16}$$

where $f_{nc\text{-}chi}$ is probability density function of the noncentral chi-square distribution with variable x, k is DOF parameter, λ is noncentrality parameter, and $I(\cdot)$ is a modified Bessel function of the first kind, and the function is valid for $x > 0$, otherwise 0 for $k \neq 1$. To estimate the parameters σ and γ in Eq. (4.15), a probability function needs to be used, similar to the previous probability distribution's estimation process. The clustered $\eta_j^{(i)}(t)$ obtained from the previous step can be used as a basis for estimating σ and γ. We assume that the energy in the spectrogram index (τ, ω) follows Eq. (4.15) with parameters $\sigma = \sigma^{(i)}(\tau, \omega)$ and $\gamma = \gamma^{(i)}(\tau, \omega)$. Additionally, in the view of signal processing, σ is the energy of noise, and γ is the energy of deterministic signal. Clearly, both the energy of the noise and deterministic signal can be different for different (i, τ, ω). Using this assumption, we can compute the mean and variance as shown in Eq. (4.17) and Eq. (4.18).

$$\mathrm{E}_j\left[C_{\eta_j^{(i)}}\left(\tau,\omega\right)\right]=\sigma^{(i)}\left(\tau,\omega\right)^2+\gamma^{(i)}\left(\tau,\omega\right) \tag{4.17}$$

$$\mathrm{Var}_j\left[C_{\eta_j^{(i)}}\left(\tau,\omega\right)\right]=\sigma^{(i)}\left(\tau,\omega\right)^4+2\sigma^{(i)}\left(\tau,\omega\right)^2\gamma^{(i)}\left(\tau,\omega\right) \tag{4.18}$$

where $\mathrm{Var}_j[\cdot]$ denotes the variance operator with respect to j, and the other description is same as the equation (4.14). Thus, the method of moments for 1st and 2nd can be readily implemented for parameters estimation. From the simple mathematical implementation, and the constraint that $\gamma = \gamma^{(i)}(\tau, \omega) > 0$, the parameters

can be estimated as:

$$\sigma^{(i)}(\tau,\omega)^2 = \mathrm{E}_j\left[C_{\eta_j^{(i)}}(\tau,\omega)\right] - \sqrt{\mathrm{E}_j\left[C_{\eta_j^{(i)}}(\tau,\omega)\right]^2 - \mathrm{Var}_j\left[C_{\eta_j^{(i)}}(\tau,\omega)\right]} \tag{4.19}$$

$$\gamma^{(i)}(\tau,\omega) = \sqrt{\mathrm{E}_j\left[C_{\eta_j^{(i)}}(\tau,\omega)\right]^2 - \mathrm{Var}_j\left[C_{\eta_j^{(i)}}(\tau,\omega)\right]} \tag{4.20}$$

Regrettably, unlike the scenario where only a noise signal is present, the distribution is neither exponentially nor normally distributed. Therefore, there is no appropriate test method available for validating the model. Instead, we can evaluate the suitability of the model based on the fact that σ and γ, which serve as constraints for the parameters, are real numbers. Therefore, the constraint for applying the probabilistic modeling suggested in the equations (4.15), (4.19), (4.20) is simply expressed as:

$$\mathrm{E}_j\left[C_{\eta_j^{(i)}}(\tau,\omega)\right]^2 > \mathrm{Var}_j\left[C_{\eta_j^{(i)}}(\tau,\omega)\right] \tag{4.21}$$

To verify the effectiveness of the proposed estimation method and equation, a simulation was conducted on a basic sinusoidal signal $s(t) = 0.5\sin(2000\pi t + \varphi) + \varepsilon$, $\varphi \sim U(0, 2\pi)$, $\varepsilon \sim N(0,1)$ as illustrated in Figure 4-7 (c) to (f). The window function is Hanning function with the length 1024, and the spectrum results are analyzed at frequency = 1000 (Hz).

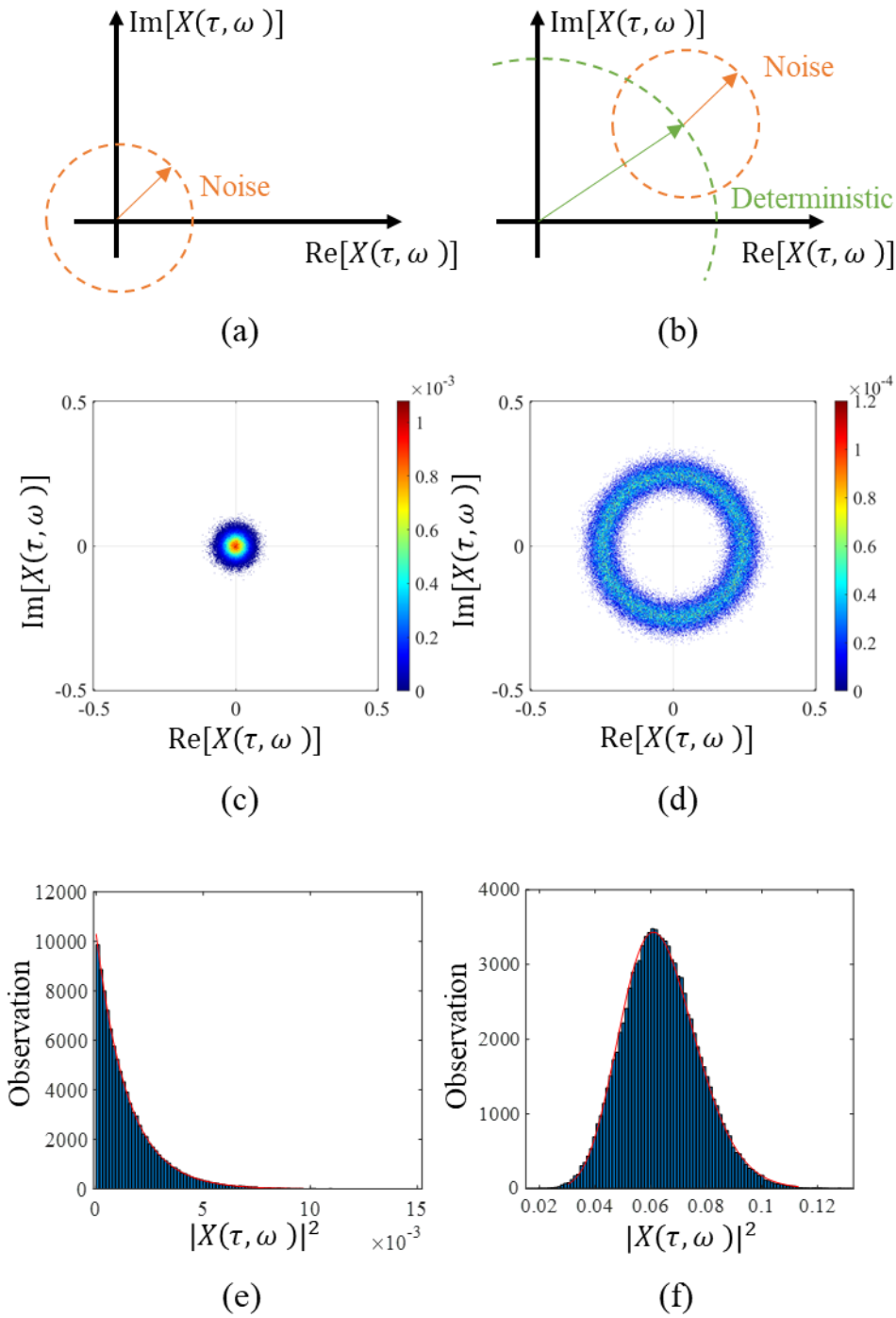

Figure 4-5 Conceptual illustration of (a) Noise signal, (b) Noise + Deterministic signal, simulation result of (c) Noise signal, (d) Noise + Deterministic signal, histogram of simulation (e) Noise signal, (f) Noise + Deterministic signal.

The final stage of probabilistic modeling involves modeling the energy distribution that cannot be captured by any combination of the probabilistic distributions suggested earlier. There are various reasons why this energy distribution cannot be modeled by the previous suggestions. These include:

1) When multicomponent signals overlap, irrespective of the driving conditions

2) When the randomness of the noise itself varies, irrespective of the driving conditions

3) When signals with unknown sources are transmitted or generated in a non-periodic manner.

Thus, it would be inefficient and beyond the scope to create individual probability distributions by making assumptions in such cases. To address this issue, we can use a well-known nonparametric probabilistic modeling method called Kernel Density Estimation (KDE). The KDE is defined as:

$$f_{\mathrm{KDE}}\left(x\right)=\frac{1}{n}\sum_{i=1}^{n}\phi\left(x,x_i;h\right) \tag{4.22}$$

where f_{KDE} is probability density function using KDE with variable x, ϕ is kernel, h is hyper-parameter of ϕ, and x_i is the i-th observation of x, and n is the number of observation. In our research, the kernel is Gaussian basis function, and h is generally used optimal value given as [86]:

$$h=\left(\frac{4\sigma^5}{3n}\right)^{0.2} \tag{4.23}$$

where σ is estimated standard deviation from x_i. Therefore, the equations (4.22) and (4.23) can be modified for our expression as:

$$f^{(i)}\left(X\left(\tau,\omega\right)\right)=\frac{1}{n^{(i)}h^{(i)}\left(\tau,\omega\right)}\sum_{j=1}^{n^{(i)}}G\left(\frac{X\left(\tau,\omega\right)-C_{\eta_j^{(i)}}\left(\tau,\omega\right)}{h^{(i)}\left(\tau,\omega\right)}\right) \tag{4.24}$$

Here, $f^{(i)}(X(\tau, \omega))$ represents the KDE-based probabilistic energy distribution model for the spectrogram index (τ, ω) corresponding to the signal labeled as i. The value $n^{(i)}$ represents the number of signals labeled as i. The function $h^{(i)}(X(\tau, \omega))$ denotes the optimal bandwidth calculated using Eq. (4.23), and $G(\cdot)$ represents the Gaussian kernel defined by the parameter $h^{(i)}(X(\tau, \omega))$. In fact, the KDE method can be used to model the probability distribution for any kind of situation, including those mentioned previously. However, it can be vulnerable to outlier data, requires a sufficient number of data points, has a high computational cost, and lacks physical interpretation. Therefore, it was used as a last resort in this study.

4.2.2 Fault-affected signal extraction

Based on the probabilistic energy modeling for all $\eta_j^{(i)}(t)$ described above, we now discuss how the fault-affected signal can be extracted from the newly measured signal by probabilistic manner. From this section, the individual samples of each i labeled data for constructing the probabilistic modeling do not need. Therefore, the mean value of energy $\eta_j^{(i)}(t)$ at (τ, ω), denoted as $C^{(i)}(\tau, \omega)$, is used for matching the new signal to the constructed energy probabilistic modeling, which has similar operating condition. The expression for $C^{(i)}(\tau, \omega)$ are followed:

$$C^{(i)}(\tau,\omega) = \mathrm{E}_j\left[{C_{\eta_j(t)}}^{(i)}(\tau,\omega) \right] \tag{4.25}$$

Additionally, the PDF for $C^{(i)}(\tau, \omega)$ can be denoted as $f^{(i,\tau,\omega)}(C^{(i)}(\tau, \omega))$. Then, the probabilistic boundary is calculated by cumulative density function (CDF) expressed as:

$$F^{(i,\tau,\omega)}\left(b^{(i)}\left(\tau,\omega\right)\right) = \int_0^{b^{(i)}(\tau,\omega)} f^{(i,\tau,\omega)}({x^{(i)}}_{(\tau,\omega)})d{x^{(i)}}_{(\tau,\omega)} = k_p \tag{4.26}$$

where k_p is a margin value for the probabilistic boundary and $b^{(i)}(\tau, \omega)$ is the probabilistic boundary of the time-frequency indices (τ, ω) of i labeled signal, satisfying $0 < k_p < 1$. Even if a new signal is a consecutively measured fault signal, it can still be truncated by phase-matching to improve its suitability for analysis. Then, whether or not each time-frequency index is statistically regarded as the fault symptom is determined by comparing the TFR of the truncated signal with the probabilistic boundary $b(\tau, \omega)$. If the energy of the fault signal in a certain time-frequency index is larger than the $b(\tau, \omega)$ when $k_p > 0.5$, the corresponding index can be regarded as being fault affected. On the other hand, when k_p <=0.5, the corresponding index does not statistically have enough separability for fault detection. Therefore, $k_p > 0.5$ in experimental validation of our research in Section 4.3. This process allows us to explain why probabilistic modeling should be conducted while considering the operating condition mentioned in section 4.2.1. As

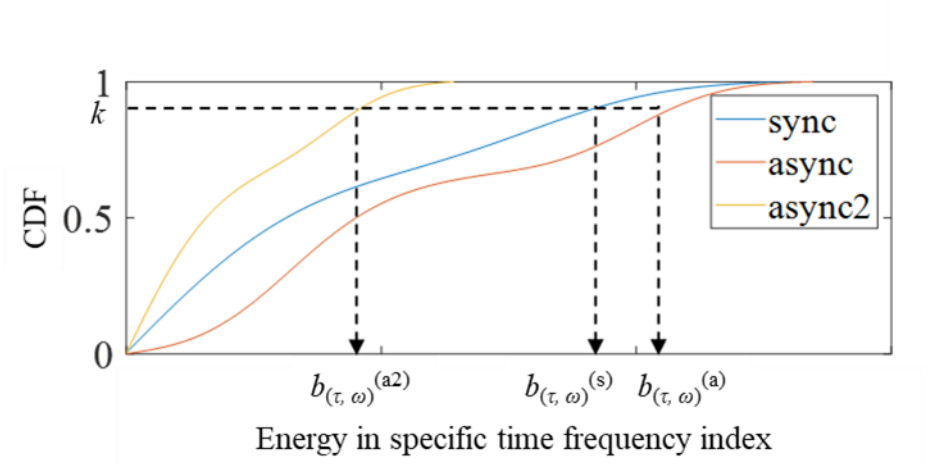

Figure 4-6 The effect of operation phase mismatching to the probabilistic modeling and probabilistic boundary.

illustrated in Figure 4-6, if the probabilistic model is constructed from a set of different operation signals, the resulting energy distribution may vary. Specifically, the 'sync' case represents a scenario where the operating condition is synchronized, and the energy distribution is accurately modeled. In contrast, the 'async' case arises when the energy is overestimated due to unsynchronized conditions, and the 'async2' case arises when the energy is underestimated for the same reason. This suggests that a fault signal could be misclassified as a normal state, as the probabilistic boundary shifts from $b_{(\tau,\omega)}^{(s)}$ to $b_{(\tau,\omega)}^{(a2)}$. Conversely, even if another signal is from the same state, it is more likely to be misclassified as a fault state because the probabilistic boundary is decreased from $b_{(\tau,\omega)}^{(s)}$ to $b_{(\tau,\omega)}^{(a)}$.

So far, it have been organized x to find the operating condition when new data comes in, and set the energy boundary on the time and frequency index for each. Then, the newly measured signal denoted as $a(t)$ can be applied to the algorithm with following steps.

The first step of the proposed method involves transforming the input signal $a(t)$ into a spectrogram using the equations (4.1) and (4.2). To ensure consistency in energy measurements, the same parameter values are used for calculating the

spectrogram and for probabilistic modeling. These parameters include the window function type (e.g. Gabor, Hanning), window function length, window function hyperparameter, overlap ratio of the window function, and FFT length for frequency resolution. By applying these parameters, $C_a(\tau, \omega)$ is calculated, and the spectrogram is segmented into several spectrograms having the same number of time indices, which are used for probabilistic modeling. Additionally, STFT involves performing FFT by dividing the vibration signal by the size corresponding to each time index's resolution. Since the spectrogram obtained energy by multiplying the conjugate of the coefficients calculated in STFT, independent calculation of the trailing process does not change the results.

During the segmentation process, the number of time indices of $C_a(\tau, \omega)$ is not an integer multiple of $C^{(i)}(\tau, \omega)$, it makes the scenario that some of segmented $C_a(\tau, \omega)$ can be ignored. When building an energy probability model, a large amount of data is required to express the range of possible operating conditions for the reference signals if several time indices are included so the length of the reference signal is long. This may result in inaccurate results due to the lack of representativeness of reference signals. To avoid this, the number of time indices for probabilistic modeling should not be long. This ensures that the remaining part to be discarded is only a small part of the overall data and does not significantly affect the result.

The segmented spectrograms, denoted as $C_{aj}(\tau, \omega)$, which correspond to the spectrogram of the signal $a_j(t)$, are now compared with $C^{(i)}(\tau, \omega)$, which is the spectrogram of the i-th reference signal $\eta^{(i)}(t)$, using the Kullback-Leibler Divergence (KLD) as described in the equation (4.8). The expression for this is as follows:

$$\operatorname{argmin}_i D_{\mathrm{KL}} \left\{ aj(t) \middle\| \eta^{(i)}(t) \right\} = h(j) \tag{4.27}$$

where $aj(t)$ is j^{th} segmented signal from the newly measured signal $a(t)$, and $h(j)$ is

the labeling for the *aj*(t) by comparing the set of reference signals based on KLD. From this step, the operating condition matched probabilistic energy distribution modeling, denoted as $f^{(h(j),\,\tau,\,\omega)}(C^{(h(j))}(\tau,\,\omega))$, for each segmented spectrogram, denoted as $S_{aj}(\tau, \omega)$, is prepared.

On the assumption that the fault symptom increases the energy of the corresponding time-frequency index, the fault affected time-frequency index for signal *aj*(t) labeled as *h*(*j*) can be expressed as:

$$W^{(j)}(\tau,\omega)=\begin{cases}1 & \text{if } C_{aj}(\tau,\omega) > b^{h(j)}(\tau,\omega) \\ 0 & \text{otherwise}\end{cases} \tag{4.28}$$

where $W^{(j)}(\tau,\,\omega)$ is matrix for selecting the time-frequency index (τ, ω) having the fault information, $C_{aj}(\tau, \omega)$ is the energy of the signal *aj*(t) in the corresponding index (τ, ω), and $b^{h(j)}(\tau, \omega)$ is the probabilistic boundary calculated by the equation (4.26). Based on the results of the statistically separable calculated indices, $W(\tau\,, \omega)$ can be used as a time-frequency filter to calculate FASER as a fault feature. Graphical illustration for section 4.2.2 is given in Figure 4-7 for the summary.

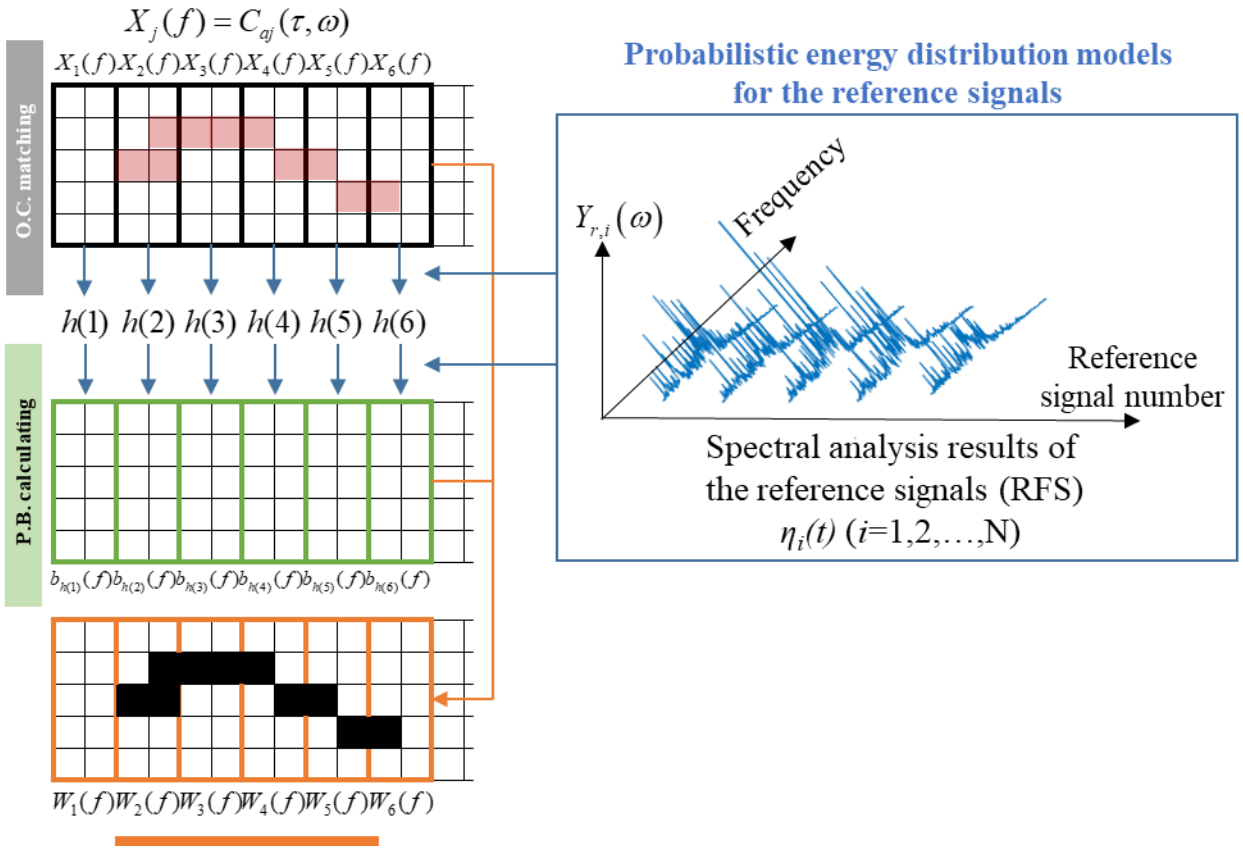

Figure 4-7 Graphical illustration for Section 4.2.2.

4.2.3 FASER calculation and adaptive thresholding

In section 4.2.2, the signals are segmented into several spectrograms, denoted as $S_{aj}(\tau, \omega)$, and then matched with the probabilistic energy distribution model, denoted as $f^{(h(j),\,\tau,\,\omega)}(C^{(h(j))}(\tau, \omega))$, that is suitable for the operating environment. This matching is performed using the KLD method described in the equation (4.8), which allows for the identification of indexes that can be considered to be affected by fault, based on the probabilistic boundary, denoted as $b^{h(j)}(\tau, \omega)$, obtained from the matched probabilistic energy distribution model. This process enables the detection of fault signals that deviate from the normal state, and facilitates the diagnosis of faults in the system. In this section, the fault-affected index obtained in Section 4.2.2 is used to calculate the fault-affected signal energy ratio (FASER). The FASER is a measure of the energy ratio of the fault-affected signal to the total signal energy, and it can be used to detect the presence of a fault. The threshold for FASER is calculated based on the energy probability model and the energy correlation between the STFT indices. The threshold can vary depending on the signal being analyzed.

First, the segmented spectrogram and fault-affected indices are concatenated as follows in the opposite way of segmentation.

$$W_a(ct,\omega) = \left[W^{(1)}(\tau,\omega),\, W^{(2)}(\tau,\omega),\, ...,\, W^{(n)}(\tau,\omega) \right] \tag{4.29}$$

$$C_a(ct,\omega) = \left[C_{a1}(\tau,\omega), C_{a2}(\tau,\omega), ..., C_{an}(\tau,\omega) \right] \tag{4.30}$$

$$C_\mu(ct,\omega) = \left[C^{(h(1))}(\tau,\omega), C^{(h(2))}(\tau,\omega), ..., C^{(h(n))}(\tau,\omega) \right] \tag{4.31}$$

where $W_a(ct, \omega)$ is concatenated fault-affected indices, $C_a(ct, \omega)$ is concatenated spectrogram, $C_\mu(ct, \omega)$ is the mean of concatenated reference spectrogram, ct is concatenated time index, and n is number of segmented signal a(t). From the equations (4.29) ~ (4.31), FASER is defined as:

$$\mathrm{FASER}\left(a(t)\right) = \frac{\sum_{(ct,\omega)\in(\mathrm{T},\Omega)} C_a(\tau,\omega) W_a(\tau,\omega)}{\sum_{(ct,\omega)\in(\mathrm{T},\Omega)} C_\mu(\tau,\omega) W_a(\tau,\omega)} = \frac{\mathbf{1}^{\mathrm{T}}\left(C_s(\tau,\omega)\circ W_a(\tau,\omega)\right)\mathbf{1}}{\mathbf{1}^{\mathrm{T}}\left(C_\mu(\tau,\omega)\circ W_a(\tau,\omega)\right)\mathbf{1}} \tag{4.32}$$

where **1** is a column vector of one, Ω is domain of frequency ω, and $\circ$ is Hadamard product, which is the elementwise multiplication between two matrix. It represents the deviation of FASER from the normal signal's energy tendency. The normalization is done by dividing the energy of the filtered signal by the mean energy of the filtered normal signal, considering the nonhomogeneous uncertainty of the energy in the time-frequency domain.

To classify the health state of a measured signal, the threshold for FASER must be determined. If a new signal is measured in a fault state, $W(\tau, \omega) = 1$ in Eq. (4.28). If a new signal is measured in the normal state, it is desired that $W(\tau, \omega) = 0$ for all the time-frequency indices (τ, ω); however, this is unlikely due to the definition of $W(\tau, \omega)$. Statistically, from the equation (4.26), $k \times$ (the total number of indices) indices is expected to be $W(\tau, \omega) = 1$, even when the signal is measured in the normal state. Furthermore, the correlation between time-frequency indices exists [59]. Therefore, the threshold for FASER is calculated based on the probabilistic properties of FASER and the window function of the spectrogram. The threshold is determined by analyzing the energy probability model and the energy correlation between the STFT indices. Specifically, the threshold is calculated by considering the mean and standard deviation of the FASER values of the normal signals with considering the selected probabilistic energy model. The threshold is set such that the probability of false positives is minimized while maintaining a high probability of detection. In addition, the threshold can be adjusted depending on the specific signal and the desired level of detection accuracy. The conditional probability distribution when a specific time frequency index's energy exceeds the time-frequency energy boundary can be expressed as:

$$f_b^{(\tau,\omega)}\left(x_{(\tau,\omega)}\right) = f^{(\tau,\omega)}\left(x_{(\tau,\omega)} \middle| \left(x_{(\tau,\omega)} > b_{(\tau,\omega)}\right)\right)$$
$$= \frac{f^{(\tau,\omega)}\left(x_{(\tau,\omega)}\right)}{\int_{b_{(\tau,\omega)}}^{\infty} f^{(\tau,\omega)}\left(x_{(\tau,\omega)}\right) dx_{(\tau,\omega)}} = \frac{f^{(\tau,\omega)}\left(x_{(\tau,\omega)}\right)}{1-k} \tag{4.33}$$

where $f_b(\tau, \omega)(x_{(\tau, \omega)})$ is the conditional probability when the energy in (τ, ω) exceeds the probabilistic boundary of the (τ, ω) domain index, denoted as $b(\tau , \omega)$. Therefore, if a new signal is in the normal state, the energy of the time-frequency index where $W(\tau , \omega) = 1$ follows $f_b(\tau, \omega)(x_{(\tau, \omega)})$. If the energy in each time-frequency index is independent from each other index, when the signal is in the normal state, the expectation and the variance of the filtered spectrogram follow, respectively, as:

$$\mathrm{E}\left[\sum_{(\tau,\omega)\in(\mathrm{T},\Omega)} C_s(\tau,\omega) W_s(\tau,\omega) \middle| s = s_{\text{normal}}\right] =$$
$$\int_{W(\tau,\omega)=1}\left[\int_{b_{(\tau,\omega)}}^{\infty} x_{(\tau,\omega)} f_b^{(\tau,\omega)}\left(x_{(\tau,\omega)}\right) dx_{(\tau,\omega)}\right] d\tau d\omega \tag{4.34}$$

$$\mathrm{Var}\left[\sum_{(\tau,\omega)\in(\mathrm{T},\Omega)} C_s(\tau,\omega) W(\tau,\omega) \middle| s = s_{\text{normal}}\right]$$
$$= \int_{W(\tau,\omega)=1}\left[\int_{b_{(\tau,\omega)}}^{\infty}\left(x_{(\tau,\omega)} - \int_{b_{(\tau,\omega)}}^{\infty} x_{(\tau,\omega)} f_b^{(\tau,\omega)}\left(x_{(\tau,\omega)}\right) dx_{(\tau,\omega)}\right)^2 f_b^{(\tau,\omega)}\left(x_{(\tau,\omega)}\right) dx_{(\tau,\omega)}\right] d\tau d\omega \tag{4.35}$$

where $\mathrm{Var}[\cdot]$ is the variance operator.

Correlation between time-frequency indices may exist due to the window function and overlap ratio used in spectrogram calculation [59]. Therefore, the variance should be calculated considering the covariance of the time-frequency indices where $W(\tau, \omega) = 1$. Also, it is possible to estimate the correlation with the observed energy to construct the energy distribution of each of the time-frequency indices; however, the condition $W(\tau, \omega) = 1$ can make it hard to gather enough samples to estimate the correlation. Therefore, the effects of the window function are considered. The correlation between the time-frequency indices in the case of the time-adjacent

indices ($\tau + \Delta\tau, \omega$) satisfying $W(\tau + \Delta\tau, \omega) = 1$ together is estimated from the window function, considering the overlapped region.

$$\mathrm{Corr}\left[C_a(\tau,\omega), C_a(\tau+\triangle\tau,\omega)\right] = \frac{\sum_{n=0}^{N-l-1} w^2[n]w^2[n+l]}{\sum_{n=0}^{N-1} w^4[n]} \tag{4.36}$$

where Corr[·] is the correlation operator, $w[\cdot]$ is the window function used in the discrete notation, and l is the sample hop size corresponding to $\Delta\tau$. From Eq. (15), it is possible to calculate the covariance when $W(\tau, \omega) = 1$ and $W(\tau + \Delta\tau, \omega) = 1$. Additionally, $\Delta\tau \leq$(overlap length).

Similarly, it is possible that a correlation exists between time-frequency indices because of the spectral leakage when the length of the FFT is larger than the window size. It is impossible to know exactly at what frequency the signal comes out; however, it is possible to know how much the energy of each of the time-frequency indices could be affected by considering the frequency response function of the window function. Therefore, the correlation effect of the spectral leakage is used for the estimation, considering the magnitude of the frequency response function of the window function. When the uncertainty is only from Gaussian noise, the correlation can be calculated using the published method [59]; however, as explained in Chapter 1, there is a high possibility that the noise is different for each frequency in a mechanical system. Therefore, the correlation is estimated in a form similar to the time-adjacent case. Unlike the time-adjacent case, spectral leakage occurs in all frequency domains; however, it has a negligible value outside the main lobe, so the calculation is performed only within the main lobe.

$$\mathrm{Corr}\left(C_a(\tau,\omega), C_a(\tau,\omega+\triangle\omega)\right) = \frac{\sum_{n=0}^{N-m-1} F_w^{\,2}\left(-\omega_{eff}+n\triangle\omega\right) F_w^{\,2}\left(-f_{eff}+n\triangle\omega+m\triangle\omega\right)}{\sum_{n=0}^{N-1} F_w^{\,4}\left(-\omega_{eff}+n\triangle\omega\right)} \tag{4.37}$$

where ω_{eff} is half the width of the main lobe of the window's frequency response function, F_w is the frequency response function of the window function, $\Delta\omega$ is the spectral resolution of the spectrogram, which is determined by the window function and the length of FFT, and $m\Delta\omega$ is the frequency gap corresponding to $\Delta\omega$. Additionally, $\Delta\omega \leq$ (main lobe width)/2. Moreover, it is possible to utilize the observation that a high amount of energy can be obtained even in the normal state. Specifically, when a significant amount of energy is acquired at two adjacent frequency indices, it implies that the ideal frequency energy is high even without the presence of spectral leakage. Based on this observation, it can be assumed that only the energies of the corresponding frequencies affect each other through spectral leakage, leading to the derivation of the following equation. The detailed derivation process can be found in Appendix. The conceptual illustration for this condition is shown in Figure 4-8.

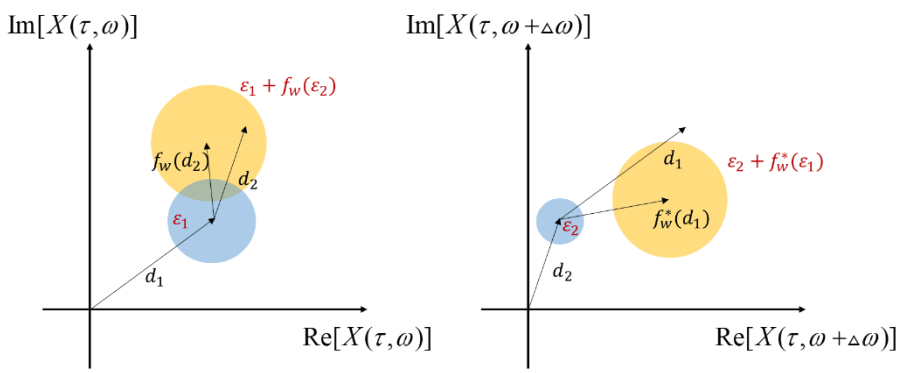

Figure 4-8 Graphical illustration for deriving correlation effect from spectral leakage.

$$E_\omega - \sqrt{E_\omega{}^2 - V_\omega} = \psi_\omega \tag{4.38}$$

$$\sigma_\omega{}^2 = \frac{\psi_\omega - k^2\psi_{\omega+\triangle\omega}}{1-k^4}, \sigma_{\omega+\triangle\omega}{}^2 = \frac{\psi_{\omega+\triangle\omega} - k^2\psi_\omega}{1-k^4} \tag{4.39}$$

$$r_\omega = \mathrm{E}\left[X(j\omega)\right] \tag{4.40}$$

$$\begin{aligned}&\mathrm{Cov}(\left|Y(j\omega)\right|^2, \left|Y(j(\omega+\triangle\omega))\right|^2) = \\ &k_w{}^2\left(\sigma_\omega{}^2 + \sigma_{\omega+\triangle\omega}{}^2\right)^2 + 2\,\mathrm{Re}\left[r_\omega{}^* r_{\omega+\triangle\omega} k_w(\sigma_\omega{}^2 + \sigma_{\omega+\triangle\omega}{}^2)\right]\end{aligned} \tag{4.41}$$

where E_ω is mean energy of signal's spectrogram, V_ω is variance of signal's spectrogram, ψ_ω refers the energy variance from the noise at frequency ω, r_ω is the deterministic signal's STFT coefficients, * is conjugate symbol, and k_w is spectral leakage effect from window function w at difference of frequency is $\Delta\omega$. Equations (4.38) to (4.41) show the covariance between two adjacent frequency indices affected by spectral leakage. However, certain constraints exist for these equations. Firstly, according to Eq. (4.38), ψ_ω must be a real value, which means that it cannot be obtained from the third probability model proposed in section 4.2.1 (as this model cannot be constructed as Gaussian noise + deterministic signal). Specifically, ψ_ω represents the variance of energy excluding the deterministic signal. Thus, if the variance of the deterministic signal is considered as a noise effect, ψ_ω can be regarded as the variance value of the energy distribution estimated by KDE. Secondly, Eq. (4.39) introduces another constraint, which states that k^2 should be less than the minimum value of ($\psi_\omega/\psi_{\omega+\Delta\omega}$, $\psi_{\omega+\Delta\omega}/\psi_\omega$) in order to satisfy σ_ω as a real number. This is because the assumption used to derive the equation is that the energy of two frequencies ($X(\omega)$ and $X(\omega+\Delta\omega)$) other than the other frequencies is negligible. If this assumption is violated, then correlation cannot be calculated from Eq. (4.41), and instead must be calculated using Eq. (4.37). Using both the covariance effect derived above and the variance by conditional distribution, the threshold can be set as follows.

$$\mathrm{Var}\left[\sum_{(\tau,\omega)\in(\mathrm{T},\Omega)} C_s(\tau,\omega)W(\tau,\omega)\middle|s=s_{\mathrm{normal}}\right]=\int_{W(\tau,\omega)=1}\sigma^2{}_{(\tau,\omega)}d\tau d\omega$$
$$+2\int_{\Omega_A}\sigma_{(\tau,\omega)}\sigma_{(\tau+\triangle\tau,\omega)}\mathrm{Corr}\left(C_s(\tau,\omega),C_s(\tau+\triangle\tau,\omega)\right)d\tau d\omega$$
$$+2\int_{\Omega_B}\sigma_{(\tau,\omega)}\sigma_{(\tau,\omega+\triangle\omega)}\mathrm{Corr}\left(C_s(\tau,\omega),C_s(\tau,\omega+\triangle\omega)\right)d\tau d\omega \tag{4.42}$$

$$\sigma^2{}_{(\tau,\omega)}=\int_{b_{(\tau,\omega)}}^{\infty}\left(x_{(\tau,\omega)}-\int_{b_{(\tau,\omega)}}^{\infty}x_{(\tau,\omega)}f_b^{(\tau,\omega)}\left(x_{(\tau,\omega)}\right)dx_{(\tau,\omega)}\right)^2 f_b^{(\tau,\omega)}\left(x_{(\tau,\omega)}\right)dx_{(\tau,\omega)} \tag{4.43}$$

where Ω_A is the set of time-frequency indices where $W(\tau, \omega) = 1$ and $W(\tau + \Delta\tau, \omega) = 1$ and Ω_B is the set of time-frequency indices where $W(\tau, \omega) = 1$ and $W(\tau, \omega + \Delta\omega) = 1$. $\sigma^2(\tau, \omega)$ is the square of the standard deviation using the conditional probability given in the equation (4.33).

Finally, FAT, which is FASER's adaptive threshold, can be determined adaptively by normalizing the expectation of the filtered spectrogram as:

$$\mathrm{FAT}=\frac{\mathrm{E}\left[\sum_{(\tau,\omega)\in(\mathrm{T},\Omega)} C_s(\tau,\omega)W(\tau,\omega)\middle|s=s_{\mathrm{normal}}\right]}{\mathbf{1}^{\mathrm{T}}\left(C_\mu(\tau,\omega)\circ W_s(\tau,\omega)\right)\mathbf{1}}$$
$$+\frac{2\mathrm{Std}\left[\sum_{(\tau,\omega)\in(\mathrm{T},\Omega)} C_s(\tau,\omega)W(\tau,\omega)\middle|s=s_{\mathrm{normal}}\right]}{\mathbf{1}^{\mathrm{T}}\left(C_\mu(\tau,\omega)\circ W_s(\tau,\omega)\right)\mathbf{1}} \tag{4.44}$$

As assumed in Section 4.2.2, the time-frequency indices are $W(\tau , \omega) = 1$ when a fault symptom increases the energy of the corresponding indices. If the FASER result of the measured signal is larger than the threshold FAT, it can be inferred that the measured signal is in a fault state.

4.3 Experimental Validation of the Propose Method

This section describes how we validate the propose method, FASER, by measuring the vibration signal under the non-stationary operating condition. The first case is for a wind-turbine simulator, and the second case is for a 6-DOF industrial robot used in Chapter 3. We also compare the proposed method with conventional non-stationary signal diagnosis method. In this case study, a wind turbine simulator with a two-stage planetary gearbox is employed. The drive motor speed controls the overall operating condition. A fault is artificially introduced in the planet gear of the second stage planetary gearbox. To validate the proposed method, three levels of tooth with line spall defects were demonstrated under the same operating conditions as the normal signal. This is done under the assumption that the constructed probabilistic modeling should contain the operating condition of the newly measured signal. The testbed setup and location of the accelerometer sensors to measure the vibration signal are shown in Figure 4-9. Additionally, Figure 4-10 shows the target planetary gearbox and the normal/ three-level fault specimens for the planet gear. The study employed three different levels of spall diameter, namely 0.75mm (F1), 1.00mm (F2), and 1.25mm (F3).

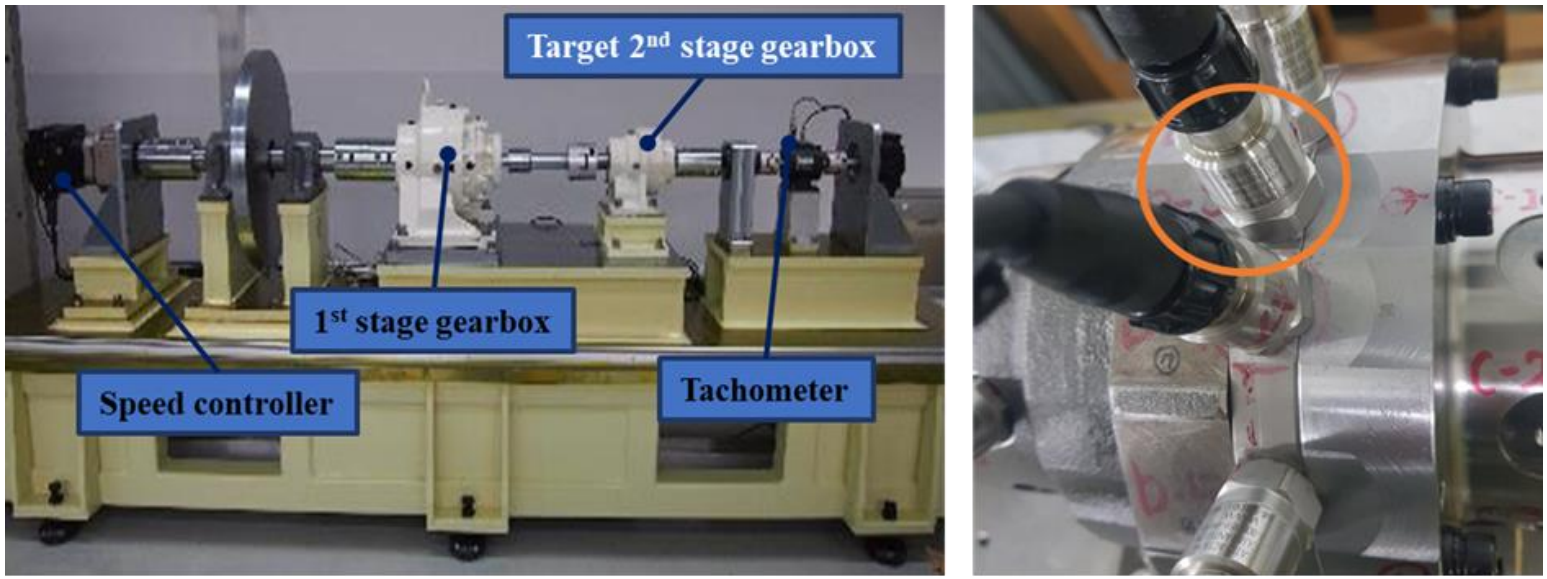

Figure 4-9 (a) A wind turbine testbed, (b) The location of the accelerometer sensor attached on the casing of the gearbox.

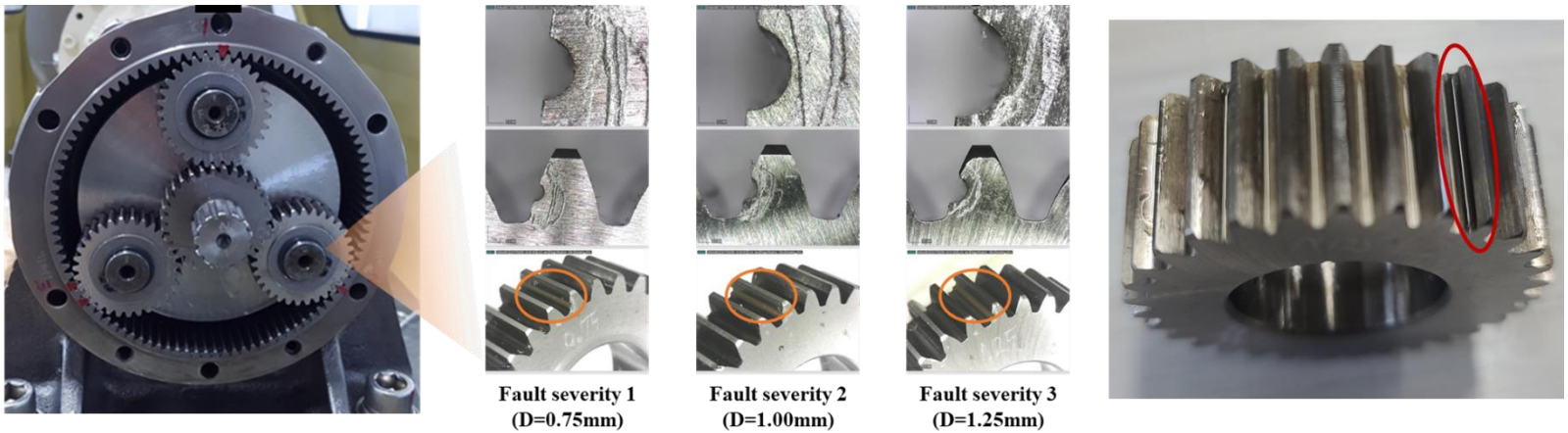

Figure 4-10 Faulty planet gear having half-circle-shaped line spall; (a) Cross section of the target planetary gearbox, (b) Different 3-level fault specimen (c) Upper view of fault specimen.

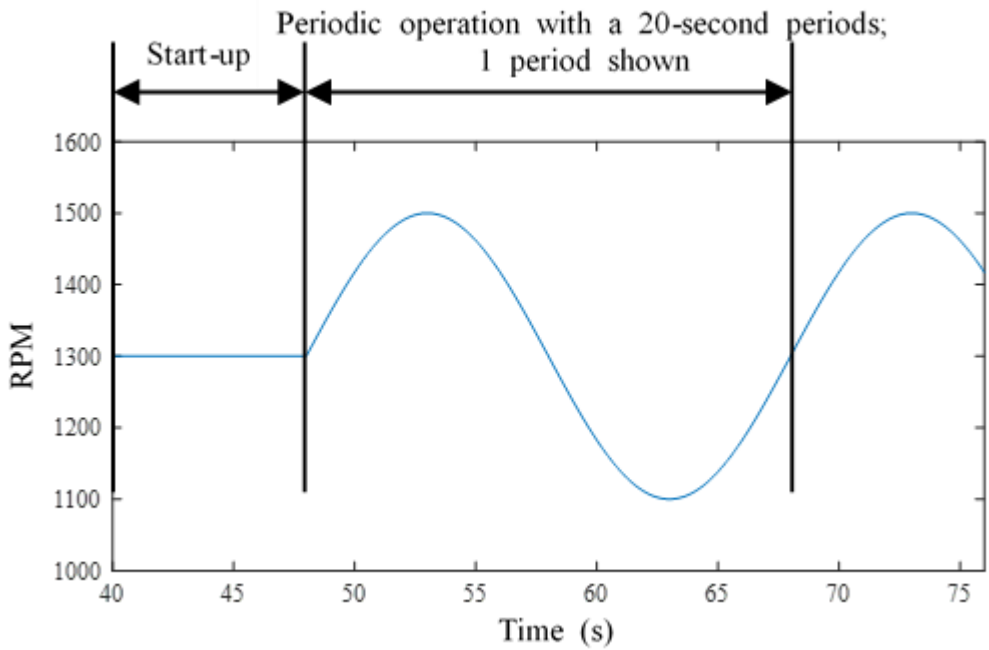

Figure 4-11 The variable-speed profile used in the experiment.

As shown in Figure 4-11, sinusoidal speed condition with a period of 20 seconds was imposed as a variable-speed condition; the speed varies from 1100 to 1500 rpm. These operating conditions were set to consider non-stationary conditions, to validate the proposed method. The inverse torque and temperature values were controlled at 2 N•m and 60 ◦C, respectively, to remove the effects from the uncertainty that arise from the temperature and the torque.

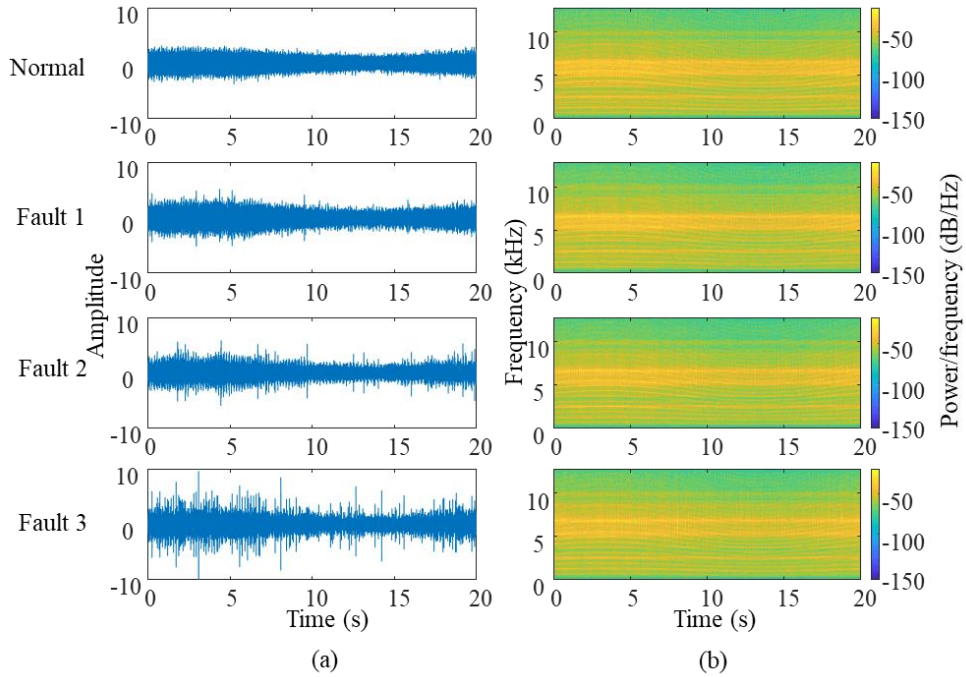

Figure 4-12 Vibration signals for a normal condition and fault conditions with three different levels of severity: (a) in the time domain, (b) in the time-frequency domain.

Figure 4-12 shows the vibration signals and the corresponding STFT results under a normal condition and for three different levels of fault conditions. The parameters for the spectrogram are selected as follows: the window function is a Hanning function with length of 1024, the overlap ratio is 0.5 (512 samples), and the length of the FFT is 4096. As shown in both figures, the signals are both frequency and amplitude modulated. The fault symptom can be observed in the time domain as a peak, where the amplitude increases as the fault size increases. In the STFT domain, however, the existence of a fault is not clear, due to the noise effect, as described in Section 4.1.

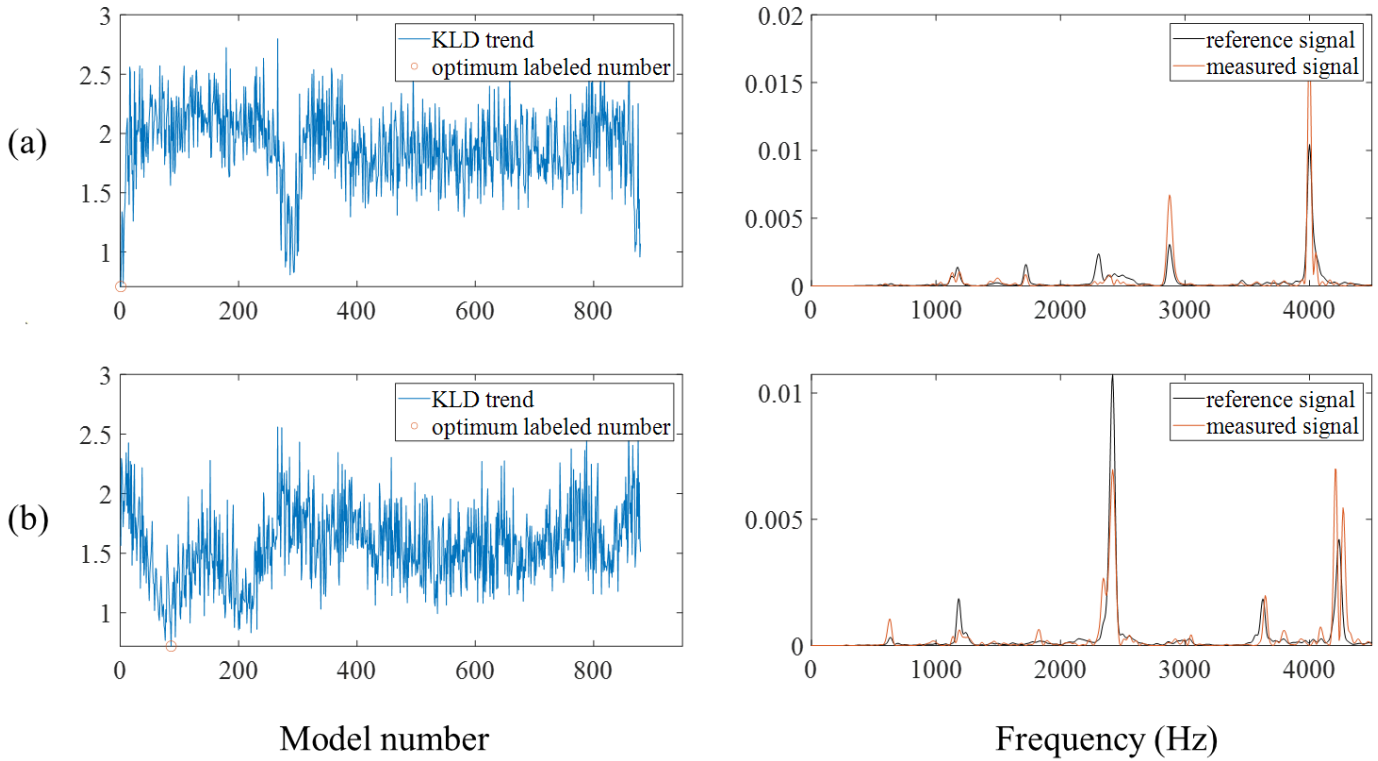

Figure 4-13 KLD based similar operating condition model matching for the normal signal (left) and comparison of spectrum (right); (a) 1st point (b) 2nd point.

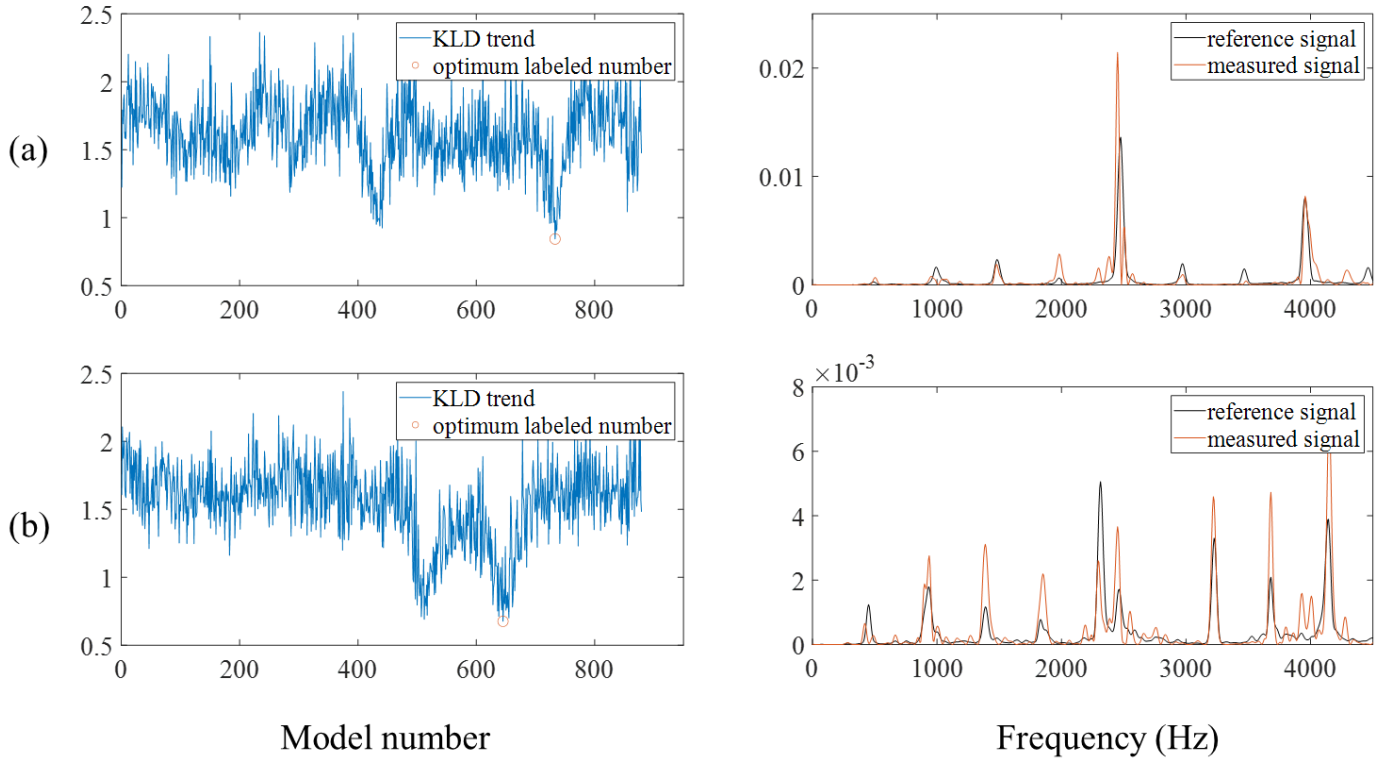

Figure 4-14 KLD based similar operating condition model matching for the normal signal (left) and comparison of spectrum (right); (a) 3rd point (b) 4th point.

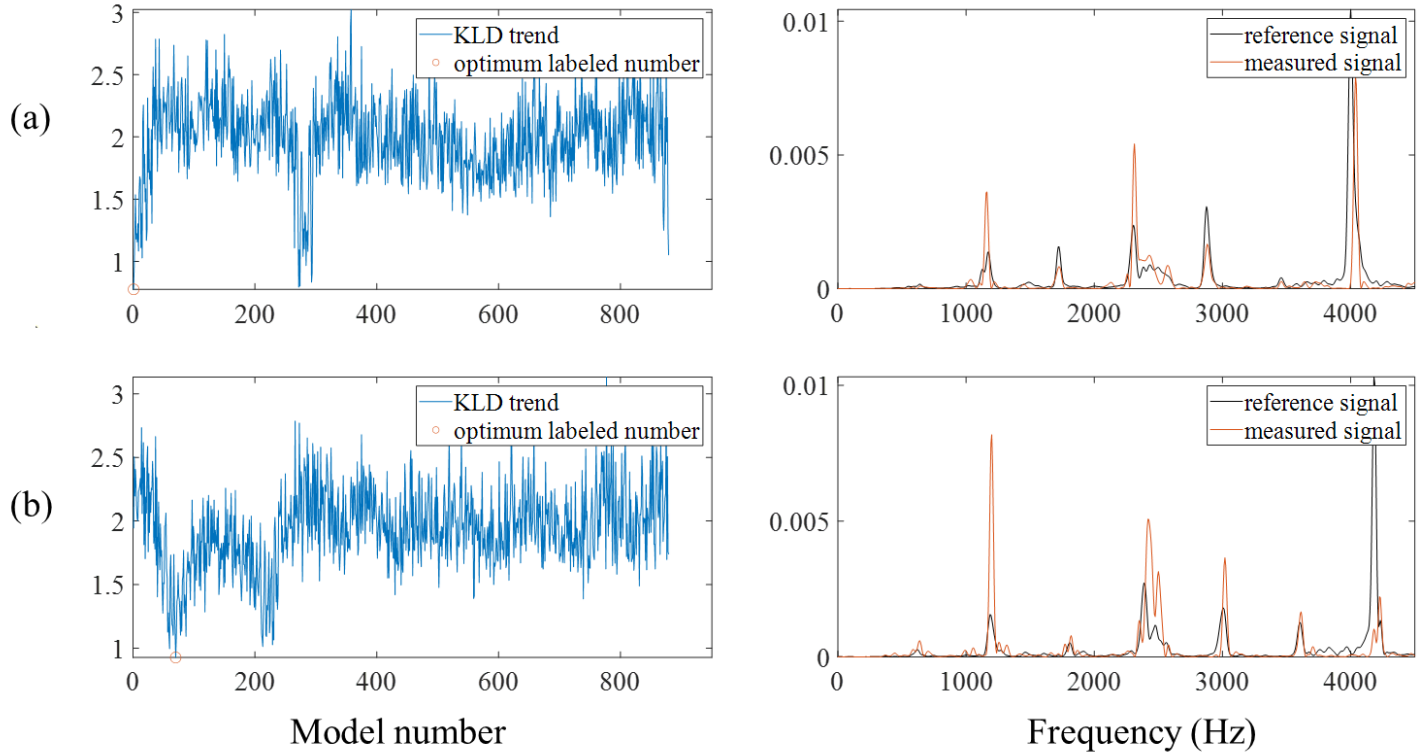

Figure 4-15 KLD based similar operating condition model matching for the fault level 3 signal (left) and comparison of spectrum (right); (a) 1st point (b) 2nd point.

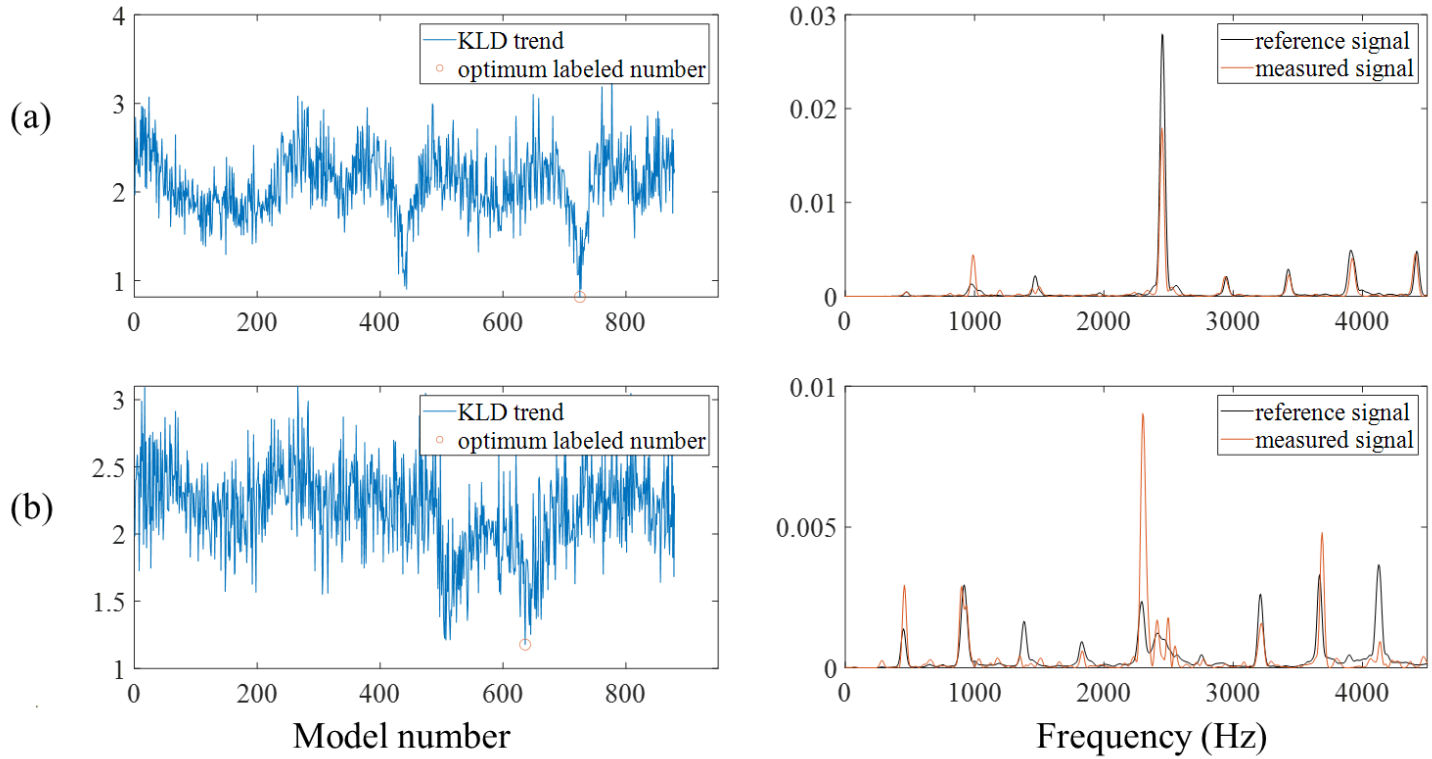

Figure 4-16 KLD based similar operating condition model matching for the fault level 3 signal (left) and comparison of spectrum (right); (a) 3rd point (b) 4th point.

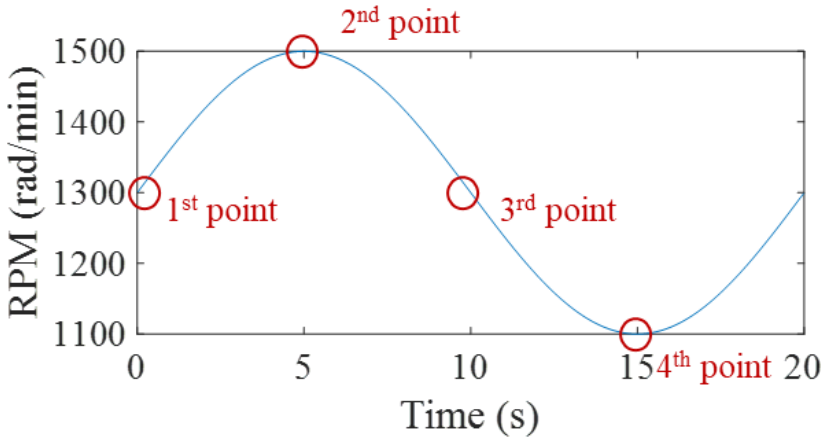

Figure 4-17 Speed condition of points for Figure 4-13 to 4-16.

Figure 4-13 to Figure 4-16 demonstrate the process of constructing a probability model using KLD for signals measured under different operating conditions and the corresponding spectrum results. Figure 4-17 shows the speed and acceleration conditions at each point corresponding to Figure 4-13 to Figure 4-16. The operating speeds and accelerations at each point are as follows: (21.7, 1.05), (25, 0), (21.7, -1.05), and (18.3, 0). The process of finding a probability model built for signals with different operating environments through KLD and the results through the spectrum are presented in Figure 4-13 (a) to Figure 4-16 (a). The results indicate that the proposed KLD method finds a model with a uniquely small minimum number of models, which is the optimum model's number, compared to other model numbers. Interestingly, in several models, a local minimum that is not the optimum model number appears because each corresponding model does not have a significant difference in frequency energy distribution. This indirectly indicates that there is no significant difference in terms of operating conditions of the corresponding models. Secondly, the proposed model matching process can identify whether the signal in a faulty state causes a significant change in the frequency energy distribution due to the fault. As depicted in Figure 4-15 and Figure 4-16, it can be observed that the energy in the frequency domain with high energy is generally greater than that of the reference signal in the faulty state. However, the KLD shows a high probability value

only in the frequencies with a high probability value, indicating that the results obtained are in good accordance with the operating condition. This is further supported by the similarity between the optimal model numbers Figure 4-15 and Figure 4-16, and the optimal model numbers in Figure 4-13 and Figure 4-16. In conclusion, the proposed method showed good results even in the most severe fault condition and under the largest velocity/acceleration, as shown in Figure 4-13 to Figure 4-16. Therefore, it is predicted that the results will also be satisfactory for fault levels 1 and 2, as well as for regions where the velocity/acceleration is not at its maximum value.

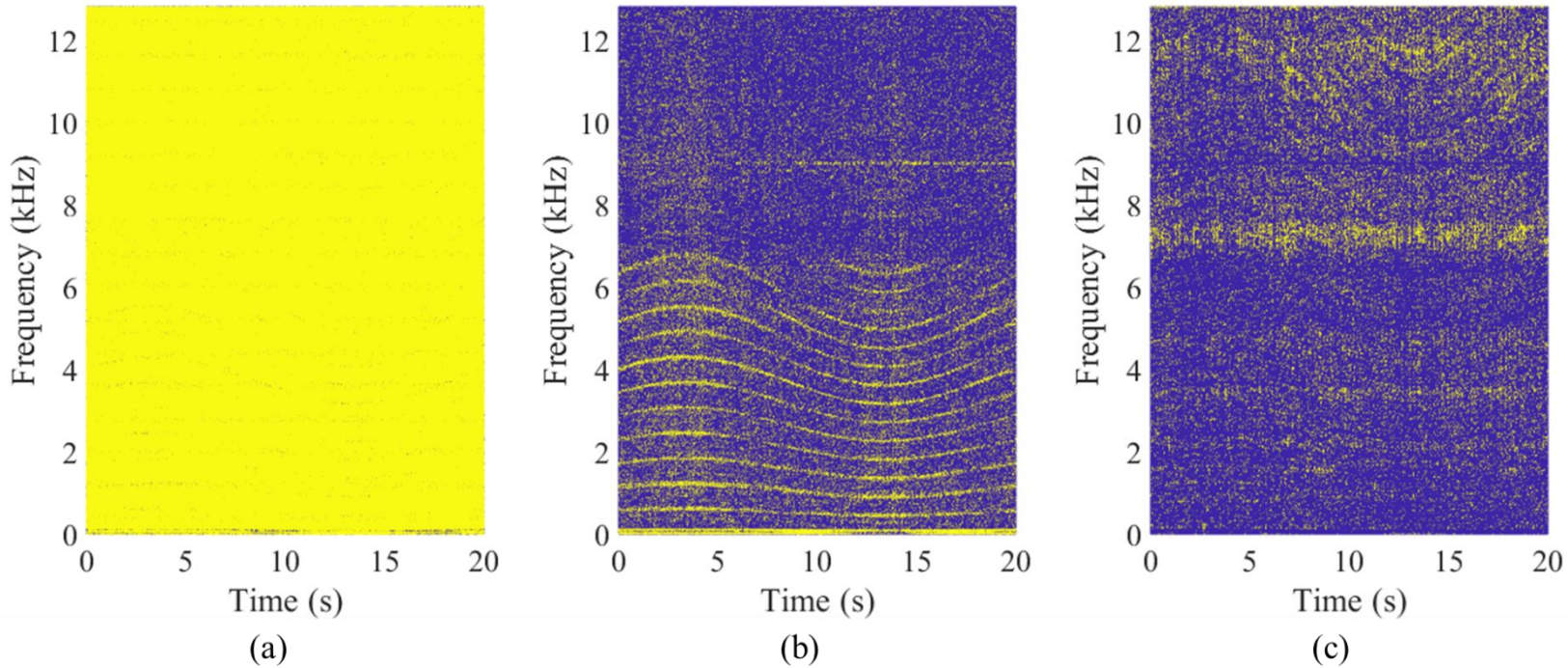

Figure 4-18 Type of the probabilistic energy modeling; (a) Noise dominant signal's indices, (b) Noise + deterministic signal's indices, (c) Neither of two types signal's indices.

Figure 4-18 illustrates the modeling type of each time-frequency index for one period of the vibration signal shown in Figure 4-12, obtained through the probabilistic energy modeling proposed in Section 4.2.1. Since the accelerometer sensor is mounted on the casing of the 2nd stage gearbox, the time-frequency indices corresponding to the gear mesh frequency (GMF) and its harmonic of the 2nd stage gearbox should include the deterministic signals. As depicted in Figure 4-18 (b), the modeling region of 'deterministic signal + noise' is the GMF and its harmonic. Moreover, the modeling of energy distribution for low-frequency indices (less than 100Hz) should also consider the deterministic signal because the signal carries the shaft rotational frequency of the gearbox, which can be treated as a deterministic signal. Figure 4-18 (c) shows that although most of the frequency ranges corresponding to 7000 ~ 8000 Hz were modeled dominantly with noise, some indices exhibit deterministic signals, but the energy distribution modeling failed with only simple phase changes in the noise + deterministic signal model. Therefore, the modeling was performed using KDE, which does not assume any specific energy distribution model. Finally, in the high-frequency region above 10kHz, the assumed modeling could not be applied, indicating that KDE modeling was utilized. Although the pattern is similar to the operating speed, this is attributed to the significant influence of the aliasing effect on the energy observed at the index of 10kHz or higher because the Nyquist sampling frequency is 12.8kHz.

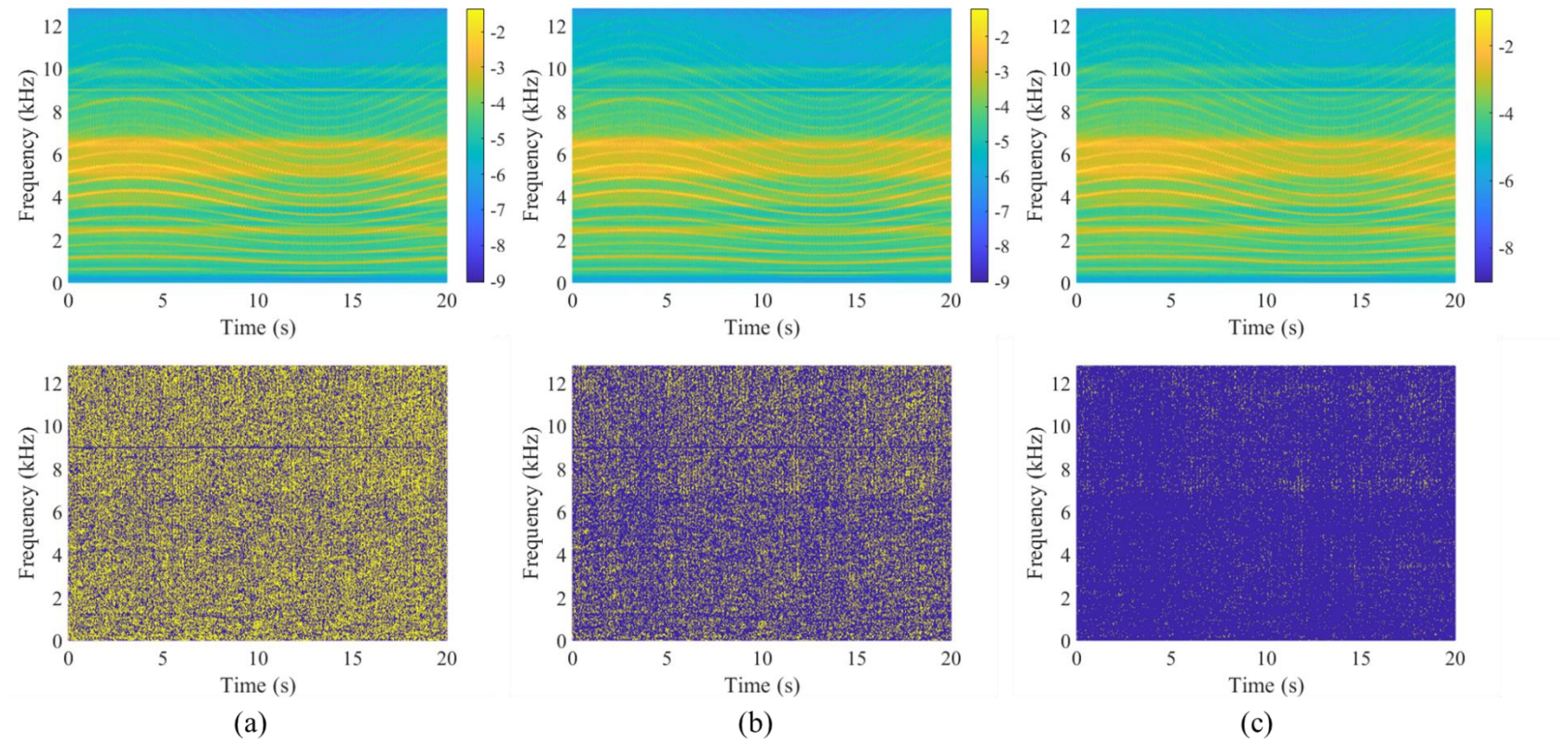

Figure 4-19 Probabilistic boundary (upper) & fault affected indices (lower) for the normal; (a) $k_p = 0.7$, (b) $k_p = 0.8$, (c) $k_p = 0.9$.

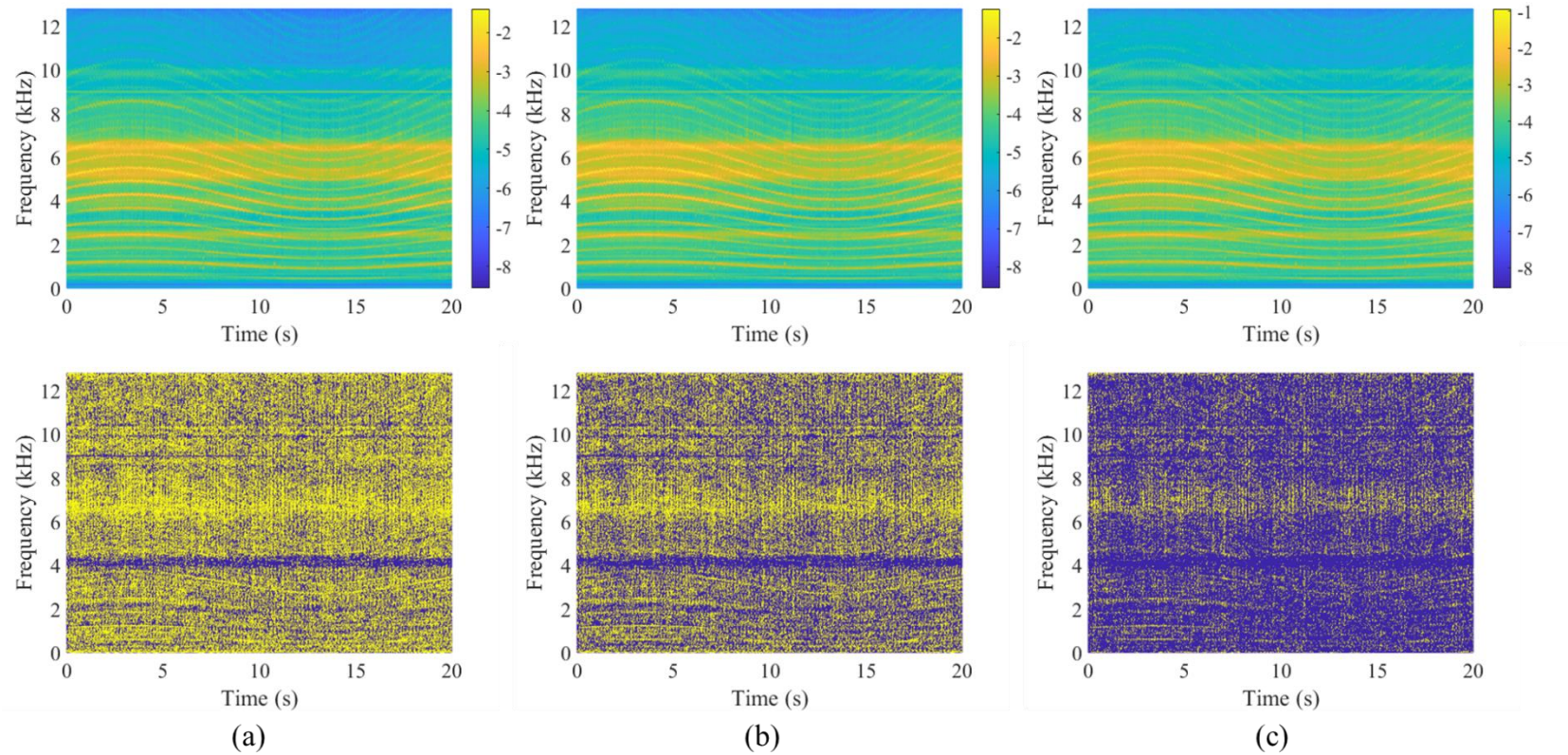

Figure 4-20 Probabilistic boundary (upper) & fault affected indices (lower) for the F1; (a) $k_p = 0.7$, (b) $k_p = 0.8$, (c) $k_p = 0.9$.

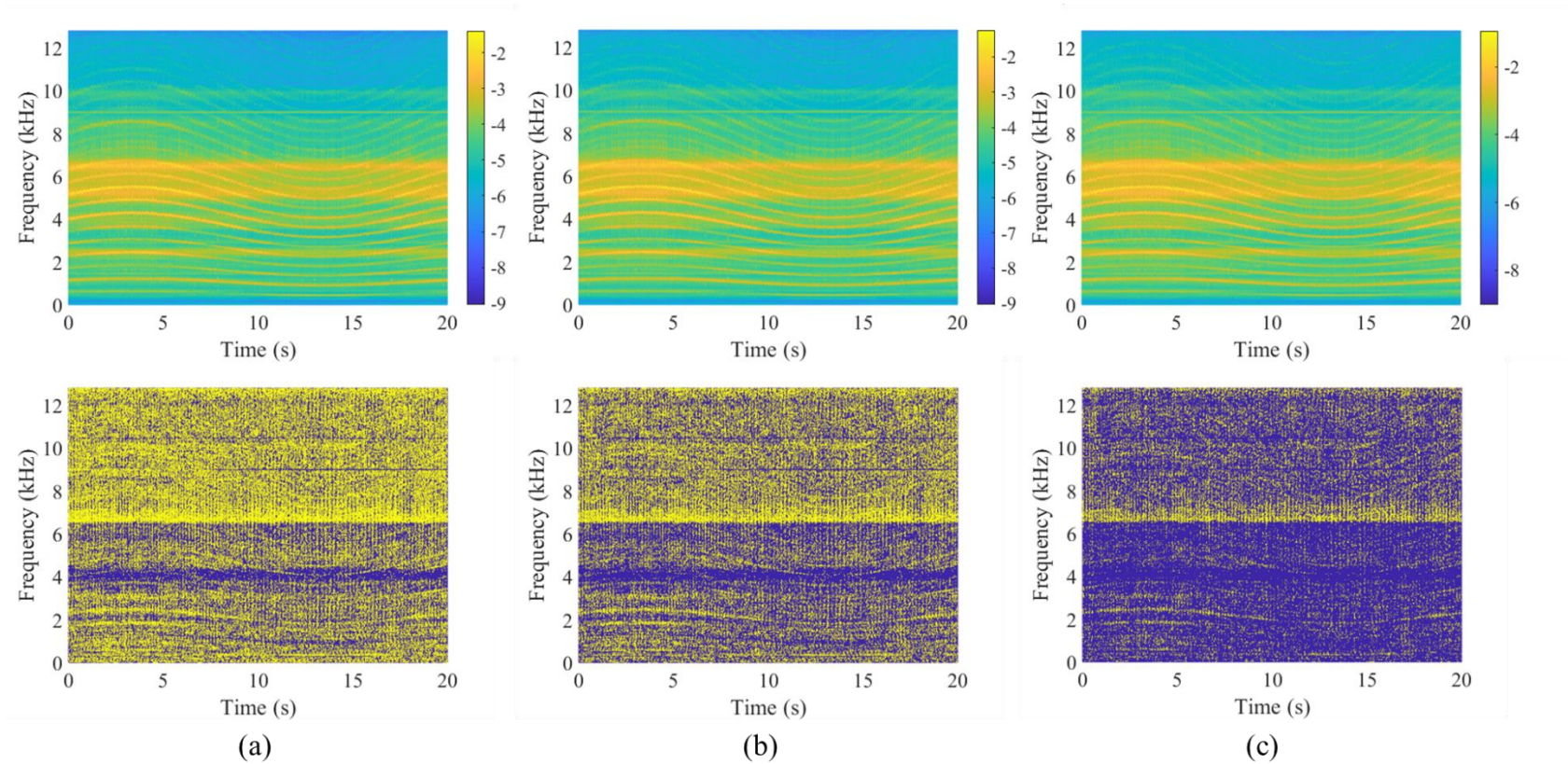

Figure 4-21 Probabilistic boundary (upper) & fault affected indices (lower) for the F2; (a) $k_p = 0.7$, (b) $k_p = 0.8$, (c) $k_p = 0.9$.

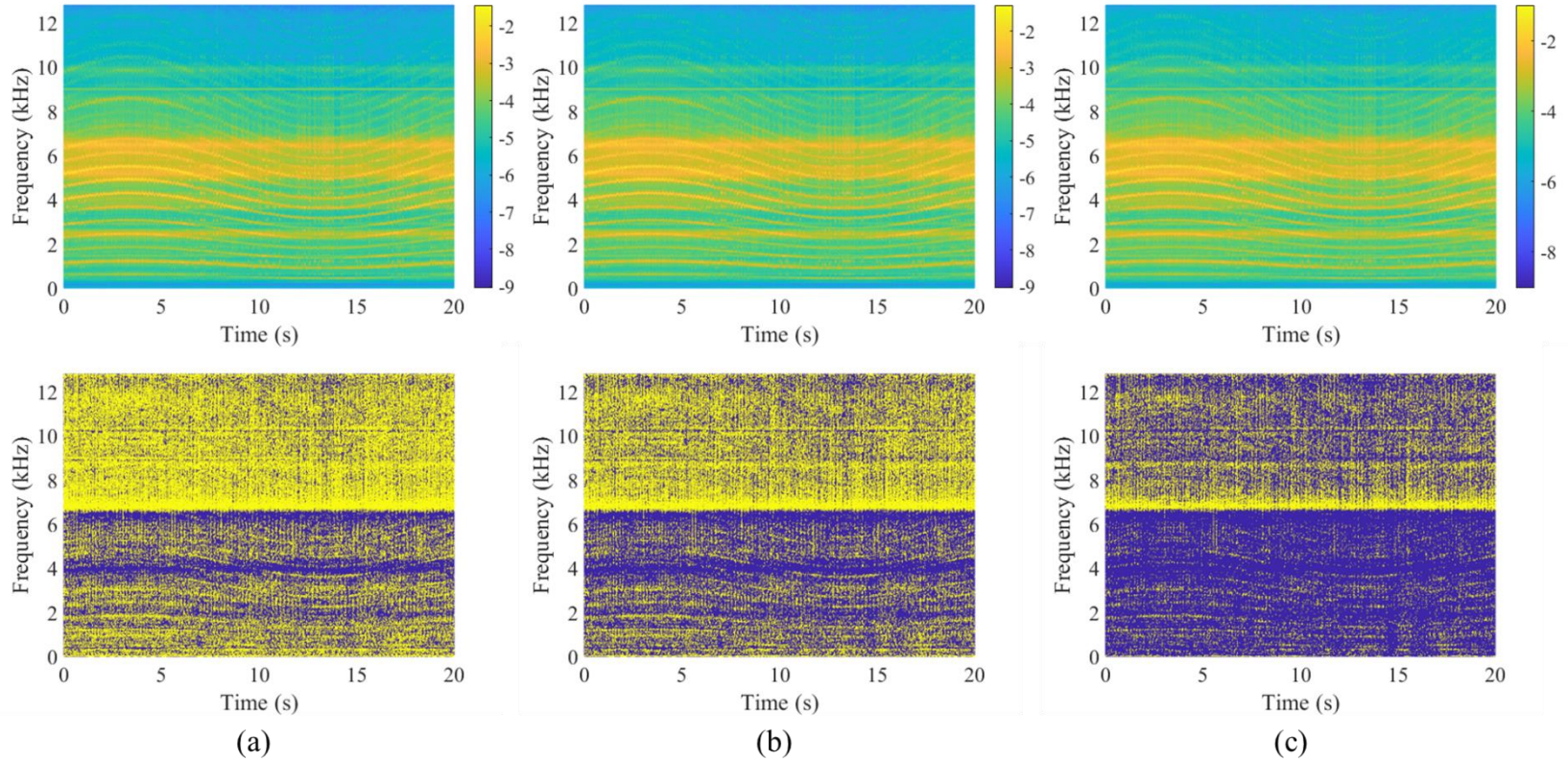

Figure 4-22 Probabilistic boundary (upper) & fault affected indices (lower) for the F3; (a) $k_p = 0.7$, (b) $k_p = 0.8$, (c) $k_p = 0.9$.

The selection of the parameter k_p is related to how robustly the indices activate and how well they secure separability. If the probabilistic boundary is set too low, which can occur by selecting k_p near 0.5, there is a high possibility that small energy increases due to noise can be regarded instead as a symptom of a fault. This means that the indices where $W(\tau, \omega) = 1$ could show meaningless information. On the other hand, if the probabilistic boundary is set too high, which can occur by selecting k_p to be close to 1, there is a high possibility that the energy increases due to a fault symptom could be thought to be an uncertainty issue from the noise. Therefore, in the case of a small fault, the feature FASER may not have sufficient separability because the fault-informative indices would be $W(\tau, \omega) = 0$.

To determine the appropriate k_p value, the conditional distribution of the probability model is considered, and an adaptive threshold value is set. Figure 4-19 shows $W(\tau, \omega) = 1$ when the new signal is from the normal state. From the definition of W described in the equation (4.26) and equation (4.28), the energy $C_s(\tau, \omega)$ could be larger than $b(\tau, \omega)$ because of the energy variation from the uncertainty. As shown in the figure, the indices where $W(\tau, \omega) = 1$ are randomly distributed without a pattern. The spectral leakage effect from the window function used to obtain the spectrogram may result in the existence of vertically consecutive indices that satisfy $W(\tau, \omega) = 1$. Figures 4-20 to 4-22 show the probabilistic boundary (upper plot) and fault-affected indices (lower plot) for the normal state and different fault states (F1, F2, and F3). F1 to F3 represent different levels of fault severity.

The yellow-colored indices in the lower plots of these figures represent the corresponding time-frequency filter $W(\tau, \omega) = 1$, which indicates that the corresponding time-frequency indices have enough separability. As shown in these figures, the probabilistic boundary for $W(\tau, \omega)$ is obtained differently depending on the selection of k_p. A higher margin value of k_p results in a higher boundary, as shown in the upper plots of each figure.

In the fault states (F1 to F3), the indices where $W(\tau, \omega) = 1$ are generally composed of 1) curved lines related to the GMF (Gear Mesh Frequency) and its harmonics, where the fault state increases the energy of the sidebands of the GMF, 2) horizontal lines related to the resonance frequency, and 3) a vertical line related to the impact signal from the fault state. The vertical lines induced from the impact signal and the horizontal lines from the resonance can be visualized better when kp = 0.9 is used compared to k_p = 0.7 or 0.8. This is because the number of indices where $W(\tau, \omega) = 1$ due to the energy increasing from the noise is comparatively less when k_p = 0.9. Additionally, as shown in Figure 4-20 (a) to Figure 4-22 (a), the curve related to the GMF is not noticeable because the number of indices where $W(\tau, \omega) = 1$ is too large in the surrounding area of the GMF, due to the stochastic property of noise. The results also suggest that the separability of the proposed feature, FASER, may be degraded if it has relatively high energies at the $W(\tau, \omega) = 1$ index due to noise. Based on these considerations, the posterior experimental result is analyzed with k_p = 0.9.

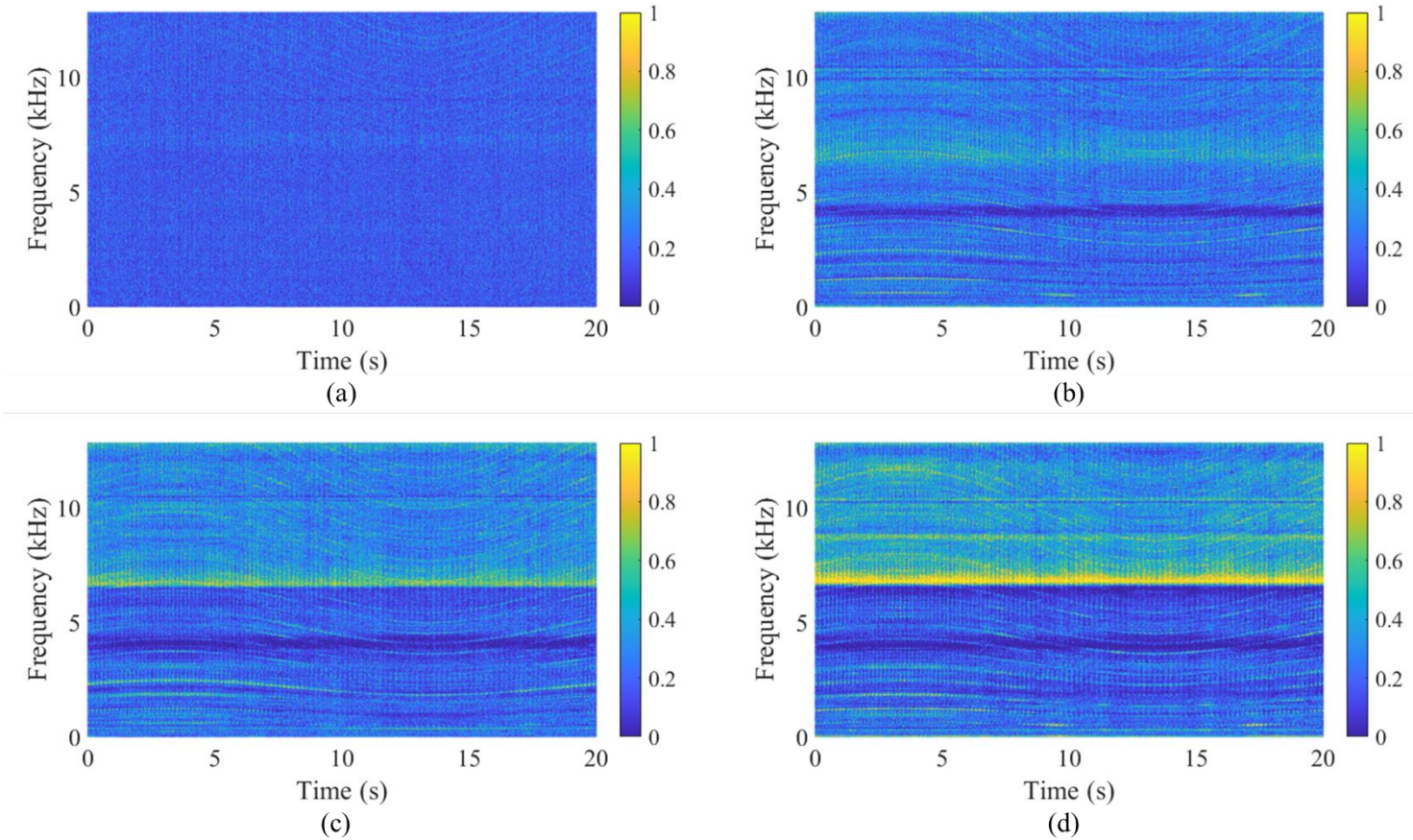

Figure 4-23 Proportions where each index satisfies $W(\tau, \omega)=1$ using $k_p = 0.9$; (a) Normal, (b) F1, (c) F2, (d) F3.

Figure 4-23 shows the proportion of each index that satisfies W=1 for each state using k_p = 0.9. As seen in Figure 4-23 (a), most of the time frequency indices for normal state conditions have a value around 1 - k_p = 0.1, indicating that they are not fault-affected indices. However, for the frequency range above 10 kHz, which corresponds to the locally high harmonic component of the GMF, the proportion of fault-affected indices is higher than the expected probability value. This could be due to the error in the estimated energy distribution that occurred during the modeling construction process, as KDE modeling was performed in this region. This suggests that excluding frequency energy near the Nyquist frequency or using sophisticated modeling could lead to more accurate results, but such measures were not out of scope in this study. The index that shows the most noticeable change according to the fault level is around 6200 Hz. Figure 4-23 (b), (c), and (d) indicate that the proportion of fault-affected indices increases as the severity of the fault increases. This tendency can be attributed to the fact that the energy of the resonance frequency increases due to the fault condition. In addition, the indexes corresponding to the GMF are selected with a higher proportion as the fault state becomes more severe, indicating that a fault in the gear teeth increases the sideband frequency energy of the GMF. However, due to the limitation of frequency resolution, it is highly likely that indices corresponding to the sideband of GMF are not always selected as fault-affected indices. Therefore, it can be considered that indices corresponding to the sideband of GMF are not always selected close to 1.

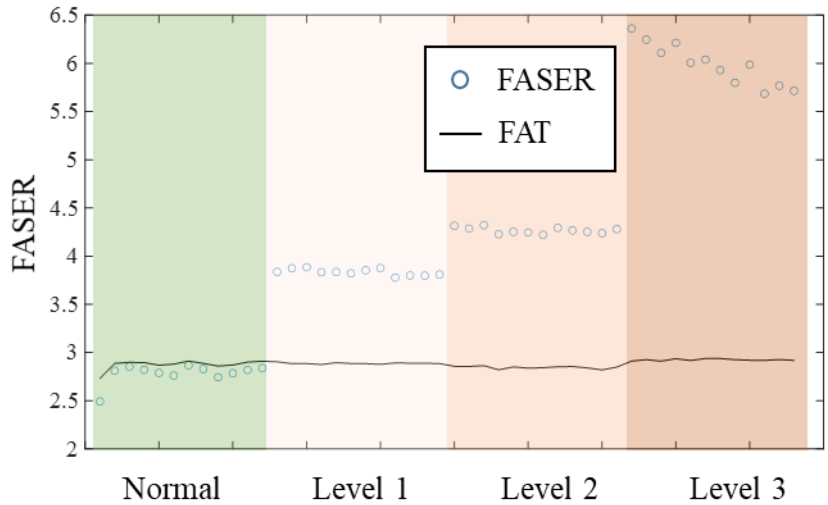

Figure 4-24 FASER and FAT of the measured signal (Normal, Fault level 1, Fault level 2, Fault level 3) having 1 period operating cycle.

Figure 4-24 displays the FASER trends for both the normal and faulty conditions. The FASER values increase as the fault level increases. It is also evident that all FASER values in the faulty state exceed their adaptive threshold (FAT), while FASER values in the normal state are smaller than their adaptive threshold. Moreover, most of the adaptive thresholds are formed around 3 for both normal and faulty conditions. This can be explained by the probabilistic spectral energy distribution model used in Section 4.2.1 and the results obtained in Figure 4-24 (a). Since most of the time-frequency indices are composed of energy modeling that follows the form of Gaussian noise, the distribution of the energy sum corresponding to the denominator of FASER follows the chi-square distribution derived from Gaussian noise modeling. As a result, the average value of the conditional probability distribution obtained from k_p is about three times the average value obtained from Gaussian energy signal modeling. Hence, it can be concluded that the FAT value is formed in the form of fluctuation around 3.

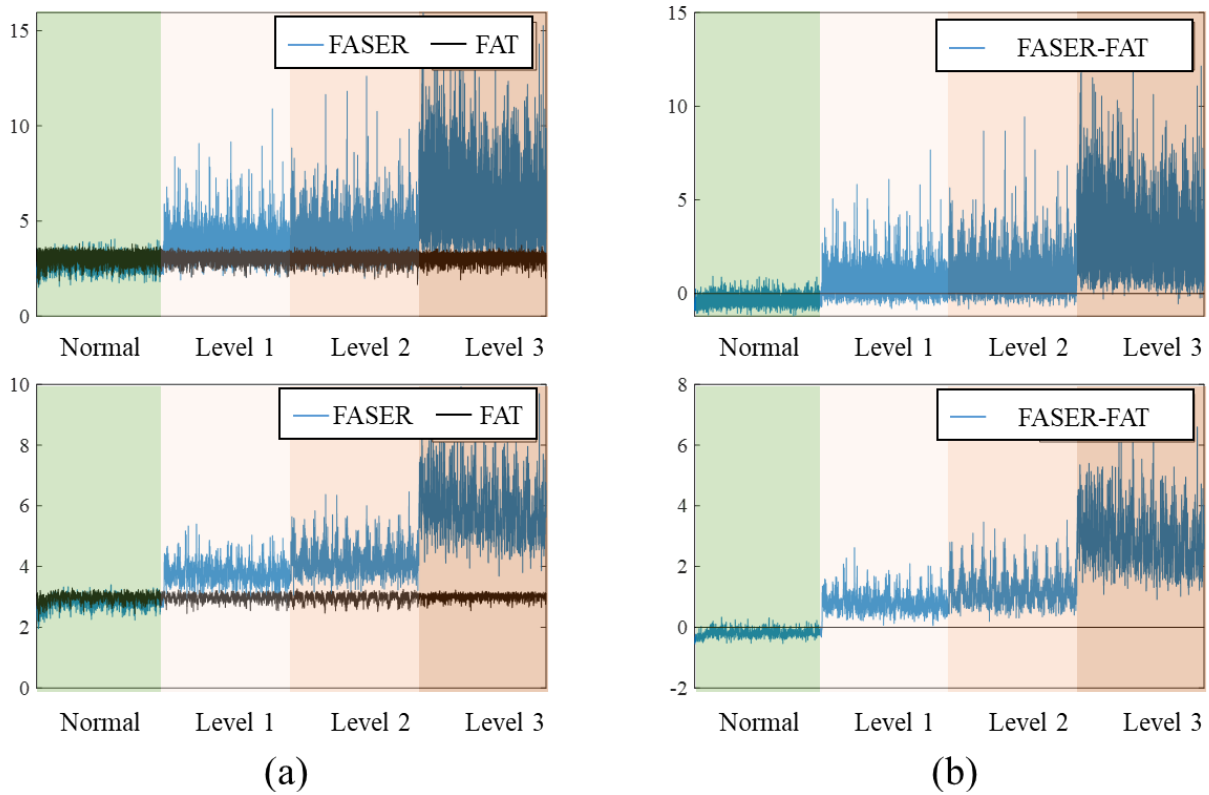

Figure 4-25 Effect of the length (0.04sec. – upper, 0.2sec. – lower) of signal for FASER; (a) FASER and FAT (b) difference of FASER and FAT.

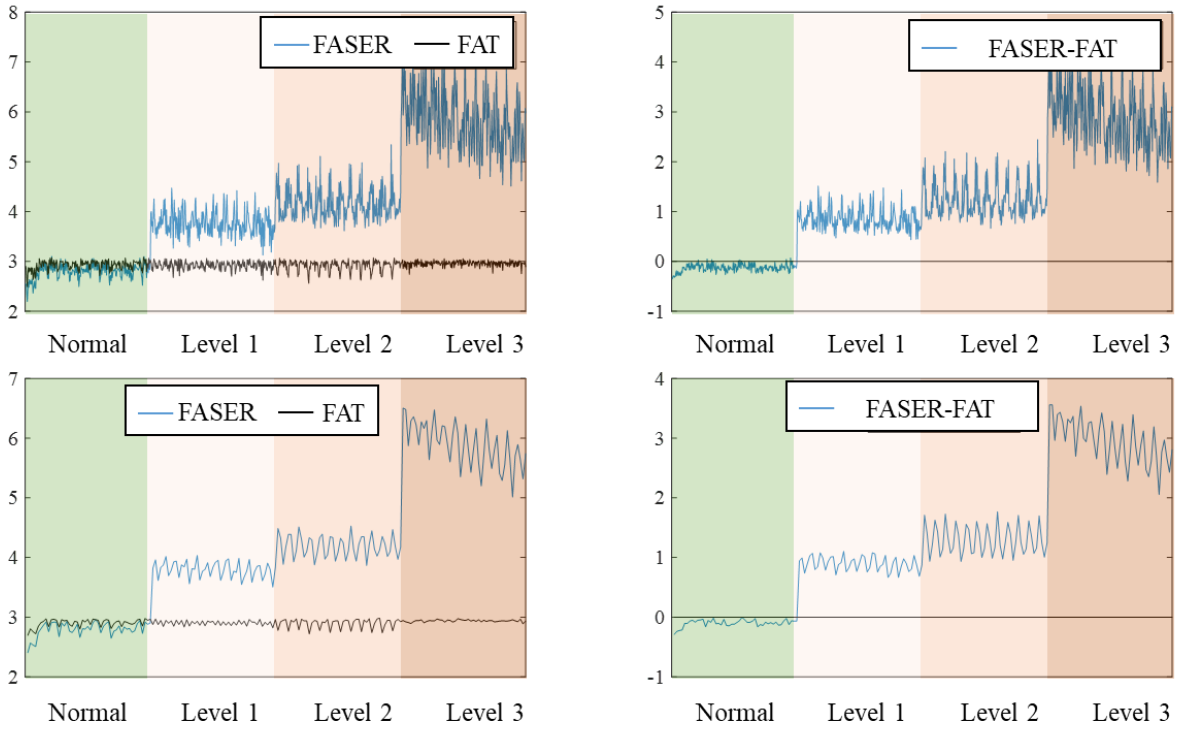

Figure 4-26 Effect of the length (1sec. – upper, 5sec. – lower) of signal for FASER; (a) FASER and FAT (b) difference of FASER and FAT.

Figures 4-25 and 4-26 demonstrate the impact of signal length on the calculation of FASER and its adaptive threshold, FAT. The signals used to calculate FASER were not overlapped to avoid correlation dependency, which could lead to incorrect analysis. The figures illustrate that as the signal length for calculating FASER increases, the fluctuation of FAT decreases. This phenomenon is closely related to the proportion of modeling distribution types, as shown in Figure 4-18.

When the time interval for calculating FASER is very short, such as 0.02 seconds in Figure 4-25, there is a higher likelihood of encountering modeling types that do not conform to the local Gaussian noise shape, depending on where the fault frequency is generated. In this case, the ratio between the conditional mean and the total mean of the matched energy distribution decreases more than in Gaussian noise modeling, resulting in more severe fluctuations.

Moreover, shortening the time interval means that even if FASER is calculated for the same fault type, the corresponding operating conditions may differ, leading to different degrees of fault effects. This tendency is more apparent in Figure 4-28, where it can be observed that the FASER value becomes similar every cycle when the operating conditions are the same. The proposed method can accurately classify between faulty and normal states using only 0.2 seconds of data, as shown in the results. However, in order to estimate the severity of the fault state, it is necessary to model the changes in features separately according to the operating conditions.

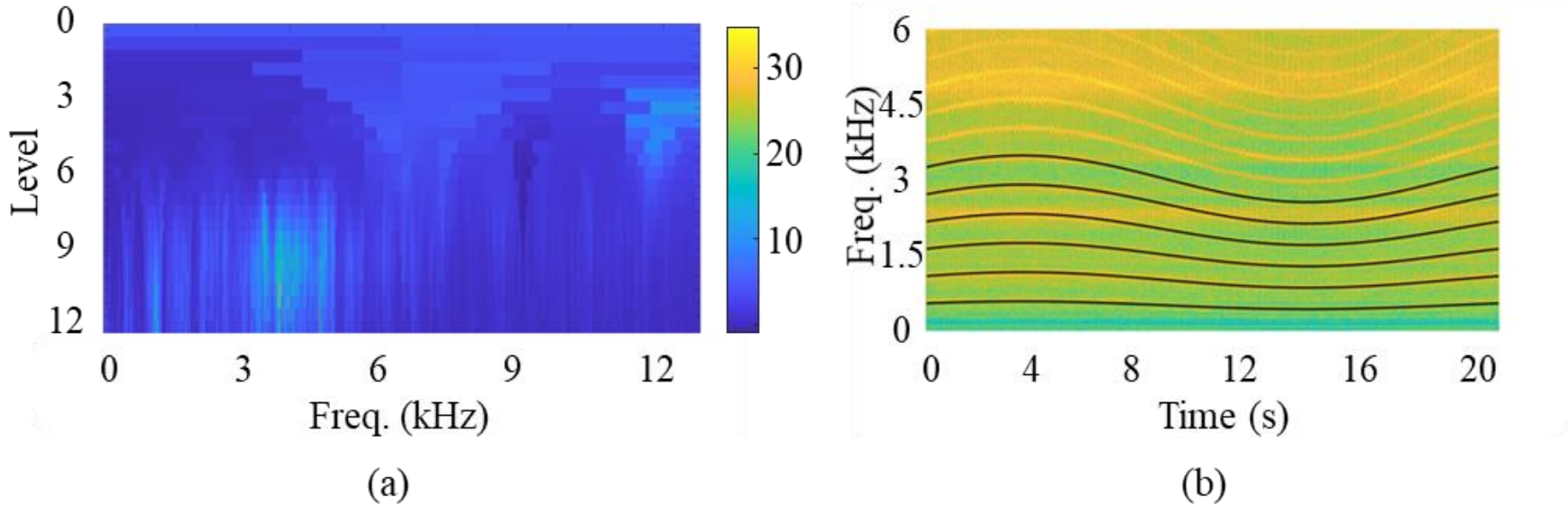

Figure 4-27 (a) Spectral kurtosis result for the normal state signal, (b) GMF and its harmonic trend with the spectrogram.

Lastly, the RMS (Root Mean Square) of the raw signal is used to compare the sensitivity of our method, considering the fact that the RMS is greatly related to the energy of the signal. Additionally, another energy extraction method based on spectral kurtosis is used for comparison of the performance of the proposed method. In this case study, the optimal frequency band for each sample is generally calculated with a center frequency of 4300~4500 Hz and a bandwidth of 6.25 Hz, as shown in Figure 4-27 (a). The level equals to log2 (the window size), which is related to the frequency bandwidth. The colorbar is based on the spectral kurtosis. Furthermore, considering that the harmonics of the GMF and their sidebands are generally analyzed for fault diagnosis of a gearbox, the GMF and sidebands of the corresponding time-frequency indices based on the operating speed was calculated; it is shown as a black curved line in Figure 4-27 (b). The feature was calculated as the energy sum of the indices corresponding to the GMF and their sidebands; this is indicated by the black curved line in the figure. The parameters for calculating GMF is listed in Table 4-1.

Table 4-1 Specifications of the experimental gearbox.

Parameter	Value
Number of sun gear teeth	31
Number of planet gear teeth	31
Number of ring gear teeth	95

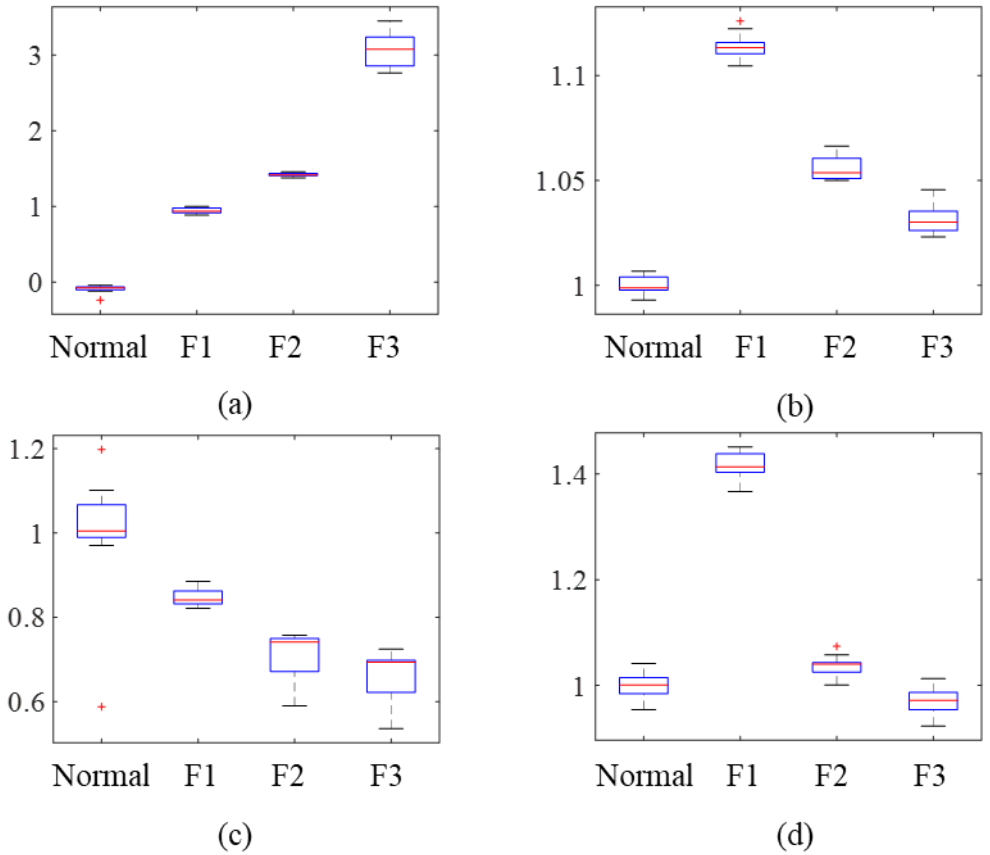

Figure 4-28 Comparative study for the proposed method (the length of signal = 20 s); (a) Proposed method, (b) RMS, (c) SK, (d) 1st GMF's sideband energy.

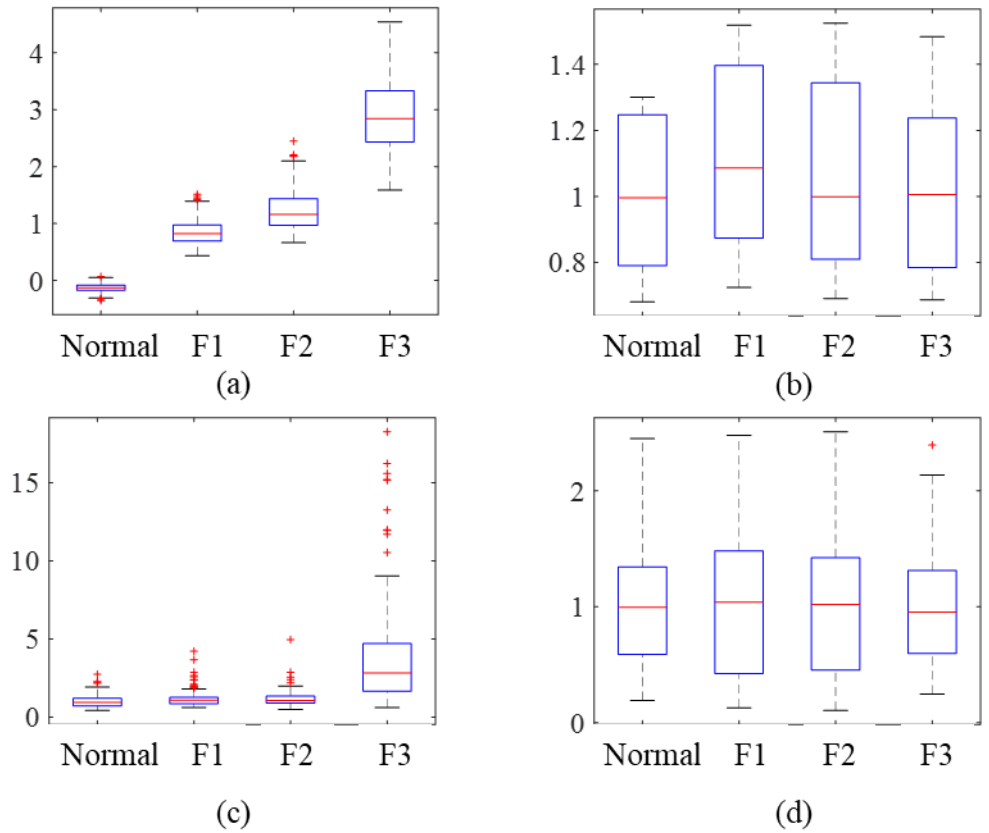

Figure 4-29 Comparative study for the proposed method (the length of signal = 1 s); (a) Proposed method, (b) RMS, (c) SK, (d) 1st GMF's sideband energy.

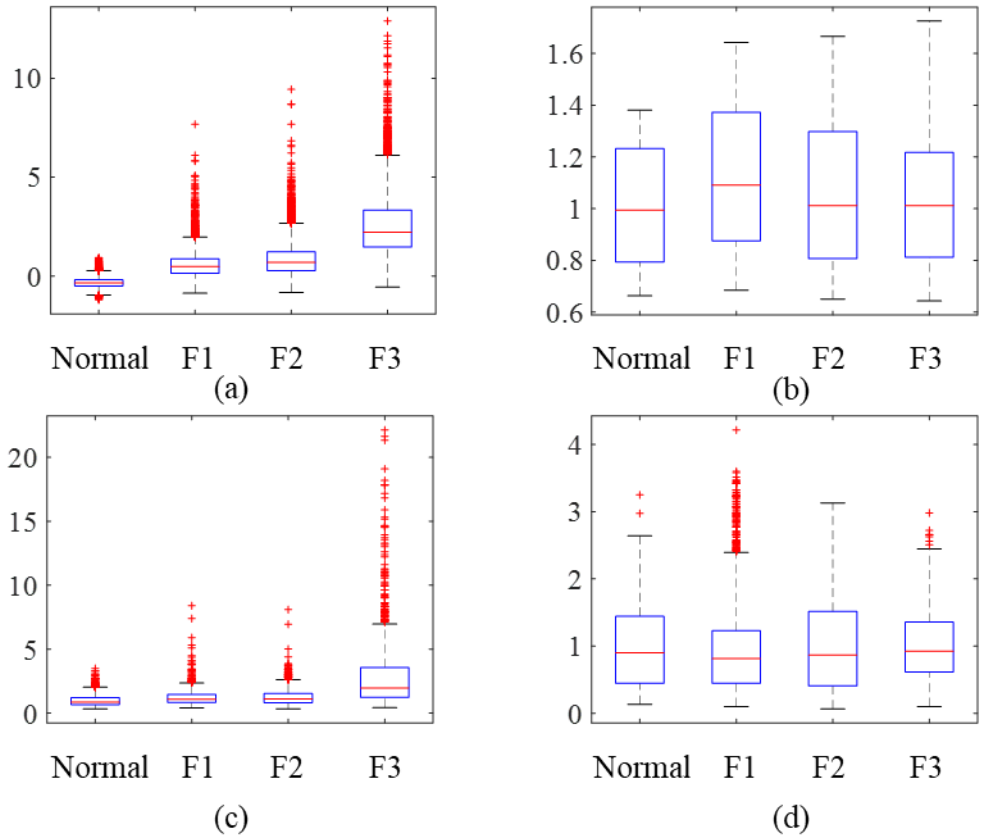

Figure 4-30 Comparative study for the proposed method (the length of signal = 0.1 s); (a) Proposed method, (b) RMS, (c) SK, (d) 1st GMF's sideband energy.

Figure 4-28 to Figure 4-30 show the results of the comparative study in a box plot. F1 to F3 means fault levels 1 to 3, as shown in Figure 4-10. All of the features were calculated based on the energy value of the operating condition's synchronized signal, according to the proposed KLD method, and were normalized by the mean value of each of the features of the normal state. The RMS feature shows good performance in terms of fault diagnosis because the features of F1 to F3 are larger than those of the normal condition; however, this approach has a disadvantage in that the feature becomes smaller even when the size (level) of the fault increases. Furthermore, as can be seen from the y-axis value, the difference in size is very small compared to the proposed method; thus, even a slight change in the experimental environment could lead to different results. As shown in Figure 4-28 (c), in the case of the results using SK, the feature value decreases in the fault state. Since a fault state in a gearbox causes a modulation effect, SK generally aims to find the frequency band where this effect is maximized by calculating the kurtosis. However, in the case study, the increase in energy around the GMF that arises due to modulation is not dominant, as shown in Figure 4-28 (d) and Figure 4-23. In addition, the operating speed has a change of about ±15% of the mean value; thus, even if the frequency domain is selected, GMF components of other harmonic numbers are included, which adversely affects the aim of SK. Therefore, in the context of fault diagnosis methods, SK may not effectively find the optimum frequency band. Similarly, when considering the feature distribution of each state, the energy trend shown in Figure 4-28 (d) is difficult to use as a criterion for diagnosing fault states. There are times when it has a large feature, like F1 in Figure 4-28 (d), but it seems that the energy increase effect of the wideband noise component is affected greatly, as shown in Figure 4-27 (b). This problem also occurs in the proposed method; however, since the energies of the corresponding indices are not large compared to the energies of the overall $W(\tau, \omega) = 1$ indices in the proposed method, the effect is relatively small and this issue does not cause a major problem for the proposed

method. Figure 4-29 and Figure 4-30 show the comparative study when the length of the measured signal are 1 and 0.2 (s), which means the utilized signals only have the part of the periodic operating condition. For the RMS feature, as shown in each Figure (b), the distribution of feature is overlapped for each state. This is because the operating condition of data are different. Generally, the vibration signal increases as the operating speed increases. Therefore, the variation from the speed makes impossible to diagnose the state of signal using RMS feature. For the SK feature, as shown in each Figure (c), the performance for the fault diagnosis is better as the length of the signal decreases. This phenomenon can be attributed to the fact that shorter time length lead to a more stationary operating condition with less variation. Therefore, it appears that the better frequency selection in signals with strong stationarity may be the reason for this, but it is generally possible to use the SK method even in non-stationary conditions. Lastly, for the GMF sideband feature, which is conventionally utilized as the CFF, the performance of fault diagnosis is worst compared with the other methods. The reason for this is that the frequency resolution is set by the STFT parameter, and since the frequency resolution is relatively large compared to the size of the GMF sidebands, it can be assumed that even if the energy of the GMF sidebands is extracted, it is heavily influenced by other components or noise. Based on the analysis results, the proposed method demonstrated superior performance, which is attributed to the fact that the features were selected by taking into account the signal length and STFT parameters.

4.4 Summary and discussion

This chapter proposed a method for fault diagnosis of gearboxes using vibration signals from non-stationary operating speed conditions. The proposed method, called fault-affected signal energy ratio (FASER), aims to extract the fault-related pattern from the vibration signals and quantify the uncertainty of the signal representation.

The proposed method first extracts vibration data using 2d-KLD based on the normalized spectrogram for a consecutively measured signal with several operation cycles. From this method, a consecutively measured signal can be extracted as the set of signals that has the target operation cycle. Then, the signals in the set are transformed to spectrograms and KDE is applied to model the energy distributions of each index of a spectrogram for quantifying the uncertainty that arises from the noise and time-frequency representation. These probabilistic models from KDE can then be used to calculate the probabilistic boundary to discriminate whether the calculated energies of each index of the spectrogram of the new signal are statistically separable. The time-frequency filter is defined to select those that are statistically separable, and the proposed FASER is calculated by using the time-frequency filtered signal. An adaptive threshold (FAT) that considers the property of the window function is used to improve the robustness of the FASER for classifying the state. In the case study, which examined a wind turbine simulator, the proposed method was able to classify the state of the signal and showed the possibility of estimating the severity of the fault.

The proposed method has several contributions, including the ability to extract the desired signal automatically from a consecutively measured signal without additional equipment, such as an encoder. Additionally, the uncertainty of the signal represented as a spectrogram is quantified through a KDE model, and statistically separable indices for calculating the fault-affected signal can be found by the model.

An adaptive threshold that considers the window function to transform the spectrogram and the conditional probability of probabilistic distribution model is also proposed, which helps to prevent misdiagnosis of normal signals as being from a fault state. Furthermore, the proposed method does not require any kind of fault-related knowledge, such as a fault frequency calculated by a fault mechanism, making it more efficient in scenarios where identifying the fault frequency becomes infeasible due to security issues that restrict the disclosure of physical or mechanical properties of the system under consideration. The proposed method can be applied to any type of nonstationary signal, such as motor torque signals in robots or current signals in motors. However, there is a disadvantage of the proposed approach in that its probabilistic modeling must be rebuilt when the target operating condition changes. Future research will examine ways to overcome these problems by roughly extracting the operating conditions, mapping the probability model to the operating conditions, and updating the probability model when the operating conditions change.

Sections of this chapter have been submitted as the following journal articles:

1) **Kyumin Na,** Heonjun Yoon, and Byeng D. Youn. "FASER: Fault-affected Signal Energy Ratio for Fault Diagnosis of Gearboxes Under Repetitive operating Conditions." *Reliability Engineering & System Safety*

Chapter 5

Integration of LSR and HSR approach

This chapter presents a methodology that combines PERL, an LSR-based approach described in Chapter 3, with FASER, an HSR-based approach described in Chapter 4, for efficient fault diagnosis. The evaluation of results using the LSR signals allows for the estimation of the probability of fault presence at each location. Consequently, it becomes possible to select a sensor that is sensitive to faults and data that provides the highest fault information based on the sample with the highest estimated probability. Since each sample represents a signal obtained by converting a high-sampling signal into an energy standard, it can be assumed to contain more fault-related information when analyzing the corresponding high-sampling signal. Hence, the subsequent step employs the FASER method based on the HSR signal corresponding to the sampled LSR signal. By focusing on data that already possesses relatively more failure information in the HSR-based approach, the time required to derive results is reduced, and the performance in terms of failure sensitivity is enhanced. Experimental verification of this methodology is conducted on an industrial robot system in this chapter. Initially, the data from the industrial robot system is introduced, followed by the presentation of failure location estimation through the LSR approach and fault diagnosis results through the HSR approach. Finally, the effectiveness of the proposed integrated method is demonstrated by deriving the results obtained through the LSR-HSR approach.

5.1 Experimental setup and preliminary work for PERL method

This case study examines a cycloidal gearbox fault in the joint of a 6-DOF industrial robot used for a welding motion in industrial fields. The results of this case study show that the proposed integrated framework. The target component is a cycloidal gearbox in the 4th joint of the industrial robot. Figure 5-1 (a) shows an experimental validation setup comprising a 6-degree-of-freedom (6-DOF) industrial robot. Indeed, there have been studies focusing on current signals for diagnosing robot systems [87, 88], the proposed methods in this research employ vibration sensors. While current signals may offer their own advantages in certain contexts, the use of vibration sensors allows for a more direct measurement of the mechanical behavior and performance of the system. This choice is based on the assumption that the fault state will affect the energy of the measurement data in terms of vibrations. Therefore, in the proposed methods, the adoption of vibration sensors is driven by the aim to capture and analyze the energy characteristics of the measurement data in order to validate the suggested fault diagnosis framework for robot system. An

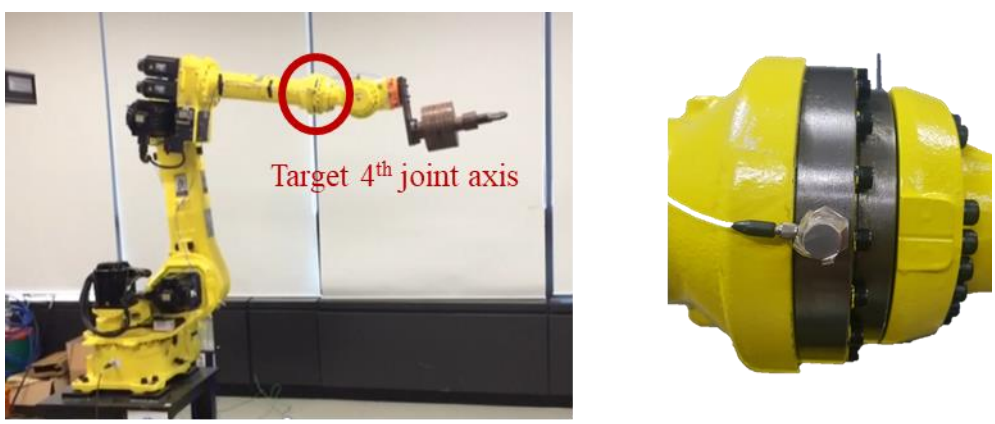

Figure 5-1 Testbed setup: (a) A 6-DOF industrial robot, (b) The location of the accelerometer sensor attached on the 4th joint of the casing of the cycloidal gearbox.

accelerometer attached on the casing of the gearbox is utilized the experimental data shown in Figure 5-1 (b). A faulty cycloidal gearbox was acquired from an actual industrial manufacturing line; the type of a fault considered was wear on the pin-bearing. The imposed variable-speed condition was from an arc welding motion, as shown in Figure 5-2. During the experiment, temperature values were controlled at 50◦C to remove the effects from factors other than the variable speed. Actually, the vibration signal is obtained with high sampling of 25600 Hz, for verification of LSR based approach, the RMS of the signal obtained for 1 second was converted and applied.

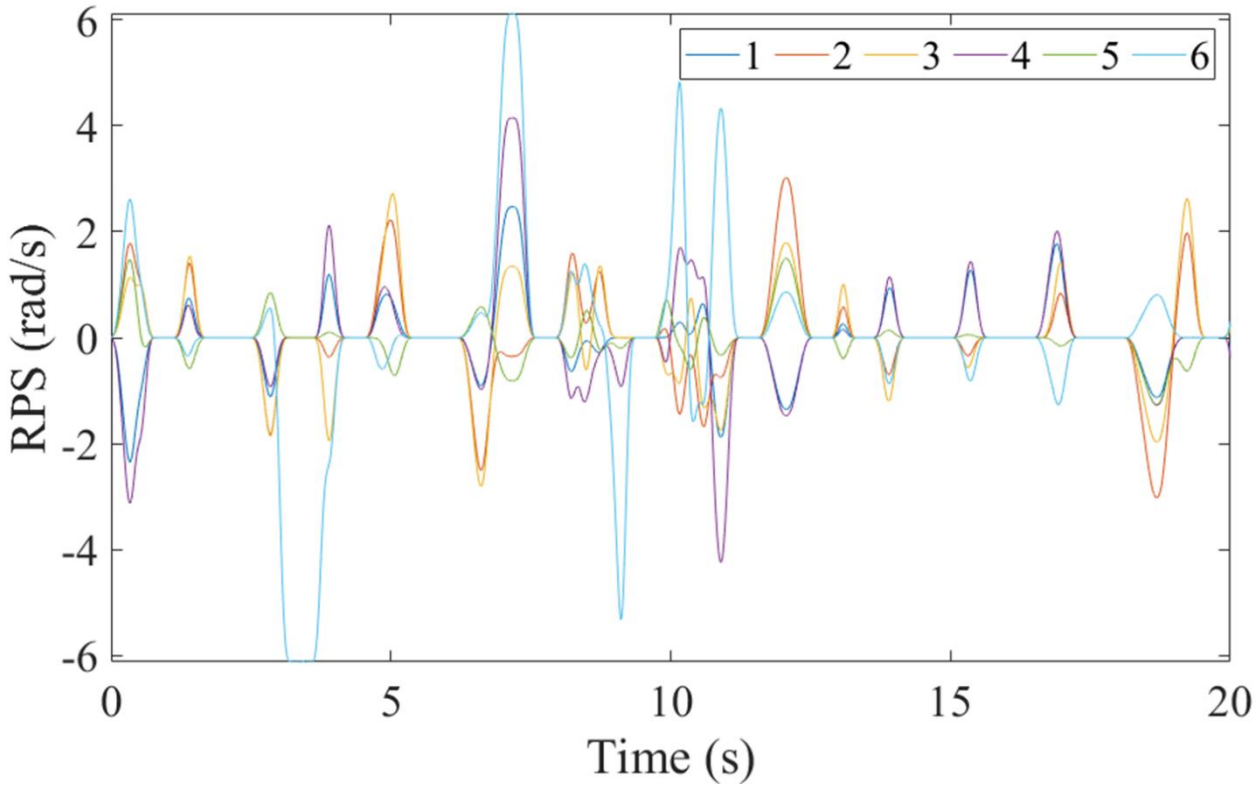

Figure 5-2 Operating speed profile of welding motion at each joint axis.

In Figure 5-3 and Figure 5-4, the RMS trends of each sensor are shown without any signal filtering applied. The first 180 samples represent the RMS values in the normal state, where no fault is present. The next 180 samples represent the RMS values when a fault is present on the four axes. This allows for a comparison of the RMS values between the normal and fault states, and can help in detecting the presence of a fault. As shown figures, the RMS values of each sensor are highly variable and dependent on the operating speed. This is because the operating speed affects the vibration frequency and amplitude of the machine components, and these changes are reflected in the RMS value. Therefore, it is difficult to set a single threshold value for all sensors without considering the operating condition. To address this issue, the author apply a method to set the threshold value based on the statistical characteristics of each sensor's RMS values considering the operating condition. Therefore, the threshold values set by this method are shown for each sensor. Threshold values are different for each sensor and are set based on the statistical properties of the RMS values for that sensor. By setting individual threshold values for each sensor, the proposed method can better detect abnormal behavior of each sensor, and reduce false alarms caused by the fluctuations in RMS values due to changes in operating speed.

Actually, the fault location is 4 axis, and accordingly, only sensor 4 should have a part where the RMS-threshold value exceeds 0. However, when the above method is applied, it can be seen that the RMS exceeds the threshold not only sensor #4 but also sensor #5. Based on the information provided, it is possible that the fault on the 4^{th} axis is causing vibrations that are also affecting sensor #5, even though it is not directly located on the faulty axis. It is not uncommon for faults or failures to affect multiple components or sensors in a system due to their interconnectedness and shared operational environment. Therefore, it is important to consider the possibility of such cross-component effects when analyzing the data from a system with

multiple components.

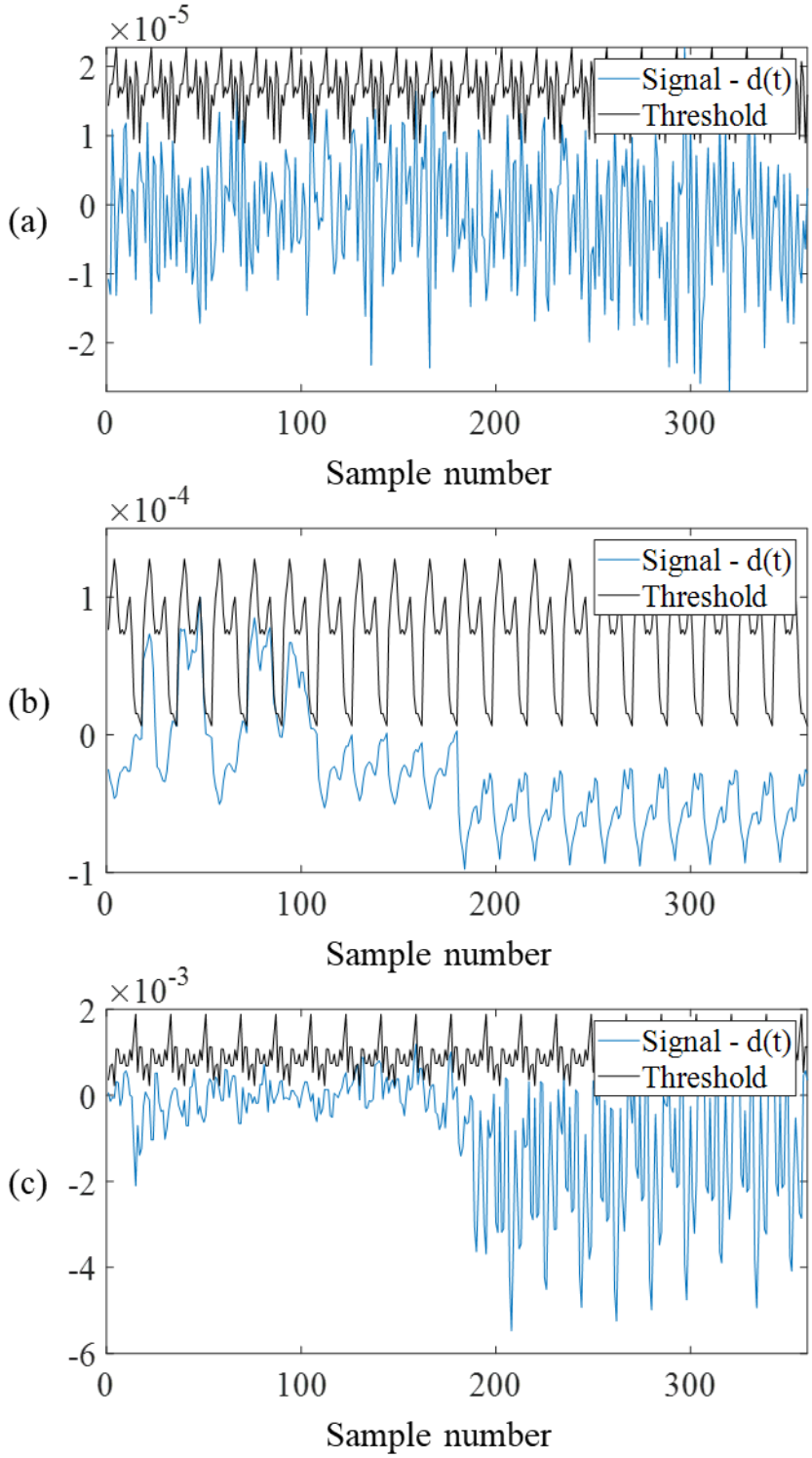

Figure 5-3 Signal trends of non-deterministic signal and corresponding threshold; (a) Sensor #1, (b) Sensor #2, (c) Sensor #3.

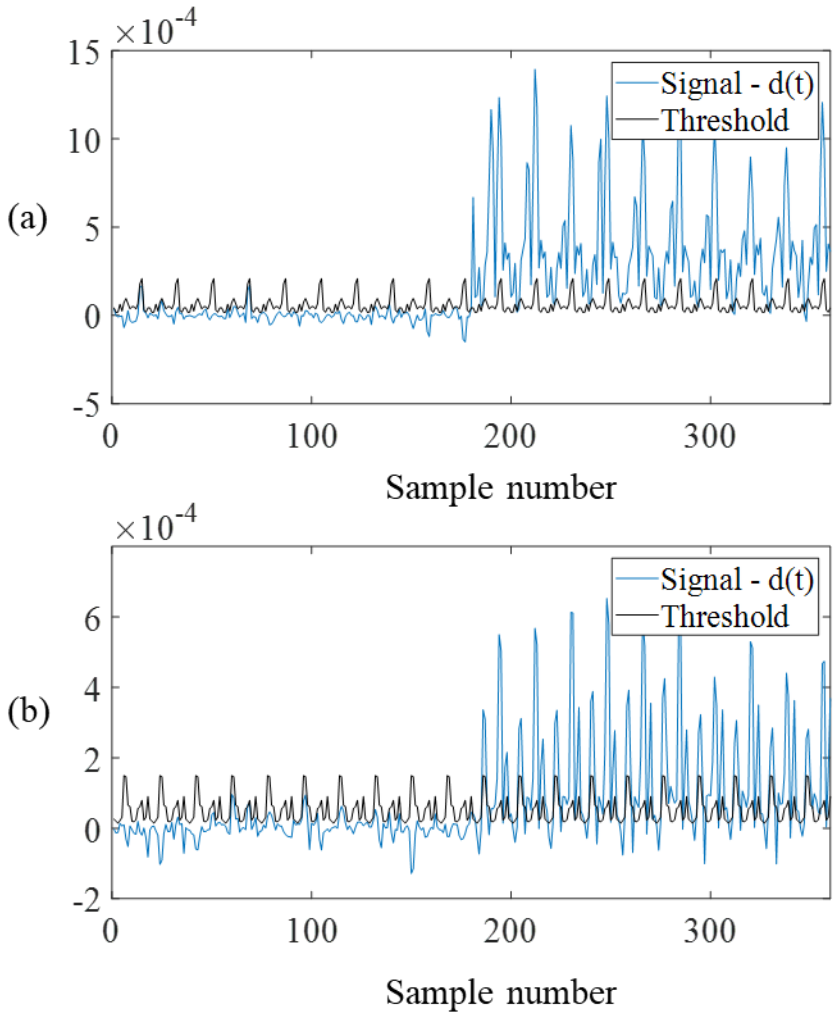

Figure 5-4 Signal trends of non-deterministic signal and corresponding threshold; (a) Sensor #4, (b) Sensor #5.

When dealing with robots, it can be challenging to model the changes in the energy aspect of the vibration signal as it travels from the CFL to the sensor. Accurate modeling would require vibration modeling based on computer-aided engineering (CAE) modeling or n-DoF problem, but it is the beyond of this research. Since this study does not cover such modeling, a different approach was adopted from referencing the published literature [90]. The equation (3.13) results in the ratio of the energy profile transferred from the location of the fault to the two different sensors. Therefore, it is possible to interpret the energy when a specific signal is generated as the rate at which the sensor is transmitted. Assuming that a specific

joint has a fault, we will apply the mean value of the equation (3.13) based on the ratio of frequency energy delivered to the sensors attached to the joints by a single movement at that joint. The graphical illustration for these steps are given in Figure 5-5 for better understanding.

To apply the proposed method for the robot system, it needs to apply the equation (3.13) in following way:

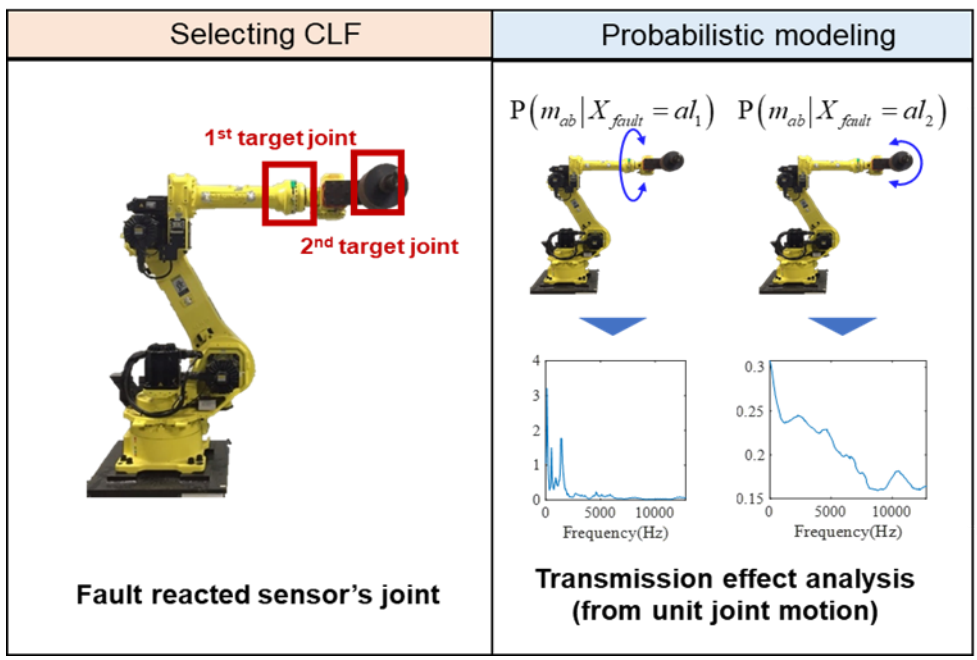

Figure 5-5 Graphical illustration for preliminary work of robot system.

$$\ln(m_{ab}|\mathrm{CFL}=a) \sim N\left(\ln\left(\frac{\mathrm{RMS}(s_a|u_a)}{\mathrm{RMS}(s_b|u_a)}\right), {\delta_{r,a}}^2+{\delta_{r,b}}^2+{\delta_k}^2\right) \quad (5.1)$$

where CFL= a means the assumed(candidate) fault location is 'a', RMS($s_i|u_j$) is RMS from the signal measured at sensor i under the unit axis motion only in the axis j.

As shown in Figure 3-2, the CFL was defined for the joint axis where the RMS of the attached vibration sensor exceeded the threshold. Therefore, based on the trend shown in Figure 5-4, the joints corresponding to sensors #4 and #5 were selected as CFLs. Firstly, the vibrations are measured from each target joint's sensor and Fourier transform is applied. Figure 5-7 presents the results of vibration analysis for the 2nd CFL joint unit motion using Sensor 4 (upper) and Sensor 5 (lower) in the time domain (a) and frequency domain (b). Similarly, Figure 5-8 shows the vibration analysis results for the same unit using Sensor 4 (upper) and Sensor 5 (lower) in the time domain (a) and frequency domain (b). In the time domain signal, the vibration data was collected for a duration of 0.4 seconds under constant velocity conditions for each condition. The frequency domain signal was obtained by taking the average of Fourier transform results obtained from 20 repetitions of this joint motion unit. The transmission function estimated from each spectral analysis result is presented in Figure 5-6. To account for the frequency sliding effect during the transmission process, the spectral energy ratio is calculated using the moving mean with a window size of 10Hz applied to the FFT result. Based on equation (3.22), the results can be summarized as follows: If the fault is located at the 1st target joint, the energy ratio calculated by the root mean square (RMS) value of sensor 5 divided by that of sensor 4 is 0.1135. On the other hand, if the fault is located at the 2nd target joint, the energy ratio calculated by the RMS value of sensor 4 divided by that of sensor 5 is 0.1155.

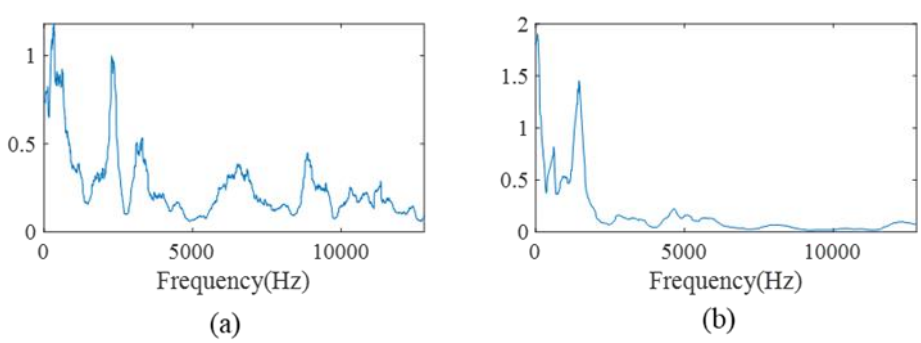

Figure 5-6 Estimated transmission function; (a) 1st target unit joint motion based, (b) 2nd target unit joint motion based.

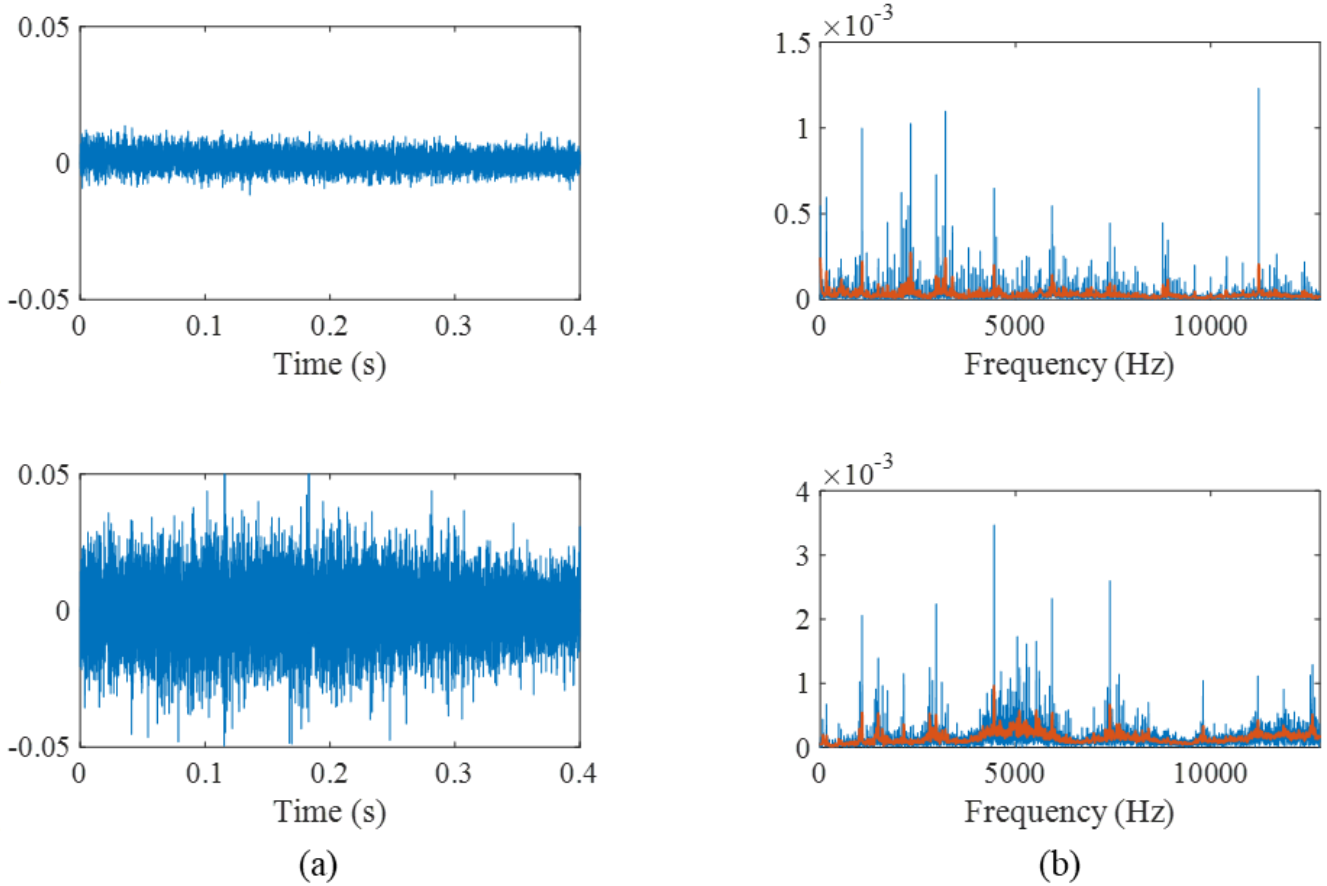

Figure 5-7 Vibration analysis result of Sensor 4 (upper) and Sensor 5 (lower) under 2nd CFL joint unit motion; (a) time domain, (b) Frequency domain.

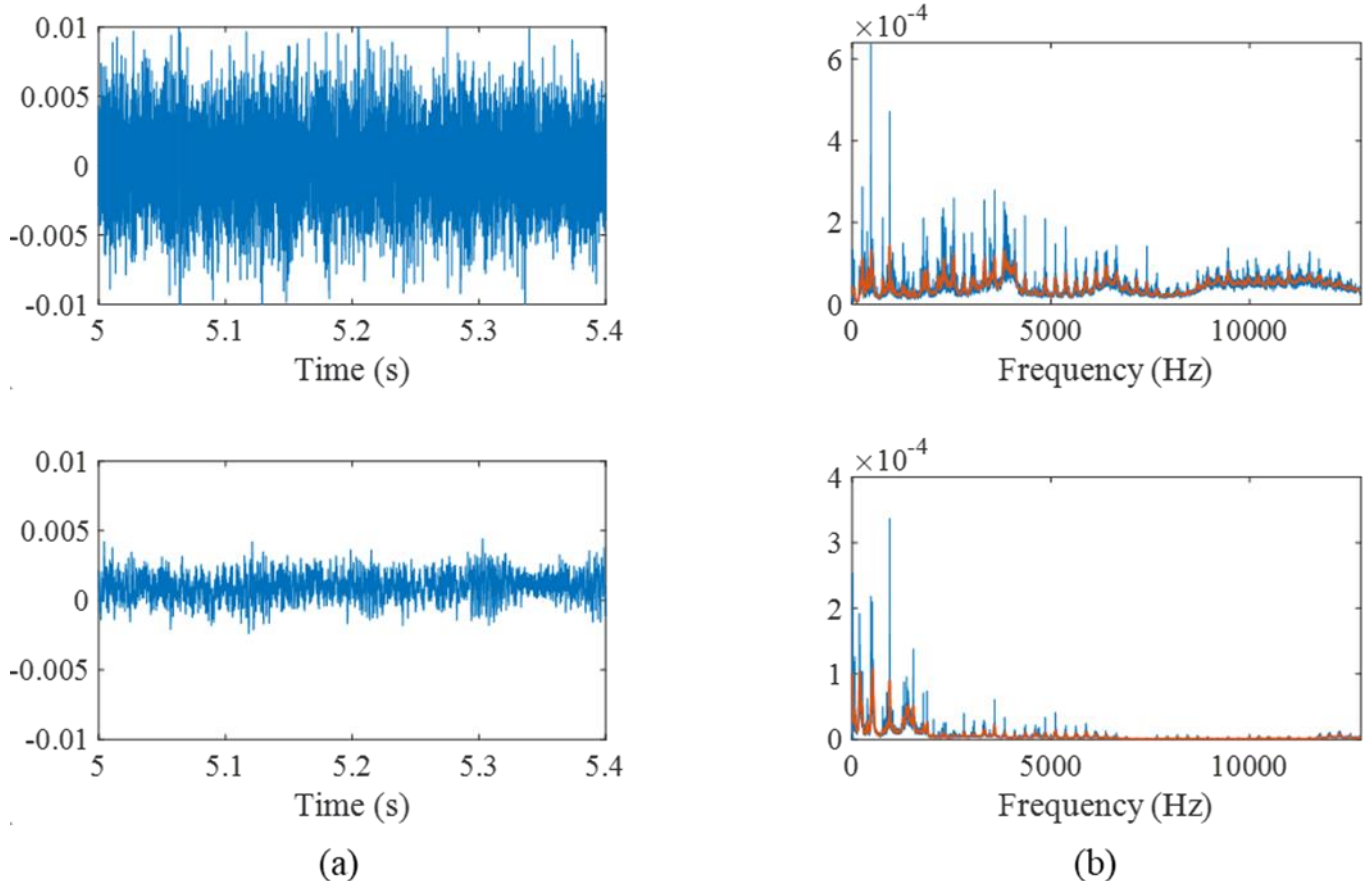

Figure 5-8 Vibration analysis result of Sensor 4 (upper) and Sensor 5 (lower) under 1st CFL joint unit motion; (a) time domain, (b) Frequency domain.

5.2 Applying LSR based method (PERL) for robot system

The probability calculation process requires a sufficient level of observed failure energy to exceed a certain threshold. Therefore, in Figure 5-4, the calculation was performed only for the area where the value of 'signal-$d(t)$' exceeded the threshold in both Sensor #4 and Sensor #5. Figure 5-9 presents the trend of fault energy ratio, the mean energy ratio estimated from the transmission function obtained in Figure 5-6, and the standard deviation estimated from the equation (3.11). The black curve line denotes the boundary of the estimated mean ± 2 × estimated standard deviation for both conditions where the CFL is at the 1st and 2nd target joint. As observed from the figure, the measured fault energy ratio does not exceed this boundary for both conditions, indicating that the proposed model's calculated probability value cannot determine the location of fault with a 95% confidence level. Based on the estimated mean values, it appears that the measured fault energy ratio is relatively closer when the CFL is the 1st target joint. Thus, by examining the main parameters of the probability model and the energy ratio trend before implementing the proposed method, it is possible to make a decision that the 1st target joint is likely to be the actual location of fault.

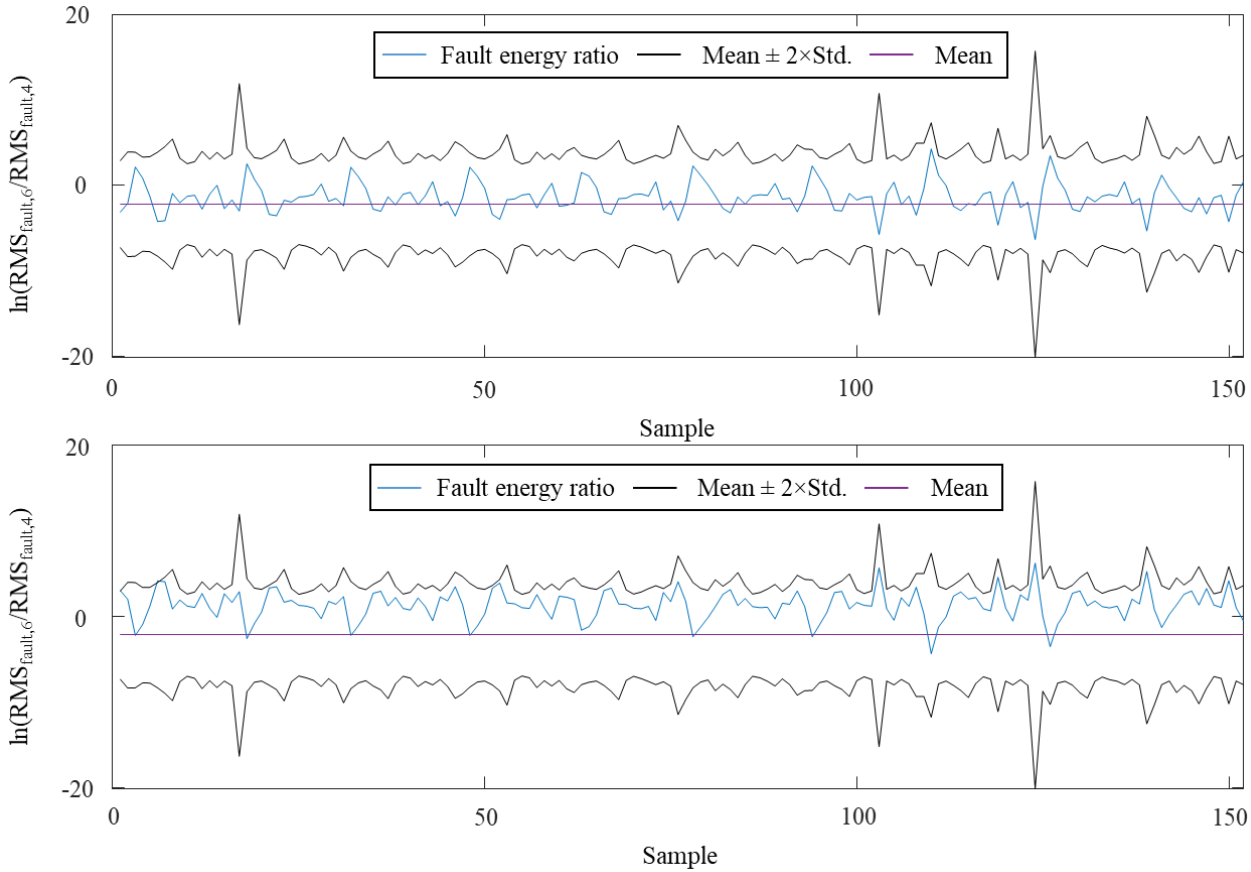

Figure 5-9 Fault energy ratio between sensors & estimated mean energy ratio with estimated standard deviation; upper (when the CFL is 1st target joint), lower (when the CFL is 2nd target joint).

In the previous steps, the results were generated assuming $\delta_k = 0$, which means that the energy of the fault is distributed equally in the frequency domain. However, this assumption may lead to overestimation of the estimated probability for one of the fault probabilities. To investigate this, parametric studies were performed, as shown in Figure 5-10. The results showed that a high δ_k value leads to a reduction in the difference between the fault probabilities calculated in the CFL. Since δ_k represents the uncertainty of the measured energy, a higher δ_k value indicates lower reliability of the measured result due to larger uncertainty, which results in similar fault probabilities in each CFL.

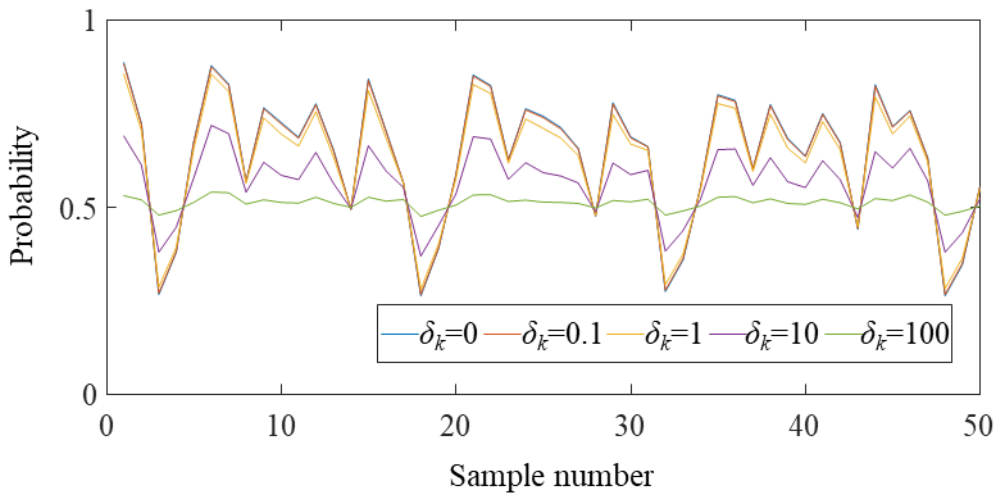

Figure 5-10 Parametric study for the proposed method; the effect of δ_k for the fault probability on 1st target joint.

Similar to the Section 3.3.3, the fault probability on each CFL for time sequential updating can be applied using the time sequential data. Figure 5-11 shows the result calculated from the equation (3.16). As observed in the figure, the fault probability on the 1st target joint increases over time, while it means that the fault probability on the 2nd target joint decreases over time. This is a desirable result as the actual fault location is the first target joint. Additionally, the convergence of fault probability to 1 over time observed in the figure indicates the effectiveness of the time sequential updating method in accurately identifying the fault location. The

figure also shows the effect of δ_k on the fault probability. As δ_k increases, the fault probabilities calculated for each CFL on each time become slower to the desired result, indicating a reduction in the speed of convergence, which means the fault probability converges to 1, for the fault location determination. Therefore, it is important to keep δ_k as low as possible to ensure fast fault detection and location estimation.

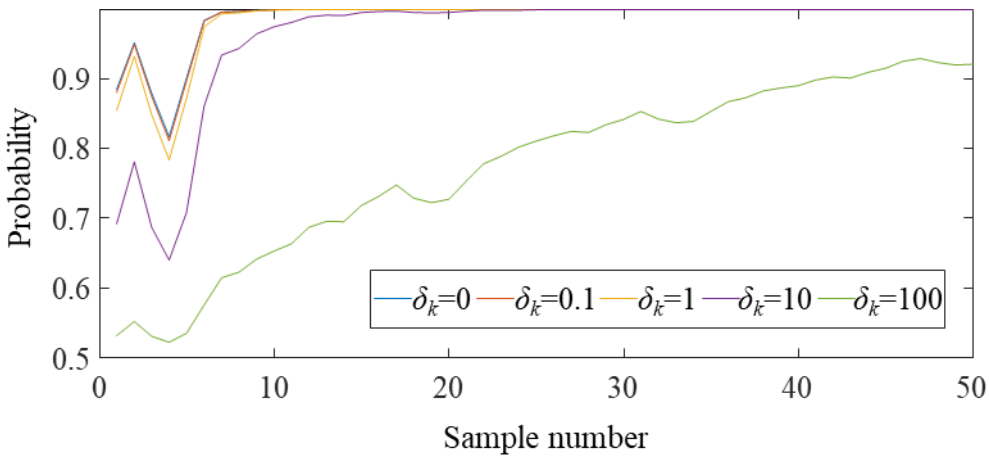

Figure 5-11 Parametric study for the proposed method; the effect of δ_k for the fault probability on 1st target joint using time sequential updating method.

Figure 5-13 displays the outcome of applying FFT-based spectral analysis to three representative datasets obtained at different times as shown in Figure 5-12. In Figure 5-12, the blue color plot is related with the 4th sensor attached at the 1st target joint, and the orange color plot is related with the 5th sensor attached at the 2nd target joint. These three datasets consist of: 1) when the fault probability is higher in the 1st target joint, 2) when the fault probability is the same between the 1st target joint and the 2nd target joint, and 3) when the fault probability is higher in the 2nd target joint. The process of extracting the energy of the fault data in the frequency domain involves several steps. First, the average value of the spectrum is calculated based on the normal state data acquired in the same operating state as each point. Then, this average value is subtracted from the spectrum of each point. Finally, only the

values that exceed 0 are plotted to extract the energy of the fault data in the frequency domain. This process helps to filter out any noise or background signals and focus only on the relevant information related to the fault.

Figure 5-13 (a) indicates that the energy of the fault spectrum in the 4th sensor, attached to the 1st target joint, is notably high across most of the frequency range. This suggests that the measured fault energy in the 5th sensor is transmitted through the link between the 1st and 2nd target joint via the original vibration generated by the fault state of the 1st target joint. Therefore, from the proposed method, the fault probability of 1st target joint is higher than that of 2nd target joint, which is clearly illustrated from that the first. Figure 5-13 (b) shows that the energy of the fault spectrum in the 5th sensor, attached to the 2nd target joint, nearly does not exist in all the frequency region. In order to apply the proposed method, the fault energy must be sufficiently observed for two or more sensors, which can be seen as a violation of this assumption. Therefore, the energy ratio is much higher than the expected energy ratios calculated from both conditions, which means the fault probabilities of each joint are nearly 0. In Figure 5-13, the two probabilities at the 2nd point are almost equal to 0.5 for both probability, indicating that they have little effect even when updated time-sequentially. Although this result is not ideal, as the fault probability of the 1st target joint is not determined to be larger than that of the 2nd target joint, it can still be considered a positive outcome, since it demonstrates that the result cannot be probabilistically determined due to the presence of uncertainty in the measured fault energy ratio. Figure 5-13 (c) displays that the energy of the fault spectrum in the 5th sensor, attached to the 2nd target joint, is notably high in the 10 – 12 kHz frequency range. Therefore, considering the results of the frequency analysis, it can be considered that the fault of the 1st target joint generated high-frequency failure-related vibration in the 2nd target joint. Additionally, from the vibration transmission through the link between the 1st and 2nd target joint, the measured fault energy from

sensor #4 exists. Also, the data of the 2nd point corresponds to the 9 second point on the operating condition shown in Figure 5-2, and at this time, it can be confirmed that the angular speed of the 2nd target joint (6th joint) appears very larger compared with the other joint. Based on these facts, it can be concluded that the result obtained through the proposed method is not ideal, but it is reasonable to say that the source of the fault energy is the 2nd target joint.

Based on these findings as shown in Figure 5-12 and Figure 5-13, it can be confirmed that data which exhibits a high probability of fault at a confirmed fault location contains more information when analyzing fault-related information in a high-sampling region. In other words, when the fault location is already known, the data that demonstrates a higher probability of fault provides richer details and insights for further analysis in the high-sampling analysis.

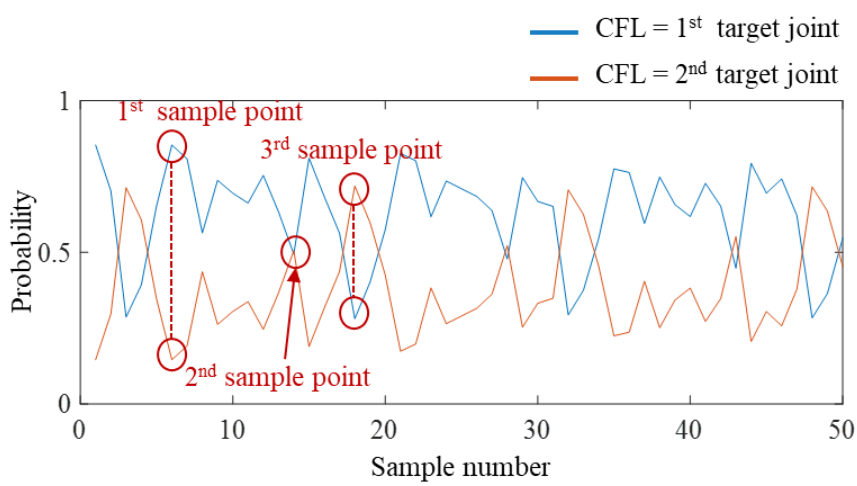

Figure 5-12 The location of sample point for spectral analysis given in Figure 5-13 with fault probability plot under δ_k=1.

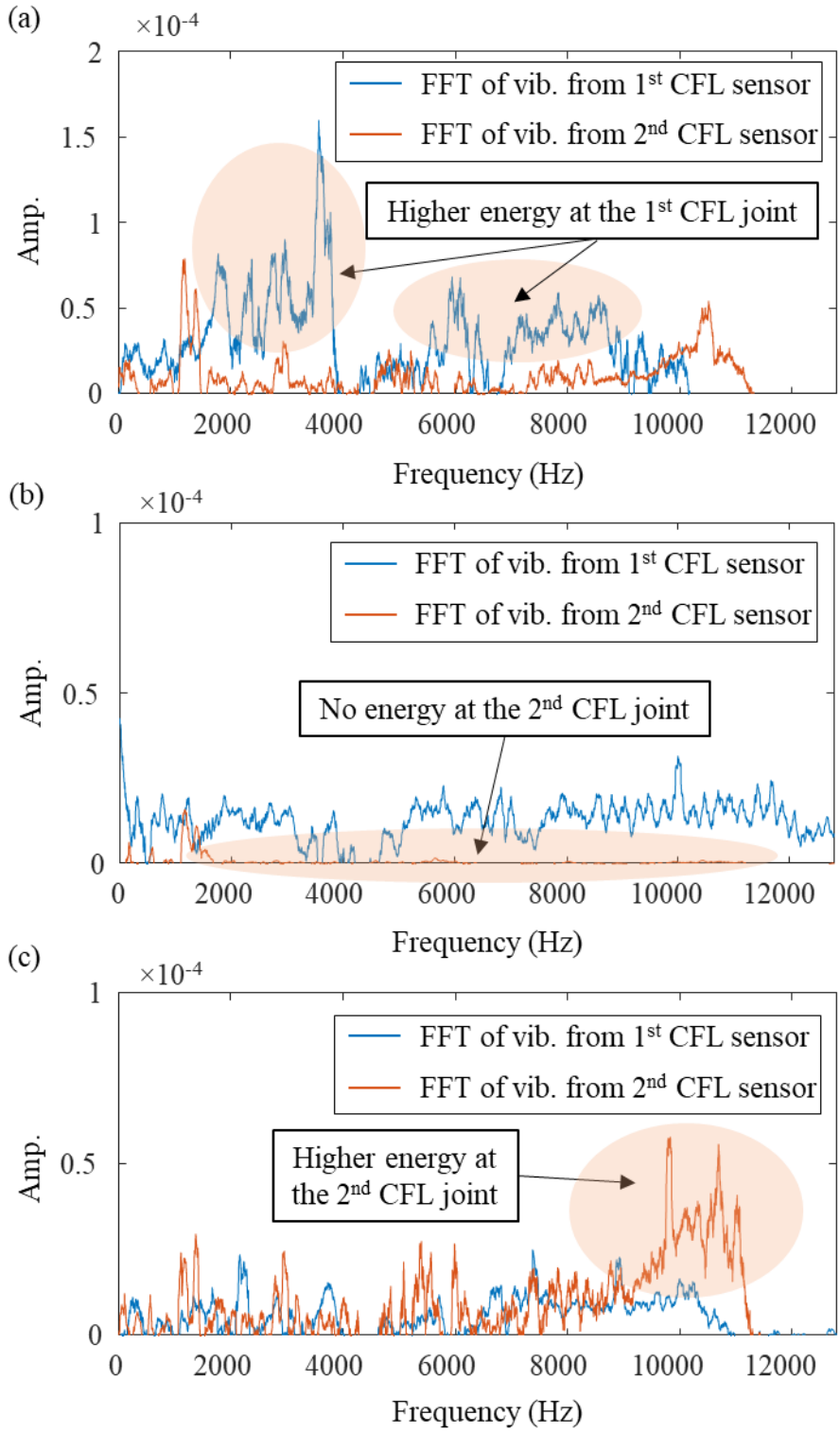

Figure 5-13 Spectral analysis on each sample data; (a) 1st sample point, (b) 2nd sample point, (c) 3rd sample point.

In order to verify the transmission effect assumed in Section 5.1, the frequency response function is applied to the fault signal. Specifically, for the data point with the highest probability shown in Figure 5-12 (Sample number = 1), the frequency energy distribution of the fault signal obtained from the 1st target joint is calculated. Then, by multiplying this distribution with the derived transmission function shown in Figure 5-6, the estimated frequency energy distribution of the fault signal at the 2nd target joint is obtained. As depicted in the Figure 5-14, the estimated distribution and the actually measured distribution exhibit a high degree of similarity. This observation indicates that the assumption that fault energy is transmitted through the estimated frequency response function is valid. Therefore, the results of this analysis support the notion that the transmission effect, as characterized by the frequency response function, plays a significant role in the transmission of fault energy within the robot system. This finding further validates the assumptions made in Section 5.1 regarding the transmission of fault energy.

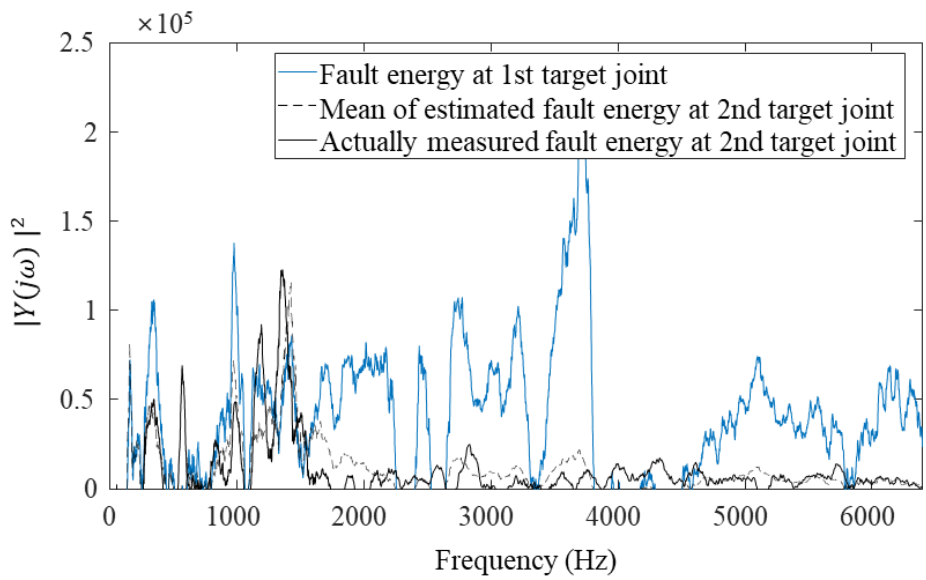

Figure 5-14 Validation of transmission effect assumption on the fault signal of robot system.

5.3 Applying HSR based method (FASER) for robot system

The target component is a cycloidal gearbox in the 4th joint of the industrial robot as same with Section 5.2. The specifications of the cycloidal gearbox used for the research in this section are shown in Table 5-1. The imposed variable-speed condition was from an arc welding motion, as shown in Figure 5-15. The operating condition is almost 20 seconds in each period, and varies from -4.183 to 4.144 (rad/s). This operating condition is calculated from the motor speed, which is automatically recorded. The recovery time exists between the end point of previous operation and starting point of next operation. Therefore, synchronizing the signal from the known period of operation or recorded operating information, which is calculated from the motor, is impossible.

Table 5-1 Specifications of the experimental cycloidal gearbox.

Parameter	Value
Number of input gear teeth	28
Number of spur gear teeth	23
Number of pins	40

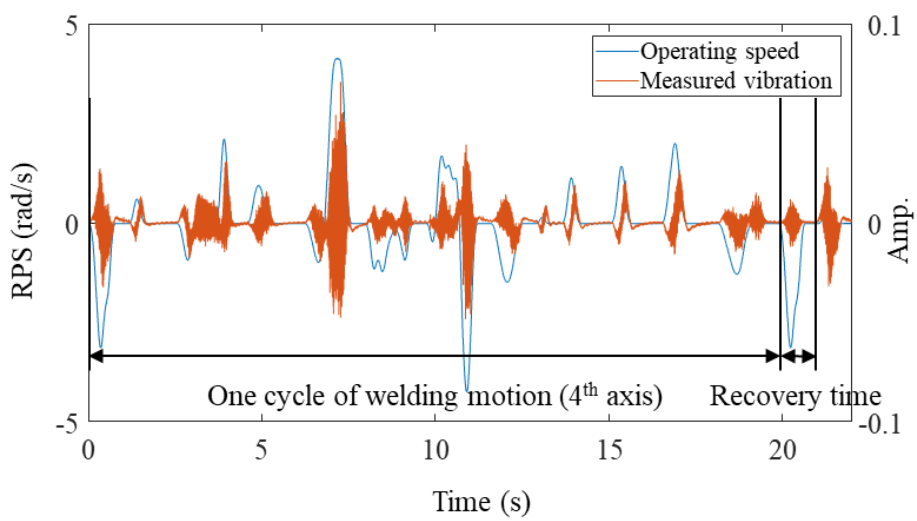

Figure 5-15 The operating speed profile used of 4th joint under the arc welding motion.

Figure 5-16 shows the vibration signals and the corresponding STFT results under a normal condition and fault condition. The parameters for the spectrogram are selected as follows: The window function is a Hanning function with length 1024, the overlap ratio is 0.5 (512 samples), and the length of the FFT is 4096. For both conditions, amplitudes of vibration are modulated with operating speed, as shown in Figure 5-16 (a). More interestingly, in the time domain, the fault signal has more peaks and some of the signal (e.g., at 12 and 19 seconds) shows a larger amplitude than the normal signal. Further, even when the operating speed is zero, the fault signal has more energy, as compared with the normal signal. However, the total energy of each of the signals, the RMS, is similar, as is shown later, because the differences between the normal signal and the fault signal occur locally, not globally in the period.

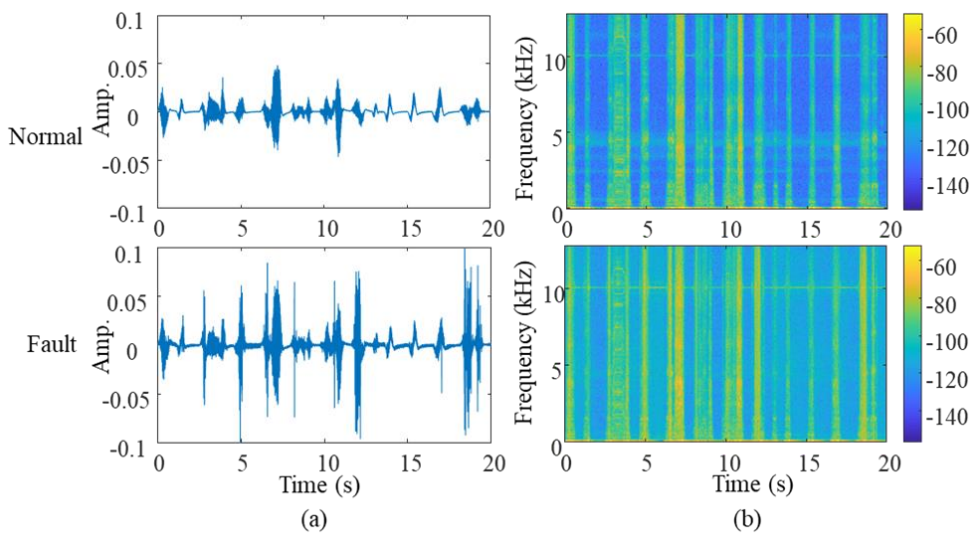

Figure 5-16 Vibration signals of one period in the time domain and in the STFT domain for (a) normal condition, (b) fault condition.

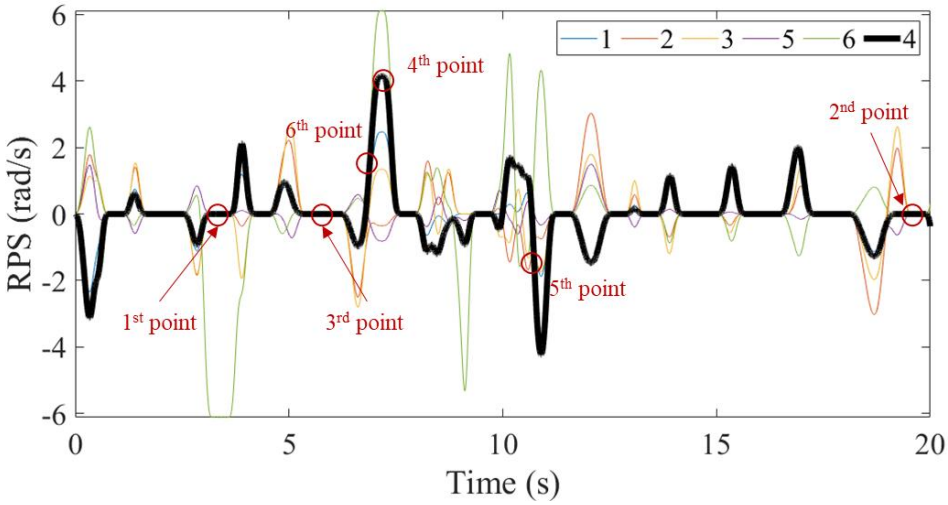

Figure 5-17 Speed condition of sample points for Figure 5-18 to 5-23.

Figure 5-18 to Figure 5-23 demonstrate the process of constructing a probability model using KLD for signals measured under different operating conditions and the corresponding spectrum results. Figure 5-17 shows the speed and acceleration conditions at each point corresponding to Figure 5-18 to Figure 5-23. The operating speeds and accelerations at each point are as follows: (0, 0), (0, 0), (7.13, 0), (-3.11, 0), (-2.00,-2.90) and (1.89, 2.30). The first two points were set to compare the effects of the other components. The process of finding a probability model built for signals with different operating environments through KLD and the results through the spectrum are presented in Figure 5-18 (a) to Figure 5-23 (a). The results indicate that the proposed KLD method finds a model with a uniquely small minimum number of models, which is the optimum model's number, compared to other model numbers. Interestingly, in several models, a local minimum that is not the optimum model number appears because each corresponding model does not have a significant difference in frequency energy distribution. This indirectly indicates that there is no significant difference in terms of operating conditions of the corresponding models. Secondly, the proposed model matching process can identify whether the signal in a faulty state causes a significant change in the frequency energy distribution due to

the fault. The vibration signal obtained from the robot in this case study is different from the one discussed in Section 4.3 in the view of energy distribution in frequency domain. In the robot's vibration signal, the energy from low frequency band motion is much greater than the energy from the high frequency component affected by the fault. Therefore, even though there are slight differences in the high frequency region from the fault effect, they do not have a significant impact on the results. It is also confirmed that the optimum (selected) model numbers for same operating condition with different state are similar to each other. Additionally, Figure 5-18, Figure 5-19 (upper), Figure 5-21, and Figure 5-22 (upper) demonstrate that even when the target component does not have its own vibration, the measured transmitted signal from other components can cause the signal to cluster, resulting in homogeneity in the labeled vibration data. This indicates that it is possible to perform probabilistic modeling in the posterior step.

In short, the proposed method showed good results even under the largest velocity or acceleration. Therefore, it is predicted that the results will also be satisfactory for regions where the velocity or acceleration is within at its minimum to maximum value.

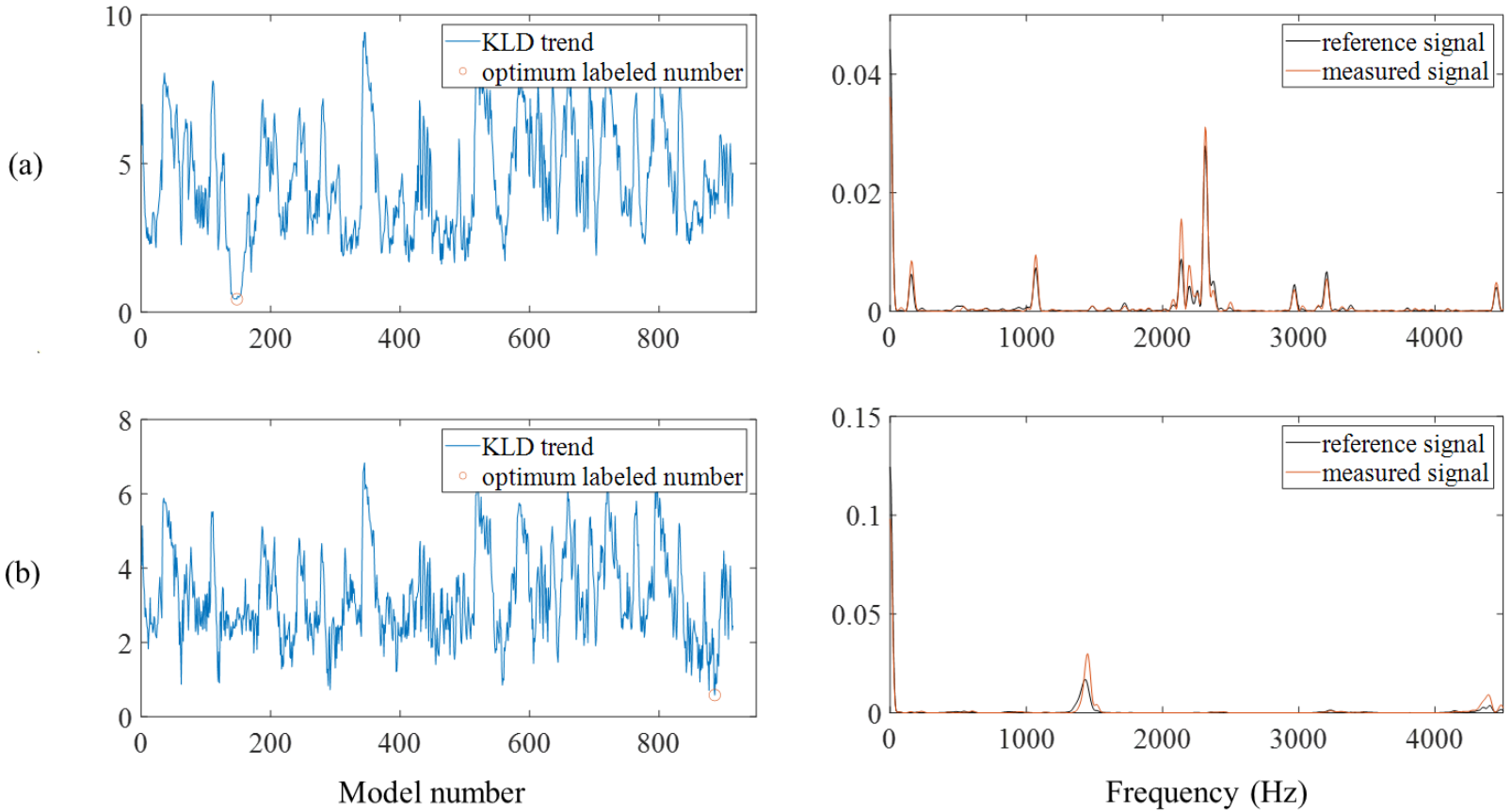

Figure 5-18 KLD based similar operating condition model matching for the normal signal (left) and comparison of spectrum (right); (a) 1st point (b) 2nd point.

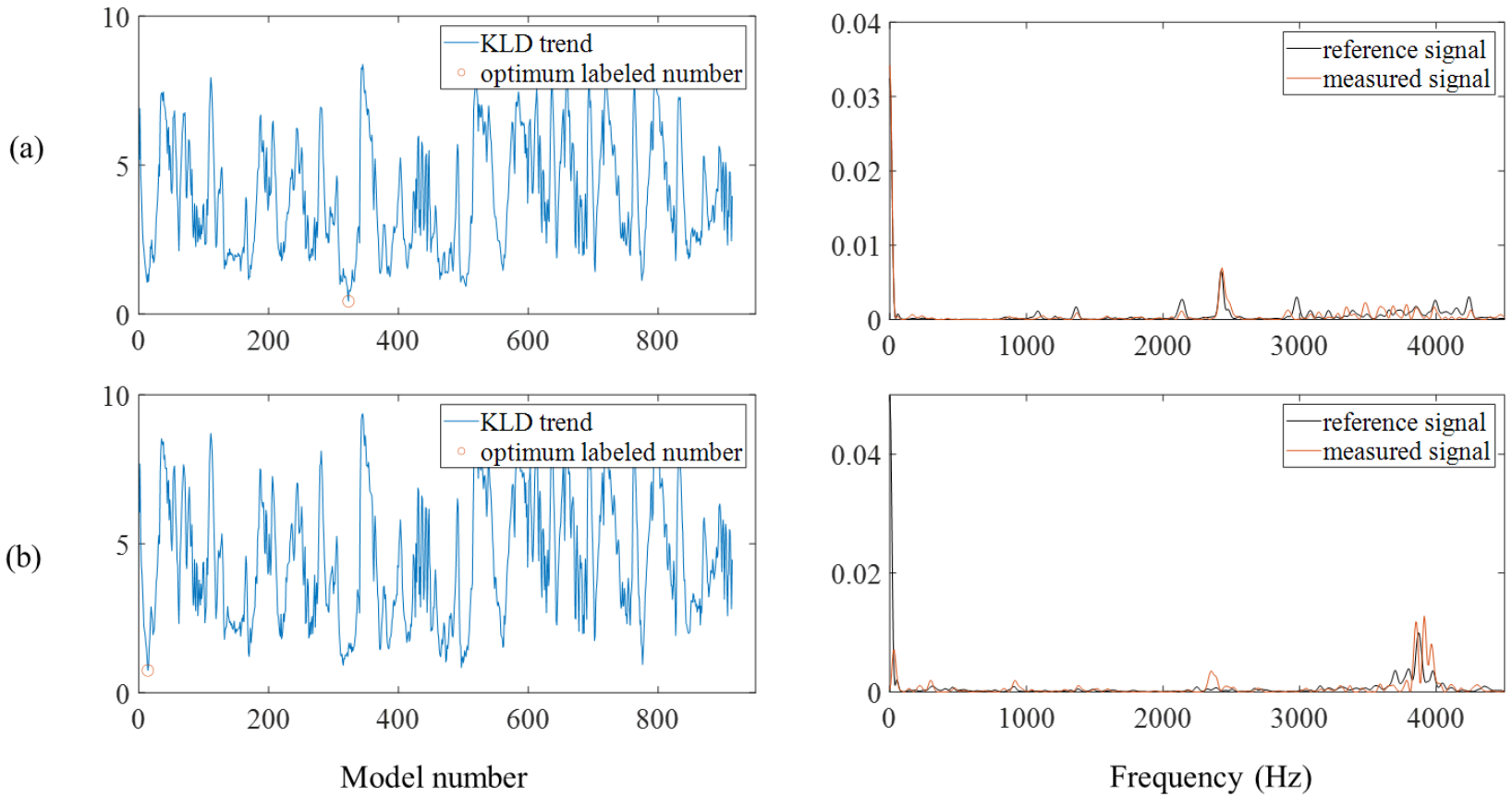

Figure 5-19 KLD based similar operating condition model matching for the normal signal (left) and comparison of spectrum (right); (a) 3rd point (b) 4th point.

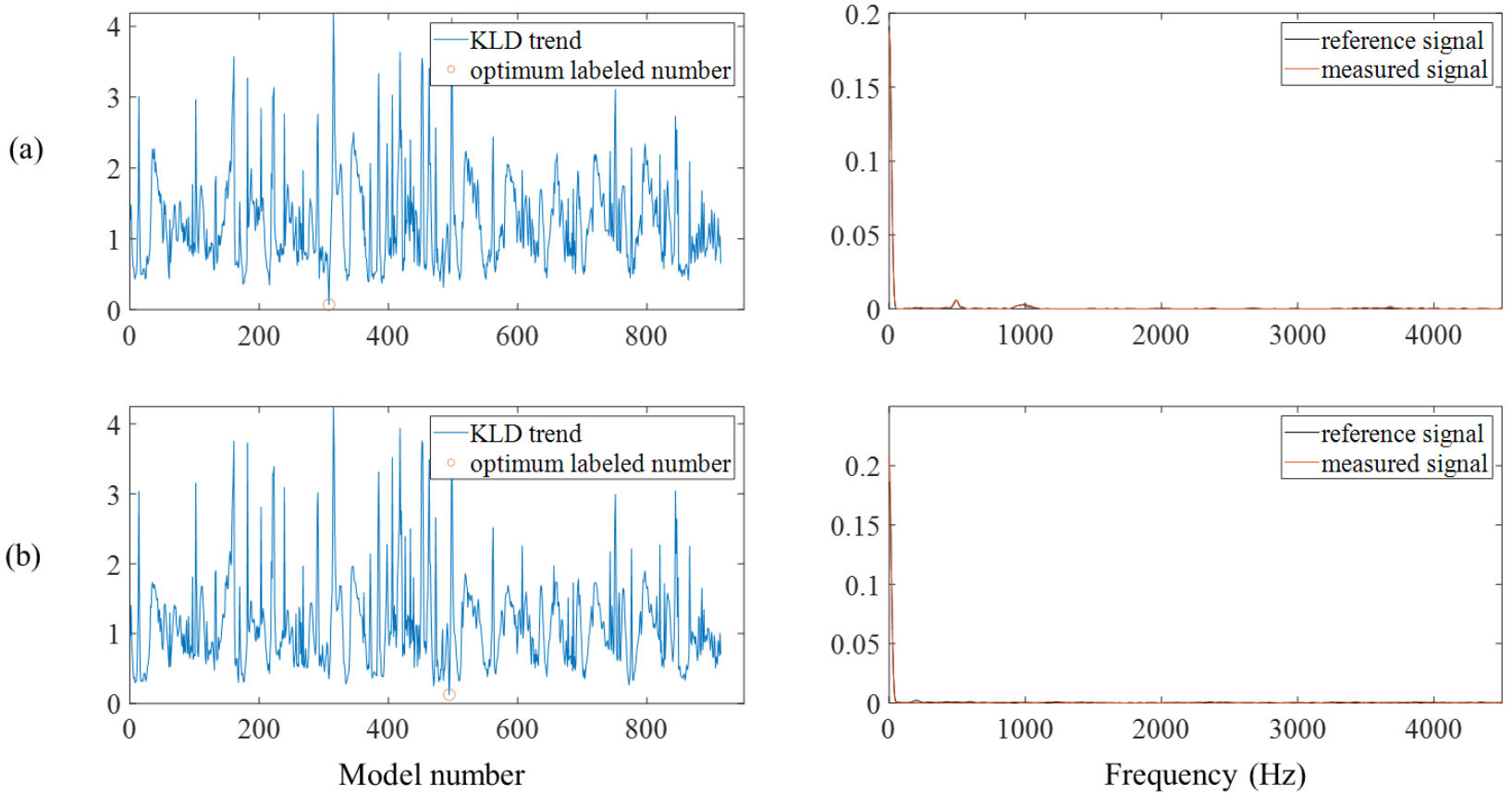

Figure 5-20 KLD based similar operating condition model matching for the normal signal (left) and comparison of spectrum (right); (a) 5th point (b) 6th point.

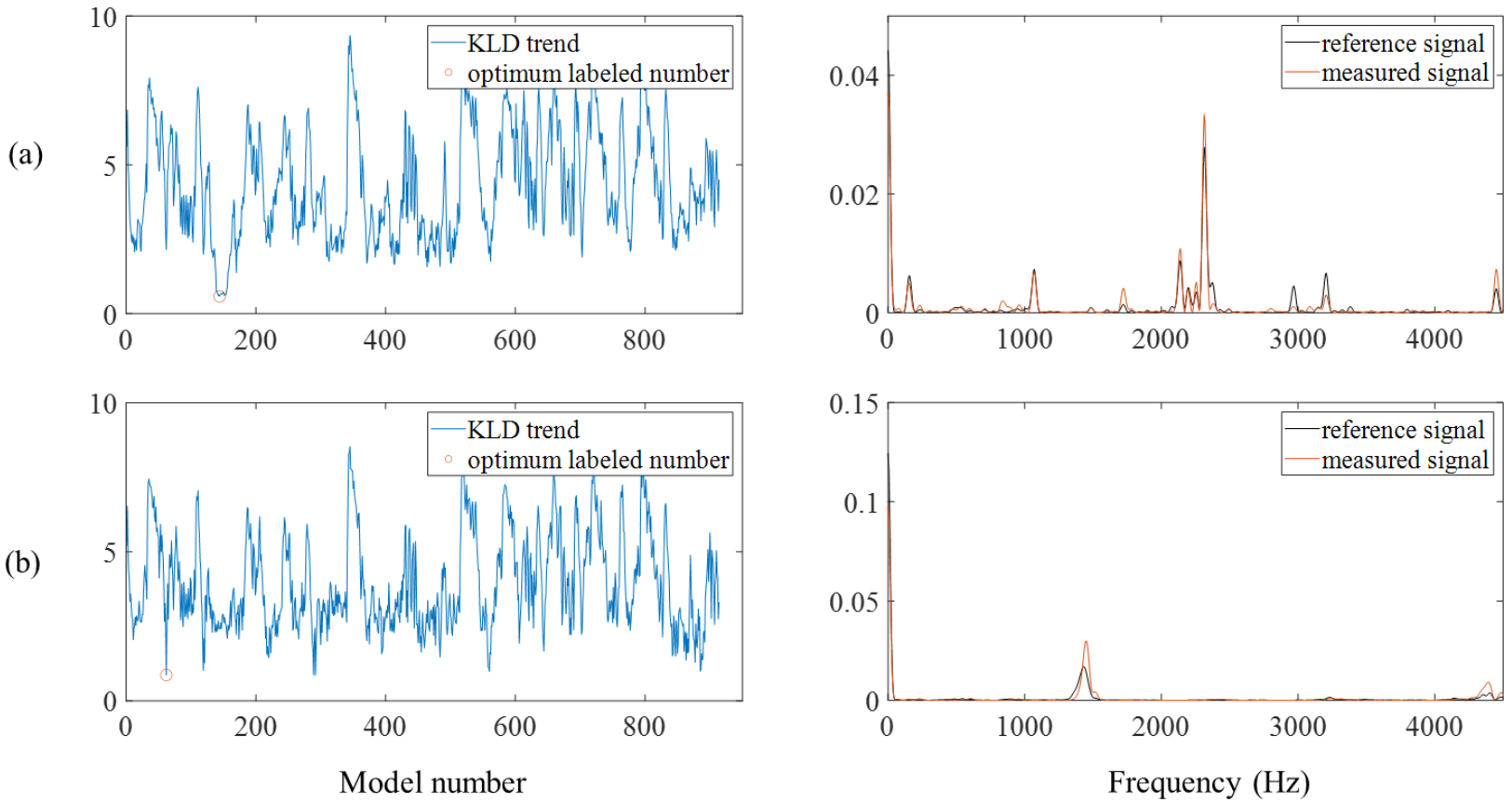

Figure 5-21 KLD based similar operating condition model matching for the fault signal (left) and comparison of spectrum (right); (a) 1st point (b) 2nd point.

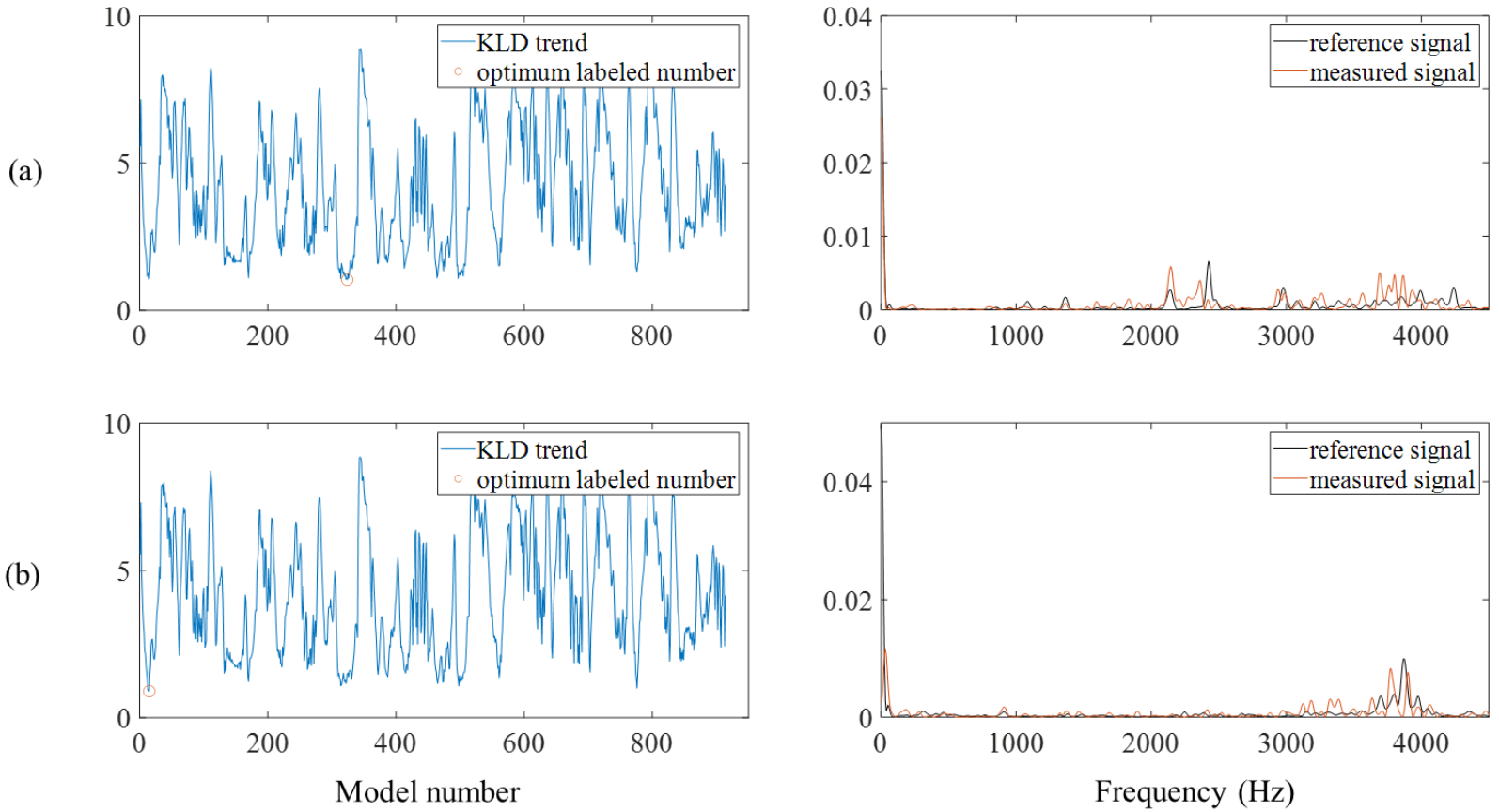

Figure 5-22 KLD based similar operating condition model matching for the fault signal (left) and comparison of spectrum (right); (a) 3rd point (b) 4th point.

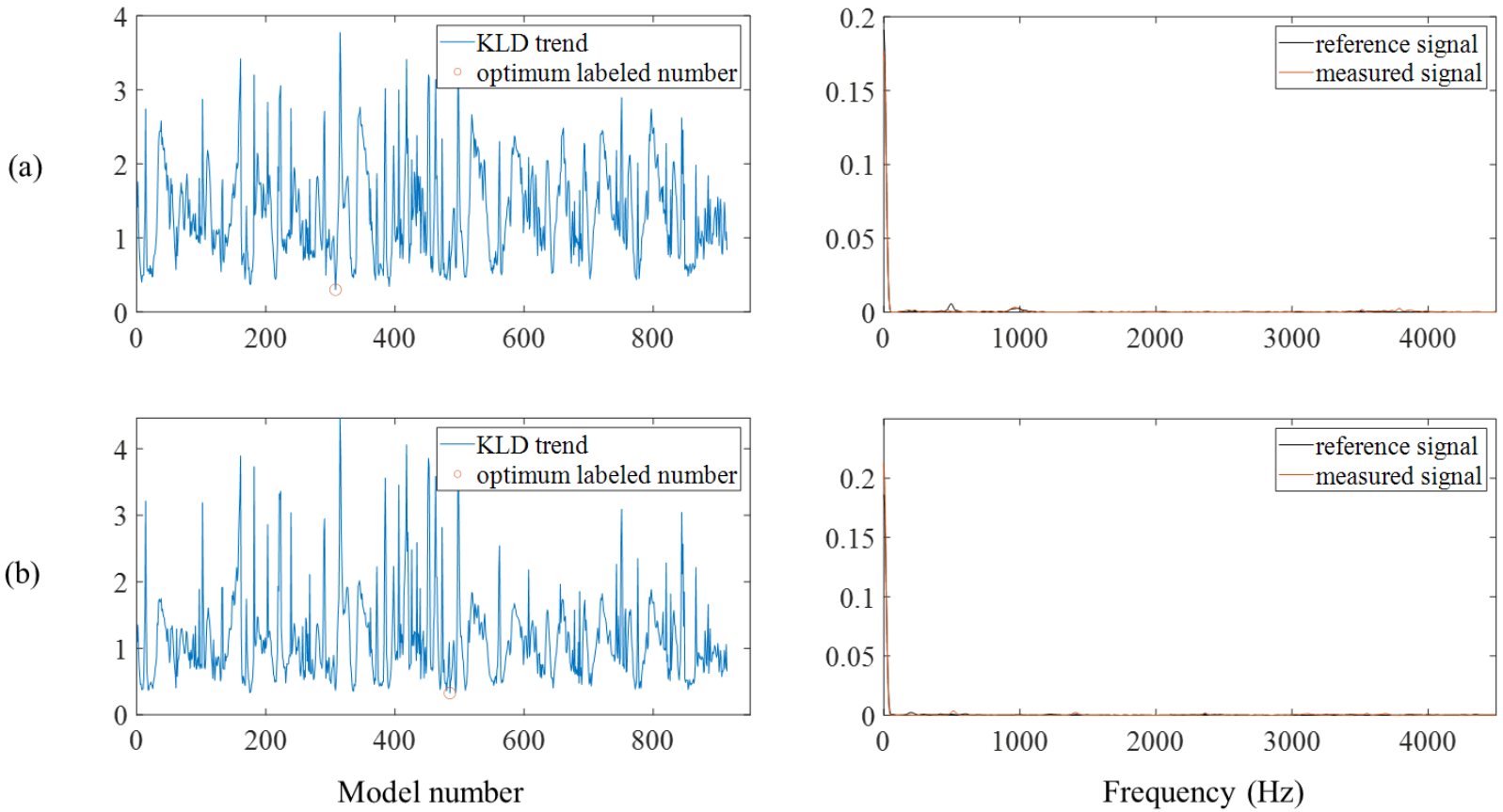

Figure 5-23 KLD based similar operating condition model matching for the fault signal (left) and comparison of spectrum (right); (a) 5th point (b) 6th point.

Figure 5-24 displays the modeling type of each time-frequency index for one period of the vibration signal shown in Figure 5-15, obtained using the probabilistic energy modeling proposed in Section 4.2.1. In this case, the accelerometer sensor is mounted on the casing of the RV gearbox, so the time-frequency indices corresponding to the GMF and its harmonic of the 4th joint gearbox should include the deterministic signals. As shown in Figure 5-24 (b), the modeling region of "deterministic signal + noise" can be considered as the GMF and its harmonic. With the exception of the region from time = 3 to 4 (s), most of the time-frequency indices with non-zero speed region have been modeled as "deterministic signal + noise". Since the acceleration of the target component is too fast and the non-zero velocity region is very short for each section, the pattern of the GMF component could not be observed clearly with the STFT parameter, but it was mostly considered as a deterministic signal at the point where the velocity was not zero. Thus, it can be concluded that the result was produced by the GMF component. Interestingly, the reason why it is regarded as 'noise + deterministic' in the 3 to 4 second region, which is actually 0 speed condition, can be regarded as the fact that the vibration induced by the motion of the 6th joint is transmitted to the 4th joint's sensor, as shown in Figure 5-2. Additionally, it is observed that the signal of a component around 10 kHz is classified as 'deterministic + noise signal'. This is due to the resonance frequency of the target component, which is around 10 kHz. This is supported by two observations: 1) 10 kHz is acquired in most areas regardless of speed, and 2) frequency modulation around the 10 kHz is only observed in a non-zero speed area. Hence, it can be concluded that the finding suggesting the component around 10 kHz being a deterministic signal is reasonable.

In addition to the previously discussed deterministic and noise components, Figure 5-24 (c) also shows the presence of a wideband noise component around 5 kHz. However, the size of this noise component is not constant, and its energy is

influenced by the signals from other components. As a result, the energy probability distribution modeling has been performed using KDE modeling. As for the remaining vertically existing indices and components below 1 kHz, as mentioned earlier, the speed changes too quickly, resulting in various GMF harmonic components overlapping in the low frequency band. Therefore, it is difficult to categorize them into either deterministic or noise components, and their energy probability distribution cannot be explained using the two types of modeling discussed earlier in Section 4.2.1.

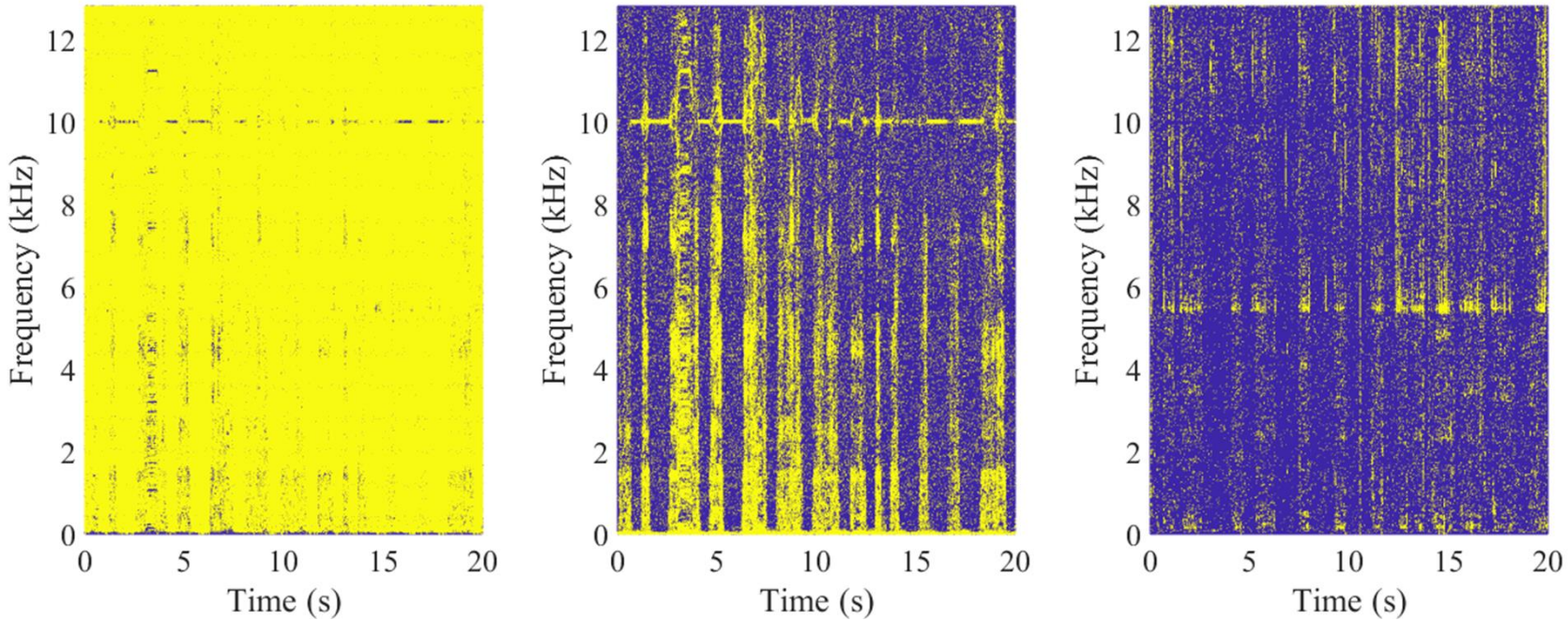

Figure 5-24 Type of the probabilistic energy modeling; (a) Noise dominant signal's indices, (b) Noise + deterministic signal's indices, (c) Neither of two types signal's indices.

Next, the parametric dependency analysis for margin value k_p, which is utilized to determine the fault-affected indices, are performed. As shown in Figure 5-25 and Figure 5-26 (a)-(c), the boundary for activation is obtained differently; here, a higher margin value k_p makes a higher boundary. In each figure, the probabilistic boundaries and fault-affected indices for the normal state are shown for different values of the parameter k_p (0.7, 0.8, and 0.9).

In Figure 5-25, it is necessary to investigate whether a specific pattern is present under normal operating conditions. If all time-frequency indices are independent, it would be challenging to observe a distinct pattern in practice. However, as depicted in Figure 5-25 (c), an impact signal is observed in a specific time region even when a high k_p value is set, indicating the presence of a unique pattern. These vertically-oriented indices, resulting from the impact signals, could be attributed to motion braking or actual impact faults. To address this issue, additional physical interpretation or filtering techniques specific to the impact signal would need to be applied. However, these aspects were not considered within the scope of this study. Instead, the study later examined whether this pattern tendency could be accounted for through the adaptive threshold proposed in section 4.2.3.

Figure 5-26 illustrates the appearance of fault-related patterns. By examining the selected ratio of fault-affected indices in each figure, it is evident that there is no significant variation. This suggests that fault-affected indices generally exhibit considerably higher energy levels compared to the energy distribution observed under normal operating conditions. Furthermore, a noticeable difference is observed in the pattern of fault-affected indices between indices where the speed condition is zero and indices where it is nonzero. Further details regarding this observation will be explained in the subsequent figure.

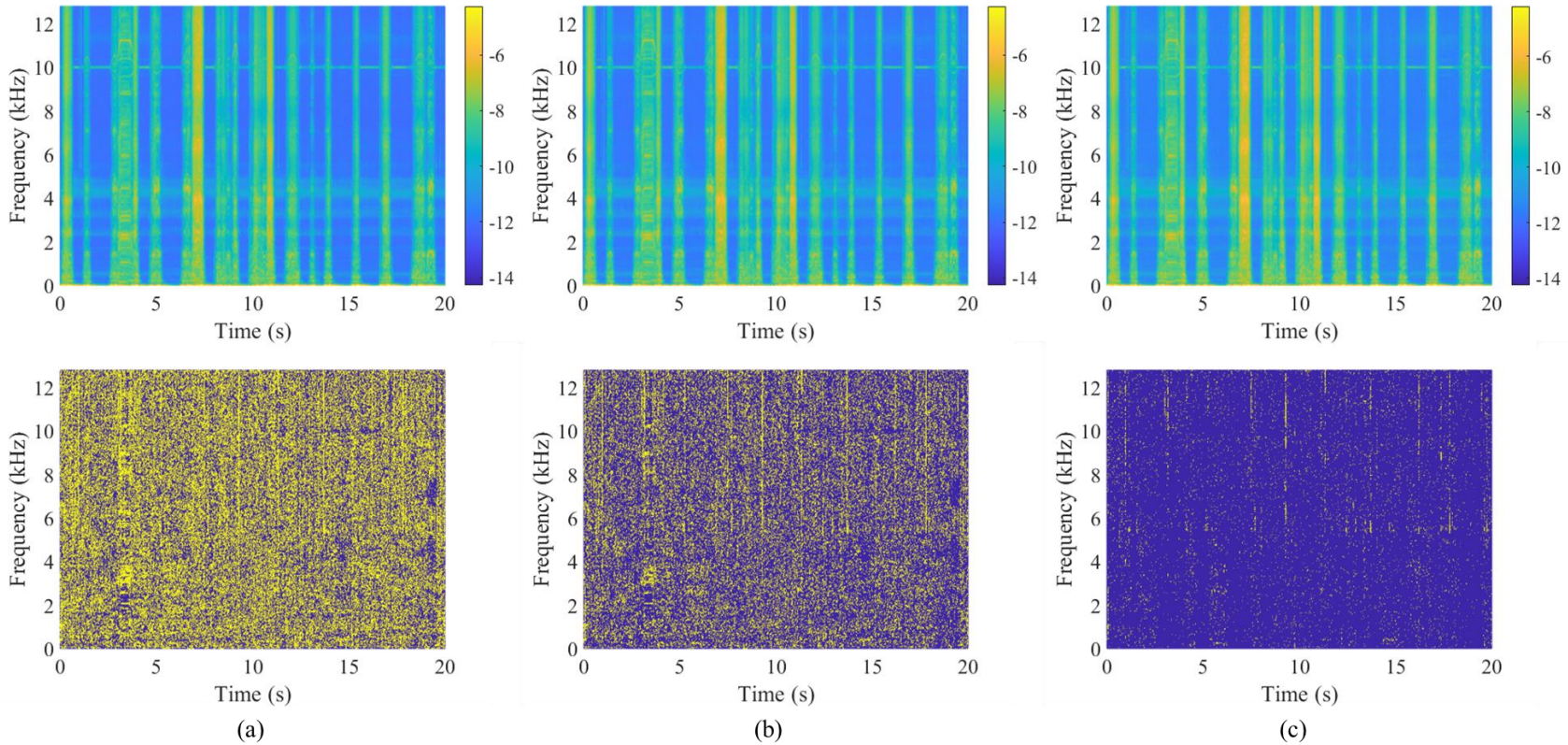

Figure 5-25 Probabilistic boundary (upper) & fault affected indices (lower) for the normal; (a) k_p = 0.7, (b) k_p = 0.8, (c) k_p = 0.9.

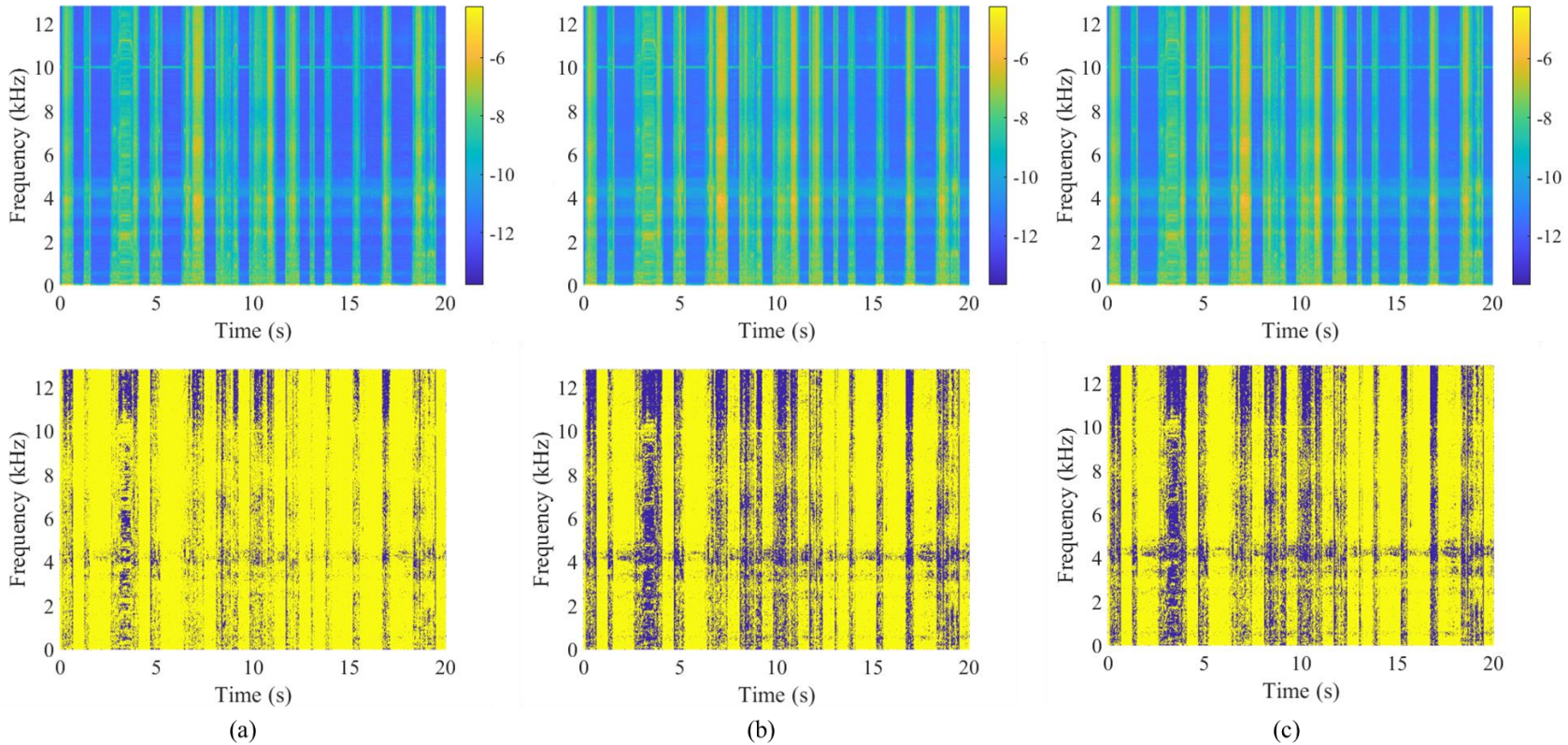

Figure 5-26 Probabilistic boundary (upper) & fault affected indices (lower) for the fault; (a) $k_p = 0.7$, (b) $k_p = 0.8$, (c) $k_p = 0.9$.

Figure 5-27 shows how frequently each index is calculated as $W(\tau, \omega)=1$, using the signals from both the normal state and a fault state. As seen in Figure 5-27 (a), the proportion at which each index satisfies $W(\tau, \omega)=1$ converges to a value of 1- k = 0.1 when the measured data is from the normal state. On the other hand, as seen in Figure 5-26, the trend described in Figure 5-27 can be confirmed visually. Most of the proportion is calculated close to 1 at the region where the operating speed is 0; this seems to be because the background noise is increased by uncontrolled environmental factors, rather than the fault condition affecting the vibration in the motionless state. However, since the vibration energy in the zero-speed state is very small and the rate of energy increase is much smaller than the rate of energy increase due to the fault state, the proposed FASER approach is not significantly affected. It can be seen that the proportion is relatively lower around 5000Hz; this can be interpreted to be because the increase in energy due to the fault state was neglected by the external noise component. Additionally, since this frequency band occurs regardless of operating speed, it is likely to be Narrowband Gaussian noise. Figure 5-27 (b) shows a region between 3 and 4 seconds where the ratio is notably high only for specific frequencies similar to Figure 5-26. Intriguingly, the operating speed of 4^{th} joint during this time interval is zero. As revealed in Figure 5-2, only the 6^{th} joint is in operation at that time, implying that the operation of 6^{th} joint affected the vibration of the 4^{th} joint. Therefore, it is reasonable to conclude that the fault at the 4th axis had an impact on the vibration of the 6^{th} axis, and that this vibration subsequently transmitted to the 4th axis, leading to the emergence of the specific frequencies with high separability. Finally, it can be confirmed that in the region where the operating speed is not zero, the proportion is high only at the specific frequencies. However, the speed tends to change very quickly; thus, it is difficult to observe a specific pattern related with the operating speed.

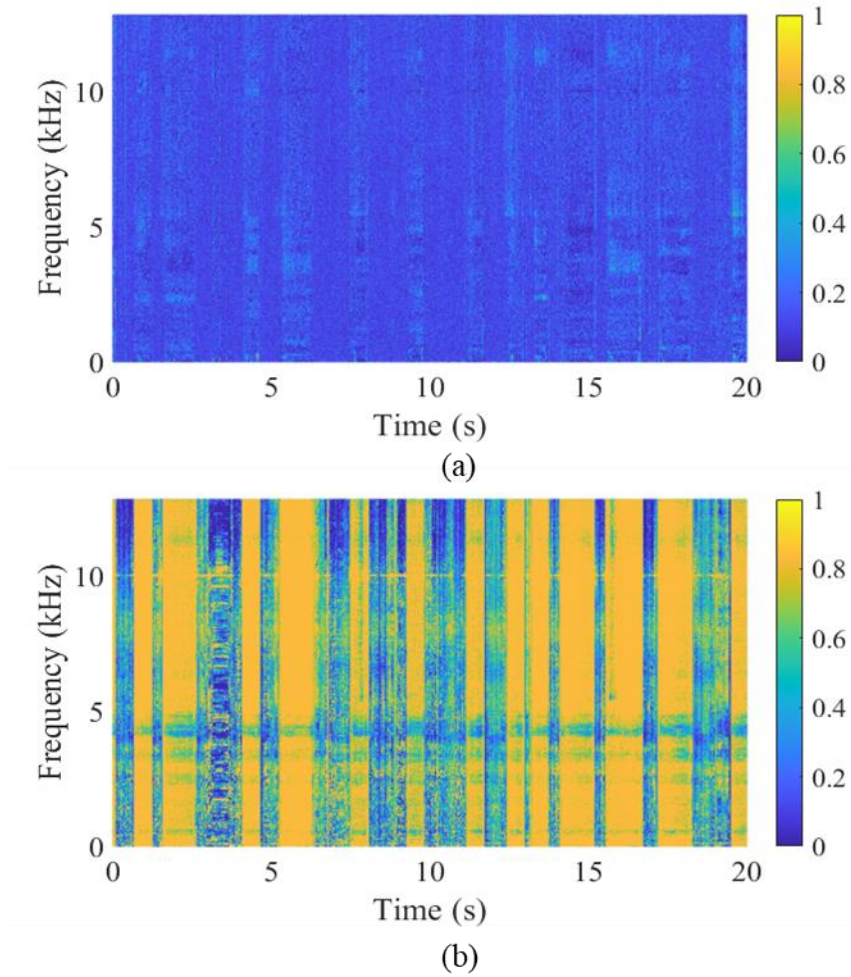

Figure 5-27 Proportions where each index satisfies $W(\tau, \omega)$=1 using k_p = 0.9; (a) Normal, (b) Fault

Figure 5-28 shows the FASER trends obtained for both the normal and fault states. It can be seen that all FASERs in the faulty state exceed the adaptive threshold FAT; whereas, FASERs in the normal state are smaller than the adaptive threshold FAT. Unlike what was observed in Section 4.3, it can be seen that the FAT value, which is an adaptive threshold in the normal state, varies greatly depending on the data. Since the deterministic energy is small in the index where noise is dominant, the ratio of energy to mean energy changes greatly. Therefore, this is considered to be because there are a relatively large number of indexes with a corresponding operating speed of 0; thus, there is a high possibility of selecting a relatively large

number of indexes with predominant noise in the normal state. On the other hand, in the fault state, it can be confirmed that the change of the adaptive threshold is small for each data, as compared with the normal state. This result is because the indices whose energy increases due to the fault state are similarly selected as $W(\tau, \omega)=1$ and the energies of the corresponding indices are generally greater than those of the indices in which noise dominates.

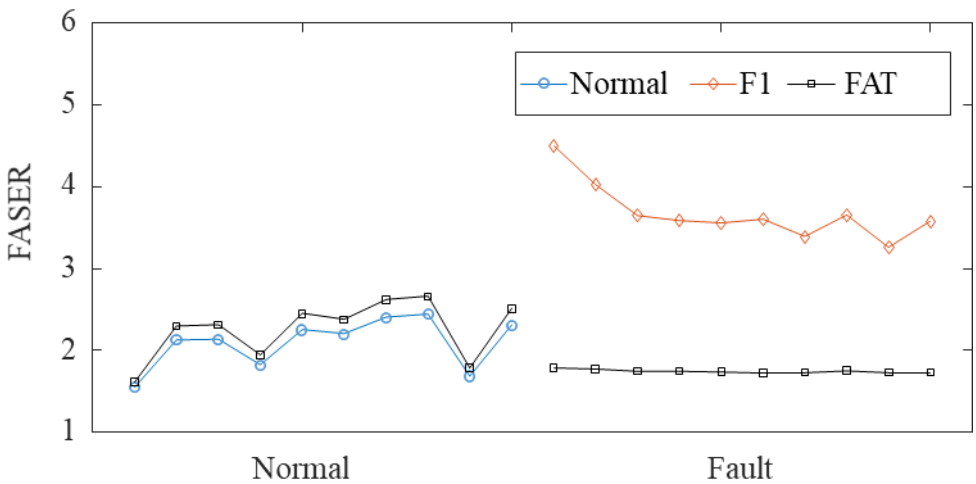

Figure 5-28 FASER and FAT for normal and fault.

In industrial systems, it is often challenging to acquire and utilize high-sampling data for extended periods of time. Therefore, an analysis was conducted to investigate the trends exhibited by the proposed method based on the duration of data acquisition. Figure 5-29 and Figure 5-30 demonstrate the impact of signal length on the calculation of FASER and its adaptive threshold, FAT. The signals used to calculate FASER were not overlapped to avoid correlation dependency, which could lead to incorrect analysis. The figures illustrate that as the signal length for calculating FASER increases, the fluctuation of FAT decreases. This phenomenon is closely related to the dependency of fault information with regard to the operating condition.

When the time interval for calculating FASER is very short, such as the 0.2

seconds duration shown in Figure 5-29 (a) and (b), there is a higher likelihood of encountering modeling types that do not conform to the local Gaussian noise shape, depending on where the fault frequency is generated. In such cases, the ratio between the conditional mean and the total mean of the matched energy distribution decreases more significantly than in Gaussian noise modeling, resulting in more severe fluctuations. Furthermore, the aperiodic nature of impact signals negatively affects the feature to have more fluctuation. In particular, FASER with a very short length is inevitably more susceptible to this tendency. Therefore, although the value of FASER itself is very large when the length is very short, and it may perform well in fault diagnosis, there are numerous instances where normal data is erroneously identified as faulty data. This problem can be mitigated by using a time length of more than 4 seconds shown in Figure 5-30 (a) and (b), as the impact-like FASER disappears briefly, resulting in a reduced false diagnosis rate, which can be considered the optimal time length for fault diagnosis.

In short, similar to the case study shown in Section 4.3, shortening the time interval for calculating FASER can lead to encountering different types of modeling and varying degrees of fault effects. This is more pronounced in Figure 5-30 (c) and (d), where the FASER value becomes similar every cycle when the operating conditions are the same. Despite these challenges, a time length of 0.2 seconds can yield near-perfect fault diagnosis performance when FASER is calculated together with FAT. However, it should be noted that the degree of fault energy influence may still vary depending on the operating situation, indicating that optimizing the time length by the proposed method will require considering various aspects, such as fault conditions, modeling conditions, and STFT parameters. This study shows that the proposed method can achieve accurate fault diagnosis by reflecting the operating condition, albeit with varying results depending on the signal length for calculating FASER.

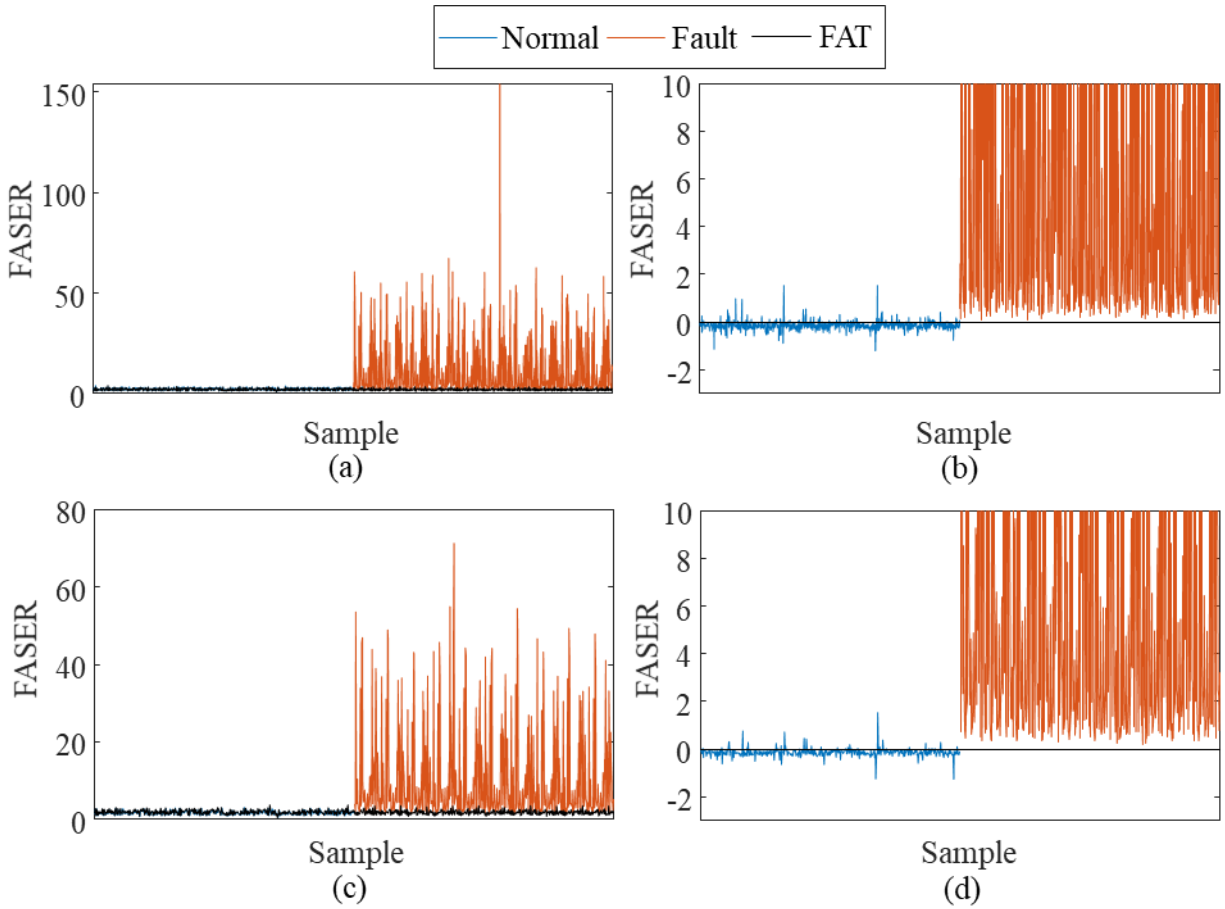

Figure 5-29 Effect of the length of the signal for FASER; (a) FASER and FAT (0.2 sec.) (b) difference of FASER and FAT (0.2 sec.) (c) FASER and FAT (0.4 sec.) (d) difference of FASER and FAT (0.4 sec.).

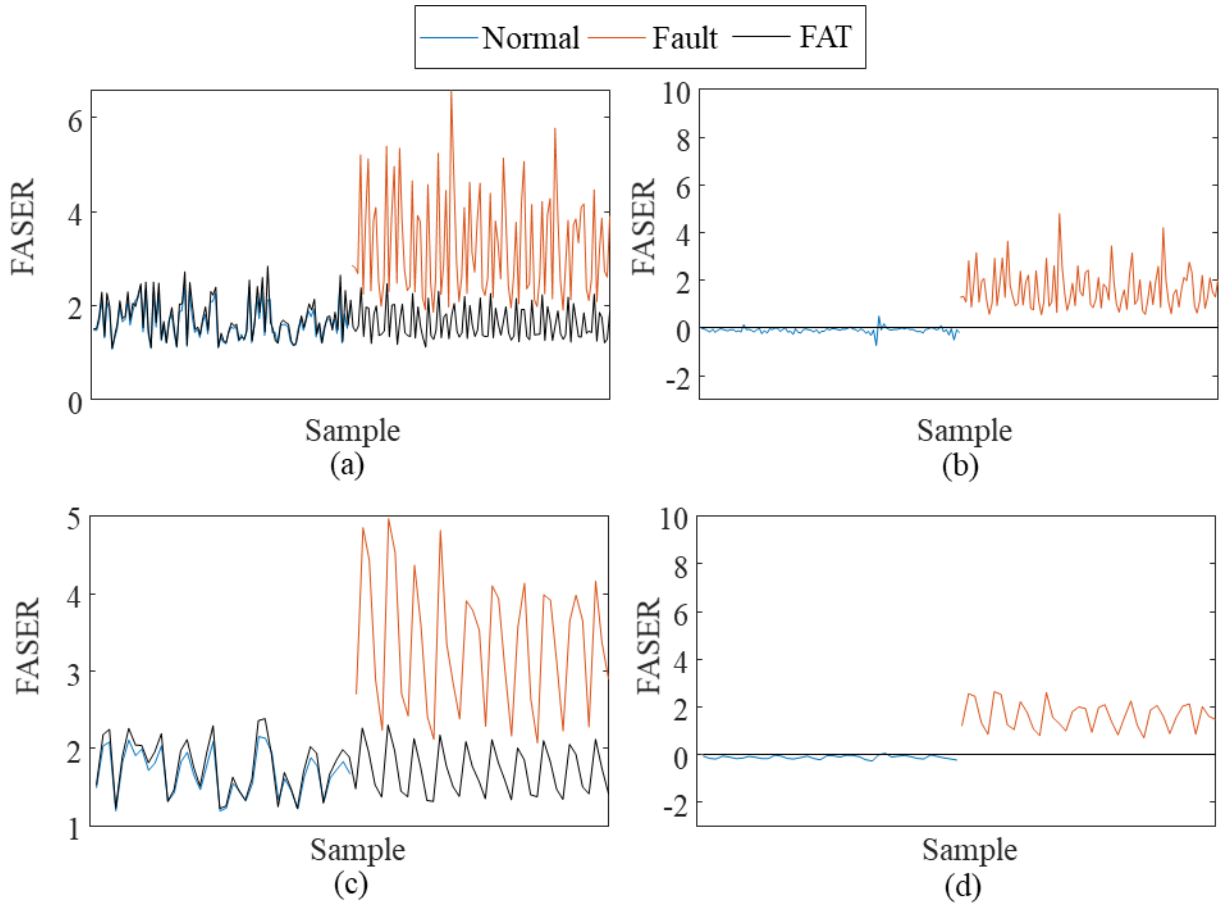

Figure 5-30 Effect of the length of the signal for FASER; (a) FASER and FAT (2 sec.) (b) difference of FASER and FAT (2 sec.) (c) FASER and FAT (5 sec.) (d) difference of FASER and FAT (5 sec.)

Lastly, the comparative study with conventional method is performed. RMS of the raw signal is used to compare the sensitivity of our method, considering the fact that the RMS is greatly related to the energy of the signal. Additionally, another energy extraction method based on spectral kurtosis is used to compare the performance of the proposed method. In this case study, the optimal frequency band for each sample is generally calculated with a center frequency of 2700~2900 Hz and a bandwidth of 70.71 Hz, as shown in Figure 5-31 (a). The level equals to log2 (the window size), which is related to the frequency bandwidth. The colorbar is based on the spectral kurtosis. Furthermore, considering that harmonics of GMF and their sidebands are generally analyzed for gearbox fault diagnosis, the GMF corresponding to the time-frequency indices based on the operating speed was calculated and is shown as the black curved line in Figure 5-31 (b). The GMF is calculated based on the operating speed shown in Figure 5-15 and the parameters of gear system given in Table 5-1 [8]. The feature was calculated as the energy sum of the indices corresponding to the GMF and their sidebands; this is indicated by the black curved line in the figure.

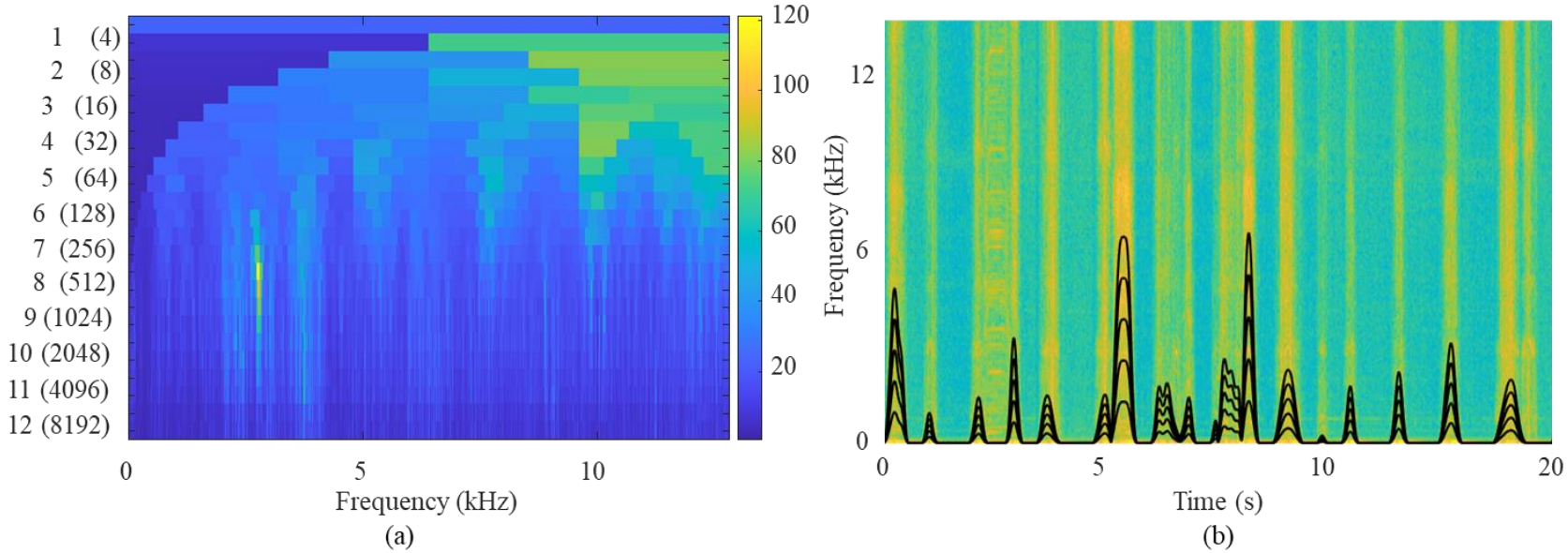

Figure 5-31 Preliminary work for comparative study; (a) Spectral Kurtosis (Kurtogram) result (b) GMF extraction with spectrogram

Figure 5-32 to Figure 5-34 show the results of the comparative study in a box plot. All features were calculated based on the energy value of the operating condition synchronized signal, according to the proposed method, and were normalized by the mean value of each feature of the normal state. The RMS feature shows good performance in terms of its fault diagnosis. However, as mentioned in Section 4.3, as can be seen from the y-axis value, the difference is small compared to the proposed method. Therefore, a slight change in the experimental environment could lead to different results. As shown in Figure 5-32 (c) to Figure 5-34 (c), in the case of the results using SK, in contrast, the mean value of the feature decreases in the fault state, and there is considerable overlap. Similar to the case study shown in Section 4.3, the increase in energy around the GMF that arises due to modulation is not dominant, as shown in Figure 5-32 (d) to Figure 5-34 (d). Furthermore, the variation in operating speed is significant, making it challenging to obtain fault-related information within a fixed frequency range, even when the modulation effect from the fault is apparent. These conditions make it difficult for SK-based methods to select the proper frequency for fault diagnosis. This feature calculates the GMF's sideband energy for harmonic components, which are conventionally utilized as the characteristic fault frequency, to show the normal and fault state energy trends, respectively. Considering the feature distribution, it can be seen that the energy of the indices – including harmonic components and sidebands – is not appropriate for diagnosing the fault condition. Finally, Conventional methods exhibit significant variability in their results depending on the duration of the sample data. In contrast, the proposed method consistently demonstrates superior diagnostic performance across all time durations. This highlights the exceptional robustness of the proposed method.

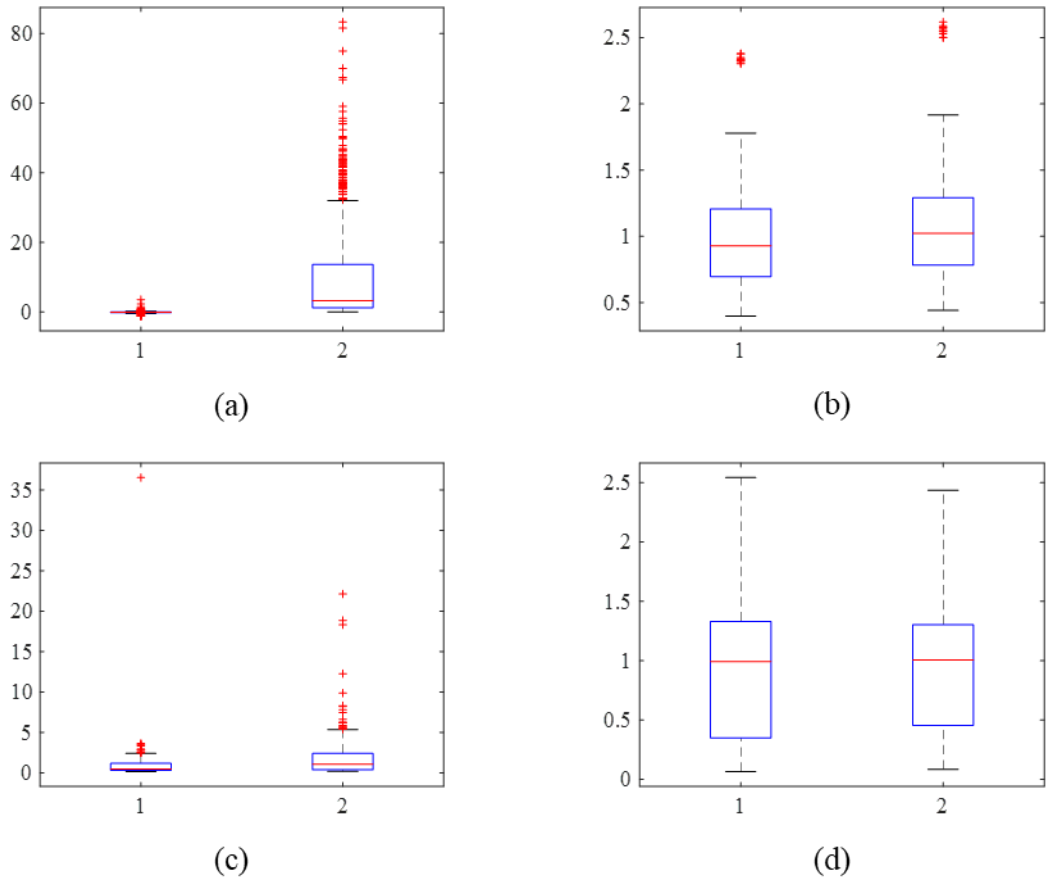

Figure 5-32 Comparative study for the proposed method (the length of signal = 1 sec.); (a) Proposed method, (b) RMS, (c) SK, (d) 1st GMF's sideband energy.

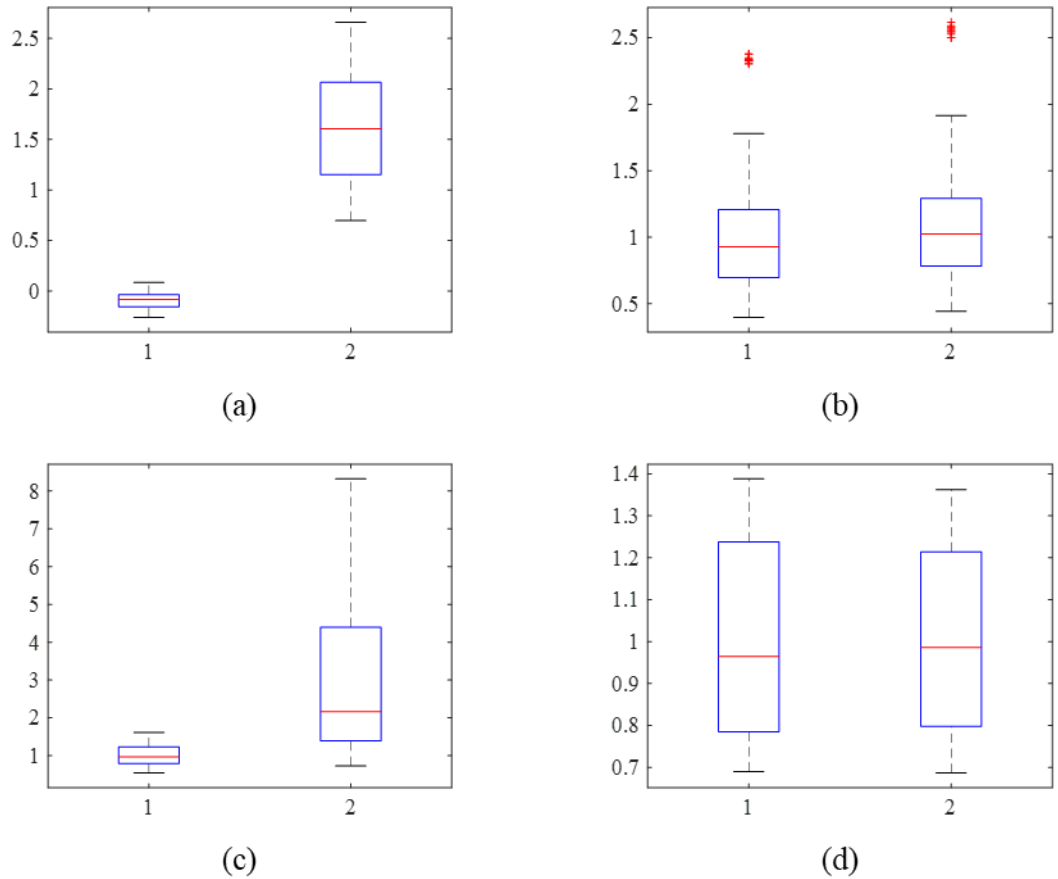

Figure 5-33 Comparative study for the proposed method (the length of signal = 5 sec.); (a) Proposed method, (b) RMS, (c) SK, (d) 1st GMF's sideband energy.

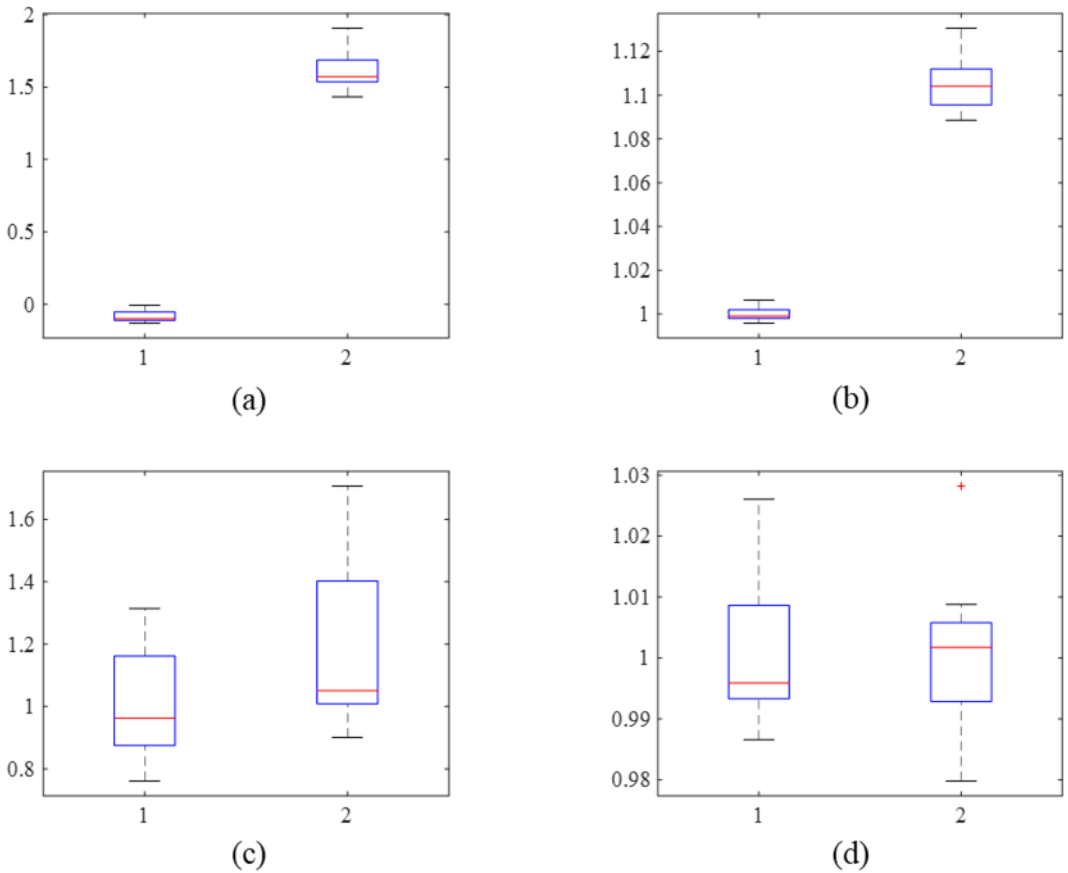

Figure 5-34 Comparative study for the proposed method (the length of signal = 20 sec.); (a) Proposed method, (b) RMS, (c) SK, (d) 1st GMF's sideband energy.

5.4 Applying results from the LSR approach (PERL) to the HSR approach (FASER)

The LSR approach is based on a probability model that takes into account the uncertainty introduced during the conversion process of high-sampling signals. It quantifies the contribution of each sample to the fault probabilistically using equation (3.13), considering the energy distribution of individual LSR signals. While the LSR method does not perfectly align with the results of the HSR method that utilizes a single sensor, as it considers the energy proportion from different sensors, it generally provides valuable insights. In particular, the HSR method analyzes the sensor adjacent to the fault location, which typically exhibits higher fault energy compared to other sensors. Therefore, when utilizing the LSR approach and focusing on sampled data with high probability results, the overall impact of uncertainty distortion is expected to be minimized. Consequently, the sampled data obtained from the LSR approach can enhance the performance of the HSR approach. The LSR approach provides valuable information about the fault probabilities at each sample. By utilizing this information, the HSR approach can focus on the sensor adjacent to the fault location, which generally exhibits higher fault energy. This integration of the LSR and HSR approaches helps to improve the overall diagnostic performance by leveraging the probabilistic insights from the LSR approach to enhance the analysis conducted in the HSR approach.

First, in order to verify the correlation between the analysis results of the LSR signal based approach and the HSR signal based approach, an analysis is conducted using the vibration data that was utilized in Sections 5.2 and 5.3. The vibration signals used for both approaches had a duration of 1 seconds. The operating condition synchronizing technique, which was employed in the HSR analysis, is also applied to ensure a fair comparison of the analysis results.

The figure shows the difference between the fault probability value of the

location obtained from the LSR signal and the FASER and FAT values obtained from the HSR signal in the form of a scatter plot. In the case of data exhibiting a large FASER-FAT value, as indicated by the red box in the figure, it is evident that the dominant signal type is an impulse signal as shown in figure. In the fault state of the robot system, impulse signals tend to have concentrated energy in the high-frequency region, resulting in a lower amount of energy being transmitted to other sensors. Consequently, the performance of the LSR analysis is not optimal in capturing such signals. Therefore, it can be thought as the limitation of the integration of PERL and FASER method. On the other hand, the data enclosed in the yellow box represents cases with a low probability value obtained from the LSR analysis. These instances can be considered as scenarios where the failure information itself is present, albeit in a localized frequency region. While the proposed FASER method enables fault diagnosis by applying filtering within a narrow frequency range, it becomes challenging to conduct additional frequency-

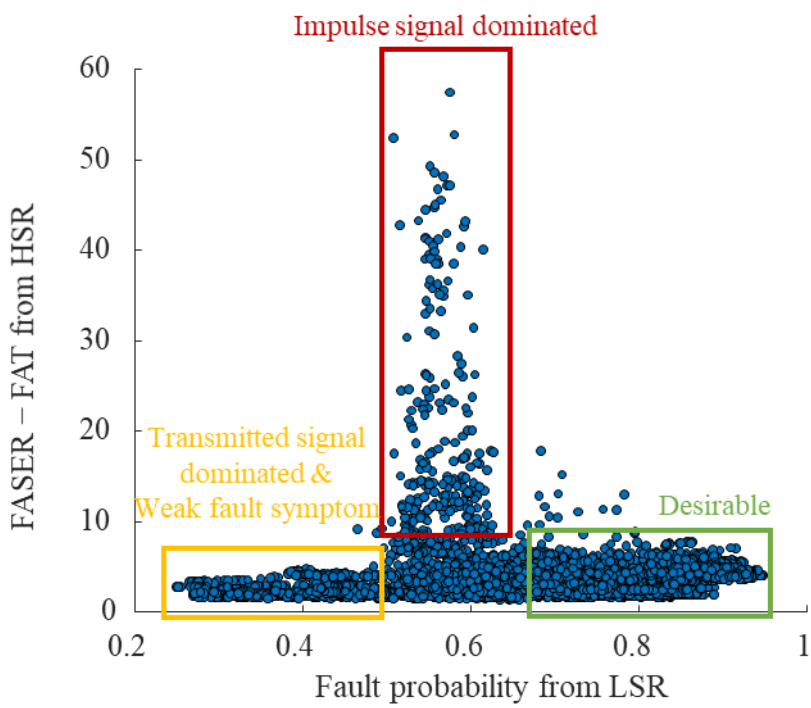

Figure 5-35 Scatter plot for visualizing the results from PERL and FASER method.

based analysis due to the limited amount of fault information available in these cases. Therefore, the in the view of robustness and further analysis, the data filtered by results from LSR approach is effective. Finally, detail analysis was performed on the desirable data represented by the green box. According to the proposed framework, it is desirable to perform the HSR approach to obtain better results when data is sampled based on the probability values from LSR approach. Therefore, when a specific value is obtained from the LSR, the analysis for the distribution FASER-FAT and corresponding fault frequency analysis are performed.

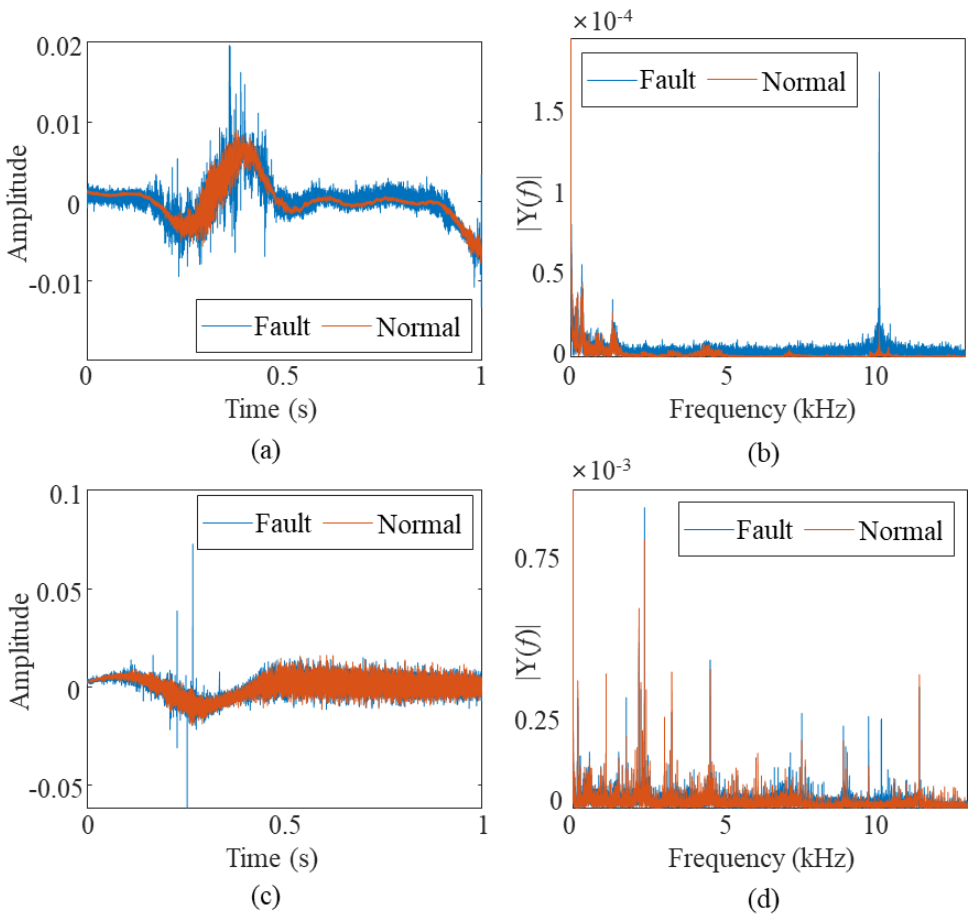

Figure 5-36 Fault and Normal state signal for representative data of Figure 5-34; (a) Impulse dominant (time domain), (b) Impulse dominant (frequency domain), (c) Weak fault energy (time domain), (d) Weak fault energy (frequency domain).

For the analysis of the desirable region shown in Figure 5-35, the focus was on the region where the fault probability obtained from the PERL method was greater than 0.5 and the FASER-FAT value was less than 10. In this analysis, the sampling data was based on the values obtained from the PERL method. A conditional distribution was created with the value obtained from PERL as the condition. Figure 5-37 illustrates the marginalized probability density function of the FASER-FAT value with respect to the fault probability value obtained from the PERL method. This analysis provides insights into the relationship between the fault probability and the FASER-FAT value, allowing for further understanding of the fault characteristics and their influence on the diagnostic results. First, it can be observed that the trend of conditional expectations. Generally, the trend is upward, indicating that as the fault probability increases, the corresponding FASER-FAT value tends to increase as well. However, until the fault probability reaches 0.8, there is no significant difference in the FASER-FAT values. Beyond the 0.8 threshold, there is a noticeable increase in the FASER-FAT values. Furthermore, the variance tendency of FASER-FAT can be observed through the confidence interval. Similar to the trend in the average values, it is evident that the fault probability decreases rapidly in the region exceeding 0.8. This implies that as the fault probability increases beyond this point, the variability in the FASER-FAT values also decreases. These observations provide insights into the relationship between the fault probability and the FASER-FAT values, indicating how the FASER-FAT value changes with different levels of fault probability and the associated variability. In summary, the analysis showed that as the fault probability exceeded a certain threshold value, the expectation of the FASER – FAT obtained through FASER method increased while the variance decreased. This suggests that the robustness of the diagnosis improved. To further validate this observation, representative data is analyzed following a similar approach as shown in Figure 5-35.

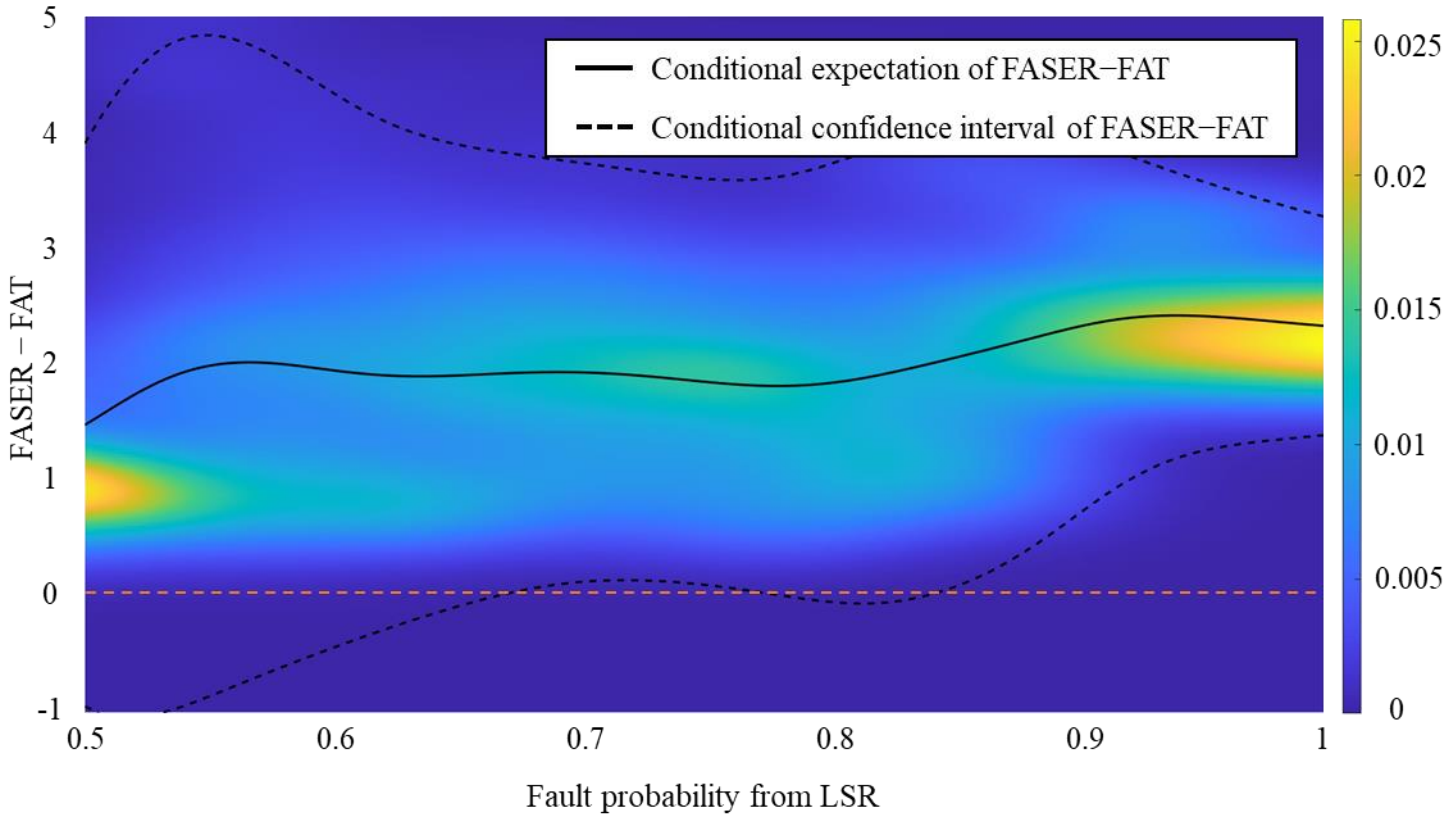

Figure 5-37 Marginalized probability density function of FASER−FAT value w.r.t. the fault probability value from PERL method.

Based on the coordinates in Figure 5-37, analysis is performed in the time domain and frequency domain for the data corresponding to (0.5, 1) and (0.95, 3). The results for the data corresponding to the point (0.5, 1) are presented in Figure (a) and (b). Upon analyzing the temporal behavior of the data in both normal and fault conditions, a resemblance in the overall energy trends can be observed, except for a distinct deviation occurring after 0.7 seconds. Up until the mentioned point, the energy patterns in the normal and fault conditions exhibit similarities, suggesting a lack of substantial differentiation between the two states within that time interval. Furthermore, it is worth noting that the energy characteristics of the analyzed data are heavily influenced by the signal preceding 0.7 seconds. Therefore, it is reasonable that the probability of determining as fault state is low. Similarly, when applying the FASER method (as depicted in Figure (b)), no substantial differences are observed in the frequency domain. Therefore, it is reasonable to observe a low FASER-FAT value. By combining these two results, it can be concluded that the likelihood of obtaining a low FASER − FAT value is high when utilizing data with low probability values obtained through the PERL method in the FASER method. The results for the data corresponding to the point (0.95, 3) are shown in Figure (c) and (d). Upon examining the time domain data, an increase in energy can be observed when the signal is measured from the fault state. In contrast to the previous case, it is evident that overall fluctuations are relatively small due to the limited impact of motion. Consequently, the variation of energy caused by motion is minimal. When applying the PERL method, this factor can have a positive effect by reducing uncertainty arising from operating conditions. This tendency becomes more apparent in Figure (d) where frequency analysis is performed. In the fault state, there is a clear increase in energy across all frequency bands. This indicates a higher likelihood of aligning with the assumed model, which suggests that the transmission effect can be derived from the frequency response function in the frequency domain when applying the PERL method to the robot system. Consequently, there is an increased

probability of obtaining high probability values through the PERL method. Moreover, when applying the FASER method in the presence of such frequency trends, the range of frequencies that can be identified as fault frequencies widens. As a result, it is expected that the FASER-FAT value is more likely to increase. By comparing the results of the time and frequency domain analysis for the two sets of data and the outcomes of the FASER and PERL methods, the following summary can be made.

In summary, the analysis of the data corresponding to different points (0.5, 1) and (0.95, 3) revealed interesting findings. For the first data point, which is filtered by the low fault probability value from PERL method, the energy trends in the time domain were similar between normal and fault conditions. This led to a low FASER-FAT value, indicating a lower robustness of fault detection. On the other hand, for the second data point, which is filtered by the high fault probability value from PERL method. In this case, the energy increased significantly in the fault state, and there was relatively less fluctuation due to motion. This resulted in a higher FASER-FAT value and a greater likelihood of fault identification. Furthermore, frequency analysis showed that energy levels across all frequency bands increased in the fault state, reinforcing the effectiveness of the FASER method in capturing fault-related information. Overall, the combination of the PERL and FASER methods proved valuable in analyzing both time and frequency domain data, enhancing the understanding and detection of faults in the system.

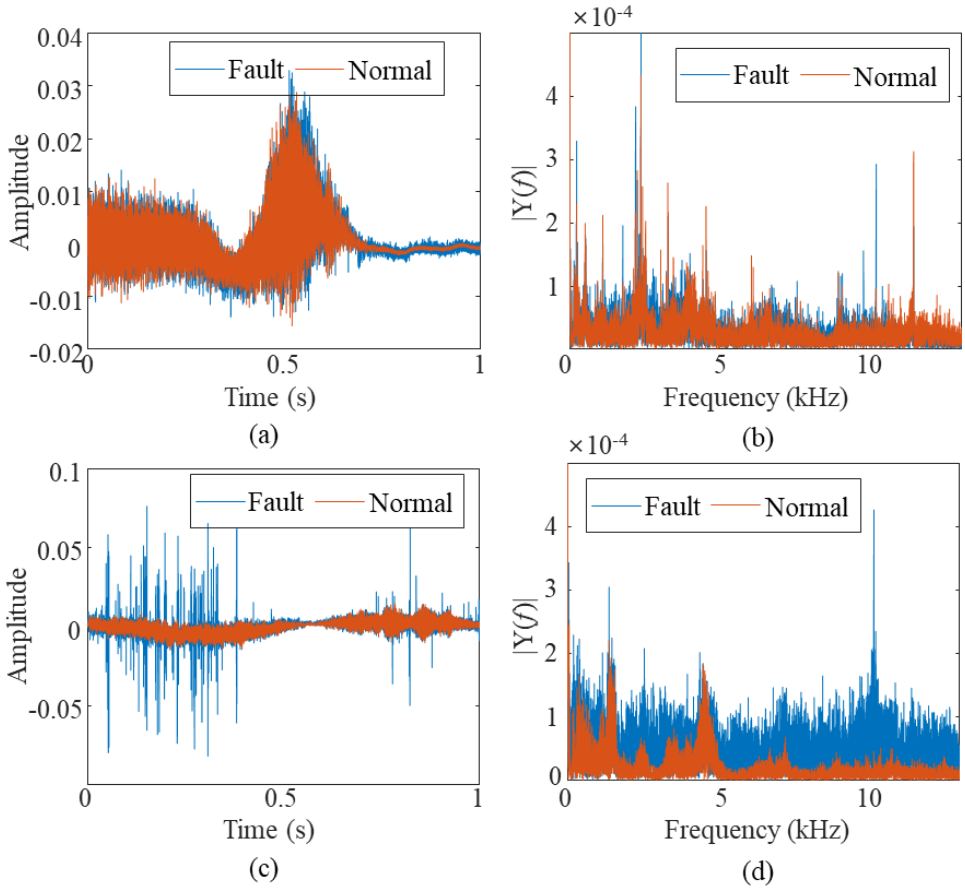

Figure 5-38 Fault and Normal state signal for representative data of Figure 5-36; (a) Data corresponding to (0.5, 1) (time domain), (b) Data corresponding to (0.5, 1) (frequency domain), (c) Data corresponding to (0.95, 3) (time domain), (d) Data corresponding to (0.95, 3) (frequency domain).

Finally, the results obtained according to the proposed methodology integrating PERL and FASER are compared with those obtained when FASER alone is performed. The comparison between applying only FASER and simultaneously applying FASER and FAT over time reveals interesting trends in the final features. The figure shows that when FASER and FAT are used together, the results exhibit lower variation with a smaller amount of data. Furthermore, there is a distinct periodic pattern observed in the results. This observation can be understood by considering the findings described in Figures 5-37 (c) and (d) above. Specifically, the data selected by PERL represents favorable operating conditions within one

operating cycle, which can be repeatedly extracted in each cycle when applying the FASER method. Therefore, the combination of FASER and FAT not only reduces variation but also captures the optimal extraction of the operating conditions, leading to more reliable and consistent results. To further analyze the robustness in the view of accurate diagnosis in the normal state, the normal state's FASER-FAT values under the same operating conditions are extracted and compared by boxplot shown in the figure. When applying FASER alone without PERL, it becomes evident that outliers occur more frequently in the normal state, resulting in a larger overall variance. This indicates a higher probability of misdiagnosis as the normal state. On the other hand, when the combined method is utilized, the occurrence of outliers in normal state becomes rare, and the variance decreases significantly. This suggests that the combined approach yields a more robust result. Furthermore, when examining the feature of the fault state, it can be observed that the combined method yields a higher mean value with a smaller variance. These characteristics contribute to the enhanced reliability and accuracy of the diagnostic outcome.

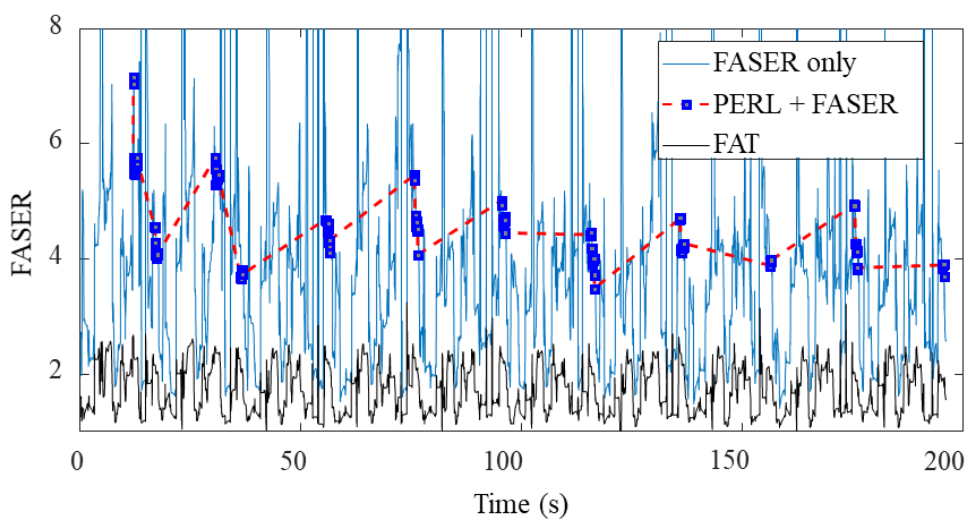

Figure 5-39 Trend comparison of FASER only and proposed integrated method.

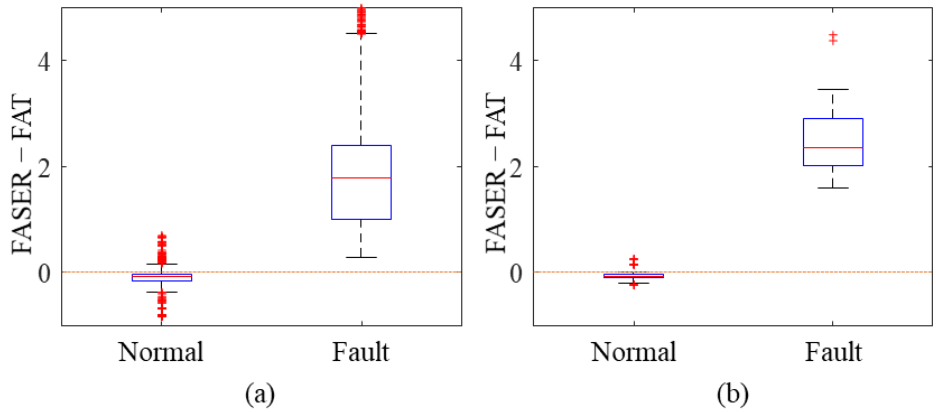

Figure 5-40 Boxplot of FASER-FAT values for FASER only and proposed integrated method; (a) FASER only, (b) Proposed integrated method.

5.5 Summary and discussion

In this chapter, it was focused on integration of the proposed PERL method based on LSR signals and the FASER method based on HSR signals. To validate the effectiveness of the integrated approach, a 6-DoF robot system with multiple sensors was utilized. Initially, it was reconfirmed the performance of each method individually by applying them separately and analyzing the results. Subsequently, it was compared and analyzed the results obtained from the PERL method and the FASER method to explore the correlation between them.

In most cases, except for instances where only the impact signal was detected as the fault symptom for a very short duration, it was observed that the FASER method produced favorable results when the result values obtained from the PERL method were high. This can be attributed to the fact that when data is extracted based on high probability values obtained from the PERL method, the extracted data is less influenced by operating conditions and contains sufficient fault energy.

In conclusion, the proposed integration method demonstrate that by selectively extracting data for FASER application using the PERL method, the overall computational cost can be reduced while ensuring result robustness. This integration

approach provides a more efficient and reliable fault diagnosis solution for industrial systems.

Chapter 6

Conclusion

6.1 Contributions and Significance

This doctoral dissertations proposes an uncertainty-aware framework for fault diagnosis in industrial systems using low and high sampling rate signals. The proposed fault diagnosis method includes two novel techniques: (1) a low-sampling-rate signal based probabilistic energy ratio based localization (PERL) method that enables the estimation of fault position; (2) a high-sampling-rate signal based fault affected signal energy ratio (FASER) method that enables the robust fault diagnosis and extracts fault-related frequency information. The proposed research offers the following potential contributions and significance in the field of system-level fault diagnosis.

Contribution 1: Solution for the practical issues of handling exorbitant amount of data in industrial system

This doctoral dissertation proposes an uncertainty-aware fault diagnosis framework for industrial systems using both high and low sampling rate signal approaches under non-stationary operating conditions. In general, high-sampling signals are often not fully utilized in industrial settings due to limitations in processing power needed to handle large amounts of data. On the other hand, when only low-sampling signals are used, fault diagnosis tends to be limited to severe faults due to their lower sensitivity. The proposed framework combines the advantages of each approach to

achieve efficient fault diagnosis. Faults are diagnosed using indirect low-sampling rate signals from wide-ranging sensors, such as acoustic emission sensors, and the fault location is estimated using the proposed PERL method. Then, the corresponding location's high-sampling rate signals are analyzed using the proposed FASER method to identify the fault type based on fault affected frequency information and verify if it's a misdiagnosis due to noise. By combining these two methods, the framework can efficiently estimate the fault location, select the optimal sensor for further analysis using low-sampling rate signals, and improve the robustness of results using high-sampling rate signals.

Contribution 2: Novel low sampling rate signal based fault localization considering the transmission effect of signals under severe fault symptom

The proposed probabilistic model can estimate the location of a fault using only the energy-related descriptor of the signal. By accurately reflecting the measurement uncertainty caused by the operating conditions or the disturbance noise of the AE sensor itself, it is possible to estimate a probable leak without much error, even in real-world operating conditions. The results derived by the proposed method can be calculated effectively even if only two or three sensors respond to a boiler tube leak. This has a great effect when the size of system is huge and does not meet the conditions for reacting to four or more sensors, as required by conventional methods. Thus, this can solve the difficulty in finding a convergence point that must arise for success of conventional methods; this issue can arise in real-world situations due to an insufficient number of fault-responsive sensors. From the point of view of establishing a maintenance strategy in the case of a large-scale system, efficient operation is possible by considering the probability distribution about the fault.

Contribution 3: High sampling rate signal based robust fault diagnosis considering the stochastic nature of signals represented as STFT

This doctoral dissertation proposes the method having the ability to match the desired operating signal automatically from a consecutively measured signal without additional equipment, such as an encoder. Additionally, the uncertainty of the signal represented as a spectrogram is quantified through a suggested frequency energy model, and statistically separable indices for calculating the fault-affected signal can be found. An adaptive threshold that considers the window function to transform the spectrogram and the conditional probability of probabilistic distribution model is also proposed, which helps to prevent misdiagnosis of normal signals as being from a fault state. Furthermore, the proposed method does not require any kind of fault-related knowledge, such as a fault frequency calculated by a fault mechanism, making it more efficient in scenarios where identifying the fault frequency becomes infeasible due to security issues that restrict the disclosure of physical or mechanical properties of the system under consideration.

6.2 Suggestions for the Future Research

This doctoral dissertation proposes technical and mathematical advancements for efficient system-level fault diagnosis using LSR and HSR signals. Although the proposed methods demonstrate improved fault diagnosis performance, further research is needed to apply these methods in real-world applications and calibrate the results considering the underlying assumptions. Specific suggestions for the future research are listed below.

Suggestion 1: Development of denoising technique combining operation related signal and probabilistic model

The research in doctoral dissertation shows the heteroskedasticity in the noise of signal in the time frequency domain, and probabilistic model is presented to quantify these uncertainty. Additionally, some of time-frequency index having the deterministic signal, which is generally related with the operating condition. Therefore, in this study, probabilistic modeling was conducted based on data with similar operating conditions, but it will be possible to apply denoising technology by extracting operating conditions and using ensemble techniques.

Suggestion 2: Extensive application to the situation under changing temperature conditions

As shown in Section 2.2, the energy of signal generally depends on the temperature. In this doctoral dissertation, the study was conducted by minimizing the effect of temperature-induced energy variability. Specifically, the proposed FASER method in Chapter 3, experimental condition for the temperature is controlled as the saturated situation. However, in an actual operating environment, there is a possibility that the temperature may change due to external factors such as the season or the condition of the internal lubricant of the component. Therefore, in the future research, the probabilistic modeling considering the difference of temperature could be considered.

Suggestion 3: Parametric probabilistic energy modeling substituting the KDE modeling

The proposed probability modeling in this doctoral dissertation was based on the assumption of a signal by a single component having a Gaussian noise form within one frequency. However, in reality, the time-frequency index is generally composed of mono-component signals and uncertainties that may not follow a Gaussian distribution, which limits the applicability of the proposed model. Therefore, KDE modeling was used to model these time-frequency indices. However, the KDE model is highly data-dependent and may overfit, making it difficult to interpret the physical meaning of the model. Furthermore, the data used to construct the KDE model needs to be saved for the application of the proposed method. To address these issues, future research could explore energy distribution models for overlapping two-component signals or investigate non-Gaussian noise to improve the proposed method. Alternatively, the signal decomposition method with only using the measured vibration signal such as empirical mode decomposition (EMD) can be applied to solve these kinds of issues.

Appendix

Derivation of correlation coefficient from the spectral leakage under the condition where each of two frequency energy is considered as fault-affected frequency

In the process of signal conversion through TFA, the TFA parameter plays a critical role in determining the resulting expression, even when the same TFA method is used. While there are various TFA methods available, this study focuses on the problem of STFT-based spectrograms. Specifically, this doctoral research analyzes parameters related to the window function. Equation (4.1) provides the basic equation for transforming the signal to TFA from STFT. While recent studies have explored the energy correlation between indices expressed in TFA, they are limited to the zero-mean condition and do not consider the energy corresponding to fault-affected frequencies, which is a focus of this study. For the correlation from the overlapped window function in time domain, the suggested equation in the published literature could be worked. Therefore, only the correlation from the spectral leakage effect from the window function is derived.

Firstly, as shown in Figure 4-8, considering the original signal, which is not the measured signal but the real signal, only exists in the frequency ω and $\omega + \Delta\omega$. Simply, the Fourier transform of the original signal is expressed as:

$$X(j\omega) = d_1 + \varepsilon_1,\ X(j(\omega + \Delta\omega)) = d_2 + \varepsilon_2 \tag{A.1}$$

where $X(j\omega)$ is the Fourier transform of the signal at the frequency ω, d_1 and d_2 are the deterministic parts of the signal at the frequency ω and $\omega + \Delta\omega$, d_1 and d_2 are the complex bivariate gaussian distribution satisfying:

$$\mathrm{Var}(\mathrm{Re}[\varepsilon_1]) = \frac{\sigma_1^2}{2}, \mathrm{Var}(\mathrm{Im}[\varepsilon_1]) = \frac{\sigma_1^2}{2}, \mathrm{Var}(\mathrm{Re}[\varepsilon_2]) = \frac{\sigma_2^2}{2}, \mathrm{Var}(\mathrm{Im}[\varepsilon_2]) = \frac{\sigma_2^2}{2} \tag{A.2}$$

where Var(·) means the variance operator. In actual measurements, the energy of the signal must exist in different frequency domains. However, when both frequencies are considered as fault-affected frequencies, their energy levels are relatively higher compared to other frequencies. This is because the fault-affected frequencies themselves indicate that the measured energy at the corresponding frequencies is probabilistically high. In addition, the effect due to spectral leakage is very small in the frequency area outside the range of the main lobe of the frequency response function of the window function. Therefore, the calculation was performed assuming that the spectral leakage effect due to energy of other frequencies is negligible. From these assumptions, the Fourier transform of the measured signal at the frequency ω can be expressed as:

$$Y(j\omega) = d_1 + f_w(d_2) + \varepsilon_1 + f_w(\varepsilon_2) = r_1 + \varepsilon_1 + f_w(\varepsilon_2) \tag{A.3}$$

where $Y(j\omega)$ is the Fourier transform of the signal at the frequency ω, r_1 is the deterministic part of the measured signal at the frequency ω, and $f_w(\cdot)$ is the spectral leakage effect from the window function w. From the equation (A.3), the mean and the variance of the measured energy at frequency ω can be calculated as:

$$\mathrm{E}\left[\left|Y(j\omega)\right|^2\right] = \mathrm{E}\left[r_1 r_1^*\right] + \mathrm{E}\left[(\varepsilon_1 + f(\varepsilon_2))(\varepsilon_1 + f(\varepsilon_2))^*\right]$$
$$\mathrm{Var}\left[\left|Y(j\omega)\right|^2\right] = \mathrm{Var}\left[(\varepsilon_1 + f(\varepsilon_2))(\varepsilon_1 + f(\varepsilon_2))^* + r_1(\varepsilon_1 + f(\varepsilon_2))^* + r_1^*(\varepsilon_1 + f(\varepsilon_2))\right] \quad \text{(A.4)}$$

where * is the complex conjugate. For the intuitive expression, we can let that $\varepsilon_1 + f(\varepsilon_2) = a_\omega + jb_\omega$ and $r_1 = c_\omega + jd_\omega$. Then, equation (A.4) can be expressed as:

$$\mathrm{E}\left[\left|Y(j\omega)\right|^2\right] = \mathrm{E}\left[a_\omega^2 + b_\omega^2\right] + c_\omega^2 + d_\omega^2$$
$$\mathrm{Var}\left[\left|Y(j\omega)\right|^2\right] = \mathrm{Var}[a_\omega^2] + \mathrm{Var}[b_\omega^2] + 4c_\omega^2\mathrm{Var}[a_\omega] + 4d_\omega^2\mathrm{Var}[b_\omega] \quad \text{(A.5)}$$

Additionally, $\varepsilon_1 + f(\varepsilon_2)$ can be expressed as the frequency response function of the window function F_w, then $\varepsilon_1 + f(\varepsilon_2) = \varepsilon_1 + k\varepsilon_2$. For simple notation, we let $F_w(\Delta\omega)$ as k. Then, equation (A.5) can be expressed as:

$$\mathrm{E}\left[\left|Y(j\omega)\right|^2\right] = (\sigma_1^2 + |k|^2\sigma_2^2) + (c_\omega^2 + d_\omega^2) = E_\omega$$
$$\mathrm{Var}\left[\left|Y(j\omega)\right|^2\right] = (\sigma_1^2 + |k|^2\sigma_2^2)^2 + 2(c_\omega^2 + d_\omega^2)(\sigma_1^2 + |k|^2\sigma_2^2) = V_\omega \quad \text{(A.6)}$$

Recalling that the mean and variance of the measured energy can be estimated from the constructing the probability equation described in the Section 4.2.1, then the unknown term can be estimated from the mean and variance.

$$(\sigma_1^2 + |k|^2\sigma_2^2) = E_\omega - \sqrt{E_\omega^2 - V_\omega} = \psi_\omega \quad \text{(A.7)}$$

Similarly, the mean and the variance of the measured energy at frequency ω can be calculated as:

$$(\sigma_2^2 + |k|^2\sigma_1^2) = E_{\omega+\Delta\omega} - \sqrt{V_{\omega+\Delta\omega} - E_{\omega+\Delta\omega}^2} = \psi_{\omega+\Delta\omega} \quad \text{(A.8)}$$

From combining the equation (4.7) and (4.8), the unknown σ_1 and σ_2 can be estimated as:

$$\sigma_1^2 = \frac{\psi_\omega - |k|^2\psi_{\omega+\Delta\omega}}{1-|k|^4},\ \sigma_2^2 = \frac{\psi_{\omega+\Delta\omega} - |k|^2\psi_\omega}{1-|k|^4} \quad \text{(A.9)}$$

Before the calculating the covariance, it needs to organize the absolute square of $Y(j\omega)$ and $Y(j(\omega+\Delta\omega))$ from the defined variables. From equation (A.3), the energy of the measured signal at the frequency ω can be expressed as:

$$\left|Y(j\omega)\right|^2 = r_1 r_1^* + (\varepsilon_1 + f(\varepsilon_2))(\varepsilon_1 + f(\varepsilon_2))^* + r_1(\varepsilon_1 + f(\varepsilon_2))^* + r_1^*(\varepsilon_1 + f(\varepsilon_2)) \tag{A.10}$$

Similarly, the measured signal at the frequency $\omega + \Delta\omega$ can be expressed as:

$$\begin{aligned}&\left|Y(j(\omega+\Delta\omega))\right|^2 = \\ &r_2 r_2^* + (\varepsilon_2 + f^*(\varepsilon_1))(\varepsilon_2 + f^*(\varepsilon_1))^* + r_2(\varepsilon_2 + f^*(\varepsilon_1))^* + r_2^*(\varepsilon_2 + f^*(\varepsilon_1)))\end{aligned} \tag{A.11}$$

where $Y(j(\omega+\Delta\omega))$ is the Fourier transform of the signal at the frequency $\omega + \Delta\omega$, and r_2 is the deterministic part of the measured signal at the frequency $\omega + \Delta\omega$.

The deterministic term can be neglected to calculate the covariance. Additionally, following equation are satisfied from the property of gaussian noise's independency.

$$\begin{aligned}&\mathrm{E}(\varepsilon_1^*\varepsilon_2\varepsilon_2^*) = \mathrm{E}(\varepsilon_1^*\varepsilon_1\varepsilon_2) = \mathrm{E}(\varepsilon_1^*\varepsilon_1\varepsilon_2^*) = \\ &\mathrm{E}(\varepsilon_1^*\varepsilon_1\varepsilon_1^*) = \mathrm{E}(\varepsilon_2^*\varepsilon_2\varepsilon_2^*) = \mathrm{E}(\varepsilon_2^*\varepsilon_1^*\varepsilon_2) = \\ &\mathrm{E}(\varepsilon_2^*\varepsilon_1^*\varepsilon_2) = \mathrm{E}(\varepsilon_1\varepsilon_2^*\varepsilon_2^*) = \mathrm{E}(\varepsilon_2^*\varepsilon_1\varepsilon_1^*) = 0\end{aligned} \tag{A.12}$$

Therefore, the covariance of the energies are expressed from the linearity :

$$\begin{aligned}&\mathrm{Cov}(\left|Y(j\omega)\right|^2, \left|Y(j(\omega+\triangle\omega))\right|^2) \\ &= \mathrm{Cov}\left((\varepsilon_1 + f(\varepsilon_2))(\varepsilon_1 + f(\varepsilon_2))^*, (\varepsilon_2 + f^*(\varepsilon_1))(\varepsilon_2 + f^*(\varepsilon_1))^*\right) \\ &+\mathrm{Cov}\left(r_1(\varepsilon_1 + f(\varepsilon_2))^* + r_1^*(\varepsilon_1 + f(\varepsilon_2)), r_2(\varepsilon_2 + f^*(\varepsilon_1))^* + r_2^*(\varepsilon_2 + f^*(\varepsilon_1))\right)\end{aligned} \tag{A.13}$$

To calculate the first covariance term, the definition of covariance can be applied. Then, the first term of equation (A.13) can be expressed as:

$$\mathrm{E}\left((\varepsilon_1 + f(\varepsilon_2))(\varepsilon_1 + f(\varepsilon_2))^*(\varepsilon_2 + f^*(\varepsilon_1))(\varepsilon_2 + f^*(\varepsilon_1))^*\right) - \mathrm{E}\left((\varepsilon_1 + f(\varepsilon_2))(\varepsilon_1 + f(\varepsilon_2))^*\right)\mathrm{E}\left((\varepsilon_2 + f^*(\varepsilon_1))(\varepsilon_2 + f^*(\varepsilon_1))\right)^* \quad \text{(A.14)}$$

Then, the first term of equation (A.14) is calculated:

$$\begin{aligned}
&\mathrm{E}((\varepsilon_1 + f(\varepsilon_2))(\varepsilon_1 + f(\varepsilon_2))^*(\varepsilon_2 + f^*(\varepsilon_1))(\varepsilon_2 + f^*(\varepsilon_1))^*) \\
&= \mathrm{E}[(\varepsilon_1\varepsilon_1^* + k^*\varepsilon_1\varepsilon_2^* + k\varepsilon_1^*\varepsilon_2 + kk^*\varepsilon_2\varepsilon_2^*)(\varepsilon_2\varepsilon_2^* + k^*\varepsilon_2^*\varepsilon_1 + k\varepsilon_2\varepsilon_1^* + kk^*\varepsilon_1\varepsilon_1^*)^*] \\
&= \mathrm{E}\begin{bmatrix}
\varepsilon_1\varepsilon_1^*\varepsilon_2\varepsilon_2^* + k\varepsilon_1\varepsilon_1^*\varepsilon_2^*\varepsilon_1 + k^*\varepsilon_2^*\varepsilon_1\varepsilon_1\varepsilon_1^* + kk^*\varepsilon_1\varepsilon_1^*\varepsilon_1\varepsilon_1^* \\
+k^*\varepsilon_1\varepsilon_2^*\varepsilon_2\varepsilon_2^* + kk^*\varepsilon_1\varepsilon_2^*\varepsilon_2\varepsilon_1^* + k^*k^*\varepsilon_1\varepsilon_2^*\varepsilon_2^*\varepsilon_1 + k^*kk^*\varepsilon_1\varepsilon_2^*\varepsilon_1\varepsilon_1^* \\
+k\varepsilon_1^*\varepsilon_2\varepsilon_2\varepsilon_2^* + kk\varepsilon_1^*\varepsilon_2\varepsilon_2\varepsilon_1^* + kk^*\varepsilon_1^*\varepsilon_2\varepsilon_2^*\varepsilon_1 + kkk^*\varepsilon_1^*\varepsilon_2\varepsilon_1\varepsilon_1^* \\
+kk^*\varepsilon_2\varepsilon_2^*\varepsilon_2\varepsilon_2^* + kkk^*\varepsilon_2\varepsilon_2^*\varepsilon_2\varepsilon_1^* + k^*kk^*\varepsilon_2\varepsilon_2^*\varepsilon_2^*\varepsilon_1 + kk^*kk^*\varepsilon_2\varepsilon_2^*\varepsilon_1\varepsilon_1^*
\end{bmatrix}
\end{aligned} \quad \text{(A.15)}$$

Following equations are satisfied from the property of gaussian noise's independency.

$$\begin{aligned}
&\mathrm{E}[\varepsilon_1\varepsilon_1^*\varepsilon_2^*\varepsilon_1]=\mathrm{E}[\varepsilon_2^*\varepsilon_1\varepsilon_1\varepsilon_1^*]=\mathrm{E}[\varepsilon_1\varepsilon_2^*\varepsilon_2\varepsilon_2^*]= \\
&\mathrm{E}[\varepsilon_1\varepsilon_2^*\varepsilon_1\varepsilon_1^*]=\mathrm{E}[\varepsilon_1^*\varepsilon_2\varepsilon_2\varepsilon_2^*]=\mathrm{E}[\varepsilon_1\varepsilon_2^*\varepsilon_2^*\varepsilon_1]= \\
&\mathrm{E}[\varepsilon_1^*\varepsilon_2\varepsilon_1\varepsilon_1^*]=\mathrm{E}[\varepsilon_2\varepsilon_2^*\varepsilon_2\varepsilon_1^*]=\mathrm{E}[\varepsilon_2\varepsilon_2^*\varepsilon_2^*\varepsilon_1]=0
\end{aligned} \quad \text{(A.16)}$$

$$\begin{aligned}
\mathrm{E}\left[\varepsilon_1\varepsilon_1^*\varepsilon_2\varepsilon_2^*\right] &= \sigma_1^{\,2}\sigma_2^{\,2} \\
\mathrm{E}\left[\varepsilon_1\varepsilon_1^*\varepsilon_1\varepsilon_1^*\right] &= 2\sigma_1^{\,4} \\
\mathrm{E}\left[\varepsilon_2\varepsilon_2^*\varepsilon_2\varepsilon_2^*\right] &= 2\sigma_2^{\,4}
\end{aligned} \quad \text{(A.17)}$$

The second term of equation (A.14) can be calculated as:

$$\begin{aligned}
&\mathrm{E}[(\varepsilon_1 + f(\varepsilon_2))(\varepsilon_1 + f(\varepsilon_2))^*]\mathrm{E}[\varepsilon_2 + f^*(\varepsilon_1))(\varepsilon_2 + f^*(\varepsilon_1))^*] \\
&= \mathrm{E}[\varepsilon_1\varepsilon_1^* + k^*\varepsilon_1\varepsilon_2^* + k\varepsilon_1^*\varepsilon_2 + kk^*\varepsilon_2\varepsilon_2^*]\mathrm{E}[\varepsilon_2\varepsilon_2^* + k\varepsilon_2\varepsilon_1^* + k^*\varepsilon_2^*\varepsilon_1 + kk^*\varepsilon_1\varepsilon_1^*] \\
&= (\sigma_1^{\,2} + kk^*\sigma_2^{\,2})(\sigma_2^{\,2} + kk^*\sigma_1^{\,2}) \\
&= \sigma_1^{\,2}\sigma_2^{\,2} + kk^*\sigma_1^{\,4} + kk^*\sigma_2^{\,4} + kk^*kk^*\sigma_1^{\,2}\sigma_2^{\,2}
\end{aligned} \quad \text{(A.18)}$$

Therefore, the first term of equation (A.13) can be calculated by the equation (A.15) to (A.18). Next, the second term of the equation (A.13) can be calculated as:

$$\begin{aligned}&\mathrm{Cov}\left(r_1(\varepsilon_1+f(\varepsilon_2))^*+r_1^*(\varepsilon_1+f(\varepsilon_2)),r_2(\varepsilon_2+f^*(\varepsilon_1))^*+r_2^*(\varepsilon_2+f^*(\varepsilon_1))\right)\\&=r_1r_2^*k^*(\sigma_1^{\,2}+\sigma_2^{\,2})+r_1^*r_2k(\sigma_1^{\,2}+\sigma_2^{\,2})\end{aligned}$$

(A.19)

From the equation (A.13) and (A.19), the covariance can be finally calculated as:

$$\begin{aligned}&\mathrm{Cov}(|Y(j\omega)|^2,|Y(j(\omega+\triangle\omega))|^2)\\&=\sigma_1^{\,2}\sigma_2^{\,2}(k^2+1)^2+2k^2(\sigma_1^{\,4}+\sigma_2^{\,4})-\left(\sigma_1^{\,2}\sigma_2^{\,2}+kk^*\sigma_1^{\,4}+kk^*\sigma_2^{\,4}+kk^*kk^*\sigma_1^{\,2}\sigma_2^{\,2}\right)\\&+r_1r_2^*k^*(\sigma_1^{\,2}+\sigma_2^{\,2})+r_1^*r_2k(\sigma_1^{\,2}+\sigma_2^{\,2})\\&=|k|^2\left(\sigma_1^{\,2}+\sigma_2^{\,2}\right)^2+2\,\mathrm{Re}\left[r_1^*r_2k(\sigma_1^{\,2}+\sigma_2^{\,2})\right]\end{aligned}$$

(A.20)

From the equation (A.9), the unknown terms, which are the original signal of uncertainty, denoted as σ_1 and σ_2, can be evaluated. Therefore, the covariance can be calculated by the equation (A.20).

Reference

[1] Z. Du, X. Jin, and Y. Yang, "Fault diagnosis for temperature, flow rate and pressure sensors in VAV systems using wavelet neural network," *Applied energy,* vol. 86, no. 9, pp. 1624-1631, 2009.

[2] B. A. Tama, M. Vania, S. Lee, and S. Lim, "Recent advances in the application of deep learning for fault diagnosis of rotating machinery using vibration signals," *Artificial Intelligence Review,* pp. 1-43, 2022.

[3] B. Cai *et al.*, "Data-driven early fault diagnostic methodology of permanent magnet synchronous motor," *Expert Systems with Applications,* vol. 177, p. 115000, 2021.

[4] D. Neupane and J. Seok, "Bearing fault detection and diagnosis using case western reserve university dataset with deep learning approaches: A review," *IEEE Access,* vol. 8, pp. 93155-93178, 2020.

[5] Z. Liu, X. Wang, and L. Zhang, "Fault diagnosis of industrial wind turbine blade bearing using acoustic emission analysis," *IEEE Transactions on Instrumentation and Measurement,* vol. 69, no. 9, pp. 6630-6639, 2020.

[6] O. AlShorman *et al.*, "Sounds and acoustic emission-based early fault diagnosis of induction motor: A review study," *Advances in Mechanical Engineering,* vol. 13, no. 2, p. 1687814021996915, 2021.

[7] S. J. Kim *et al.*, "Motor-current-based electromagnetic interference de-noising method for rolling element bearing diagnosis using acoustic emission sensors," *Measurement,* vol. 193, p. 110912, 2022.

[8] Y. Kim, J. Park, K. Na, H. Yuan, B. D. Youn, and C.-s. Kang, "Phase-based time domain averaging (PTDA) for fault detection of a gearbox in an industrial robot using vibration signals," *Mechanical systems and signal processing,* vol. 138, p. 106544, 2020.

[9] K. Na, H. Yoon, J. Kim, S. Kim, and B. D. Youn, "PERL: Probabilistic energy-ratio-based localization for boiler tube leaks using descriptors of acoustic emission signals," *Reliability Engineering & System Safety,* vol. 230, p. 108923, 2023.

[10] Y. Li, G. Cheng, and C. Liu, "Research on bearing fault diagnosis based on spectrum characteristics under strong noise interference," *Measurement,* vol. 169, p. 108509, 2021.

[11] C. He, H. Li, Z. Li, and X. Zhao, "An improved bistable stochastic resonance and its application on weak fault characteristic identification of centrifugal compressor blades," *Journal of Sound and Vibration,* vol. 442, pp. 677-697, 2019.

[12] T. Han and Y.-F. Li, "Out-of-distribution detection-assisted trustworthy machinery fault diagnosis approach with uncertainty-aware deep ensembles," *Reliability Engineering & System Safety,* vol. 226, p. 108648, 2022.

[13] W. Z. Khan, M. Rehman, H. M. Zangoti, M. K. Afzal, N. Armi, and K. Salah, "Industrial internet of things: Recent advances, enabling technologies and open

challenges," *Computers & Electrical Engineering,* vol. 81, p. 106522, 2020.

[14] Y. Wang, W. Ren, Y. Li, and C. Zhang, "Complex product manufacturing and operation and maintenance integration based on digital twin," *The International Journal of Advanced Manufacturing Technology,* vol. 117, pp. 361-381, 2021.

[15] O. Seryasat, F. Honarvar, and A. Rahmani, "Multi-fault diagnosis of ball bearing using FFT, wavelet energy entropy mean and root mean square (RMS)," in *2010 IEEE international conference on systems, man and cybernetics*, 2010: IEEE, pp. 4295-4299.

[16] V. Sharma and A. Parey, "Gearbox fault diagnosis using RMS based probability density function and entropy measures for fluctuating speed conditions," *Structural Health Monitoring,* vol. 16, no. 6, pp. 682-695, 2017.

[17] V. Sharma and A. Parey, "A review of gear fault diagnosis using various condition indicators," *Procedia Engineering,* vol. 144, pp. 253-263, 2016.

[18] E. Bechhoefer, R. Li, and D. He, "Quantification of condition indicator performance on a split torque gearbox," *Journal of Intelligent Manufacturing,* vol. 23, pp. 213-220, 2012.

[19] M. Brennan, M. Chen, and A. Reynolds, "Use of vibration measurements to detect local tooth defects in gears," *SV Sound and vibration,* vol. 31, no. 11, pp. 12-17, 1997.

[20] W. Wang, "Early detection of gear tooth cracking using the resonance demodulation technique," *Mechanical Systems and Signal Processing,* vol. 15, no. 5, pp. 887-903, 2001.

[21] Z. Feng, M. Liang, and F. Chu, "Recent advances in time–frequency analysis methods for machinery fault diagnosis: A review with application examples," *Mechanical Systems and Signal Processing,* vol. 38, no. 1, pp. 165-205, 2013.

[22] M. Zhang, H. Cui, Q. Li, J. Liu, K. Wang, and Y. Wang, "An improved sideband energy ratio for fault diagnosis of planetary gearboxes," *Journal of Sound and Vibration,* vol. 491, p. 115712, 2021.

[23] V. Vakharia, V. Gupta, and P. Kankar, "Bearing fault diagnosis using feature ranking methods and fault identification algorithms," *Procedia Engineering,* vol. 144, pp. 343-350, 2016.

[24] M. Biet, "Rotor faults diagnosis using feature selection and nearest neighbors rule: Application to a turbogenerator," *IEEE Transactions on Industrial Electronics,* vol. 60, no. 9, pp. 4063-4073, 2012.

[25] H. Lin, F. Wu, and G. He, "Rolling bearing fault diagnosis using impulse feature enhancement and nonconvex regularization," *Mechanical Systems and Signal Processing,* vol. 142, p. 106790, 2020.

[26] R. F. Gunst and R. L. Mason, "Fractional factorial design," *Wiley Interdisciplinary Reviews: Computational Statistics,* vol. 1, no. 2, pp. 234-244, 2009.

[27] K. Vanaja and R. Shobha Rani, "Design of experiments: concept and applications of Plackett Burman design," *Clinical research and regulatory affairs,* vol. 24, no. 1, pp. 1-23, 2007.

[28] S. K. Karna and R. Sahai, "An overview on Taguchi method," *International journal of engineering and mathematical sciences,* vol. 1, no. 1, pp. 1-7, 2012.

[29] M. Ahmadi, F. Vahabzadeh, B. Bonakdarpour, E. Mofarrah, and M. Mehranian, "Application of the central composite design and response surface methodology to the advanced treatment of olive oil processing wastewater using Fenton's peroxidation," *Journal of Hazardous Materials,* vol. 123, no. 1-3, pp. 187-195, 2005.

[30] W. Mao, Y. Liu, L. Ding, A. Safian, and X. Liang, "A new structured domain adversarial neural network for transfer fault diagnosis of rolling bearings under different working conditions," *IEEE Transactions on Instrumentation and Measurement,* vol. 70, pp. 1-13, 2020.

[31] H. Wu, J. Li, Q. Zhang, J. Tao, and Z. Meng, "Intelligent fault diagnosis of rolling bearings under varying operating conditions based on domain-adversarial neural network and attention mechanism," *ISA transactions,* vol. 130, pp. 477-489, 2022.

[32] L. Eren, T. Ince, and S. Kiranyaz, "A generic intelligent bearing fault diagnosis system using compact adaptive 1D CNN classifier," *Journal of Signal Processing Systems,* vol. 91, pp. 179-189, 2019.

[33] S.-s. Zhong, S. Fu, and L. Lin, "A novel gas turbine fault diagnosis method based on transfer learning with CNN," *Measurement,* vol. 137, pp. 435-453, 2019.

[34] T. Huang, Q. Zhang, X. Tang, S. Zhao, and X. Lu, "A novel fault diagnosis method based on CNN and LSTM and its application in fault diagnosis for complex systems," *Artificial Intelligence Review,* pp. 1-27, 2022.

[35] H. Kim *et al.*, "Opt-TCAE: Optimal temporal convolutional auto-encoder for boiler tuber leakage detection in a thermal power plant using multi-sensor data," *Expert Systems with Applications,* vol. 215, p. 119377, 2023.

[36] K. H. Hui, L. M. Hee, M. S. Leong, and A. M. Abdelrhman, "Time-frequency signal analysis in machinery fault diagnosis," *Advanced Materials Research,* vol. 845, pp. 41-45, 2014.

[37] H. Tao, P. Wang, Y. Chen, V. Stojanovic, and H. Yang, "An unsupervised fault diagnosis method for rolling bearing using STFT and generative neural networks," *Journal of the Franklin Institute,* vol. 357, no. 11, pp. 7286-7307, 2020.

[38] L.-H. Wang, X.-P. Zhao, J.-X. Wu, Y.-Y. Xie, and Y.-H. Zhang, "Motor fault diagnosis based on short-time Fourier transform and convolutional neural network," *Chinese Journal of Mechanical Engineering,* vol. 30, no. 6, pp. 1357-1368, 2017.

[39] L. Xu, S. Chatterton, P. Pennacchi, and C. Liu, "A tacholess order tracking method based on inverse short time fourier transform and singular value decomposition for bearing fault diagnosis," *Sensors,* vol. 20, no. 23, p. 6924, 2020.

[40] R. Yan, R. X. Gao, and X. Chen, "Wavelets for fault diagnosis of rotary machines:

A review with applications," *Signal processing,* vol. 96, pp. 1-15, 2014.

[41] Y. Cheng, M. Lin, J. Wu, H. Zhu, and X. Shao, "Intelligent fault diagnosis of rotating machinery based on continuous wavelet transform-local binary convolutional neural network," *Knowledge-Based Systems,* vol. 216, p. 106796, 2021.

[42] W. K. Ngui, M. S. Leong, L. M. Hee, and A. M. Abdelrhman, "Wavelet analysis: mother wavelet selection methods," *Applied mechanics and materials,* vol. 393, pp. 953-958, 2013.

[43] L. Li, L. Qu, and X. Liao, "Haar wavelet for machine fault diagnosis," *Mechanical Systems and Signal Processing,* vol. 21, no. 4, pp. 1773-1786, 2007.

[44] K. L. V. Iyer, X. Lu, Y. Usama, V. Ramakrishnan, and N. C. Kar, "A twofold Daubechies-wavelet-based module for fault detection and voltage regulation in SEIGs for distributed wind power generation," *IEEE Transactions on Industrial Electronics,* vol. 60, no. 4, pp. 1638-1651, 2012.

[45] R. Kumar and M. Singh, "Outer race defect width measurement in taper roller bearing using discrete wavelet transform of vibration signal," *Measurement,* vol. 46, no. 1, pp. 537-545, 2013.

[46] T. N. Babu, P. S. N. Ali, D. R. Prabha, V. N. Mohammed, R. S. Wahab, and S. Vijayalakshmi, "Fault Diagnosis in Bevel Gearbox Using Coiflet Wavelet and Fault Classification Based on ANN Including DNN," *Arabian Journal for Science and Engineering,* pp. 1-27, 2022.

[47] L.-Y. Zhao, L. Wang, and R.-Q. Yan, "Rolling bearing fault diagnosis based on wavelet packet decomposition and multi-scale permutation entropy," *Entropy,* vol. 17, no. 9, pp. 6447-6461, 2015.

[48] Y. Sun, Y. Cao, and P. Li, "Fault diagnosis for train plug door using weighted fractional wavelet packet decomposition energy entropy," *Accident Analysis & Prevention,* vol. 166, p. 106549, 2022.

[49] B. Tang, W. Liu, and T. Song, "Wind turbine fault diagnosis based on Morlet wavelet transformation and Wigner-Ville distribution," *Renewable Energy,* vol. 35, no. 12, pp. 2862-2866, 2010.

[50] H. Li, H. Zheng, and L. Tang, "Wigner-Ville distribution based on EMD for faults diagnosis of bearing," in *Fuzzy Systems and Knowledge Discovery: Third International Conference, FSKD 2006, Xi'an, China, September 24-28, 2006. Proceedings 3*, 2006: Springer, pp. 803-812.

[51] N. Baydar and A. Ball, "A comparative study of acoustic and vibration signals in detection of gear failures using Wigner–Ville distribution," *Mechanical systems and signal processing,* vol. 15, no. 6, pp. 1091-1107, 2001.

[52] J. Park, Y. Kim, K. Na, and B. D. Youn, "Variance of energy residual (VER): An efficient method for planetary gear fault detection under variable-speed conditions," *Journal of sound and vibration,* vol. 453, pp. 253-267, 2019.

[53] C. Ardito, Y. Deldjoo, T. Di Noia, E. Di Sciascio, and F. Nazary, "Visual inspection

of fault type and zone prediction in electrical grids using interpretable spectrogram-based CNN modeling," *Expert Systems with Applications,* vol. 210, p. 118368, 2022.

[54] A. Sapena-Bano, J. Burriel-Valencia, M. Pineda-Sanchez, R. Puche-Panadero, and M. Riera-Guasp, "The harmonic order tracking analysis method for the fault diagnosis in induction motors under time-varying conditions," *IEEE Transactions on Energy Conversion,* vol. 32, no. 1, pp. 244-256, 2016.

[55] Q. Jiang, F. Chang, and C. Liu, "A Spectrogram Based Local Fluctuation Feature for Fault Diagnosis with Application to Rotating Machines," *Journal of Electrical Engineering & Technology,* vol. 16, pp. 2167-2181, 2021.

[56] W. N. Lopes *et al.*, "An efficient short-time Fourier transform algorithm for grinding wheel condition monitoring through acoustic emission," *The International Journal of Advanced Manufacturing Technology,* vol. 113, pp. 585-603, 2021.

[57] G. Manhertz and A. Bereczky, "STFT spectrogram based hybrid evaluation method for rotating machine transient vibration analysis," *Mechanical Systems and Signal Processing,* vol. 154, p. 107583, 2021.

[58] C. Hory, N. Martin, and A. Chehikian, "Spectrogram segmentation by means of statistical features for non-stationary signal interpretation," *IEEE Transactions on Signal Processing,* vol. 50, no. 12, pp. 2915-2925, 2002.

[59] G. Parisi, A. Coluccia, and A. Fascista, "On time-frequency correlation in spectrogram samples with application to target detection," *Signal Processing,* vol. 200, p. 108648, 2022.

[60] F. Millioz, J. Huillery, and N. Martin, "Short time Fourier transform probability distribution for time-frequency segmentation," in *2006 IEEE International Conference on Acoustics Speech and Signal Processing Proceedings*, 2006, vol. 3: IEEE, pp. III-III.

[61] F. Millioz and N. Martin, "Estimation of a white Gaussian noise in the Short Time Fourier Transform based on the spectral kurtosis of the minimal statistics: Application to underwater noise," in *2010 IEEE International Conference on Acoustics, Speech and Signal Processing*, 2010: IEEE, pp. 5638-5641.

[62] K. Kim, G. Lee, K. Park, S. Park, and W. B. Lee, "Adaptive approach for estimation of pipeline corrosion defects via Bayesian inference," *Reliability Engineering & System Safety,* vol. 216, p. 107998, 2021.

[63] L. An, P. Wang, A. Sarti, F. Antonacci, and J. Shi, "Hyperbolic boiler tube leak location based on quaternary acoustic array," *Applied thermal engineering,* vol. 31, no. 16, pp. 3428-3436, 2011.

[64] D.-H. Kim, B.-S. Yang, and S.-B. Lee, "3D boiler tube leak detection technique using acoustic emission signals for power plant structure health monitoring," in *2011 Prognostics and System Health Managment Confernece*, 2011: IEEE, pp. 1-7.

[65] M. D. Kafle, S. Fong, and S. Narasimhan, "Active acoustic leak detection and localization in a plastic pipe using time delay estimation," *Applied Acoustics,* vol. 187, p. 108482, 2022.

[66] X. Li, Z. D. Deng, L. T. Rauchenstein, and T. J. Carlson, "Contributed Review: Source-localization algorithms and applications using time of arrival and time difference of arrival measurements," *Review of Scientific Instruments,* vol. 87, no. 4, p. 041502, 2016.

[67] O. Hunaidi and W. T. Chu, "Acoustical characteristics of leak signals in plastic water distribution pipes," *Applied Acoustics,* vol. 58, no. 3, pp. 235-254, 1999.

[68] X. Li, X. Zhong, H. Shao, T. Han, and C. Shen, "Multi-sensor gearbox fault diagnosis by using feature-fusion covariance matrix and multi-Riemannian kernel ridge regression," *Reliability Engineering & System Safety,* vol. 216, p. 108018, 2021.

[69] N. Li, N. Gebraeel, Y. Lei, X. Fang, X. Cai, and T. Yan, "Remaining useful life prediction based on a multi-sensor data fusion model," *Reliability Engineering & System Safety,* vol. 208, p. 107249, 2021.

[70] C. Liu, Y. Wang, X. Li, Y. Li, F. Khan, and B. Cai, "Quantitative assessment of leakage orifices within gas pipelines using a Bayesian network," *Reliability Engineering & System Safety,* vol. 209, p. 107438, 2021.

[71] D. H. Kim and S. B. Lee, "Development of precise source location and leak monitoring technique 3D point location method for power plant boiler structure," in *31st Conference of the European Working Group on Acoustic Emission*, 2014.

[72] L. Calabrese and E. Proverbio, "A review on the applications of acoustic emission technique in the study of stress corrosion cracking," *Corrosion and Materials Degradation,* vol. 2, no. 1, pp. 1-30, 2020.

[73] J. M. Valverde, "Acoustic streaming in gas-fluidized beds of small particles," *Soft Matter,* vol. 9, no. 37, pp. 8792-8814, 2013.

[74] H.-C. Zhou *et al.*, "Experimental investigations on visualization of three-dimensional temperature distributions in a large-scale pulverized-coal-fired boiler furnace," *Proceedings of the Combustion Institute,* vol. 30, no. 1, pp. 1699-1706, 2005.

[75] R. Kapoor, S. Ramasamy, A. Gardi, R. V. Schyndel, and R. Sabatini, "Acoustic sensors for air and surface navigation applications," *Sensors,* vol. 18, no. 2, p. 499, 2018.

[76] J. Park, M. Hamadache, J. M. Ha, Y. Kim, K. Na, and B. D. Youn, "A positive energy residual (PER) based planetary gear fault detection method under variable speed conditions," *Mechanical Systems and Signal Processing,* vol. 117, pp. 347-360, 2019.

[77] Z. Feng, W. Zhu, and D. Zhang, "Time-Frequency demodulation analysis via Vold-Kalman filter for wind turbine planetary gearbox fault diagnosis under nonstationary speeds," *Mechanical systems and signal processing,* vol. 128, pp. 93-109, 2019.

[78] Z. Feng and F. Chu, "Cyclostationary analysis for gearbox and bearing fault diagnosis," *Shock and Vibration,* vol. 2015, 2015.

[79] R. Zimroz and W. Bartelmus, "Gearbox condition estimation using cyclo-stationary properties of vibration signal," in *Key Engineering Materials*, 2009, vol. 413: Trans Tech Publ, pp. 471-478.

[80] R. Bai, Q. Xu, Z. Meng, L. Cao, K. Xing, and F. Fan, "Rolling bearing fault diagnosis based on multi-channel convolution neural network and multi-scale clipping fusion data augmentation," *Measurement,* vol. 184, p. 109885, 2021.

[81] E. Sejdić, I. Djurović, and J. Jiang, "Time–frequency feature representation using energy concentration: An overview of recent advances," *Digital signal processing,* vol. 19, no. 1, pp. 153-183, 2009.

[82] R. A. Ayon-Sicaeros, E. Cabal-Yepez, L. M. Ledesma-Carrillo, and G. Hernandez-Gomez, "Broken-rotor-bar detection through STFT and windowing functions," in *2019 IEEE Sensors Applications Symposium (SAS)*, 2019: IEEE, pp. 1-5.

[83] N. S. D. Brito, B. A. de Souza, W. C. dos Santos, and L. M. de Andrade Fortunato, "Analysis of the influence of the window used in the Short-Time Fourier Transform for High Impedance Fault detection," in *2016 17th International Conference on Harmonics and Quality of Power (ICHQP)*, 2016: IEEE, pp. 350-355.

[84] H. Zhivomirov, "On the development of STFT-analysis and ISTFT-synthesis routines and their practical implementation," *TEM Journal,* vol. 8, no. 1, pp. 56-64, 2019.

[85] J. Huillery, F. Millioz, and N. Martin, "On the description of spectrogram probabilities with a chi-squared law," *IEEE Transactions on Signal Processing,* vol. 56, no. 6, pp. 2249-2258, 2008.

[86] B. W. Silverman, *Density estimation for statistics and data analysis*. CRC press, 1986.

[87] Yang, Q., Li, X., Wang, Y., Ainapure, A. and Lee, J., 2020. Fault diagnosis of ball screw in industrial robots using non-stationary motor current signals. *Procedia manufacturing*, 48, pp.1102-1108.

[88] Wu, C., Guo, C., Xie, Z., Ni, F. and Liu, H., 2018. A signal-based fault detection and tolerance control method of current sensor for PMSM drive. *IEEE Transactions on Industrial Electronics,* 65(12), pp.9646-9657.

[89] Aatola, S., 1989. Transmission of vibration to the wrist and comparison of frequency response function estimators. *Journal of Sound and Vibration,* 131(3), pp.497-507.

국문 초록

저샘플링 및 고샘플링 신호를 이용한 불확실성 기반 고장 진단 프레임워크

산업 시스템은 4차 산업혁명과 더불어 급속도로 발전하고 있으며, 이에 따라 시스템의 규모는 증가하고 이를 제어 및 관리하기 위한 자동화 시스템의 도입도 전반적으로 증가하는 추세이다. 이러한 대규모 복합 시스템의 예기치 못한 고장은 막대한 사회적, 경제적, 인적 손실을 야기할 가능성이 있다. 이러한 상황을 예방하고 진단하기 위해서, 시스템을 이루고 있는 여러 요소들에 대한 고장 진단 연구가 주목을 받고 있으며, 관련된 연구가 전세계적으로 계속해서 수행되고 있다. 이러한 고장 진단 기법들은 목표 시스템에서 발생할 수 있는 고장을 분석하여 건전성 지표를 통해 수치화 하고, 건전성 상태를 관리하는 것을 목표로 하고 있다.

최근 산업계에서는 온도, 압력, 운전, 진동, 음향 신호 등 다양한 신호를 통해 산업 시스템을 제어함과 동시에 상태 진단에 활용하기 위한 신호 시스템을 구축하고 있다. 특히 이 중에서, 진동과 음향 신호는 시스템의 건전성을 평가할 수 있는 좋은 민감성을 가지고 있다고 평가되고 있다. 이러한 진동/음향 신호는 일반적으로 20kHz 이상의 높은 샘플링 주파수를 가지는 데이터 수집 센서 및 시스템을 기반으로 취득된다. 이렇게 고주파수 신호가 측정되면, 이를 바탕으로 스펙트럼 분석을 수행하여 정상 상태에서 측정될 것으로 기대되는 결과와의 차이를 바탕으로 건전성을 평가하는 방법이 주로 사용된다. 특히, 점진적인 고장의 초기단계의 진단이나 미세한 크랙등의 적은 에너지 변화를 띄는 고장의 경우 고샘플링 신호 기반 스펙트럼 분석을 통한

진단 방법론의 성능이 탁월하다. 이러한 접근법은 많은 연구에서 검증이 되었으며, 실제 산업 현장에서도 적용 가능성을 검증한 사례도 존재한다. 하지만, 현대 산업 시스템과 같이 매우 큰 규모를 가지는 시스템의 경우 이러한 고샘플링 신호를 온전히 활용하여 진단을 수행하기에는 어려운 점이 많다. 각 센서에 활용되는 데이터 수집 시스템에는 프리-앰플리파이어, 선형 주파수 필터링 등 간단한 계산을 기반으로 하는 전처리를 수행할 수 있는 계산 능력은 갖추고 있으나, 고샘플링 신호를 세분화하여 분석하는 기법을 적용하기 위한 계산 능력을 갖추고 있지는 않으며, 추가적인 설비를 필요로 한다. 따라서, 고샘플링 신호를 계산 수행을 하는데 부담이 되지 않는 저샘플링 신호 (제곱평균제곱근, 밴드패스 에너지) 등으로 변환하여 데이터를 수집하고 건전성 평가에 활용하고 있다. 이러한 이유 때문에, 실제 산업 시스템에서는 특정 주파수에서 반응하는 고장보다는 모든 주파수 대역에서 에너지가 증가하는 경향성을 보이는 급진적인 고장이나 규모가 큰 파괴 등의 고장 진단만을 수행할 수 있는 저샘플링 신호 기반 진단 방법을 제한적으로 적용하고 있다. 하지만 이러한 저샘플링 신호 기반 진단 기법 또한, 적용할 수 있는 범위가 큰 고장에 국한되기 때문에 다량의 센서가 반응한다는 문제점이 있다. 이는 고장 감지 후 정비 측면에서 큰 비효율을 야기할 수 있다. 마지막으로, 산업 현장에서 취득되는 신호는 상대적으로 실험실 단위에서 취득되는 신호보다 노이즈나 외부 신호에 의한 불확실성이 크다는 문제점이 존재한다. 따라서, 적용될 방법론에 불확실성을 감안하여 결과를 도출할 수 있는 과정이 포함되어야 실제 적용 시 발생할 수 있는 오차의 정도를 추산하거나 미연에 방지할 수 있다.

이러한 산업 시스템의 현황을 고려하여, 저샘플링 신호와 고샘플링 신호를 효율적으로 활용하는 고장 진단 연구가 수행될 수 있다. 현재 존재하는 기법들을 활용하여 산업 시스템의 고장 진단 기법을 개발하는 데 해결해야 할 문제점은 다음과 같이 세 가지로 정리할 수 있다. 첫째, 저샘플링 신호 기반 진단 시 다량의 센서가 반응하기 때문에, 효율적인

정비를 위해 고장 위치에 대한 추정 결과가 필요하다. 둘째, 고샘플링 신호 기반 진단 시 많은 계산량이 요구되기 때문에, 일부 데이터를 활용하더라도 강건한 고장 진단을 할 수 있는 기법이 요구된다. 셋째, 산업 현장에서 취득 될 신호의 불확실성을 감안하는 방법론이 저샘플링과 고샘플링 신호 기법 모두에 적용되어야 한다.

따라서 본 학위 논문에서는 이러한 문제점을 감안하여 산업 시스템의 저샘플링과 고샘플링 신호를 활용한 불확실성 기반 진단 프레임워크를 제안한다. 첫 번째 연구에서는 저샘플링 신호를 활용한 고장 위치의 추정 방법론을 제안한다. 제안하는 방법은 정상 상태에서 취득되는 신호와 고장 상태에서 취득 될 신호의 에너지 차이를 감안하여, 고장 신호가 저샘플링 신호로 변환됐을 때 센서에서 측정되는 신호의 에너지 확률 모형을 제안한다. 이후, 특정 위치에서 고장 신호가 발생했을 때, 다량의 센서에서 측정되는 에너지를 확률적으로 정량화 할 수 있다. 최종적으로 역-베이지안 기법을 활용하여, 측정된 센서 간의 에너지 비율을 토대로 여러 특정 위치에서의 확률 값을 도출함으로써, 고장 위치를 확률적으로 추정할 수 있다. 두 번째 연구에서는 고샘플링 신호를 활용한 강건한 고장 진단 방법론을 제안한다. 우선적으로 정상 상태에서 취득되는 신호를 바탕으로 운행 조건을 반영할 수 있도록, 쿨백-라이블러 발산 기반 신호 유사성 평가 기법을 제안한다. 이를 바탕으로 유사한 신호를 그룹핑하여 운행 조건에 따라 달라지는 신호의 시간-주파수 표현의 확률적 모델링을 수행한다. 이를 통해서 새롭게 측정된 신호가 운행 조건을 알 수 없는 짧은 신호라고 하더라도, 유사한 운행 조건 그룹과 비교할 수 있게 된다. 이후, 정상 상태에서 취득 될 확률 모델과 새로운 측정 신호를 비교하여 고장 상태를 판별할 수 있는 새로운 특성값과, 고장 상태별로 달라질 수 있는 시간-주파수 정보 및 상응하는 특성값의 범위를 반영하는 적응형 임계값을 제안하여 강건한 고장 진단을 수행한다. 마지막으로 저샘플링 신호를 통해 나온 결과값을 기준으로 데이터 샘플링을 적용하여, 고샘플링 평가 기법을

적용함으로써 계산시간의 단축과 최종 결과의 확률적 강건성을 확보한다.

주요어: 고장 진단
불확실성 확률 모델링
주파수 분석
저샘플링 신호
고샘플링 신호
건전성 예측 및 진단

학 번: 2016-29867